NON-COLLINEAR SPIN-TORQUE DRIVEN EXCITATION IN NANOMAGNETS

A Dissertation

Presented to the Faculty of the Graduate School

of Cornell University

in Partial Fulfillment of the Requirements for the Degree of

Doctor of Philosophy

by

OukJae Lee

January 2013

NON-COLLINEAR SPIN-TORQUE DRIVEN EXCITATION IN NANOMAGNETS

OukJae Lee, Ph.D.

Cornell University 2013

This dissertation summarizes my investigations in non-collinear spin-transfer-torque (ST) effects on nanomagnets. The Slonczewksi-like ST mostly competes with the damping torque in a device structure where the spin polarization (SP) is collinear to the magnetic moment of a free layer (FL) at equilibrium. Contrarily the ST has both (anti-)damping and an equivalent field torque effects in non-collinear configurations in which the SP is close to perpendicular to the FL. The additional field effect of the ST shifts the equilibrium or dynamic offset angle of the FL and thereby changes the characteristics of the excitations.

In my first study, I demonstrated the ST-driven ultrafast nanomagnet switching in nanopillar spin-valve devices incorporating both an out-of-plane spin-polarizer and an in-plane polarizer/analyzer, with pulse widths down to 50 ps. I also explained the physical origin of the observed asymmetric threshold currents as functions of the switching direction and the pulse polarity, which is beneficial for a non-toggle write operation. In addition I proposed methods to suppress the magnetic ringing that occurs after the ballistic switching.

In my second study, I discovered quasi-linear behavior of a spin-torque nano-oscillator under an external hard axis magnetic field that controls the precession axis of the FL and its offset angle from the SP. The observed linewidth ($\sim$ 5 MHz) was very close to the fundamental limit determined by thermal driven noise. The quasi-linearity, or the cancellation of the nonlinear coupling between

the amplitude fluctuation and phase noise, was achieved by obtaining a small frequency agility together with a negative feedback effect from the ST causing the enhancement of the dynamical damping.

In my third study, I investigated perpendicularly magnetized Co nanodot switching via spin-Hall-induced spin currents. In the thermally activated reversal regime I estimated the current-induced effective field (H_s) that has a magnitude within the predicted range due to the large spin-Hall angle in Pt when the Joule heating effect is taken into account for the magnetic system. In addition an excitation of a subvolume drove the entire magnetization switching, thus even a small but heat-assisted H_s was able to reverse such a Co dot with a strong perpendicular magnetic anisotropy.

BIOGRAPHICAL SKETCH

OukJae Lee received his Bachelor's degrees in Physics and Mathematics from Seoul National University in Korea. He enrolled in the PhD program of Applied Physics at Cornell University in 2005 and joined the Buhrman research group later. He met his wife, JinKyung Kwak, who was also a PhD student in the Johnson Graduate School of Business at Cornell University at that time. They got married in 2010 and a year later, their adorable daughter, Diane (DaYeon) Lee, was born on the Valentine's Day. OukJae is expecting the doctoral degree.

To my parents, wife and daughter, for their love.

ACKNOWLEDGEMENTS

This dissertation could not have been completed without help from a lot of people. I would like to acknowledge all the people who have encouraged, inspired, motivated, helped and supported me over the years.

First of all, I owe my sincere gratitude to Prof. Robert Buhrman. I have been very fortunate to have him as my advisor. I have learned from him how to identify and to solve problems definitely. He knows what will get attentions and how to convince people. This dissertation has not been possible without his encouragement, guidance, and support. I would also like to thank my other committee members, Profs. Dan Ralph and Bruce VanDover, for their time, support, and assistance. Dan has asked always keen questions and I respect his deep insight on physics and experiments. Bruce is a big master in the fields of thin-film growth and magnetism. I am very lucky to have them as my advisors.

My lab-mates, Praveen Gowtham, Taka Moriyama, Luqiao Liu, Hsinwei Tseng, Yun Li, Junbo Park, Chi-Feng Pai, Vlad Pribiag, Pat Braganca, Ozhan Otazay, Ziphan Li, John Read, Eric Ryan, Yongtao. Cui, Lin Xue, Sufei Shi, Chen Wang, Ted Gudmundsen and Greg Fuchs, have been giving me lots of inspiration and help. I also thank the very professional CNF staffs, CNS/CCMR staffs. Special thanks to my parents, my brother, and my wife for their endless support and trust. I am also grateful to my friends who always encourage me. Finally, I would like to give my gratitude to my baby girl Diane, whose smile has encouraged me to finalize this dissertation.

TABLE OF CONTENTS

LIST OF FIGURES

CHAPTER 1

INTRODUCTION AND BACKGROUND

1.1 Brief introduction of Spintronics

Spintronics explores phenomena that interconnect the spin and charge degrees of freedom in the solid-state whereas information is encoded in carriers' spin rather than their charge [1, 2, 3, 4, 5, 6]. This field has been at the center of condensed matter physics during the last two decades. And it has suggested pathways to overcome the limitations faced by the conventional charge-based electronics because reorientation of electron's spin is fundamentally faster and requires less energy than moving electron or atom from one place to another.

One big successful example in Spintronics is the giant magnetoresistance (GMR) effect [7, 8] that has had broad scientific and technological impact and the discovery of GMR awarded 2007 Nobel Prize in Physics to Peter Grünberg and Albert Fert [9, 10]. GMR is an electric transport phenomenon that arises in magnetic and non-magnetic multilayer thin-films, resulting in giant changes in the electrical resistance due to an external magnetic field. The device resistance is a function of the relative angle (θ) between the magnetization in the two ferromagnetic layers. The fractional resistance change, the GMR ratio, is $\frac{\Delta R}{R_P} = \frac{R_{AP}-R_P}{R_P} \approx 2-20\ \%$. This discovery has led to the development of novel magnetic devices such as GMR based magnetic field sensors (used to read data in current hard-disk drives) or magnetic random access memory (MRAM).

For MRAM to be realized, more efficient methods of manipulating spin should be developed because the generation of magnetic field (typically current-

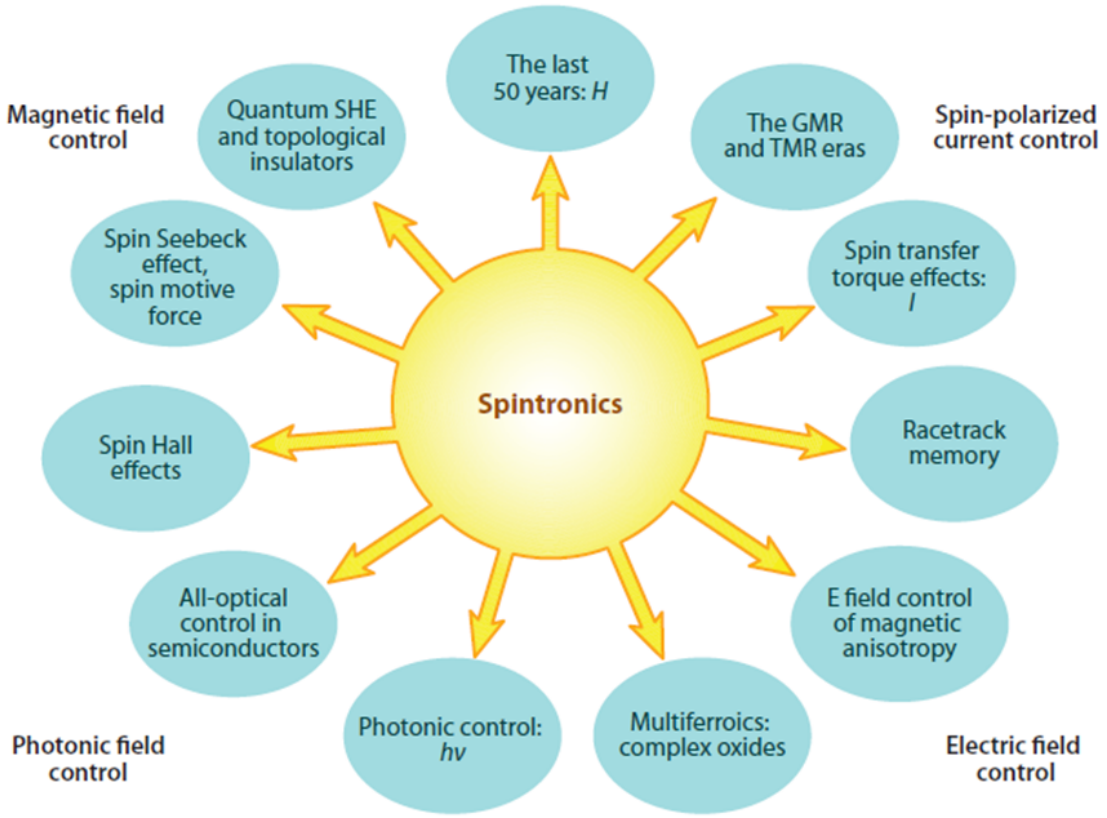

Figure 1.1: Glimpse of sub-fields featured in Spintronic phenomena. (From [1]). We can manipulate the magnetization or spin by applying a magnetic field, a spin-polarized current, an electric field or a circularly polarized light pulse. See Ref. [1, 2, 3, 4, 5, 6] for comprehensive review on Spintronics.

induced Oersted field) is usually energy inefficient. One promising approach to change the magnetization is by injecting spin-currents (in order to transfer spin-angular momentum and to exert a torque) or recently by controlling magnetic anisotropy via external electric fields. Another promising application is the current-controlled microwave generator based on the spin-torque induced precession of magnetization, which converts a DC current into an AC voltage output. The frequency can be tuned from a few hundred MHz to over 100 GHz with an applied magnetic field or a DC current. Alternative developed technology is the utilization of current-driven domain-wall motion of a ferromag-

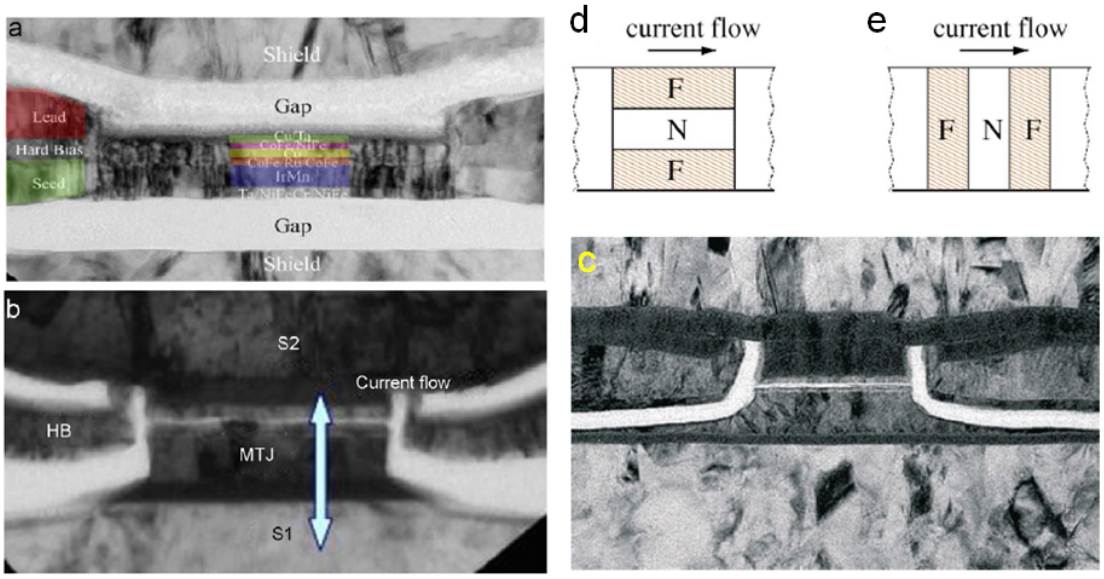

Figure 1.2: (a) Illustration of transmission electron microscopy (TEM) cross-section image of a current-in-plane (CIP) read head sensor. (b) Illustration of TEM cross-section image of a current-perpendicular-to-the-plane (CPP) read head sensor based on a magnetic tunnel junction (MTJ). (c) Another TEM example of a MTJ read head sensor. The tunnel barrier clearly appears at the center with a white horizontal line. (d) Device scheme of the CIP configuration. (e) Device scheme of the CPP configuration. The directions of current flow are indicated. (a)-(b) from [13], (c) from [4]. (d)-(e) from [5].

netic wire for memory (called Racetrack memory [11]) and logic applications [12]. Utilization and control of spin and magnetism in a variety of materials and nanostructures will also have broad impact.

In the following sections, I will overview some of the important topics that are very closely related to the rest of this dissertation, with emphases on the spin-transfer-torque effect, MRAM, magnetic tunnel junctions, spin-torque nano-oscillator (STNO) and the non-linear auto-oscillator model.

1.2 Overview of Spin-Transfer-Torque

Spin currents consist of a flow of spin angular momentum when there is an imbalance between up- and down-spins [2, 3, 5]. Spin-transfer torque is an electric transport phenomenon that spin currents transport spin angular momentum, and thereby exert a torque on the local magnetic moment [14, 15, 16, 13, 17, 18, 19, 20, 21, 22, 23]. The basic physics of spin-transfer torque is the exchange interaction between the electrons in the spin currents and the localized spin-polarized electrons in ferromagnets. This results in a reorientation of transmitted electron spins through the thin ferromagnetic layer, and the conservation of angular momentum leads to a torque or a change in the local magnetic moments (see Fig. 1.3).

Since Sloncwezski [14] and Berger [15] theoretically predicted the spin-transfer torque effect in magnetic multilayers in 1996, the existence of the torque has been demonstrated in most of magnetic materials including ferromagnetic transition metals [16, 24], dilute magnetic semiconductors [25, 26], and moreover in ferrimagnets [27, 19], antiferromagnets [28, 19] or at the interface of ferromagnetic insulators [29, 30]. The experiments have been carried out in various device geometries including nanoscale point contacts [31, 32, 33, 34], nanopillar spin-valves [16, 24, 35], magnetic tunnel junctions [36, 37, 38], and lateral spin-valves [39, 40]. The spin-torque phenomenon has been the mainstream in the field of spintronics during the last decade because it promises technological development of next-generation of high areal density (> 1 Tbit/in^2) magnetic memories [13, 41, 42, 43], microwave components [13, 44, 45, 46], high-performance logic-in-memory architectures [47, 48], and domain-wall memory (see Fig. 1.8) and logic devices [11, 12, 49, 50].

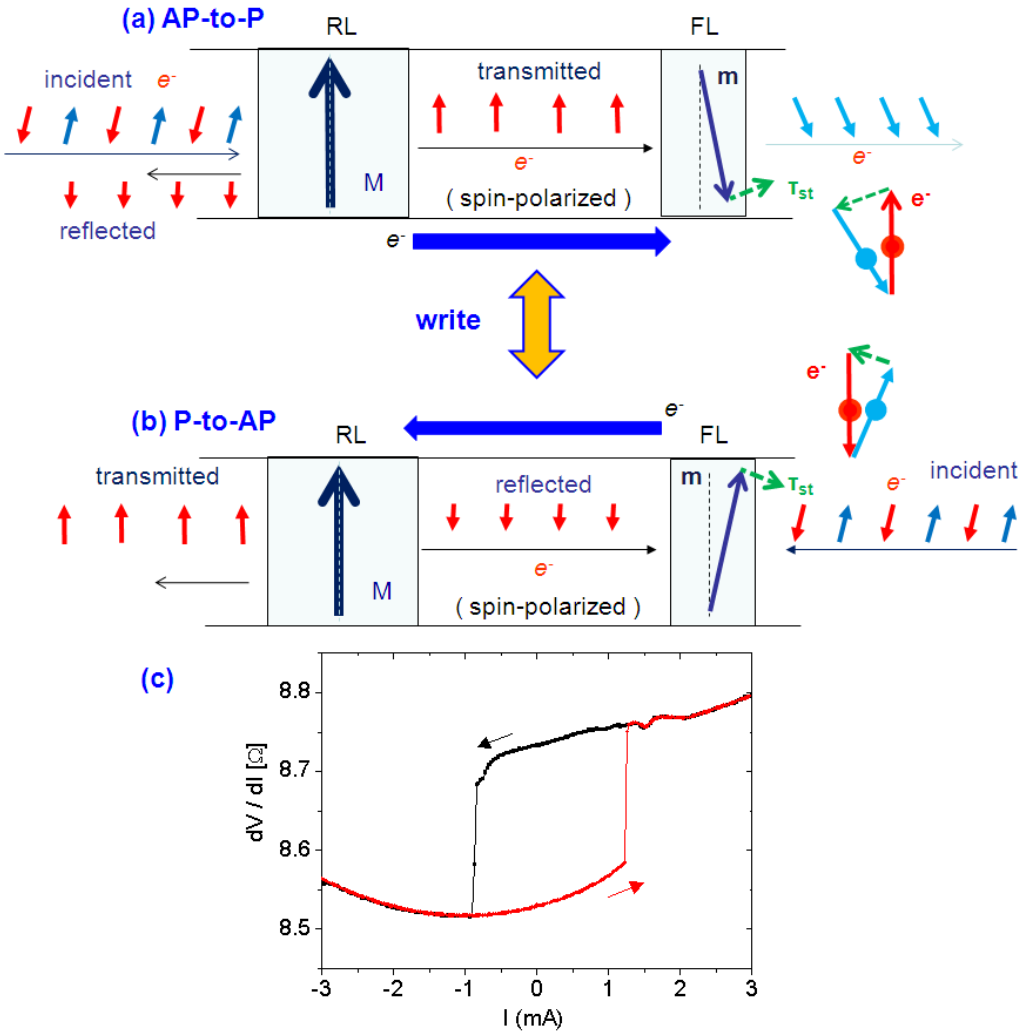

Figure 1.3: Illustration spin angular momentum transfer via spin-polarized moving electrons (a) for anti-parallel or (b) for parallel configuration between the magnetic free layer (FL) and the reference layer (RL). (c) Example of measured spin-torque-driven magnetization switching. When unpolarized moving electrons encounter the RL, the magnetic moments of transmitted electrons become polarized to the parallel of the magnetization of the RL layer (in (a)) while reflected electrons have opposite magnetic moments (in (b)), due to the exchange interactions between the electrons in the currents and the electrons in the local ferromagnets. Upon incidence on the FL, the transverse component of the spin is absorbed at the interface. The conservation of spin angular momentum, in the absence of spin-orbit coupling, leads to a torque on the FL moment, referred to as spin-transfer-torque. Direction of spin-torque on the FL depends on the current polarity.

The spin torque (ST) consists of the in-plane torque ($\tau_{\parallel}$: alternatively called adiabatic or Sloncwezski-like torque) and the perpendicular torque ($\tau_{\perp}$: alternatively called non-adiabatic, out-of-plane torque, or field-like), that are added to the right side of the Landau-Lifshitz-Gilbert equation (in the macrospin limit):

$$\frac{d\hat{m}}{dt} = -\gamma \hat{m} \times \vec{H}_{eff} + \alpha \hat{m} \times \frac{d\hat{m}}{dt} + \tau_{\parallel} + \tau_{\perp},$$

where γ is the gyromagnetic ratio, α is the magnetic damping of the magnetic free layer (FL) and H_{eff}, the total effective magnetic field on the FL, is derived from the total magnetic energy (E), $H_{eff} = -\frac{\partial E}{\partial \hat{m}}$. Here "in-plane" refers to the plane defined by two vectors: the direction of the local moment ($\hat{m}$) and the one of spin-polarization ($\hat{p}$). A variety of theoretical [14, 15, 51, 52, 53, 17] and experimental [54, 16, 24, 35, 17] works have confirmed that the spin transfer torque has the following picture (see Fig. 1.3). The current spins that flow through the magnetic reference layer (RL) are spin-polarized along the magnetization ($\hat{p}$) of the RL, which is called spin-filtering effect. If $\hat{p}$ and $\hat{m}$ are not collinear, the conduction electron spins that encounter the magnetic free-layer (FL) generally possesses a component of angular momentum that is transverse to the $\hat{m}$ and this transverse component of angular momentum is largely absorbed at the interface between the FL and the non-magnetic spacer. In the macrospin approximation, the absorbed angular momentum generates the in-plane ST,

$$\tau_{\parallel} = \gamma \frac{\hbar/2}{e} \frac{PJ}{M_s t} g(\theta) \hat{m} \times (\hat{p} \times \hat{m}) \tag{1.1}$$

where M_s is the saturation magnetization of the FL, t is the thickness of the FL, J is the current density, $g(\theta)$ is the angular dependence of ST efficiency (from the spin-dependent transport and/or reflection/transmission), and θ is the angle between the RL and FL (see Ref. [53, 17] for the $g(\theta)$). The $\tau_{\parallel}$ accounts for non-equilibrium processes that cannot be described by a magnetic energy. First-

principle calculations [51, 52, 55] showed that a transverse spin current at the interface of a FL is not perfectly absorbed, especially when the thickness of the FL is comparable or thinner than its spin decoherence length. The survived spins (not absorbed by the FL) are polarized to both $\hat{m}$ and $\hat{p}$ and give the perpendicular ST,

$$\tau_{\perp} = \beta\gamma \frac{\hbar/2}{e} \frac{PJ}{M_s t} g(\theta) \hat{m} \times \hat{p}, \tag{1.2}$$

to the FL. The contribution of $\tau_{\perp}$ is usually neglected in spin-valve devices because the calculations and experiments have found that β is negligible in metallic spin-valve devices [56]. In the mean time, several groups have conducted experiments such as spin-torque ferromagnetic resonance (ST-FMR) or magnetic switching in order to identify and estimate the magnitudes of the $\tau_{\parallel}$ and $\tau_{\perp}$ in magnetic tunnel junctions with MgO tunnel barriers (MgO-MTJs) [22, 57, 58, 59]. They have found that the β is significant in MgO-MTJs and that the $\tau_{\perp}$ substantially affects the magnetic dynamics of the FL, although the bias-dependence of the torques ($\tau_{\parallel} = a_1 V + a_2 V^2$ and $\tau_{\perp} = b + b_1 V + b_2 V^2$) are dissimilar in details between materials, ferromagnetic electrodes or research groups [57, 58, 60, 59]. The relative magnitude of two ST components depends on the insulating or ferromagnetic materials and device structures [23, 22], and engineering it is critical for determining the magnetic dynamics.

The most common device geometry utilizes a nanoscale current-perpendicular-to-the-plane (CPP) configuration with two thin metallic ferromagnetic layers separated by a non-magnetic metallic spacer (NM) or by an ultra-thin non-magnetic insulator (I): i.e. the multilayer of a typical ST device consists of FM/NM/FM or FM/I/FM where FM is a ferromagnetic electrode. The first FM layer is a spin polarizing layer (or reference magnetic layer) whose magnetization is hard to change by designing it thicker or pinned by an in-

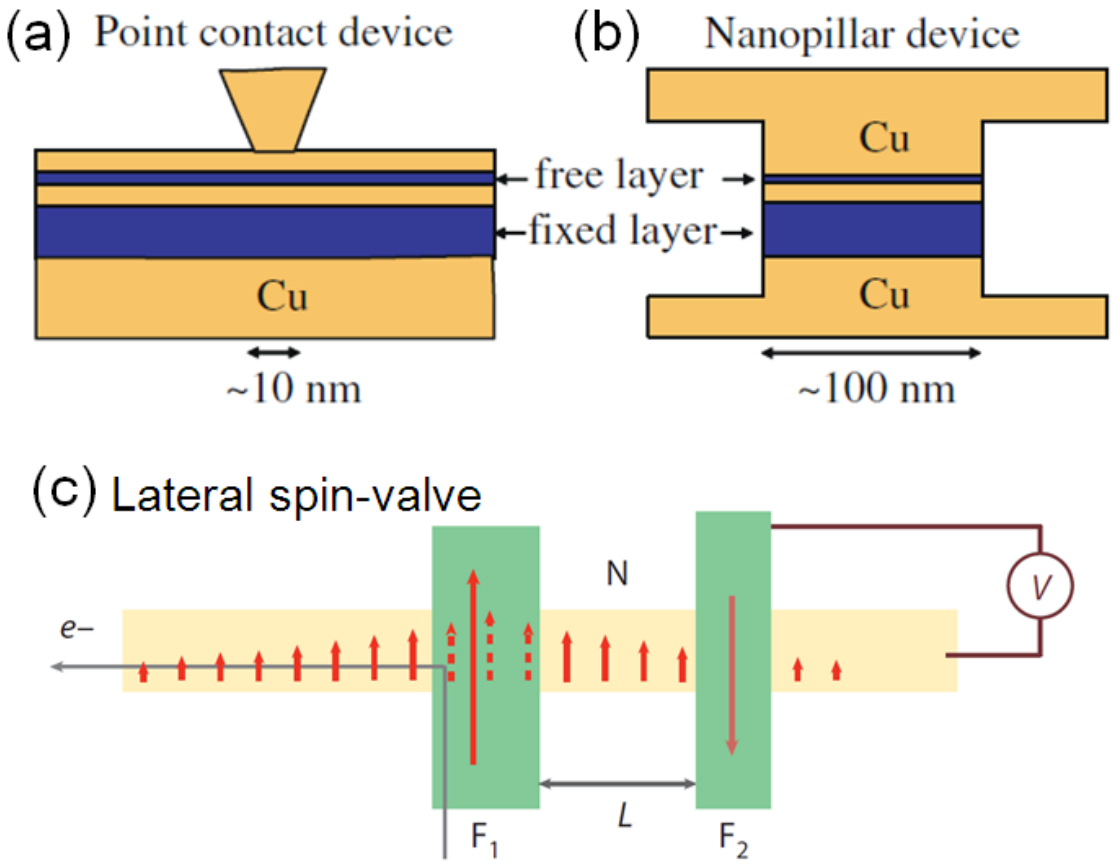

Figure 1.4: Schematic of various device configurations: (a) un-patterned nano-scale point contact (b) patterned nanopillar and (c) lateral (or non-local) spin-valve device. In a nanopillar structure at least the magnetic free layer (FL) is patterned or both the FL and the magnetic reference layer are fully patterned. A non-local device is designed to generate spin-imbalance (pure spin currents) in a normal metal that is contact with two ferromagnetic leads. One contact lead is used to generate a spin-polarized current while the other lead is for a detector by measuring a voltage. One can classify a device into metallic spin-valve or magnetic tunnel junction depending on the type of non-magnetic spacer. The ferromagnets can be magnetized to in-plane or out-of-plane depending on the utilized materials. From [17, 44]

terface anti-ferromagnetic layer. The second FM layer is a magnetic free layer (FL) whose magnetic moment is free to rotate in response to the spin-transfer torque. The lateral dimension of a ST device should be small (< 200 nm) because high current densities are required ($J > 10^6 - 10^7 A/cm^2$) for achieving significant amount of spin angular momentum in the transported electrons [13, 18].

In a ST device the thickness of a NM should be shorter than its spin-diffusion length (spin-flip relaxation length) in order to avoid depolarization of the spin-polarized carriers. Copper (Cu) is the most common material as a NM in metallic spin-valve device because the spin-flip relaxation length for Cu is very long (> 100 nm) at room temperature [61]. Alternative spacer is an ultrathin insulator (< 1 nm) that is enough to allow electrons tunneling through the barrier. The electrical properties of tunnel junctions are determined by the tunneling process, how the spin-dependent wave-functions decay in the barrier, and the density of available states in the ferromagnetic electrodes [62, 63]. The most common MTJs nowadays use MgO (001) barriers with crystallized BCC CoFeB electrodes, with which 600 % TMR was recently demonstrated at room temperature [64].

Most theoretical and experimental works of spin-transfer-torques have studied in a system where the spin-orbit coupling is very weak because it is considered to be detrimental due to the spin-memory loss from the enhanced spin-relaxation or magnetic damping induced by the spin-pumping process [65, 66]. Above in-plane and perpendicular ST's in Eq. 1.1 and 1.2 were obtained on the basis of the conservation of total spin-angular momentum, but the total spin-angular momentum is no longer conserved in a system with strong spin-orbit coupling. On the other hand, conservation law of total angular momentum indi-

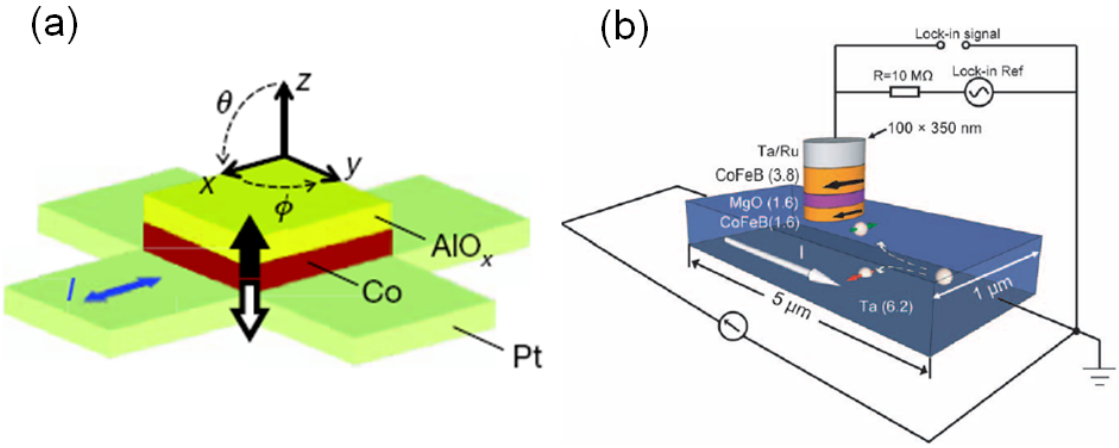

Figure 1.5: Illustration of recent devices, utilizing the spin-orbit interaction, that demonstrated the manipulation of a magnetization in an ultra-thin ferromagnetic dot in the configuration of current-in-plane. (a) Schematic of the Hall-cross bar device that showed the switching of a perpendicularly magnetized nanomagnet (b) Schematic of the three-terminal device and the circuit diagram that showed spin-Hall-effect-induced switching for an in-plane magnetized nanomagnet. The observations were interpreted with Rashba effect (in (a)) or spin-Hall-effect (in (b)). From [72, 73]

cates that there should be current-induced mechanical torques on the lattice, as a consequence changes in the local magnetization together with the spin-transfer torque [67, 68, 69, 70, 71]. The spin-orbit-induced mechanical torques or effective magnetic fields (or torques) should be further investigated theoretically and experimentally.

Recently alternative electrical methods utilizing the spin-orbit interaction have attracted considerable interests, and several experiments have demonstrated the manipulation of a magnetization in an ultra-thin (~ a few atomic layers) ferromagnetic dot or layer in a configuration of current-in-plane (CIP) [72, 73, 74]. The multilayers of the CIP structures generally consist of NM/FM/MO$_x$ where NM is a non-magnetic heavy-metal (e.g. Pt, Ta, W,...), FM is an ultra-thin

transition ferromagnet (e.g. Co, CoFeB, NiFe,...) and MOx is a metal-oxide (e..g. AlO_x, MgO, GdO_x, TaO_x...). This new geometric configuration utilizes large spin-orbit coupling to generate effective fields on the FM or to generate pure spin-currents on the NM. And this suggests a new pathway for nanomagnet controls without a magnetic spin polarizer and/or with the separation of write and read channels. The observations of current-driven magnetization control in NM/FM/MO_x structures have been interpreted with two different mechanisms; Rashba effect or spin-Hall-effect. In general recent theories [75] have suggested that the current induced torque has a form of $\vec{\tau} = -\gamma H_R \hat{m}\times\hat{y} + \gamma H_S \hat{m}\times(\hat{y}\times\hat{m})$ in both cases, but each magnitude or relative strengths could be strongly dependent on behind physics, structures and materials.

The Rashba effect is based on spin-orbit coupling in a system lacking inversion symmetry [76, 77, 78, 79]. The spin-orbit torques or current-induced torques can be generated on moving electrons by transferring the orbital angular momentum from the lattice system to the spin system due to the combined spin-orbit interaction and exchange coupling. For the simplest case in which an electrical potential (or asymmetric crystal field) is intrinsically built at the interfaces in the FM/MO_x or NM/FM and the electric field is normal to the dissimilar interfaces ($\nabla\phi = E\hat{z}$), the H_R is expected $H_R \approx \vec{J}\times\nabla\phi = \alpha_R\hat{y}$ when the electrical current is injected along the current channel ($\vec{J} = J\hat{x}$). Then the Rashba torque has a form of the field-like ST, $\vec{\tau}_R = -\gamma H_R \hat{m}\times\hat{y}$ where $\hat{m}$ is the normalized magnetic moment, while recent theoretical studies [80, 81, 75] have suggested that the torque has an additional (secondary) Slonczewksi-like ST, $\vec{\tau}_S = \gamma H_S \hat{m}\times(\hat{y}\times\hat{m})$, from the spin-precession due to the exchange coupling with the FM magnetization.

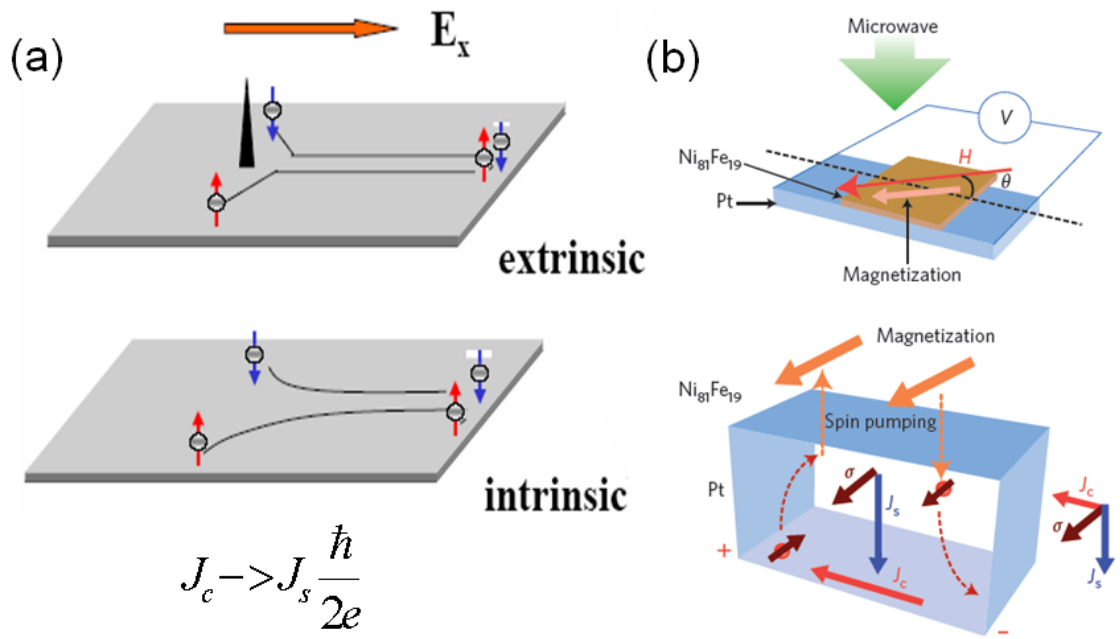

Figure 1.6: Illustration of spin-Hall effect (SHE) and inverse SHE in a paramagnetic metal. (a) SHE is a relativistic spin-orbit coupling phenomenon that generates opposite spin accumulation on the opposing lateral surface of current-carrying non-magnetic wire with a large spin-hall angle. Two different contributions for the SHE have been proposed: the extrinsic effect is due to impurities in the presence of spin-orbit-dependent scattering (top) while the intrinsic effect is caused by the spin-orbit splitting in the band structure of the non-magnetic material (below). (b) ISHE is the conversion of spin currents into electric voltage, observed in a FM/NM multi-layer structure where FM is a ferromagnetic (e.g. Py, YIG) and NM is a paramagnetic metal (e.g. Pt, Mo, Pd and Au) with a strong spin-orbit coupling. The spin currents driven by the magnetic precession in the FM are injected into the NM layer (i.e. spin pumping effect), resulting in an electric potential difference between the opposite edges of the NM via ISHE. The ISHE serves as the electrical detection method of spin-currents.

The spin-Hall-effect (SHE) is an electrical transport phenomenon originated from a relativistic spin-orbit interaction that leads a coupling between a charge current and a transverse spin current [82, 83, 84, 85]. This generates opposite spin accumulation on the opposing lateral surface of current-carrying NM wire with a large spin-hall angle (θ_{SH}). The ST can act on the magnetic moment of a FM-layer at the interface by absorbing pure spin currents (with its spin-polarization $\hat{\sigma}// \pm \hat{y}$) generated in the NM. One can consider it equivalently that the spin-polarizer lies underneath of the FM similar in a conventional CPP spin-valves or tunnel junctions. Then the SHE-ST is $\vec{\tau}_S = \gamma H_S \hat{m} \times (\hat{y} \times \hat{m})$. In the mean time, a recent theory [75] suggests the possibility of an additional torque ($\vec{\tau}_R = -\gamma H_R \hat{m} \times \hat{y}$), if the thickness of the FM is not longer than its spin-dephasing length, which is similar to the field-like ST in MgO-MTJs or the non-adiabatic ST in FM-nanowires. In Chapter 6, we study the current-induced effective field for the thermally assisted magnetic reversal of a perpendicularly magnetized Co nano-dot in the multilayer structure of Pt/Co/MgO/Ta.

By now we have overviewed the spin-transfer-torque. From recent progress and emergent phenomena on this field, spin-transfer-torque will continue to be an active area of research and development and will be investigated with a new material (especially topological insulators), structure and geometry together with many fundamental questions. The impact will be more extended to our real life and the current-induced torques will keep the mainstream in the field of Spintronics and condensed matter physics if commercial applications are realized in the near future.

1.3 Overview of Magnetic Random Access Memory (MRAM)

MRAM applications have a number of important performance requirements [13, 86]: high areal density (> 1 Tbits/in^2), low write current density (J_c < $10^5 - 10^6$ A/cm^2), fast operation (< 1 ns), good reliability (below 6σ error rates), large thermal and mechanical stability, and big signal to noise (TMR or GMR). Among them reducing switching current or lowering power is crucial for the successful realization of practical MRAM, while the high thermal-stability factor (E_a/k_BT) is required at least > 40 for sustaining a bit over 10 years, where E_a is the energy barrier between two stable equilibrium states.

Conventional magnetic-field induced switching is much less efficient and scalable than the spin-polarized current driven magnetization switching [13, 17, 41, 86]. In the field-driven writing scheme, the electrical currents through the word and bit lines generate a magnetic stray field enough to switch a magnetization of the free layer (FL) in a targeted MRAM cell (see Fig. 1.7). The required switching magnetic field can be expressed as $H_{SW} = CM_st/W + H_k$, where M_s is the magnetic moment of FL, t is the free layer thickness, W is the junction size [13, 41, 86] and C is a coefficient. This shows the writing current (field or power consumption) increases with increasing the cell density since $H_{SW} \propto 1/W$. Another problem of this scheme is the crosstalk or half-select problem in which MRAM cells in the same word or bit line with the target cell is influenced by the magnetic field ($\sim 0.7\ H_{SW}$), which is a drawback for the scalability due to the possibility of a thermally-assisted magnetization reversal in the cells, as shown in Fig. 1.7.

Spin-transfer-torque induced magnetization switching is much more effi-

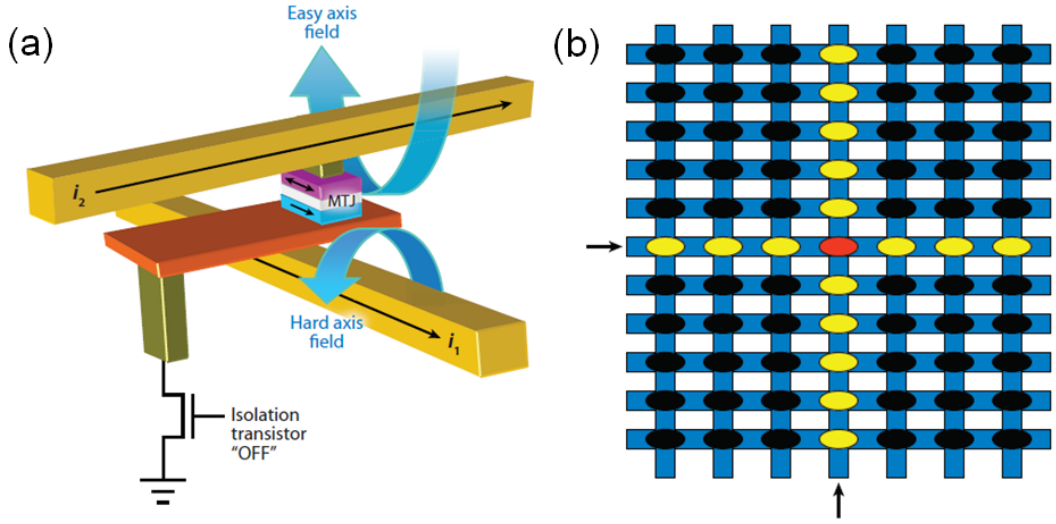

Figure 1.7: (a) Schematic of a magnetic memory cell consisting of one transistor and one magnetic tunnel junction (MTJ). In a conventional field-driven switching, a combined magnetic field from the word (i_1) and bit (i_2) lines induces the reorientation of the FL moment. In a ST-MRAM (spin-torque driven magnetic random access memory), the below word line is un-necessary because the current is directly injected into the MTJ device where spin-transfer-torque effect is used to switch the FL moment. This allows more compact design and less power consumption. (b) The yellow bits experience magnetic fields produced by the word or bit line while only the targeted red bit is exposed to the combined field. This is called half-selection problem in which the yellow bits have a significant thermal agitations, disturbing the 6σ industrial standard. To avoid the half-select problem, toggle MRAM was suggested by controlling the sequence of two fields. Instead, the ST-MRAM does not have such problem. See Ref. [41]

cient and scalable since the switching current density is less dependent on junction area. The switching current density (J_c) is on the order of $10^6 \sim 10^7 A/cm^2$, significantly less than that of magnetic writing scheme ($> 10^8 A/cm^2$) [13, 41]. However significant reduction of J_c has been required for making MRAM compatible with the standard CMOS technology. One way to reduce J_c is using a MTJ structure incorporating two anti-parallel spin-polarizing layers sandwiching the FL, enhancing spin accumulations on the FL and thereby reducing J_c

significantly [87, 88]. For an in-plane magnetized FL layer, the zero-temperature critical switching current (I_{c0}) in the macrospin limit [14, 13, 18] is given by

$$I_{c0} \approx \frac{e}{\hbar/2} \frac{\alpha M_s V}{g(\theta) P} \left(H_k + \frac{H_d}{2} \right) \tag{1.3}$$

where α is the Gilbert damping, t is the thickness, P is the spin-polarization, H_k is the in-plane anisotropy field, H_d is the effective out-of-plane demagnetization field when an external field is zero. Since H_d is typically an order of magnitude larger than H_k, the I_{c0} can be simplified to $I_{c0} \approx \frac{e}{\hbar/2} \frac{\alpha V}{g(0 \ or \ \pi) P} \left(\frac{M_s H_d}{2} \right)$. This suggests several strategies to reduce I_{c0} by optimizing the material of the FL: lower α, higher P, or lower M_s and H_d while maintaining H_k for enough thermal stability ($E_a = M_s H_k V/2$). Braganca et al [89] demonstrated the reduction of I_{c0} down to 0.4 mA (while $E_a \sim 0.8$ eV) by using a FL material with low M_s ($\sim 560 \ emu/cm^3$) while making the nanopillar spin-valve with a high aspect ratio (1:3). Liu et al [90] showed the significant reduction of J_{c0} down to $2 \times 10^6 \ A/cm^2$, by optimizing Co/Ni multilayer on a FL layer with partially cancelling the intrinsic H_d due to the perpendicular magnetic anisotropy (PMA) effect. For a perpendicularly magnetized FL the I_{c0} in the macrospin approximation is given by

$$I_{c0} \propto \frac{e}{\hbar/2} \frac{\alpha M_s V}{g(\theta) P} H_{eff} \tag{1.4}$$

where $H_{eff} = H_{K\perp} - 4\pi M_s$, $H_{K\perp}$ is the perpendicular magnetic anisotropy and $E_a = M_s H_{eff} V/2$. The I_{c0} (J_{c0}) can be further reduced than a structure with an in-plane magnetized FL by tuning the H_{eff} from the surface or volume out-of-plane anisotropy effect while making V smaller. Mangin et al [91, 92] demonstrated low $I_{c0} \sim 0.24$ mA and enough $E_a/k_B T \sim 45$ with a 45 nm diameter nanopillar spin-valve with a FL consisting of Co/Ni multilayer. The H. Ohno group [93] demonstrated very low $I_{c0} \sim 0.05$ mA and enough $E_a/k_B T \sim 43$ in a 40 nm diameter of MgO-based MTJ with multilayers of Ta/CoFeB/MgO/CoFeB/Ta,

and suggested that the PMA was induced in the ultrathin CoFeB due to the interfacial effect at MgO/CoFeB. However IBM group later proposed that both interfaces between Ta/CoFeB and CoFeB/MgO are involved in the formation of the PMA [94].

For practical applications the write operation should be at or below nanoscale time scale and faster than the current technology. In a collinear ST device in which the equilibrium offset angle between the FL and the RL is $\sim 0^o$ or 180^o, Sun et al [95, 96] suggested a linear relation between a current pulse amplitude (I) and switching time (τ) for the ST-induced magnetic reversal as

$$\tau^{-1} \approx \frac{\eta(\mu_B/e)}{M_s V\ ln(\pi/2\theta_o)}(I - I_{c0}), \quad (I > I_{c0}), \tag{1.5}$$

indicating that a faster operation can be achieved with increased I ($\sim 4 \times I_{c0}$ for 1 ns write speed), while in the thermally activation region, the relation as

$$\tau^{-1} = \tau_0^{-1} \exp\left[-\left(\frac{E_a}{k_B T}\right)\left(1 - \frac{H}{H_k}\right)^2\left(1 - \frac{I}{I_{c0}}\right)\right], \quad (I << I_{c0}). \tag{1.6}$$

Later several ways have been proposed to improve the switching efficiency and speed. Garzon et al [97] demonstrated coherent control of the switching dynamics by applying two successive short pulses with variable amplitudes and delays. Cui et al [98] carried out the experiment for efficient magnetization reversals by applying a short current pulse with a preceding resonant microwave current pulse.

In order to achieve ultrafast magnetization reversals (switching time < 200 ps), Kent et al [99] proposed an orthogonal ST device structure in which a strong out-of-plane spin polarization generates a quick rotation of the FL about the out-of-plane demagnetization field during the pulse current, followed by, after the termination of the pulse, the completion of the reversal (π-rotation) along with

the relaxation of the FL moment to the equilibrium position. I experimentally demonstrated ST-driven ultrafast switching with a short current pulse down to 50 ps pulse width in Chapter 2 and 3 while Spintec group [100] independently carried out the switching scheme in their device structure. Later the Kent group [101] and the UCLA & UCI groups [102] demonstrated its possibility in the orthogonal ST device with MgO based MTJs.

Recently new mechanisms for manipulating the magnetic FL have been attracted such as via voltage-controlled magnetic anisotropy [103] or through pure spin currents [72, 73, 74] generated by spin-orbit coupling. These may enable better magnetic devices exhibiting a high signal, ultrahigh density, low power consumption, high thermal stability, high speed operation and/or new functionality.

1.4 Overview of Magnetic Tunnel Junctions

A magnetic tunneling junction (MTJ) device consists of two metallic ferromagnets separated by a thin insulator barrier, and has been proposed as next generation of technological applications such as a magnetic field sensor, a random access memory or a spin-torque oscillator because of its high magnetoresistance (TMR) [13]. Of course the insulator barrier, together with the ferromagnetic electrodes, is of significant importance as it affects several electrical properties of a MTJ device such as TMR, spin-transfer-torque and recently interfacial effect. Therefore understanding and controlling the effects of the insulating material and the interface electrodes are imperative in fabricating MTJ devices and maximizing the performance of the electrical properties [22].

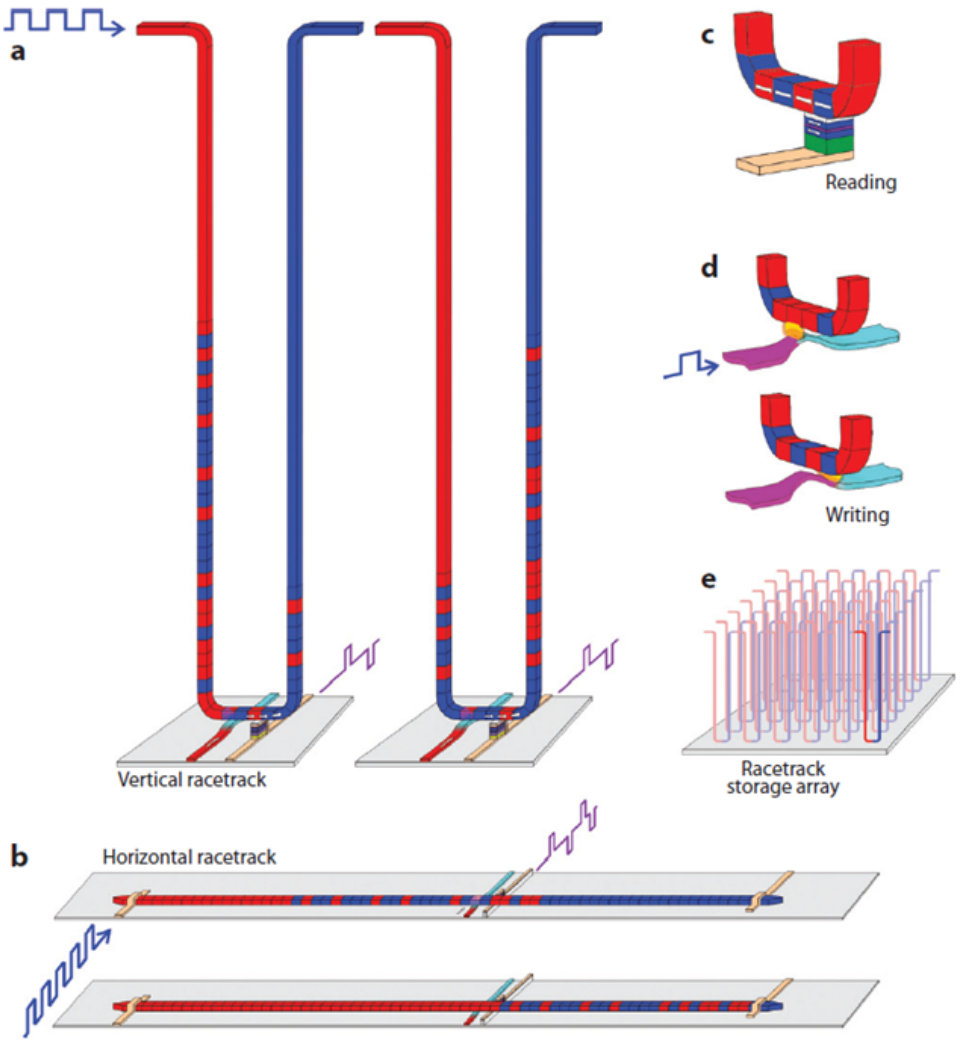

Figure 1.8: In a racetrack memory, individual bits are stored as a sequence of magnetic domains, separated by domain walls (DWs), along a ferromagnetic nanowire. The entire DWs can be coherently moved along the wire by a spin-polarized current pulse. The current polarity determines the direction of DW motions and the length of the nanowire should be at least twice as long as the stored DW pattern. The data can be read or stored when the domains move across magnetic read and write units. (a) A vertical configuration of a racetrack memory, offering the highest data density. (b) A horizontal racetrack configuration using a nanowire on a substrate, which is easy to implement in a lab. (c) Reading a data from the racetrack can be accomplished by measuring the TMR of a MTJ unit connected to the racetrack. (d) Writing a data to the racetrack can be achieved by applying an Oersted magnetic field generated by a second nanowire. (e) Arrays of racetracks for high-density storage. From [11]

The most studied insulator barrier was amorphous Al_2O_3 because an ultra-thin, pin-hole free and smooth Al_2O_3 barrier (7 $\mathring{A}$ ~ 16 $\mathring{A}$) was relatively easy to grow by depositing aluminum and then oxidizing it to create its oxide. The maximum TMR achieved experimentally for MTJs with Al_2O_3 was ~ 70 % [86]. The value is very close to what is expected as the maximum limit from theoretical calculations according to Julliere's model in which the magnitude of the TMR was solely due to the spin polarization of the density of states of the bulk ferromagnets (i.e. the tunneling probability is independent of electron spin). From the model, TMR is given as $2P_1P_2/(1 - P_1P_2)$ where P_1 and P_2 are spin-polarizations of the two ferromagnetic electrodes: a MTJ with CoFeB (P = 51 %) electrodes results in TMR ~ 70 % [86].

Later the community realized that the type of insulating barrier and electrode/insulator interface can significantly affect the spin polarization of the tunneling current and thereby the magnitude of the TMR [62, 63, 22, 23], and has conducted significant research with various oxide barriers and electrodes. In the mean time first principle calculations predicted extremely large TMR, up to 1000 %, in Fe(001)/MgO(001)/Fe(001) as a result of coherent tunneling [62, 63]. Moreover, Co/MgO/Co(001) was theoretically expected to exhibit even higher TMR than that of Fe/MgO/Fe MTJ [62, 63]. In the case of bcc Co or Fe, the majority spin band $\Delta_{1\uparrow}$ only has states at the Fermi energy E_F, whereas the minority spin band $\Delta_{1\downarrow}$ has no states at E_F, as shown in Fig. 1.9. The other band branches (Δ_2, Δ_5) are located below E_F, which does not contribute significantly to electron transport. The studies explained that the state $\Delta_{1\uparrow}$ symmetry is effectively coupled through thin MgO(001) barrier to make conduction electrons whose wave functions are totally symmetric have significant tunneling probability. This results in large TMR between parallel and anti-parallel configura-

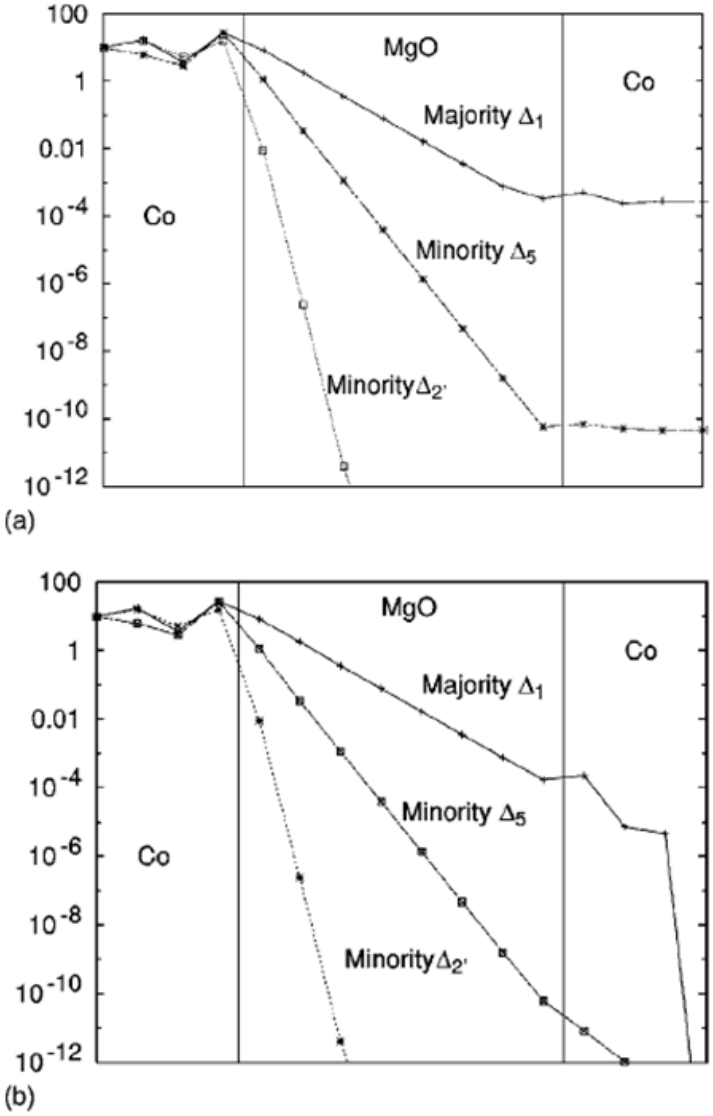

Figure 1.9: Illustration of tunneling density of states for the Co(001)/MgO(001)/Co(001) magnetic tunnel junctions for (a) parallel magnetization alignment, (b) anti-parallel magnetization alignment. First-principle calculations predicted a large tunneling magneto-resistance (TMR) of the Co/MgO/Co or Fe/MgO/Fe junctions. There is only a Δ_1 state for the majority spins at E_F whereas there is no state with Δ_1 symmetry for the minority spins. The Δ_1 state decays much more slowly than the other states within the MgO barrier. This makes R_{AP} much larger than R_P, resulting a giant TMR. From [104]

tions of electrodes. Since MTJs with MgO barrier were experimentally demonstrated to have 220 % TMR at room temperature in 2004 [105, 106], the MTJs have been extensively studied to improve TMR, and up to now a MgO-MTJ device with 600 % TMR at RT and 1100 % at 4 K were realized by improving texturing of crystal orientation and by minimal disorder at the interfaces [64].

For practical and high-speed operation, the resistance of the device should be lowered [13, 86] because a MTJ device and combined circuits have an effective capacitance (C), forming a low-pass filter. The cutoff frequency of a low-pass filter is given by $f_c = 1/2\pi RC$. For a high speed read sensor or memory cell (for example, $f_c = 1$ GHz), if C is in the pF, the optimum RA should be less than 10 $\Omega \cdot \mu m^2$, where RA is the product of resistance and junction area. Relatively large RA limits the operating frequency and makes the Johnson and shot noise high. To achieve such a low RA, the thickness of the tunneling barrier (t_{MgO}) should be reduced (< 10 $\mathring{A}$). However it is difficult to reduce RA of MTJ while maintaining a high TMR because reducing the tunnel barrier thickness will also significantly decrease the TMR and the reliability of the device fabrication. Many research groups in the world are still under work to optimize because the RA of a MJT device is also determined by its ferromagnetic electrodes, under layers, capping layers, structures and fabrications as well as its tunneling barrier.

Recently very interesting results have been reported about the interfacial effects at the MgO/CoFeB or at the MgO/Ta in MgO-MTJs. Several experiments have demonstrated that the application of an electric field through the tunnel barrier can change the magnetic anisotropy of the ferromagnetic electrode (CoFeB, Fe or FeCo) between in-plane and out-of-plane directions (see

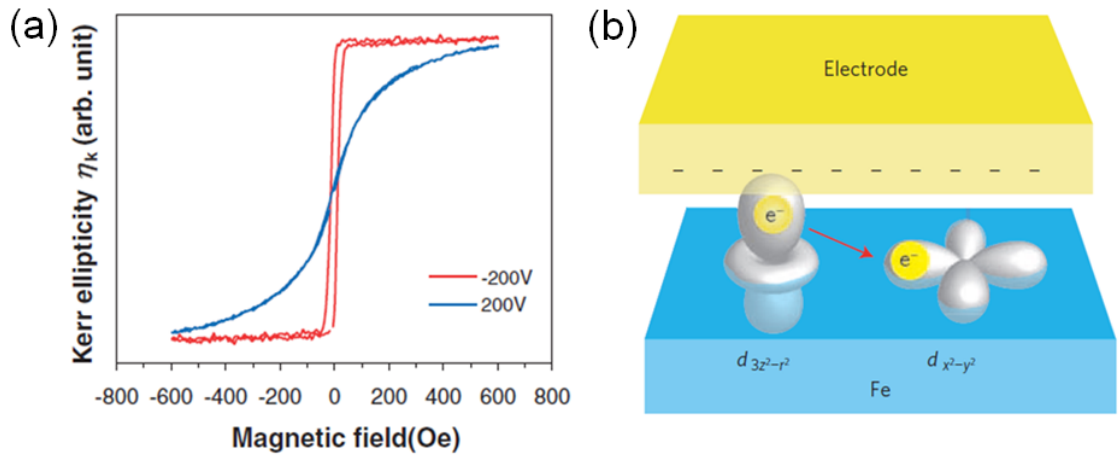

Figure 1.10: Illustration of voltage (or electric-field) induced magnetic anisotropy change. (a) Measured hysteresis loop of a ultrathin $Fe_{80}Co_{20}$ (0.58 nm) layer under positive (blue) and negative (red) bias voltage. A perpendicular magnetic anisotropy (PMA) was induced when the voltage is changed from +200 V to -200 V. The magnetic easy axis can be electrically manipulated between in-plane and perpendicular directions. This leads to the voltage-controlled magnetic anisotropy and magnetization switching. (b) Schematic illustration of the electric field effect on the electron filling of the 3d orbitals in the ultrathin Fe layer. A negative voltage application may decrease the number of electrons in the m_z = 0 states, leading to the increase of the PMA. The microscopic origin of such change in the magnetic anisotropy is attributed to the band-filling effect or the variation of the relative occupation of the electronic orbitals at the interface with an external electric field. However more experimental and theoretical works requires for the further understandings. From Y. Suzuki group [103].

Fig. 1.10), possibly suggesting a new pathway for the efficient switching. This leads to the voltage-controlled magnetic anisotropy and magnetization switching. The microscopic origin of such change in the magnetic anisotropy is attributed to the band-filling effect or the variation of the relative occupation of the electronic orbitals at the interface with an external electric field [103]. However more experimental and theoretical works are required for further under-

standing. In addition perpendicularly magnetized MTJs were demonstrated by controlling the thickness of CoFeB with the utilization of the induced perpendicular magnetic anisotropy of an ultrathin CoFeB (< 1.5 nm) originating from the interfacial effects [93, 94].

1.5 Overview of Spin-Torque Nano-Oscillator (STNO)

In a STNO [17, 44, 45, 107, 33, 108], a spin-polarized dc current (I) excites persistent magnetic precession at microwave frequencies about the effective magnetic field when the anti-damping component of spin-torque is enough to balance out the intrinsic magnetic damping of an unpinned magnetic moment, generating a microwave voltage signal via the magnetoresistance (MR) effect: i.e. a STNO is a nanomagnet device that converts a dc electrical current into microwave signals while a spin-torque diode device functions reversely [109]. The STNO promises potential application for low-power, nanoscale, current-tunable RF components that can be easily fabricated on-chip.

The oscillator frequency (f) is determined by the magnitude and direction of an external magnetic field (H) as well as I, ranging from hundreds MHz to 100 GHz but close to the FMR frequency for a uniform mode oscillation. The f can be tuned by H ($\partial f/\partial H \sim 1 - 10$ MHz/Oe) and generally increases with a magnitude of H due to a larger torque acting on the precessing magnetic moment with a larger effective magnetic field. The agility of the f via I ($\partial f/\partial I$) is $\sim \pm 10 - 1000$ MHz/mA and more complicated, strongly depending on the H, material and device geometry. It turns out that the $\partial f/\partial I$ is very closely related with the precession stability (coherence) or spectral linewidth of a STNO and

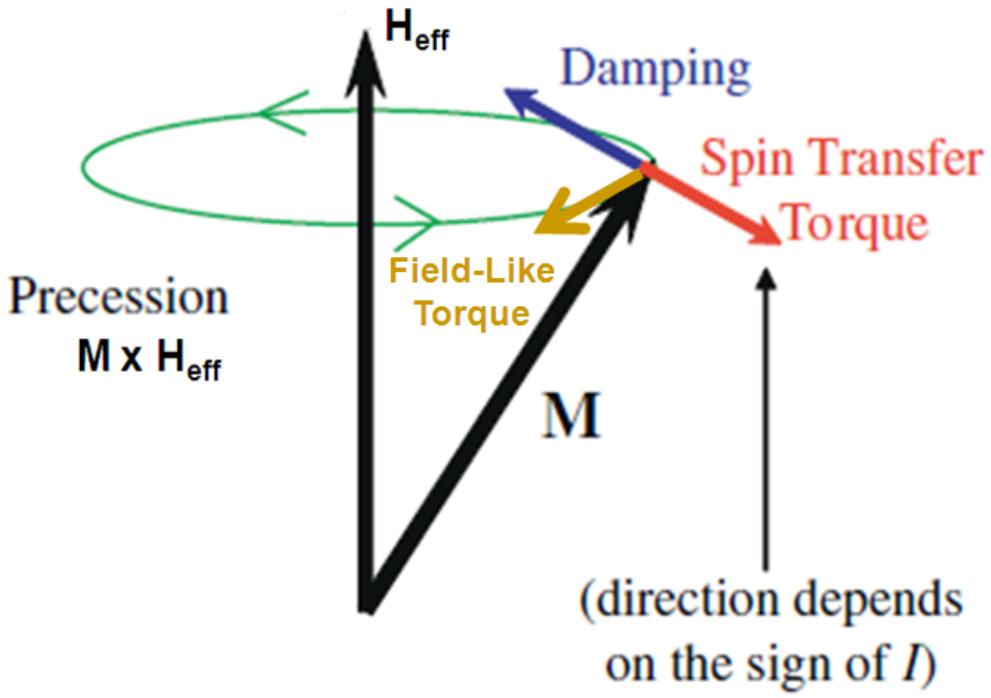

Figure 1.11: Scheme of spin-transfer-torque induced magnetic dynamics, and concept of Spin-Torque Nano-Oscillator (STNO). Spin-transfer-torque (with a proper sign of I) can excite persistent magnetic precession around the effective magnetic field (H_{eff}) when the spin-torque is sufficient to compensate for the magnetic damping torque. In ST-devices based on MgO-MTJs there is a considerable field-like torque because a transverse spin current is not perfectly absorbed at the interface of a magnetic free layer, while this torque is very small in metallic spin-valve devices. The field-like torque can change the characteristics of the magnetic dynamics. Modified from [17].

we will discuss about the behind physics in Chapter 4 and 5 for our STNOs.

The first observation of the spin-torque driven magnetic excitations was by Tsoi et al. [31] using a mechanical point contact to a magnetic multilayer. They detected peaks, in the differential resistance (dV/dI) as a function of I, that occurred for only one polarity of I and that increased linearly with H. This was the indirect evidence of spin-torque-induced precessions. Later the microwave

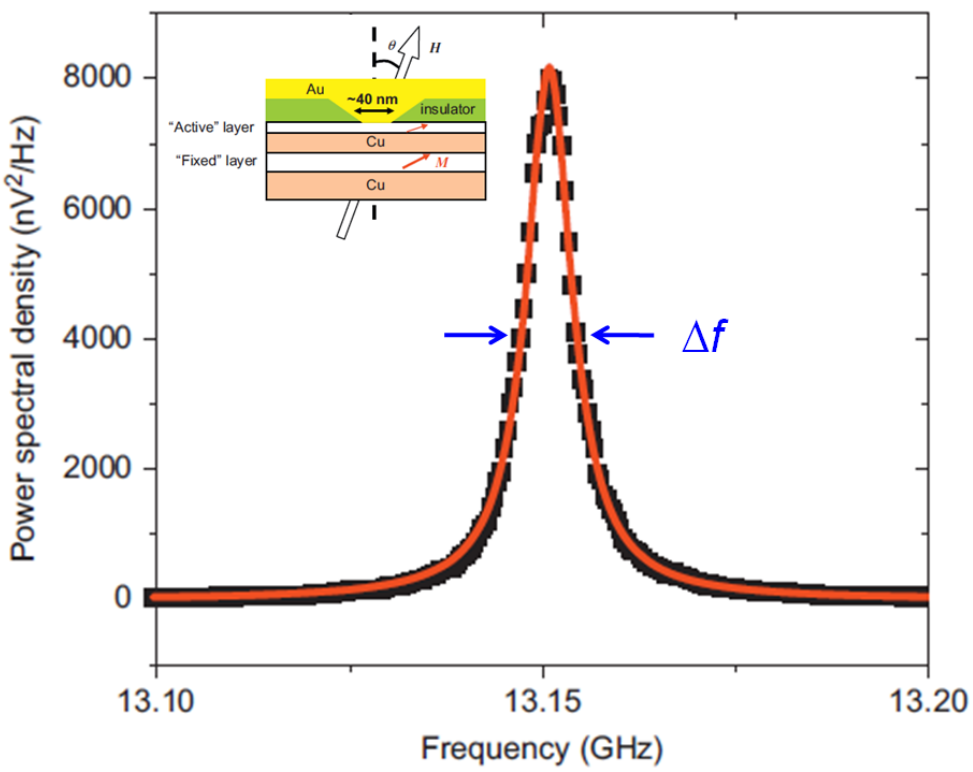

Figure 1.12: (a) Illustration of power spectral density (PSD), showing a narrow spectral linewidth (~ 7 MHz) at room temperature, emitted from a spin-torque nano-oscillator (STNO) based on a nanoscale point contact device. Inset: Cross-sectional sketch of the STNO device. The contact area is ~ 40 nm. Coherent oscillations are observed in such devices when a strong magnetic field H (> 1 kOe) is applied at some angle θ from the normal to the plane. From [44].

emission was directly observed by Kiselev et al. [107] in a nanopillar spin-valve and by Rippard et al [33, 34, 44] in a nanoscale point contact. Since then, a number of exciting STNOs have been reported, based on a magnetic vortex gyration [110, 111, 112], based on MgO-MTJs [38, 113], based on orthogonal magnetic configurations [114], and based on in-plane magnetized FLs with large offset angles [115, 116]. The STNOs have their own characteristics in oscillation frequency (f), spectral linewidth (Δf), power (P), and tunability as functions of the external H, I and temperature (T). For instance, vortex-based STNOs ex-

hibit low frequencies (< 2 GHz) of microwave emission, weak dependence of f on H (<< 1 MHz/Oe) and narrow spectral linewidth ($\Delta f \sim$ hundreds kHz) [110, 44, 111].

There are several practical requirements for the realization of such STNOs: elimination of an external H, large output power (P) and high coherency (or reduction of the Δf) of a STNO. (1) The application of large external magnetic field on a STNO can be achieved with integrated hard magnets providing bias fields up to 3 kOe [13]. For some STNOs, an external field is not necessary: a vortex-based STNO works in the absence of an external H and exhibits a very narrow Δf ($\sim$ 300 kHz) at room temperature [110, 111], and a STNO excited by an out-of-plane spin-polarizer generates a persistent oscillation of the FL around the out-of-plane demagnetization field which is the internal field [114]. (2) A few microwatts are required for practical GHz communication applications. The output power from an individual STNO can be increased by utilizing a device with a high MR [38, 113] or by generating a large-angle precession in the SNTO [117]. The reported output powers ($0.1 - 0.3\,\mu W$) from a single STNO based MgO-MTJ [38, 118, 119] are close to the minimum of the required power. Impedance matching of such RF devices is required to maximize power transfer to the waveguide. (3) Significant reduction of Δf, which is the inverse of the decoherence time, is still required at least one or two orders of magnitude ($\Delta f < 1 - 10$ kHz). Up to date the best Δf for a highly non-uniform vortex-based STNO is a few hundred kHz at room temperature, but this type of STNO is limited in the operational f (< 2 GHz) and generated P [44, 110]. The best Δf for STNOs based on point-contact geometry and spin-valve nanopillar is 1-10 MHz but the former requires a high external H (> 1 kOe). We will present our coherent STNOs based on nanopillar spin-valves in Chapter 4 and 5, exhibit-

ing a minimum $\Delta f \sim 1 - 10$ MHz at low field biases (< 1 kOe) and at room temperature.

Several sources of Δf-broadening in STNOs [44, 45, 46] have been identified such as thermal driven amplitude and phase noise [115, 46], thermally activated hopping between different dynamical modes [115, 120], spatial incoherence (non-uniform modes or chaotic motion) [121, 116], and nonlinearity or intrinsic non-linear coupling between the amplitude and phase noise [46, 122]. The understanding and improvement on the Δf for STNOs are still under research and we will discuss about the physical origins of the non-linear coupling for our STNOs in Chapter 4.

Phase-locking is referred to as frequency entrainment or synchronization between oscillators in that the whole system starts to oscillate coherently at the same frequency. Each oscillator has constant phase differences to others when they have their own frequencies and weakly interact with each other, but the interaction is strong enough to overcome the differences in free-running frequencies of the individual oscillators. This phenomenon is a subject of much interest in many research field and proposes a path to significantly enhance the oscillation stability (coherence) as well as the generated power. Synchronization of two or four closely spaced STNOs with similar frequencies has been demonstrated through spin-wave coupling [123, 124, 125], leading to significant improvements in their powers and linewidths. If mutual phase locking is achieved for a collection of N STNOs, the maximum power may grow as much as N^2 for the best case as well as the coherency of the whole system. A STNO with oscillation frequency (f_o) can start to oscillate at the frequency of a weak external microwave signal (f_e) when the frequency difference is less than the

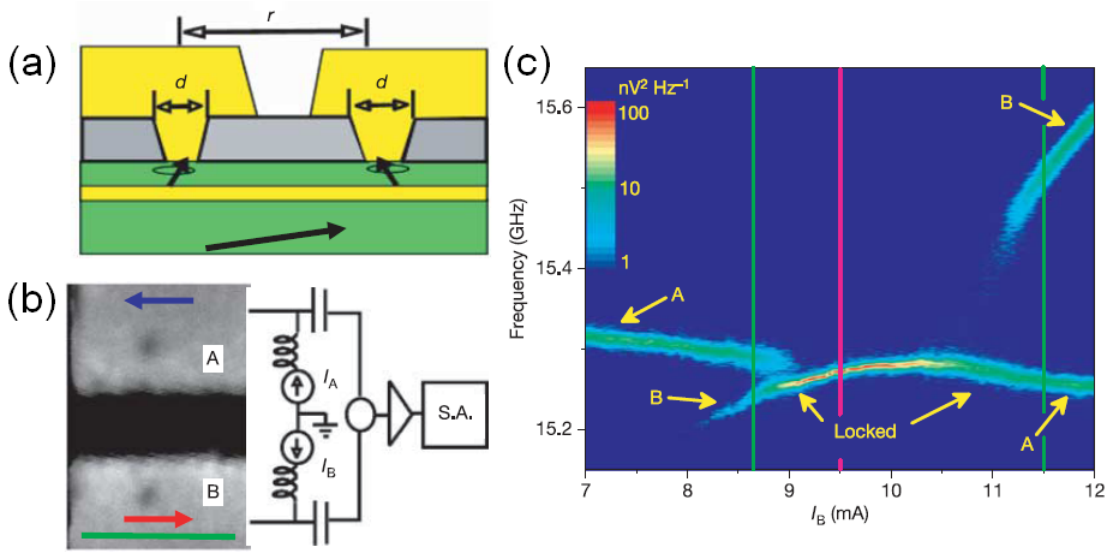

Figure 1.13: Illustration of mutual phase-locking of two spin torque nano-oscillators (STNOs) based on nano-contact device. The phase-locked state is characterized by a sudden narrowing of linewidth and an increase in power due to the coherence of the individual oscillators. The STNOs have two possible interacting means by producing magnetic (dipole) fields or propagating "spin-waves" via magnetic film. The distance between two contacts are important in their relative strengths. (a) Cross-sectional sketch of two STNOs with contact diameter d ~ 40 nm and separation r = 500 nm. (b) Scanning electron microscope image of actual two-nano-contact device with two independent leads and a measurement circuit diagram at the right. The high-frequency power output is combined in a microwave power combiner and then sent to the spectrum analyzer. (c) Contour plot of power spectral density of interacting oscillators as a function of current through contact B (or as a function of its oscillation frequency). Current through contact A is fixed at 8 mA (i.e. its oscillation frequency is fixed). When two oscillation frequencies are close each other within a certain value (locking bandwidth), two STNOs begins to synchronize through the "spin-wave" interactions. Demonstrated by NIST group [123].

phase-locking bandwidth (Δ), i.e. $|f_o - f_e| < \Delta$ [126, 127, 46]. More interestingly, a STNO can be phased locked to an external signal whose frequency (f_e) to the f_o is close to a rational number, i.e. $f_e/f_o -> p/q$ where p and q are integers, which is called fractional synchronization [128, 129]. This effect allows us to control the quality of a STNO by a small external signal (even with a different frequency) and can be used to reduce the linewidth and to increase the output power.

Spin-torque nano-oscillators are very new and exciting nanoscale devices because the magnetic auto-oscillation is unique phenomenon that can be occurred only by anti-damping component of the spin-transfer torque, not by an external magnetic field (H), not by a circularly polarized laser (at least there is no report by now) and the device concept offers many capabilities. We expect STNOs will become a useful nanoscale RF device for a variety of applications if we understand underlying physics more and overcome many practical barriers.

1.6 Overview of Non-Linear Auto-Oscillator (NLAO) model

In this section we overview the non-linear oscillator model [46, 122, 130, 131] that analyzes microwave generation in an auto-oscillator with a nonlinear frequency shift in the presence of thermal fluctuations. The main point of the model is that the additional nonlinearity of the frequency dependent on power (or oscillation amplitude) renormalizes the thermally driven phase noise, causing more substantial linewidth (Δf) broadening than a classical linear auto-oscillator. This developed theory when it is applied to a spin-torque oscillator has given a qualitative description on the angular and temperature dependences of the measured Δf, distortions of the lineshape, and phase locking phe-

nomena for certain devices.

Radio-frequency (RF) auto-oscillators have attracted a great of interest because the oscillators have been used in many electronic systems, by converting a DC input into an AC output, providing the central clock signal that controls the sequential operation. It has been well known in the classical oscillator theory that the auto-generation of constant amplitude oscillations can occur at the resonance frequency when a passive oscillating circuit, consisting of a dissipative resistance (R) and a reactive inductance (L), is connected to an external source of constant energy (e.g. battery) and an active element (e.g. transistor, vacuum tube, tunnel diode, etc.). The equilibrium amplitude of the auto-oscillations is determined by the dynamic balance between the positive damping of the system and the negative damping introduced into the system by the active element. It was established that the Δf in a classical oscillator is determined, for most cases, by the thermal phase noise:$\Delta f \propto k_B T/E(p)$ where k_B is the Boltzmann constant, T is the absolute temperature, E is the averaged energy of the oscillator having the power $p = |a|^2$ and a is complex amplitude. This is rather general and applicable to any type of conventional auto-oscillator such as resistor, vacuum tube, tunnel diode, laser, etc. in which the oscillator frequency is almost independent of its p. However, when the oscillation frequency strongly couples with the p, one can expect that small fluctuations in the amplitude at a steady state can give significant contributions to the phase noise.

In magnetic spin-torque nano-oscillators (STNOs), spin-polarized dc currents transfer spin-angular momentum to the magnetic free layer (FL), which competes to the magnetic damping and thus creates an effective negative damping which is analogous to the active element and can lead self-sustained oscil-

lations of the FL. This oscillation frequency is determined by the total effective magnetic field and in general is close to the ferromagnetic resonance frequency, while the oscillation amplitude is determined by the efficiencies of the spin-transfer-torque into the system. In almost all STNOs the oscillation frequency strongly depends on the p of the FL, and the sign and magnitude of the nonlinear frequency shift coefficient ($N = d\omega/dp$) depend on the direction and magnitude of the magnetic field bias. This gives the advantage to STNOs that the frequency is tunable by external dc currents.

The general equation of motion of the complex dimensionless amplitude ($a(t)$) in a non-linear auto-oscillator in the presence of noise can be written in the form

$$\frac{\partial a}{\partial t} + i\omega(p)a + [\Gamma_+(p) - \Gamma_-(I,p)]a = f_n(t) \tag{1.7}$$

where $\omega(p) = \omega_o + Np$ is the p-dependence of the oscillator frequency, $p = |a|^2$, $\Gamma_+(p) = \Gamma_o(1 + Qp)$ is the dissipative positive damping, and $\Gamma_-(I,p) = \sigma I g(p)$ is the negative damping from an active element (or spin-transfer torque). Note that for the case of a *collinear* STNO oscillator $g(p) = 1 - p$, neglecting corrections due to spin accumulation effects in a spin valve device [46, 122, 130]. The $f_n(t)$ is a random white Gaussian signal from the influence of the thermal noise, and the correlation function of this random noise is $< f_n(t)f_n(t') >= 2\Gamma_+ P_n \delta(t - t')$ where $P_n \propto k_B T$. For an isotropic FL the phase $\varphi \equiv arg(a)$ of a is equal to the azimuthal angle of the FL while the $p = |a|^2$ determines the polar precession angle $\theta \equiv arccos(m_z) = arccos(1 - 2p)$. The stationary solution of Eq. 1.7 in the absence of noise can be in the form $a(t) = \sqrt{p_o} e^{-i\omega(p_o)t + i\varphi(t)}$ where the equilibrium power p_o is determined by $\Gamma_+(p_o) = \Gamma_-(I_o, p_o)$. With a trial solution, $a(t) = [\sqrt{p_o} + \delta a(t)]e^{-i\omega(p_o)t + i\varphi(t)}$, we have equations for fluctuations of the amplitude

$$\frac{\partial \delta a}{\partial t} + 2\Gamma_{eff} p_o \delta a = Re(\tilde{f}_n(t)e^{-i\varphi}) \tag{1.8}$$

and phase

$$\frac{\partial \varphi}{\partial t} + 2N\sqrt{p_o}\delta a = \frac{1}{\sqrt{p_o}} Im(\tilde{f_n}(t)e^{-i\varphi}) \tag{1.9}$$

where $\Gamma_{eff} = \frac{\partial}{\partial p}(\Gamma_+(p) - \Gamma_-(I,p))$ and $N = \frac{\partial}{\partial p}\omega(p)$. In Eq. 1.9, the amplitude noise (δa) is the additional source of phase fluctuation, and consequently can lead to the Δf-broadening of the auto-oscillator. If the fluctuations take place inside a narrow frequency region, $\Delta\omega << p_o\Gamma_{eff} \equiv \Gamma_p$, $|\partial\delta a/\partial t| \sim \Delta\omega|\delta a| << 2\Gamma_{eff}p_o|\delta a|$, in which the first term in the left-hand side of Eq. 1.8 can be neglected compared to the second term, and then we obtain $\delta a \approx \frac{1}{2\Gamma_{eff}p_o} Re\{f_n e^{-i\varphi}\}$. Substituting this in Eq. 1.9, we have a closed-form equation for the phase fluctuation:

$$\frac{\partial \varphi}{\partial t} = \frac{1}{\sqrt{p_o}}\left[-\frac{N}{\Gamma_{eff}} Re(f_n(t)e^{-i\varphi}) + Im(f_n(t)e^{-i\varphi})\right] = \frac{1}{\sqrt{p_o}}\sqrt{1+\left(\frac{N}{\Gamma_{eff}}\right)^2} Im(f_n(t)e^{-i\alpha-i\varphi}) \tag{1.10}$$

where $\alpha = arctan(N/\Gamma_{eff})$.

Eq. 1.10 has the identical form to the equation for the phase fluctuation in a classical system without a nonlinear frequency shift, but with the increased noise level. Therefore, by applying general methodology of the oscillator theory for the Lorentzian linewidth, Eq. 1.10 leads the expression of the Δf of an auto-oscillator by

$$\Delta\omega = \Gamma_+(p_o)\frac{k_B T}{E(p_o)}[1+\nu^2] \tag{1.11}$$

where $\nu = \frac{\partial\omega/\partial p}{\partial(\Gamma_+ - \Gamma_0)/\partial p} = \frac{N}{\Gamma_{eff}} = \frac{N}{\Gamma_p}p_o$ is the normalized dimensionless nonlinear coupling, $E_o =< E(a) >= \beta p_o$ is the average oscillator energy and β is the power-energy proportionality. The generalized Eq. 1.11 indicates that in general Δf is proportional to the ratio of the noise energy to the averaged oscillator energy, and shows that the nonlinearity (ν) can produce a significant Δf-broadening when $|\nu| >> 1$. In addition, the theory proposed that the ν of a STNO was responsible for the asymmetry, non-Lorentzian shape of power spectral densities

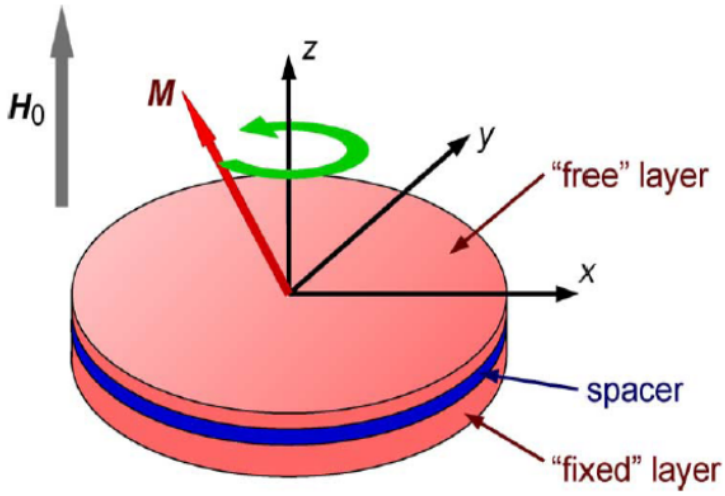

Figure 1.14: Scheme of an out-of-plane magnetization precession under a large bias magnetic field which is directed to the normal (H_o) to the plane ($H_o > 4\pi M_z$). The general auto-oscillation equation (Eq. 1.7) was derived for this simplest case where the FL precesses around the normal axis (z-direction). From [46]

near the threshold current [132]. Another important result is the prediction of low Δf at which the sign of N is changed, e.g. from red-shift $N < 0$ to blue-shift $N > 0$. N can passes through zero at a specific angle when the FL is titled to out-of-plane or on the in-plane that can be achieved by applying an external field to the out-of-plane or to the hard-axis.

Interestingly the factor $(1 + \nu^2)$ is same as the factor describing increase of the bandwidth of phase-locking of a STNO to an external microwave signal [46]. By replacing the thermal noise term, $f_n(t)$, with $F_e e^{-i\omega_e t}$, it was shown that the locking bandwidth $\Delta = |\omega_e - \omega|$, in which the STNO can be phase-locked to the external source, i.e. oscillating at ω_e rather than ω, is given by $\Delta = (F_e/\sqrt{p_o})\sqrt{1+\nu^2}$. The similar form in both expressions suggests that the Δf-broadening of an oscillator under the influence of thermal noise can be considered as a phase-locking of the oscillator to the thermally-induced random

external signal $f_n(t)$.

The NLAO model [130, 46] analytically derived the Eq. 1.7 from the LLGS eq. for the simplest STNO based on a normally magnetized isotropic magnetic nanopillar as shown in Fig. 1.14 where LLGS equation is

$$\frac{\partial \vec{M}}{\partial t} = -\gamma \vec{M} \times \vec{H}_{eff} + T_G + T_S \tag{1.12}$$

where $\vec{T}_G = \gamma \frac{\alpha}{M_o} \vec{M} \times \vec{H}_{eff} \times \vec{M}$ is the damping torque, $\vec{T}_S = \frac{\sigma_o I}{M_o} \vec{M} \times \vec{M} \times \hat{p}$ is the spin-transfer-torque and $\vec{H}_{eff} = (H_o - 4\pi M_z)\hat{z}$ is the effective magnetic field and H_o is the external bias field. For the conservative LL equation, $\partial \vec{M}/\partial t = -\gamma \vec{M} \times \vec{H}_{eff}$ or $(dM_{x(y)}/dt)_{cons} = \mp i\omega_o M_{y(x)}$ where $\omega_o = \gamma(H_o - 4\pi M_o)$ is the FMR frequency, one can convert the Cartesian coordinate to the normal coordinates of the equation with the dimensionless complex variable $\tilde{c} = (M_x - iM_y)/2M_o$. Then we have one complex equation, $(d\tilde{c}/dt)_{cons} = -i\omega_o \tilde{c}$, which is the simplest description of the linear magnetization precession. The analytical model achieved the same simplest form by introducing the complex dimensionless spin wave amplitude $c = (M_x - iM_y)/\sqrt{2M_o(M_o + M_z)}$, then the magnetization vector $\vec{M}$ can be equivalently expressed as

$$\vec{M} = M_o(1 - 2|c|^2)\hat{z} + M_o\sqrt{1 - |c|^2}[(\hat{x} + i\hat{y})c + (\hat{x} - i\hat{y})c^*]. \tag{1.13}$$

Using the $\vec{M}$ in the LL eq., we can derive an equation for the complex amplitude c,

$$\left(\frac{dc}{dt}\right)_{cons} = -i\omega(|c|^2)c \tag{1.14}$$

where $\omega(|c|^2) = \omega_o + N|c|^2$, $N = 2\omega_M$, and $\omega_M = \gamma 4\pi M_o$. Next, using Eq. 1.13 into $\vec{T}_G$, the damping torque is given by

$$\left(\frac{dc}{dt}\right)_{damp} = -\Gamma_+(|c|^2)c \tag{1.15}$$

where $\Gamma_+(|c|^2) = \Gamma_G(1 + Q|c|^2 + Q'|c|^4)$, $\Gamma_G = \alpha\omega_o$, $Q = 2\omega_M/\omega_o - 1$, $Q' = -2\omega_M/\omega_o$. For all physical ranges of c, $\Gamma_+(|c|^2) > 0$ leads the reduction of amplitude in c or the positive damping. Lastly, from the $\vec{T}_S$, we have

$$\left(\frac{dc}{dt}\right)_{spin-toruqe} = +\Gamma_-(|c|^2)c \tag{1.16}$$

where $\Gamma_-(|c|^2) = \sigma_o I(1 - |c|^2)$. For $I > 0$ $\Gamma_-(|c|^2)$ is positive, causing the increase of the amplitude in c or leading the effective negative damping for the precession of the FL. Combining all of the contributions in Eq. 1.12 we obtain

$$\frac{dc}{dt} = \left(\frac{dc}{dt}\right)_{cons} + \left(\frac{dc}{dt}\right)_{damp} + \left(\frac{dc}{dt}\right)_{spin-torque} \quad \text{or} \quad \frac{dc}{dt} + i\omega(|c|^2)c + \Gamma_+(|c|^2)c - \Gamma_-(|c|^2)c = 0$$

which is exactly coincident with the auto-oscillator equation.

In our STNO exhibiting quasi-linear behaviors in Chapter 4, the magnetic oscillations were excited under an externally applied in-plane hard axis magnetic field, which is beneficial for much lower bias field than the above out-of-plane rotation, causing the in-plane magnetization precession of the FL. For this case one may have a curiosity about their equivalency because the situation is different. Slavin et al. [131, 133] derived the perturbed equation of motion for an in-plane-magnetized anisotropic STNO with an arbitrary applied bias field. In their calculation, they used classical Hamiltonian formalism for spin waves and performed the renormalization of the non-resonant three-wave nonlinear processes. The obtained expression from the LLGS equation was

$$\frac{\partial c}{\partial t} = -i\frac{\delta H_c}{\delta c^*} + F_d + F_J$$

where $F_d = -\Gamma_o(1+Q_1|c|^2)c+\kappa\Delta^2 c$ is the dissipative force, $F_J = \lambda_J+V_J c^*+\Gamma_J(1-|c|^2)c$ is the current induced force. The $\kappa\Delta^2 c$ is the increase of the relaxation rate with the increase of the wave vector of the excited spin wave, but one can assume it to be zero for a single-mode excitation. The reference [131] mentioned that λ_J is

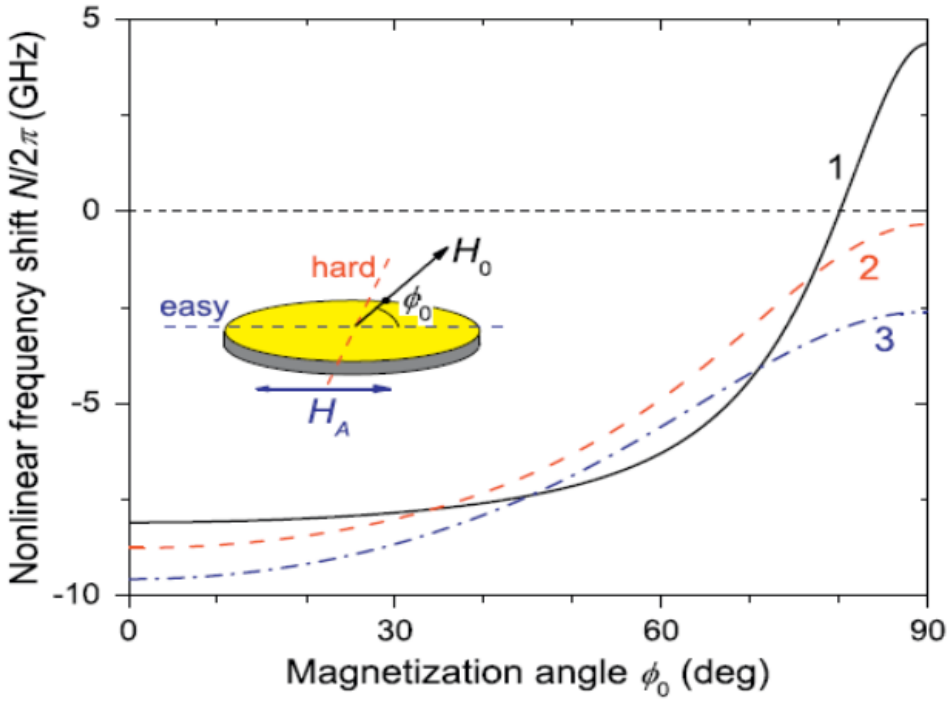

Figure 1.15: Inset: scheme of the in-plane magnetization precession of the FL under an externally applied magnetic field (H_o) that is directed to a tilt angle (ϕ_o) from the easy axis of the FL. H_A is the easy-axis anisotropy field. Main panel: calculated non-linear frequency shift $\frac{N}{2\pi} = \frac{df}{dp}$ as functions of ϕ_o and H_o (= 600 Oe for #1, 1200 Oe for #2 and 1800 Oe for #3) for $4\pi M_o$ = 8 kOe and H_A = 300 Oe. From [133]

the direct excitation of magnetization precession by the spin-polarized current and important when the current has the microwave component with the frequency close the ω_o, and V_J at $2\omega_o$. For a dc current-driven excitation these two terms can be neglected. The last term $\Gamma_J \propto \varepsilon J$ describes the effective damping driven by the spin-polarized current. However the ignorance of the extra terms (λ_J,V_J) was not clear for me in the paper because the terms did not seem to relate with microwave components in their formula. If they were not insignificant the expression of an auto-oscillator equation and the analytical linewidth formula could be different. More theoretical works are required to clarify the spin-torque

induced negative or positive feed-back effect in determining the coherence.

CHAPTER 2

ULTRAFAST SWITCHING OF A NANOMAGNET BY A COMBINED OUT-OF-PLANE AND IN-PLANE POLARIZED SPIN-CURRENT PULSE

In this chapter we report on spin valve devices that incorporate both an out-of-plane polarizer (OPP) to quickly excite spin torque (ST) switching and an in-plane polarizer/analyzer (IPP). For pulses < 200 ps we observe reliable precessional switching due largely to ST from the OPP. Compared to a conventional spin valve, for a given current amplitude ~ 2 to 3 times the zero-thermal-fluctuation critical current (I_{co}), the addition of the OPP can decrease the pulse width necessary for switching by a factor of 10 or more. The effect of the IPP also has beneficial ST consequences for the short pulse switching behavior.

2.1 Introduction

The spin torque (ST) induced in a ferromagnetic element by a spin polarized current may enable the development of ST magnetic random access memory (ST-MRAM) [16, 13]. For many applications, ST memory elements should be capable of fast switching, at or below the ns time scale, as well as having low switching currents and ultimately be implemented with tunnel junctions. Fast pulsed-current reversal experiments have previously been performed [96, 134, 135, 35, 89, 136] on current-perpendicular-to-the-plane (CPP) spin valve devices in which both the polarizing fixed magnetic layer and the switchable free magnetic layer have moments that lie in the sample plane in equilibrium (see Fig. 2.2 and 6.2). In this conventional geometry, generally there is an incubation time prior to reversal during which stochastically-initiated free layer oscillations grow gradually under ST, and the sub-ns switching process is

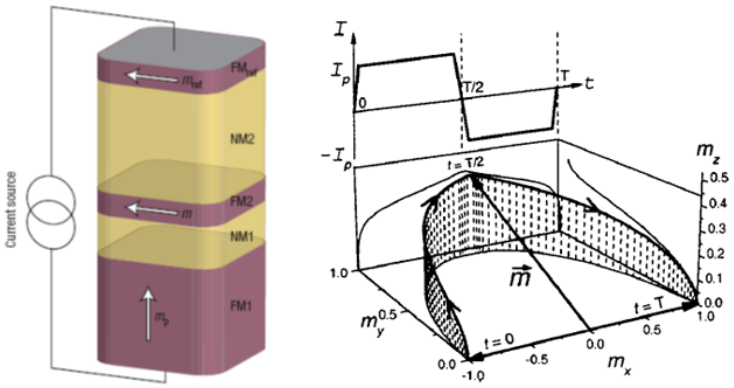

Figure 2.1: Spin-torque device structure (left) and monocycle pulse scheme (right) for the ultrafast switching, proposed by Kent. et al [99].

usually unreliable, with switching probabilities $P_S < 100$ % at the currents of interest for applications, due to thermal fluctuations in the initial magnetic orientation. Reliable switching with sub-ns pulses has been achieved in the conventional structure by adding a hard axis field [137, 97], to establish an equilibrium offset angle between the reference and free layers that is $\neq 0$ or π, although this approach adds circuit complexity.

A device modification for achieving fast ST-driven reversal has been suggested by Kent et al [99]. The proposed device has an in-plane polarized free layer (FL) and two fixed magnetic layers: one out-of-plane polarizer (OPP) in addition to one conventional in-plane polarizer/analyzer (IPP) (see Fig. 2.1 and 6.2). The spin current generated by the OPP exerts a torque on the free layer magnetization tilting it out-of-plane, inducing an out-of-plane demagnetization field that when sufficiently large can quickly rotate the free layer moment to the reversed orientation by a process similar to precessional reversal driven by hard axis magnetic field pulses [138].

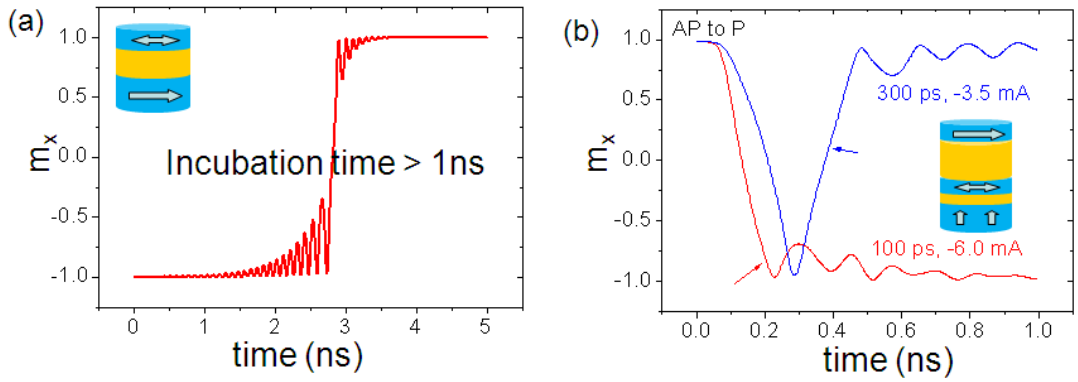

Figure 2.2: Illustration of typical switching time scales excited by (a) a collinear spin-polarizer, or by (b) an out-of-plane polarizer, obtained from macrospin simulations. In the collinear device there is typically an incubation time prior to the reversal. In the non-collinear device with an out-of-plane spin-torque, the induced out-of-plane demagnetization field can quickly rotate the FL to the reversed direction but a proper control of the pulse amplitude and width is required not to rotate the FL further or back to the original state.

Here we report the fast ST pulse (100 ps - 10 ns) switching performance of devices that incorporate such an OPP layer. These spin valve devices are similar to those previously used to examine thermally activated switching [139] and microwave emission [114, 140, 141], but differ in the choice of materials and in that our IPP layer was not designed to minimize its ST. We find that the OPP enables ST switching of a nanomagnet with simple spin current pulses with pulse width (t_p) as short as 100 ps. We demonstrate reliable switching at room temperature provided that t_p is shorter than a critical threshold and the pulse amplitude (I_p) is within a relatively broad window (~4 mA). For sub-ns switching, the I_p required for devices with the OPP is much less than for devices with just an IPP fixed layer. We also find that the ST from the IPP, if not designed [99] to be small, can have a significant and positive effect on the short-pulse reversal.

2.2 $[Co/Pt]_n$ Perpendicular Anisotropy film growth

We used a Co-Pt multilayer structure in our OPSV devices in order to obtain a "good" out-of-plane spin-polarizer (OPP), since it has been well known that $Pt/[Co/Pt]_n$ multilayers have a strong perpendicular magnetic anisotropy (PMA). The microscopic origin of the PMA lies on the enhancement of Co orbital moment which changes the direction of the spin moment to normal to the film plane through the strong and localized interfacial d-d hybridization. The PMA strongly depends on the growth conditions (method, power, pressure, tool and sometimes person), respective thickness of 3d Co and Pt, and repetition number (n).

We measured hysteresis loops of several Co-Pt multilayers with the Vibrating Sample Magnetometer (VSM) in Van-Dover's group for searching on optimized multilayers by characterizing its PMA. The thin film samples had the multi-layers of substrate/buffer/Pt10/$[Co0.44/Pt0.68]_n$/Cu/cap (in nm), deposited on the non-magnetic stage with our AJA sputtering system at room temperature. The buffer layer was $[Ta/CuN_x]_2Ta$, the cap was Pt(10) and n = 4, 8, 12. The base pressure was $< 2 \times 10^{-8}$ Torr, and low growth rates were used to obtain a better PMA with power ~20 W and Ar pressure ~2 mT. At my first trials I deposited the layers on the magnetic stage, but they did not show any PMA. The in-plane magnetic field on the stage might strongly disturb the formation of a PMA during the deposition. Or post-annealing treatment might induce a PMA although I have not checked this except Pt/Co bi-layer (see Chapter 6). Fig. 2.3 shows the measured hysteresis loops of $Pt[Co/Pt]_n$ by sweeping the out-of-plane field. With increased n the coercivity (H_c) was decreased, indicating more deterioration of the PMA. The reduction of the PMA with n may

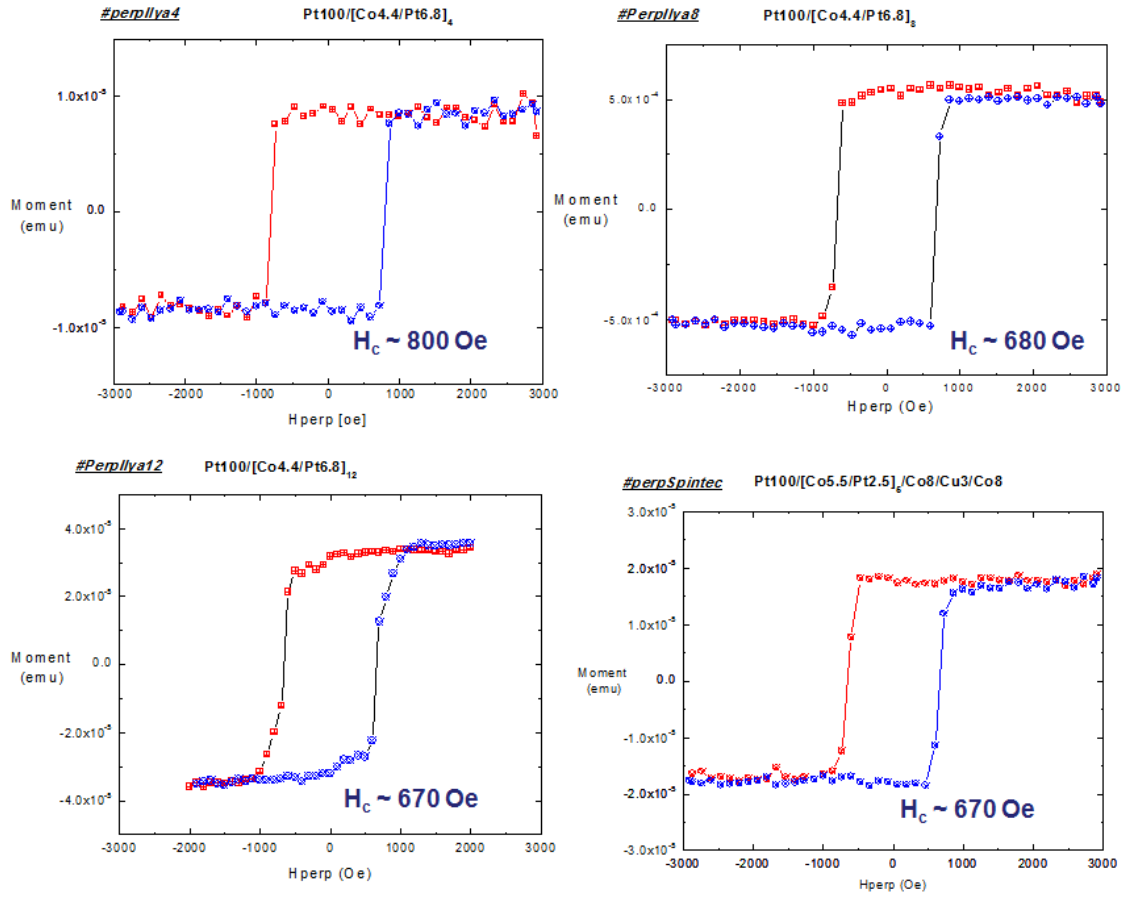

Figure 2.3: Illustration of hysteresis loops of Pt10/[Co0.44/Pt0.68]$_n$ (in nm) multilayers measured by the vibrating sample magnetometer for (a) n = 4, (b) n = 8, (c) n = 12. (d) Pt10/[Co0.55/Pt0.25]$_6$/Co0.8/Cu0.3/Co0.8. The coercive field (H_c) slightly decreases with n and multi-domains start to form when n = 12.

be associated with an interface roughness or a variation in the crystal structure of the Co layer as a result of the change in strain or grain size with increasing multilayer thickness. The layer with n = 4 was selected because it exhibited the largest PMA among the tested samples.

The OPP layer should have a high spin-polarization (SP) for producing efficient spin-torque (ST) onto the FL as well as a good PMA. However the Co-Pt multilayer does not allow having a sufficient SP because the incorporation of

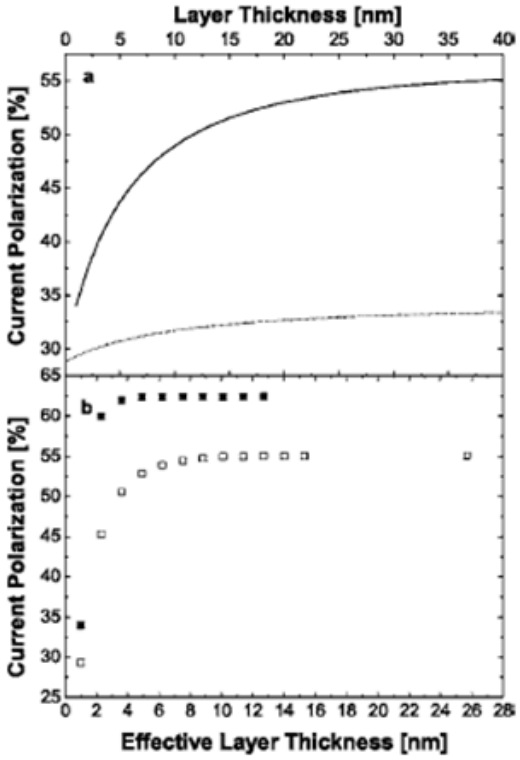

FIG. 6. Calculated current polarization in bottom electrode/ Cu 5 nm/*P*/Cu 5 nm/top electrode structure as a function of the effective thickness of layer *P*. (a) *P* is a simple Co monolayer (dotted line) or CoFe monolayer (solid line); (b) *P* is $(\text{Co 1 nm/Cu 0.3 nm/Co 1 nm})_n$ laminated multilayer (open square) or $(\text{CoFe 1 nm/Cu 0.3 nm/CoFe 1 nm})_n$ (filled square).

Figure 2.4: Calculated polarizations of polarization enhancement layers, based on $(\text{Co/Cu/Co})_n$ and $(\text{CoFe/Co/CoFe})_n$, from Ref. [142]. The introducing Cu in the laminating Co layer might reduce the effective spin-diffusion length of the multilayer and thereby increase the spin-polarization.

the Pt layers within the magnetic layers results high spin-orbit scattering and thereby reduction of the ST efficiencies. Therefore we have to deposit another polarization-enhancement layer (PEL) on top of Pt/[Co/Pt]_n, while maintaining the PMA, or at least the OPP layer should not be terminated by the Pt layer.

The terminated Co layer may give a sufficient SP as long as its thickness is comparable with its spin-diffusion length (~38 nm), but it will reduce the

PMA from the bulk effect of the Co-layer. Spintec group suggested a PEL layer composed of $[Co/Cu]_n/Co$, based on their theoretical work, that laminating the Co layers with Cu's may introduce strong spin-diffusive interfaces, thus reducing the effective spin diffusion length of the multilayer. Fig. 2.4, excerpted from the Ref. [142], shows their calculated SP's in $[Co/Cu]_n/Co$ in which the Co/Cu/Co could have very high SP ~45 %. However this value was likely over-estimated at least in our OPSV devices. About 20 % of SP seems to be more reasonable in our $Pt/[Co/Pt]_n/Co/Cu/Co$ layer when we compared the threshold currents from our micromagnetic simulation with this SP value to the measured ones at the STBPS regime. In any case the SP of our OPP layer was sufficient to generate enough ST to achieve the STBPS with short pulsed currents (< 200 ps). Nevertheless we need to perform several different types of experiments to identify the magnitude of SP in the OPP layer and eventually to improve the performance of the devices.

Figure 2.5 shows the measured hysteresis loop of the OPP layer used in our OPSV. The layer had $Pt/[Co/Pt]_4$ for the strong PMA and Co/Cu/Co for the PEL. The H_c (~750 Oe) was a little reduced compared to the one (~ 800 Oe) without the PEL. The saturation field or the anisotropy field (H_k) to the in-plane was ~7 kOe with the VSM measurement.

We could use the OPP layer based on $[Co/Ni]_n$ multilayer because this structure has a strong PMA and a high SP that satisfy the requirements as a good OPP layer. However a larger stray field is expected from the Co/Ni multilayer onto the FL, due to the composition of all magnetic materials (~higher M_s), than a $[Co/Pt]_n$ structure. From our micromagnetic studies the non-uniform stray fields from two polarizers generate asymmetric switching behaviors, but we

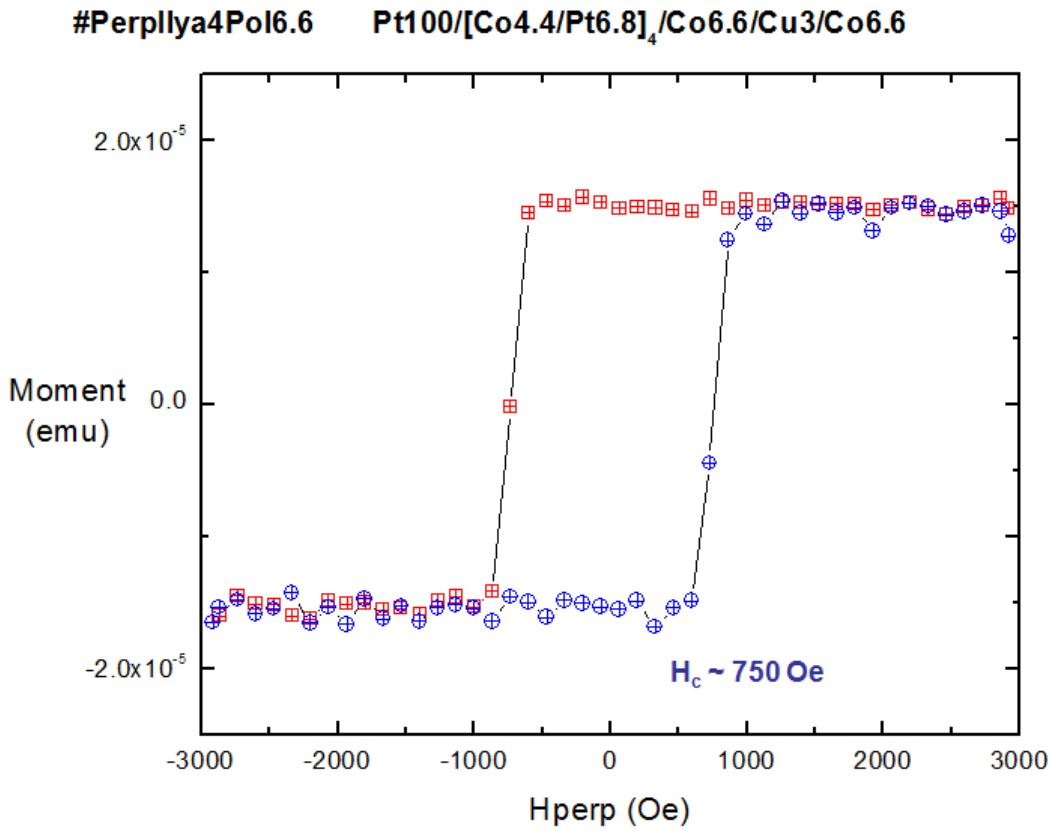

Figure 2.5: Illustration of hysteresis loops of Pt10/[Co0.44/Pt0.68]$_4$/Co0.66/Cu0.3/Co0.66 (in nm) multilayer measured by the vibrating sample magnetometer. This multi-layer structure is used as the out-of-plane spin-polarizer in this chapter for demonstrating the spin-torque driven ultrafast switching in this chapter.

desire that this is minimized for better deterministic switching windows (see Chapter 3).

I was a little worried about the possibility of the switching events in the OPP by the ST from the FL because the effective volume of this layer with n = 4 is relatively small even though it has a strong PMA. However the cited damping (α) of Co in the [Co/Pt]$_n$ multilayer are, up to now, order of magnitude larger than the usual ferromagnetic metal films. The magnetic damping in ultrathin

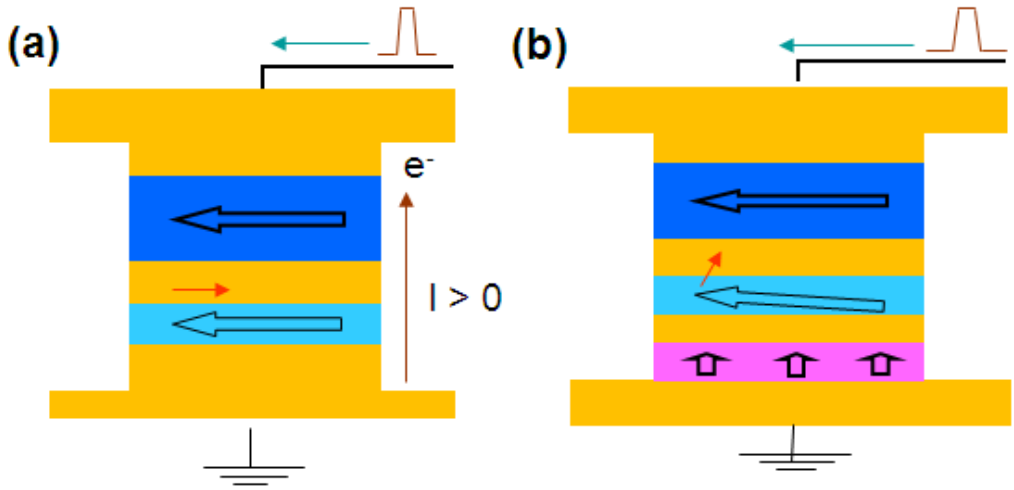

Figure 2.6: (a) Schematic of the conventional spin-valve (CSV) device. (b) Schematic of the out-of-plane spin-valve (OPSV) device.

magnetic films is generally increased with decreasing film thickness ($\alpha \sim 1/d$) due to the enhancement role of spin-orbit coupling, reflecting the general trend of large damping in ultrathin Co layer. The non magnetic layer, Pt, also has strong spin-orbit interaction, contributing to the increase of damping through the spin-pumping interaction. Additional dynamics could exist such as interfacial effect or decoherence that is the out-of-phase precession in different Co layers because the α of Co in the $[Co/Pt]_n$ films strongly depend on the periodic multilayer film structure FM/NM (Co/Pt) and the interfacial effect between the Co and Pt.

2.3 Device structure

We used sputter deposition and e-beam lithography to fabricate CPP spin valve devices with an elliptical cross-section of $\sim 70 \times 180$ nm^2 using two different layer structures. The first type had a conventional spin-valve (CSV) configu-

ration consisting of bottom-lead-1/Py(5)/Cu(12)/Py(20)/top-lead (thicknesses in nm), where Py is $Ni_{80}Fe_{20}$, the bottom-lead-1 is Py(5)/Cu(120) and top-lead is Cu(2)/Pt(30). The second type (OPSV) had the additional OPP layer. The layer configuration was bottom-lead-2/OPP/Cu(6)/Py(5)/Cu(12)/Py(20)/top-lead, where bottom-lead-2 is $[Ta(5)/Cu(N)(20)]_2/Ta(25)$ and the OPP was $Pt(10)/[Co(0.44)/Pt(0.68)]_4/Co(0.66)/Cu(0.3)/Co(0.66)$ (see Fig. 6.2).[114, 142] In both device types the 5 nm Py layer served as the magnetic FL and the 20 nm Py layer was the IPP. The out-of-plane anisotropy field required to saturate the moment of an unpatterned OPP layer in plane was ~7 kOe. All of the ST measurements we report were performed at ~ 300 K under an applied field canceling the average in-plane component of the dipole field from the IPP. Four CSV devices and five OPSV devices were studied in detail and similar results were obtained for all devices of each type.

2.4 Device Characterization

The average resistance difference ΔR between the parallel (P) and anti-parallel (AP) configurations of the CSV devices was 110 ± 15 mΩ, while for the OPSV devices ΔR = 85 ± 5 mΩ. This difference may be due to spin scattering in the OPP and/or to the effect of the dipole field from the OPP, which acts to cant the FL moment slightly out of plane.

We measured the average currents for thermally-activated switching of the free layer, both from AP to P (AP-P, relative to the IPP) and from P to AP (P-AP) as a function of the current ramp-rate to determine the energy barrier (E_a) for

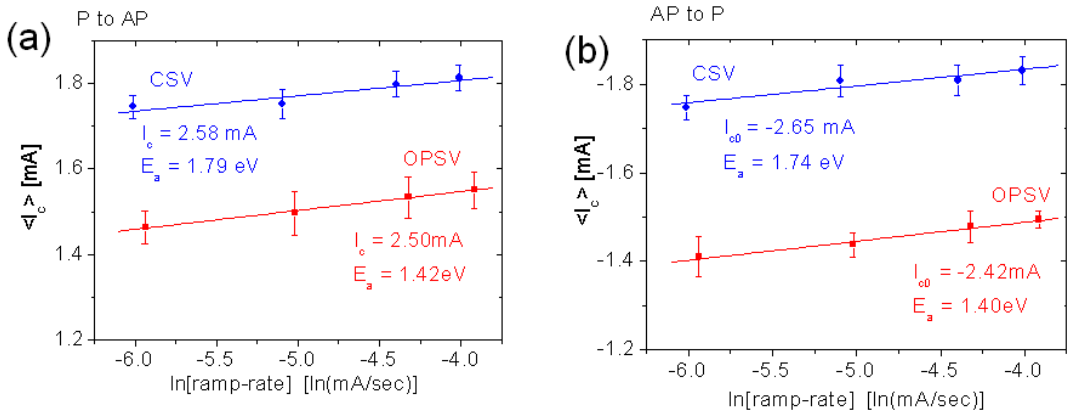

Figure 2.7: Measured average switching currents in the CSV and the OPSV as a function of the current ramp-rate for (a) P to AP and (b) AP to P. The energy barrier (E_a) for the magnetic reversal and the zero-temperature critical current (I_{co}) were determined by Eq. 2.1

magnetic reversal and I_{co} [143, 144]. In the Kurkijarvi model [143], we have

$$< I_c >= I_{c0}\left[1 - \frac{k_B T}{E_a} ln\left(\frac{k_B T |I_{c0}|}{\tau_0 E_a |R_I|}\right)\right] \tag{2.1}$$

where I_{c0} is the spin-torque reversal current in the absence of thermal fluctuations, k_B is Boltzmann's constant, R_I is the ramp-rate for current, τ_0 is the characteristic fluctuation attempt time (we assume typically 1 ns). For a representative pair of devices we obtained $I_{co}^{AP-P} \approx -2.65\ mA$, $I_{co}^{P-AP} \approx 2.58\ mA$, $E_a^{AP-P} \approx 1.74\ eV$,and $E_a^{P-AP} \approx 1.79\ eV$ for the CSV device, and $I_{co}^{AP-P} \approx -2.42\ mA$,$I_{co}^{P-AP} \approx 2.50\ mA$, $E_a^{AP-P} \approx 1.40\ eV$,$E_a^{P-AP} \approx 1.42\ eV$ and for the OPSV device. We attribute the somewhat lower values of E_a in the latter case to the effect of the dipole field from the OPP in decreasing the effective in-plane anisotropy field (H_k^{eff}).

	Conventional SV	OP-Polarizer SV
Device Name	OJI05-(6,8)-dev2	OPA13-(5,1)-dev4
Area	65 x 180 nm^2	70 x 180nm^2
R	4.13 Ω	5.64 Ω
ΔR	105 mΩ	88 mΩ
H_d	280 Oe	285 Oe
H_c	150 Oe	65 Oe
I_c (P-AP)	2.58 mA	2.50 mA
E_a (P-AP)	1.79 eV	1.42 eV
I_c (AP-P)	2.65 mA	2.42 mA
E_a (AP-P)	1.74 eV	1.40 eV

Figure 2.8: Comparison of the basic properties between the CSV and OPSV devices at low frequency (< 2 kHz). The I_{c0} and E_a were determined by fitting the ramp-rate data (see Fig. 2.7) to Eq. 2.1.

2.5 Results of pulse current switching

Results of pulsed-current ST reversals are shown in Fig. 2.9, which plots the switching probability (P_s) for quasi-rectangular (~65 ps rise and 105 ps fall time) pulses as functions of I_p and t_p. The CSV devices show reliable switching by the 6 ns (full width at half maximum) pulses, but 100% switching probability is impossible with 100 ps pulses up to $|\ I_p\ |$ ~ 16 mA (Fig. 2.9a-b). The OPSV devices exhibit three regimes of behavior in Fig. 2.9c-d: (i) a long pulse regime (e.g., t_p = 6 ns), where the switching distributions of the OPSV are very similar to the CSV, up to a certain $|\ I_p\ |$; (ii) an intermediate pulse-width regime (e.g., t_p = 600 ps), where there is no reliable switching of the OPSV; and (iii) a short pulse regime, $t_p \leq 0.2$ ns, where the OPSV reversal is very reliable (more than 998 reversals in 1000 attempts over a significant range of I_p) and efficient, with a much lower I_p required for switching compared to the CSV. For t_p = 100 ps,

at very high currents, ~ twice the onset current for first achieving P_s = 100 %, P_s begins to decrease, which we attribute to over-rotation in the precessional reversal. For 0.2 ns < t_p < 1 ns this over-rotation due to the OPP ST makes it impossible to obtain reliable OPSV reversal, while for long pulses, > 1 ns, the additional OPP ST results in only a limited range of pulse amplitude where 100 % reversal can be obtained.

Note on the pulsed switching measurement

The pulsed current measurement to a ST device is basically for characterizing the response time (or switching speed) of the ST device to the applied pulsed currents. This has been achieved by measuring the switching probabilities as functions of switching directions (P-AP or AP-P), external fields, pulse durations and/or amplitudes. The measurement has been carried out for a long time with various types of ST devices in Buhrman/Ralph group. It will be redundant if I discuss about the technique here again. I comment on the estimation of pulse current amplitude from the applied voltage amplitude generated from a short pulse generator (e.g. 10,070A). Previous dissertations [145, 146] suggested two different methods: (1) calculating the transmission/reflection coefficients by considering the impedance mismatch between the 50 Ω line and the load resistance, (2) comparing the measured P_s with/without a small applied dc current (I). In my experience the second method was not reliable in a device with a small H_c (if < 20 - 30 Oe or if there is an apparant backhopping with large pulsed currents) in which a small I could generate relatively significant amount of the thermal fluctuation in the FL. This could result in an under-estimation of the pulse amplitude to a given voltage amplitude. In addition there might be

a current-leakage for very short pulsed current to the Si-substrate through the capactitanc coupling (see Section 4.10) and we might over-estimate the amplitudes of pulsed current with $t_p < 200$ ps. Instead we have to include the effective capacitance depending on the frequency when we calculate the impedance mismatch between the load and the 50 Ω transmission line.

2.6 Comparision of two devices

In Fig. 2.10 we plot the values of I_p that yielded P_s = 95 % for the OPSV and CSV as a function of $1/t_p$ to compare the ST-induced switching speeds. In the macrospin approximation for $I > I_{co}$ the switching time τ for a CSV varies linearly with ST current amplitude [96] as $\tau^{-1} = \zeta(I - I_{co})$. Fitting to the CSV data of Fig. 2.10, assuming that $\tau \approx t_p$, we obtain $\zeta^{AP-P} = 0.158\ ns^{-1}mA^{-1}$, $I_{co}^{AP-P} = -2.55\ mA$ and $\zeta^{P-AP} = 0.131\ ns^{-1}mA^{-1}$, $I_{co}^{P-AP} = 2.44\ mA$. These I_{co} values are in close accord with the values obtained from the ramp-rate measurements for the CSV. The same linear relationship also provides a good fit for the OPSV switching data in the short pulse regime ($1/t_p > 5\ ns^{-1}$) despite the fact that the assumptions of ref. [96] do not apply. Fits to the OPSV data in Fig. 2.10 yield $\zeta^{AP-P} = 6.117\ ns^{-1}mA^{-1}$, $I_{co}^{AP-P} = -5.13\ mA$, and $\zeta^{P-AP} = 11.54\ ns^{-1}mA^{-1}$, $I_{co}^{P-AP} = 3.54\ mA$. These I_{co} values are significantly larger than those obtained from the ramp-rate data, suggesting that the OPSV reversal mechanism for short t_p is distinctly different than for long t_p. Moreover, the short-pulse ST switching speed efficiency (ζ) is approximately 40× that of the CSV device for the AP-P case, and nearly 90× that for the P-AP case. We ascribe this to the lack of an incubation delay in the OPSV, reflecting that precessional reversal in the OPSV need not be preceded by a slow spiraling of the FL moment away from the equi-

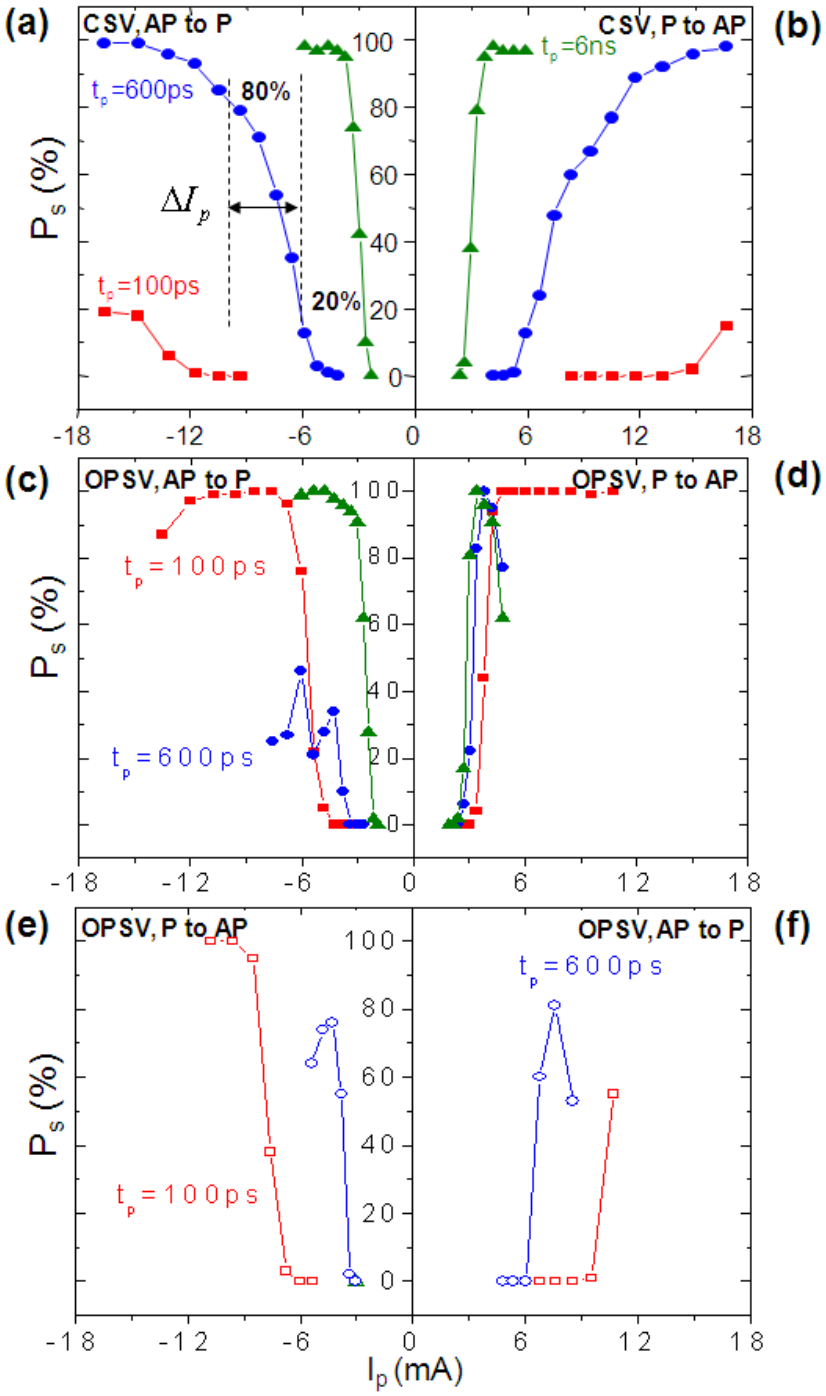

Figure 2.9: Switching probability P_s as a function of pulse amplitude I_p for 100 ps, 600 ps and 6 ns pulse widths (t_p). (a,b) Results for the CSV for (a) AP-P and (b) P-AP reversal. (c,d) Results for the OPSV for the signs of current which give switching in conventional ST devices: (c) AP-P and (d) P-AP. (e,f) Results for the OPSV with the signs of current opposite to those needed for switching in conventional ST devices: (e) P-AP and (f) AP-P.

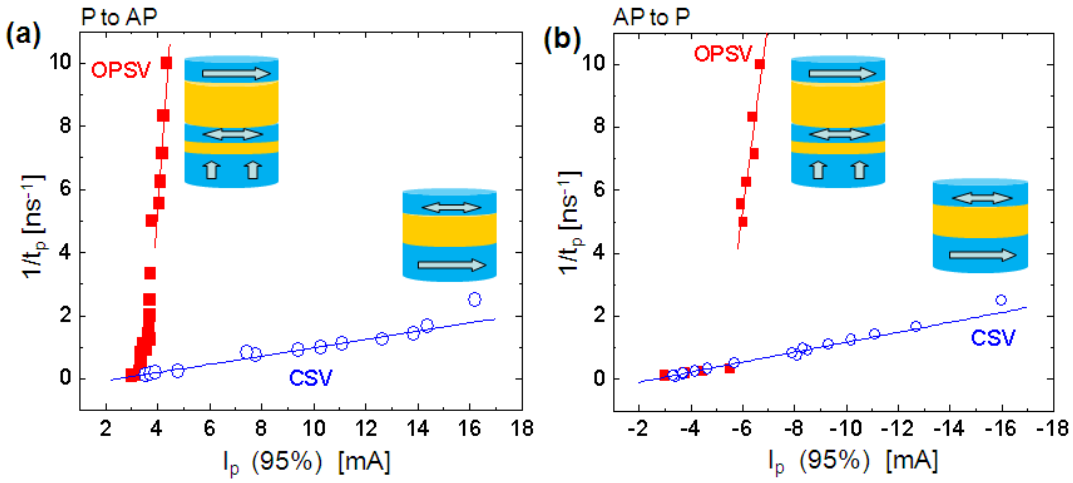

Figure 2.10: Comparison of the reversal speed between the OPSV and CSV devices. The inverse of pulse widths ($1/t_p$) is plotted as a function of the pulse amplitude I_p that yields a 95 % switching probability P_s for: (a) P to AP and (b) AP to P reversals. For the OPSV device, pulse widths between 0.3 ns and 2 ns do not achieve 95 % AP-P switching for any negative value of I_p.

librium configuration.

The difference in the mechanisms for fast-pulse switching in the OPSVs and CSVs is also illustrated by ΔI_p, the difference between the pulse amplitudes required for 20 % and 80 % switching probabilities (see Fig. 2.11). For the CSV, ΔI_p grows to be as large as 5 mA, while for the OPSVs in the short pulse regime ΔI_p is always less than 0.7 mA. (ΔI_p for OPSVs can be larger for longer pulses; see Fig. 2.11) The broad distributions for the CSVs can be explained by thermal fluctuations in the initial offset angle of the free layer about the P and AP configurations. Because the initial orientation of the FL in the OPSV is always close to perpendicular to the OPP, the effects of thermal fluctuations are minimized.

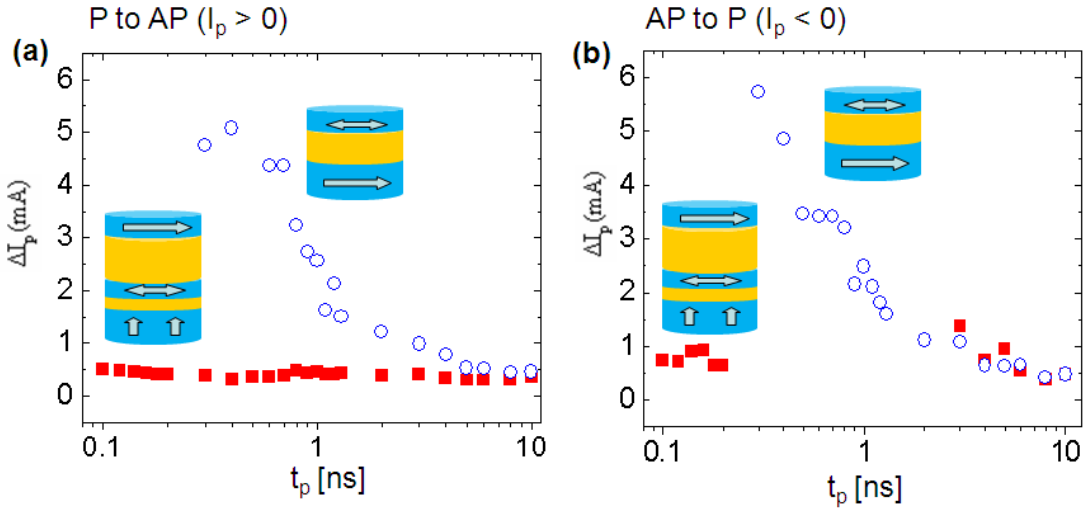

Figure 2.11: The difference ($\triangle I_p$) between the pulse current amplitudes that yield P_s = 80 % and P_s = 20 % as a function of t_p for (a) P-AP and (b) AP-P. Large values of $\triangle I_p$ indicate a significant effect of thermal fluctuations on the reversal process.

2.7 Discussion

The original proposal of Kent et al. for OPP precessional reversal anticipated that a current pulse of either bias would equally well drive magnetic reversal for either P-AP or AP-P switching [99]. This current symmetry would limit the write operation to toggle mode (or reversible) switching where the final state is always flipped from the initial state. However we observe that the minimum values of $|I_p|$ required for short-pulse reversal are different for AP-P and P-AP switching (Fig. 2.9c-d), and are also different when the current flows are reversed (Fig. 2.9e-f). For the OPSVs, P-AP switching requires lower onset currents than AP-P, and switching is also easier for the sign of I_p that gives ST-switching in the CSVs (Fig. 2.9c-d) than for reversed currents (Fig. 2.9e-f).

Based on micromagnetic simulations, we argue that the differences in onset

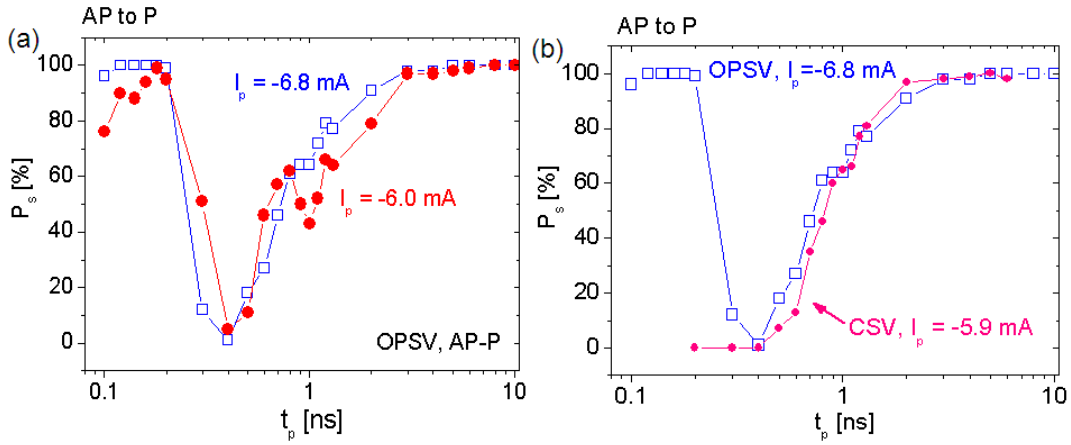

Figure 2.12: Measured switching probability (P_s) for AP to P as a function of the pulse width (t_p) at a fixed pulse current amplitude (I_p). (a) I_p = -6.8 mA and -6.0 mA for the OPSV. (b) I_p = -5.9 mA for the CSV for the comparison to the OPSV. The lowest P_s is due to the one full rotation (2π) of the FL by the I_p's with t_p = 300 to 400 ps. This time-scale might be approximately the inverse of its natural (or FMR) frequency (~ 3 GHz).

current between P-AP and AP-P reversals are due to the combined effect of the dipolar fields from the edges of the IPP and from the OPP, which add on one side of the free layer (see the inset Fig. 2.14) but almost cancel on the other. This non-uniform field causes the effective in-plane anisotropy field H_k^{eff} on the additive side (right) to increase in the AP case and decrease in the P case, giving effectively different onset currents [147] for reversal as a function of the position. The result in simulations is that reversal first occurs at one end of the FL (on the right for P-AP, and the left for AP-P, independent of the sign of I_p) and then is completed via the exchange interaction, and that the value of $|I_p|$ needed for reversal is lower in the P-AP case than for AP-P.

The effect of ST from the IPP can explain the difference in short pulse reversal behavior with current direction for a given type of switching (P-AP or

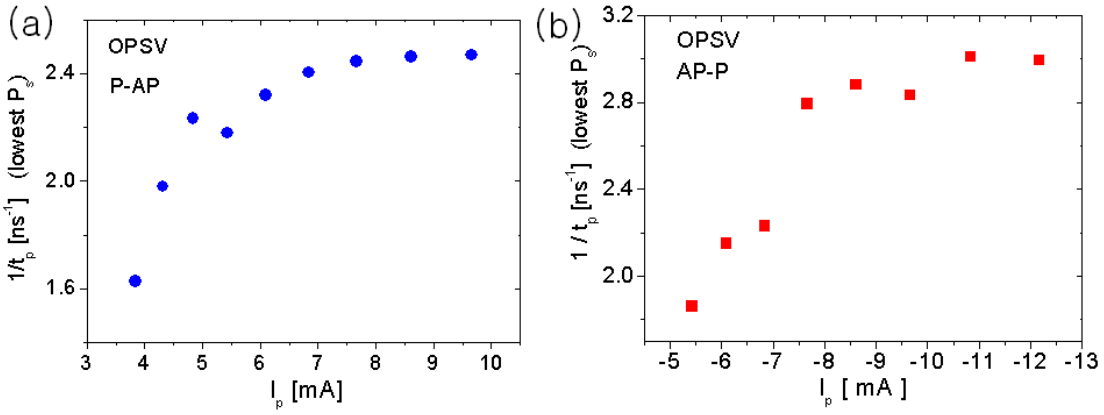

Figure 2.13: Measured inverse of pulse widths ($1 / t_p$) for the lowest switching probability (P_s) (see Fig. 2.12) as a function of the pulse amplitude (I_p) for OPSV (a) for P-AP (b) for AP-P. We can interpret that the switching speed increases with the pulse amplitude due to the larger out-of-plane demagnetization field, if we assume that the switching time is close to the t_p.

AP-P), in that just as in CSV devices the ST from the IPP promotes P-AP switching for $+I_p$ and AP-P switching for $-I_p$. Due to the greater non-uniformity in the starting magnetization in the AP configuration, the effect of the IPP ST is enhanced, giving a larger difference between the two signs of current for AP-P reversal (compare Fig. 2.9f and 2.9c). These differences provide a current window [$\Delta(+I_p) \approx 6$ mA] in which a $+I_p$ can reliably drive P-AP switching without AP-P. This can alleviate the need to employ a read-before-write approach in short pulse OPP ST-MRAM devices that would be required if the threshold values of I_p were equal.

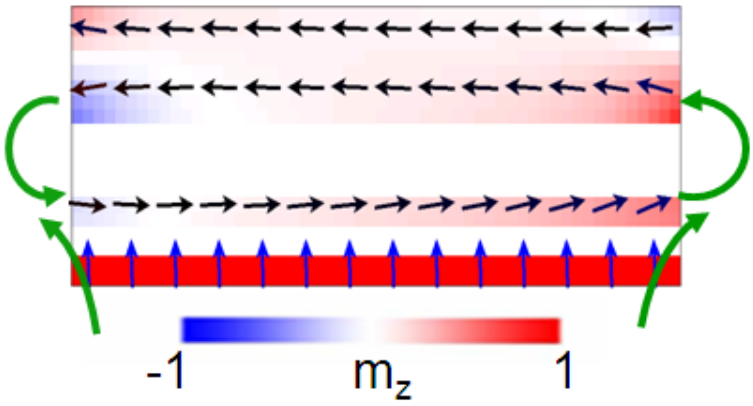

Figure 2.14: Micromagnetic configurations for the initial AP state. Color-Scale: Out-of-plane component of the normalized magnetization (M_z). The non-uniform stray field from the two polarizers causes the effective in-plane anisotropy field H_k^{eff} on the additive side (right) to increase in the AP case and decrease in the P case, giving effectively different onset currents for reversal as a function of the position. The details of this effect will be discussed in the next chapter.

2.8 Conclusion

In summary, we show that reliable precessional switching with short ($t_p < 0.2$ ns) rectangular pulses can be achieved in ST devices incorporating both OPP and IPP fixed layers. Due to the effects of the IPP ST and non-uniform local dipole fields, we find different threshold currents for the four cases $+I_p^{P-AP}$, $-I_p^{P-AP}$, $+I_p^{AP-P}$, and $-I_p^{AP-P}$. The results indicate that it is possible to optimize pulse amplitudes and widths within significant parameter windows so that a pulse with a given sign of current produces only the desired state (P or AP). Such devices could lead to a very high-speed non-volatile magnetic memory cell with sub-100 ps write pulses.

CHAPTER 3

SPIN-TORQUE-DRIVEN BALLISTIC PRECESSIONAL SWITCHING WITH 50 PS IMPULSES

In this chapter I demonstrate reliable spin-torque-driven ballistic precessional switching using 50 ps current impulses in a spin-valve device that includes both in-plane and out-of-plane spin polarizers. Different threshold currents as functions of switching direction and current polarity enable the final orientation of the magnetic free layer to be steered, in accord with a macrospin analysis, by the sign of the pulse, eliminating the need for read-before-write toggle operation. The pulse amplitude windows for this deterministic operation are wider and more symmetric as a function of current polarity for shorter impulses, while inhomogeneous fringe fields from the polarizers lead to asymmetries as a function of current direction.

3.1 Introduction

The fast reversal of a nanomagnet is of active interest because its study can enhance understanding of fundamental magnetic dynamics and because of the technological advantages that a successful high-speed non-volatile magnetic memory could provide. Several schemes [13, 138, 148, 97, 96, 99, 147] have been explored for fast nanomagnet switching, with the perhaps most scalable approach being demonstrated by recent experiments [149, 100, 101, 102] which achieved reliable high-speed reversal of a thin film nanomagnet by using the spin torque (ST) from a spin-polarized current pulse as short as 100 ps. These experiments utilized devices in which a thin film free layer (FL) is located between an out-of-plane (OP) spin polarizer (OPP) and an in-plane (IP) ana-

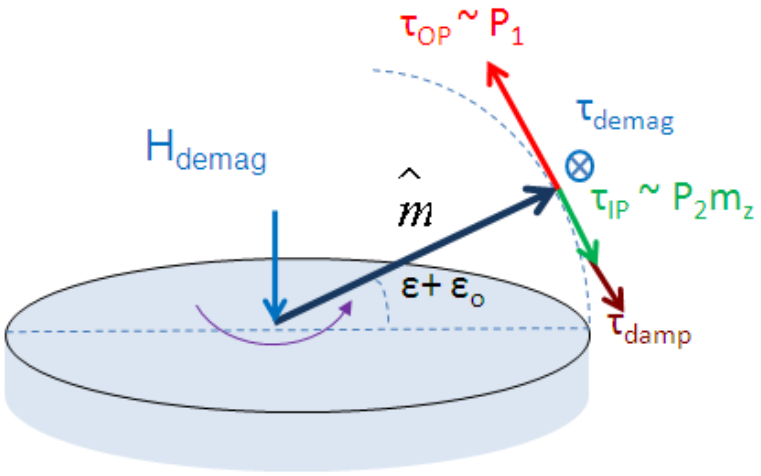

Figure 3.1: Scheme of spin-torque driven ballistic precessional switching (STBPS). In the case shown, the current polarity and orientations of the fixed layers are such that the OP torque promotes upward (positive z) displacement of $\hat{m}$ and the IP torque retards it.

lyzer/polarizer (IPP). In this configuration the ST (τ_{OP}) generated by a strong OP-polarized current pulse incident upon the FL forces the FL moment out of plane, inducing a demagnetization field (H_{demag}) about which the FL begins to precess [99, 147]. If the pulse width and amplitude are properly controlled the result can be a rapid rotation of the moment by 180^o to the reversed equilibrium position. The simplest form of this OP-precessional reversal scheme has the potential disadvantage of being a toggle operation, in which both P-to-AP and AP-to-P switching occur for either sign of current. This is in contrast to a deterministic operation in which the final state is controlled by the current polarity, as is the case for ST devices only utilizing IP polarized currents. However, previous OP-ST experiments [150, 100, 101] in which the IPP also exerted a strong ST, τ_{IP}, on the FL obtained differences in the threshold currents for switching as functions of current polarity and switching direction. This indicated that the final state in OP-ST devices may be determinable by pulse-current polarity,

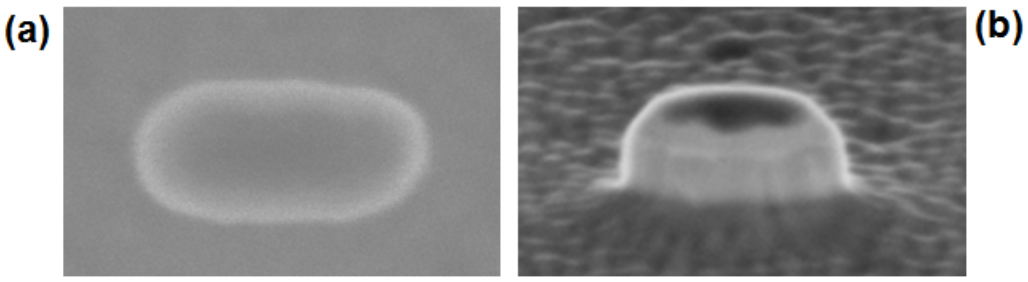

Figure 3.2: Scanning Electron Microscope Image for a nanopillar spin-valve device. (a) top-view (b) side-view.

although with pulse widths ≥ 100 ps only one current polarity showed a sufficiently wide window between the switching currents for P-to-AP and AP-to-P to yield reliable writes [149].

Here we report the achievement of reliable and deterministic spin torque ballistic precessional switching (STBPS) by using 50 ps current impulses, demonstrating that shorter and stronger pulses can enhance the influence of τ_{IP}, providing wider current windows for deterministic switching. Based on micromagnetic simulations, we also conclude that inhomogeneous stray magnetic fields from the two polarizers induce asymmetries in the deterministic switching windows for the two current polarities.

3.2 Device Structure and Information

I fabricated nanopillar spin valve devices from thin-film multilayers with the structure: bottom lead/OPP/Cu(6)/Py(5)/Cu(12)/Py(20)/top lead (thicknesses in nm), where Py is $Ni_{80}Fe_{20}$. The OPP was Pt(10)/[Co(0.44)/Pt(0.68)]$_4$ /Co(0.66)/Cu(0.3)/Co(0.66). The 5 nm Py layer served as the magnetic FL and

the 20 nm Py layer was the IPP. The devices were fabricated into approximately elliptical cross-sections with dimensions 50×170 nm^2, with the etch producing slightly tapered side walls (20-30^o from vertical) [136]. The thickness of the IPP (20 nm) was chosen to be much greater than the spin-diffusion length (~5 nm) to ensure a strong τ_{IP}. For pulses longer than 200 ps, these devices exhibited precessional switching characteristics similar to previous meausurements [149]. Here we focus on results obtained with 50 and 100 ps impulses.

3.3 50 ps impulses generation

For the pulsed switching measurement in our spin-torque (ST) devices, we have used the commercial pulse generator (PPLS 10,070A), a shared equipment in CNS at Cornell, that provides a rectangular shape of voltage pulse with duration from 100 ps to 10 ns and with amplitude from -7.5 to 7.5 V. The shortest pulse width, nominally 100 ps but actually ~ 130 ps, was enough to show the ultrafast ST-driven ballistic switching in our orthogonal ST devices. However my desire has been laying on the experimental demonstration of the STBPS with shorter current impulses and ultimately exploring the investigation of the fundamental limit in the switching speed driven by the ST. Then the challenge is the generation of sub 100 ps electrical impulses, eventually sub 10 ps current pulses if possible. In this section I will describe one electrical method for generating 50 ps current impulses used for demonstrating the STBPS in this chapter.

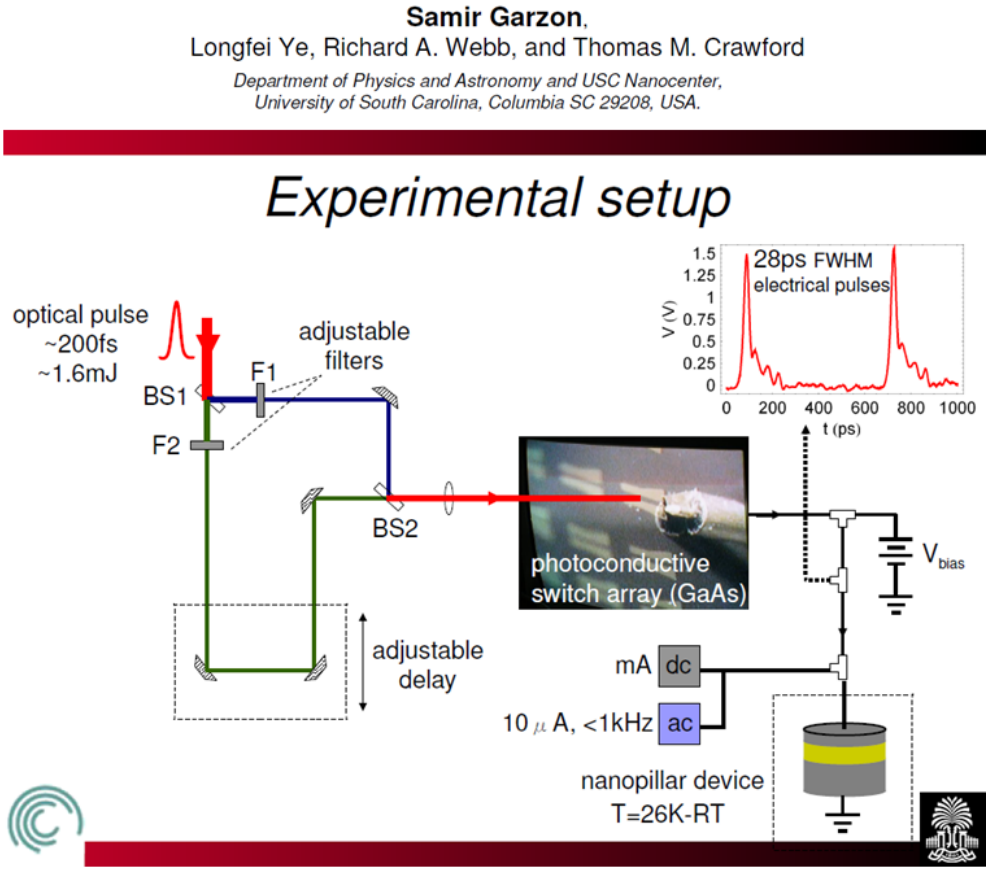

Figure 3.3: Optical setup for generating ~30 ps electrical impulses at room temperature demonstrated by S. Garzon et al [97].

3.3.1 Survey of other techniques

I considered several techniques. First one was by using Picosecond Pulse Labs (PSPL) 3500D that generates a 65 ps impulse from their specification document. Consulting with PSPL, however, the actual FWHM of output impulses was ~ 75 ps which was not much advanced from the 100 ps pulse generator. Secondly S. Garzon et al [97] demonstrated very exciting experimental technique for generating a short electrical impulse. By utilizing a femto-second mode-locked laser in single-shot mode, a single optical pulse with adjustable amplitudes was gen-

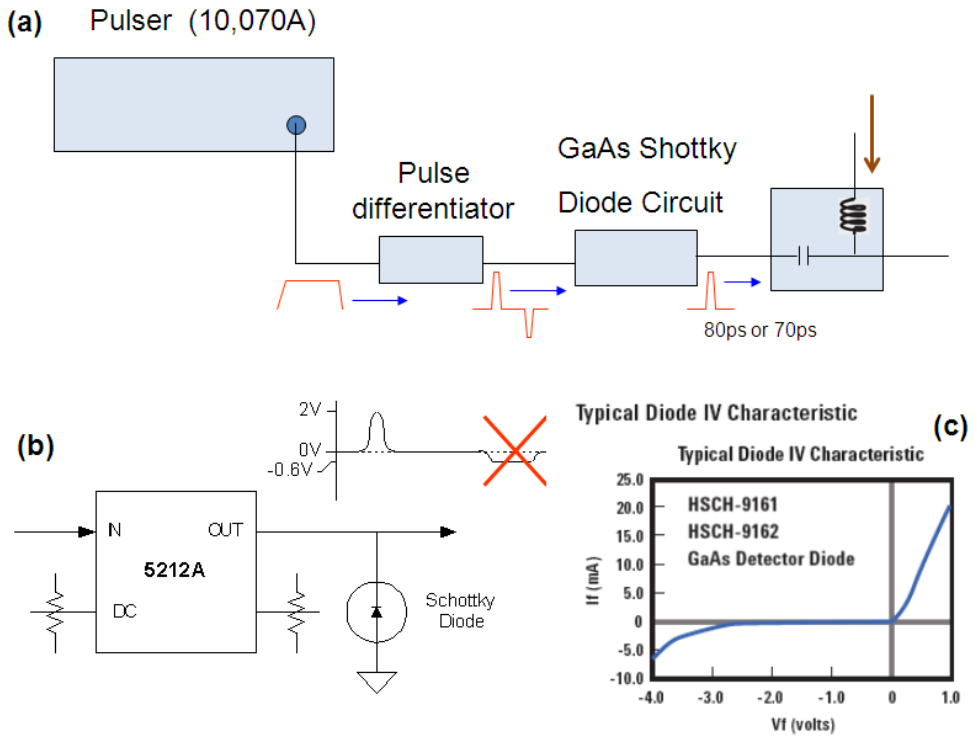

Figure 3.4: Circuit for generating a sub 100 ps impulse by suppressing the negative part of an Impulse Forming Network (IFN) output voltage as an input voltage from a pulse generator (e.g. 10,070A).

erated and then was converted to an electrical impulse using a LT-GaAs/Au photoconductive switch. In their paper they said that typical pulse widths were ~30 ps at room-temperature. This is an amazing technique I hope to have a chance to use it. However, from their pre-print posted on the arXiv [0806.2297] and their presentation on the internet (see Fig. 3.3), the proposed waveform had a broad (~100 ps) and significant (~ 25 % of peak amplitude) tail that would give a significant ST-impact in their pulsed switching and that could change the dynamics. Lastly, as the advice from PSPL, a single shorter impulse can be obtained if we can suppress the negative part of an Impulse Forming Network (IFN) output as an input voltage from 10,070A. A GaAs Schottky diode (HSCH-9161) could be used to block the negative voltage pulse up to ~ 2 V, which is

enough in our measurement, as the experimental scheme was suggested in Fig. 3.4. However I was not convinced with this technique because I could not find a commercial mounted GaAs diode circuit and the expected pulse widths were still ~70 or 80 ps if considering the risetime of 10,070A.

3.3.2 Basic concept for generating the impulse

For the spin-torque driven ballistic precessional switching (STBPS) experiment in this chapter, a short 50 ps voltage impulse was generated by differentiating a sharply falling step pulse, while pulses with 100 ps widths were generated with the 10,070A. A step pulse has generally a sharp leading edge, a flat line and a much slower (>10 times) trailing edge. The 4015D step pulse generator, we used, produces a negative polarity pulse with ~12 ps falltime at the leading edge, followed by a fixed 5 ns duration at -5 V. The risetime of the signal at the trailing edge is ~20 ns. The step pulse is generated in a small external head, 4015D-RPH (Remote Pulse Head), that is attached to the main unit (4015D) via a 50 Ω coaxial cable. This 4015D-RPH eliminates the falltime (or risetime) slowing effects of interconnecting coaxial cables.

The step pulse generator has been designed with very slow trailing edges to optimize the performance when combined with an IFN. The IFN produces an output voltage (V_{out}) that is approximately the derivative of the input voltage signal (V_{in}), i.e $V_{out} \approx T_c dV_{in}/dt$ where T_c is the derivative time coefficient, while the component also maintains an excellent impedance match on all ports. For instance, the V_{out} will be an impulse if the V_{in} is a step pulse, or the V_{out} will be a monocycle if the V_{in} is an impulse. The trailing edge of the step pulse from the

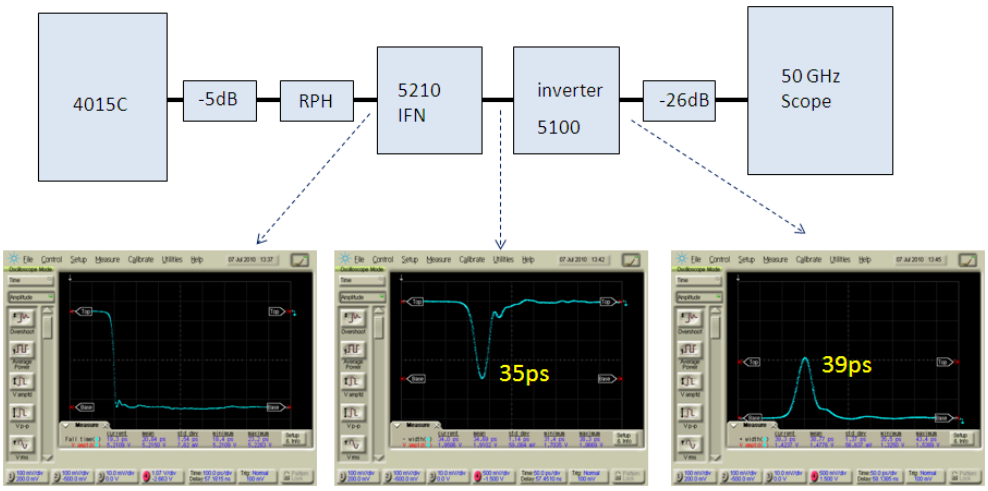

Figure 3.5: A short impulse voltage (~ 39 ps) was generated with 4015C (or 4016C) step pulse generator, 5210 Impulse Forming Network (IFN), 5100 Inverter. Pico-second Pulse Labs (PPLs) provided the concept of the circuit and the tested pulse shapes in their hardwares.

4015D is more than 100 times slower than the leading edge. When the 5210 IFN is connected to the 4015D, the V_{out} will be a very short impulse created from the leading edge while the trailing impulse will be negligible because its amplitude will have less than 100th of the amplitude of the leading V_{out} impulse.

3.3.3 Test of electrical impulse generation

PSPL performed the pre-tests with their 4016C step pulse generator, 5210 IFN and 5100 inverting transformer. Fig. 3.5 shows the measured waveforms after the RPH (a step-pulse), after the IFN (a negative impulse) and after the Inverter (a positive impulse). The pulse width of the impulse after the 5100 was increased a little bit, contributed from the Inverter. I checked the generated pulse shapes after each component with 4015D, 5210 IFN, 5100 Inverter, 5510 attenuators and 5541A bias tee. Typically 1-3 ps pulse widths were increased after each

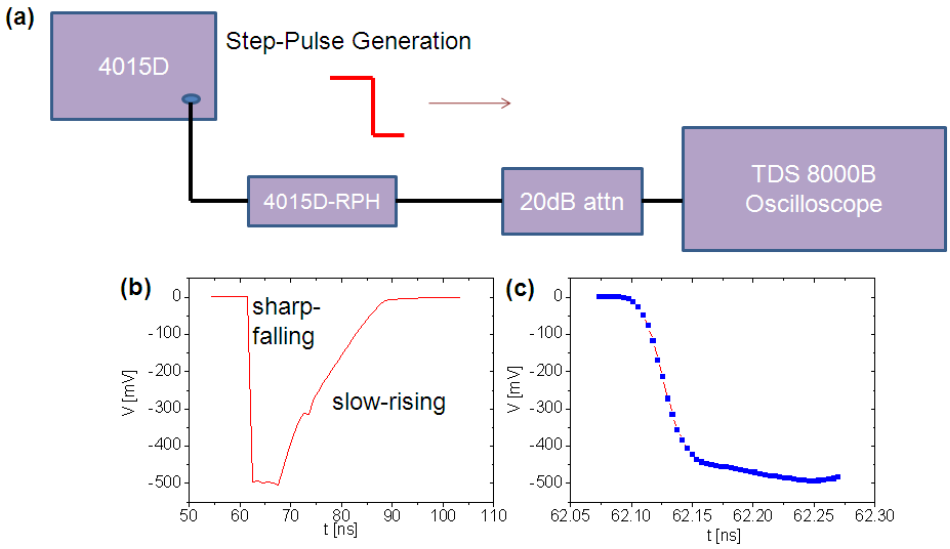

Figure 3.6: (a) Time-domain measurement of a sharply falling step pulse with 4015D step-pulse generator, 4015D-RPH (Remote Pulse Head) edge compressor, 20 dB attenuator and TDS 8000B sampling oscilloscope, (b) Measured falltime (10 % - 90 %) is < 20 ps and risetime (10 % - 90 %) is ~20 ns. (c) Enlarged waveform of the step pulse at the falltime.

component. Fig. 3.6 shows the measured step pulse while Fig. 3.7 shows the differentiated impulse shape. The pulse width was ~ 43 ps while it was increased to ~ 50 ps after the bias-tee. After 11 ns of the impulse we observed a bundle of waves corresponding to a small perturbation in the middle of the slow trailing edge of the step pulse. From the manual of the 4015D these small garbage pulses are generated from the inside of 4015D, even PSPL had not been able to solve the problem by the time. The maximum amplitude of this garbage pulse was about 12 % of the leading impulse, so we neglected its ST effect in our STBPS experiment. The expected maximum current (~2.2 mA) of the garbage pulses, when the maximum applied impulse currents were ~18 mA, was smaller than the DC reset currents (2.5 to 3.0 mA).

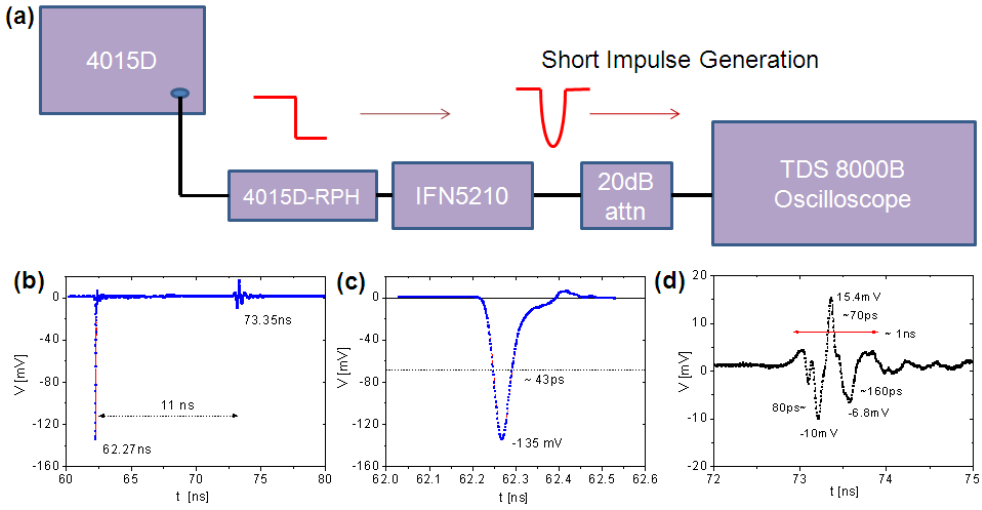

Figure 3.7: (a) Time-domain measurement of an impulse (~ 43 ps) with 4015D step pulse generator, 4015D-RPH edge compressor, IFN5210 Impulse Forming Network, 20 dB attenuator and TDS 8000B oscilloscope. (b) Measured waveform. A negative impulse was generated from the sharply falling step pulse (see Fig. 3.6). After 11 ns a bundle of waves were observed. These originates from the internal 4015D and can be ignored since the maximum pulse amplitude is less than 12 % of the impulse amplitude. The magnetic free layer in this chapter does not switch with such low amplitude and short pulses. (c) Enlarged impulse shape. (d) Enlarged garbage waves.

3.3.4 Experimental setup for impulsed switching

Fig. 3.8 shows the experimental setup used in the pulsed switching measurement in this chapter. The polarity of the generated impulses was controlled with the inverter while the amplitude was adjusted by combination of the attenuators (1, 2, 3, 6, 10 or 12 dB). Since 4015D does not provide any programmable function, the inverter and the attenuators were manually replaced while the high frequency probes were lifted for protecting the devices. The 10,070A was still used for generating an external trigger signal into the 4015D. Except the high frequency part of the bias tee the setup was similar with the previous

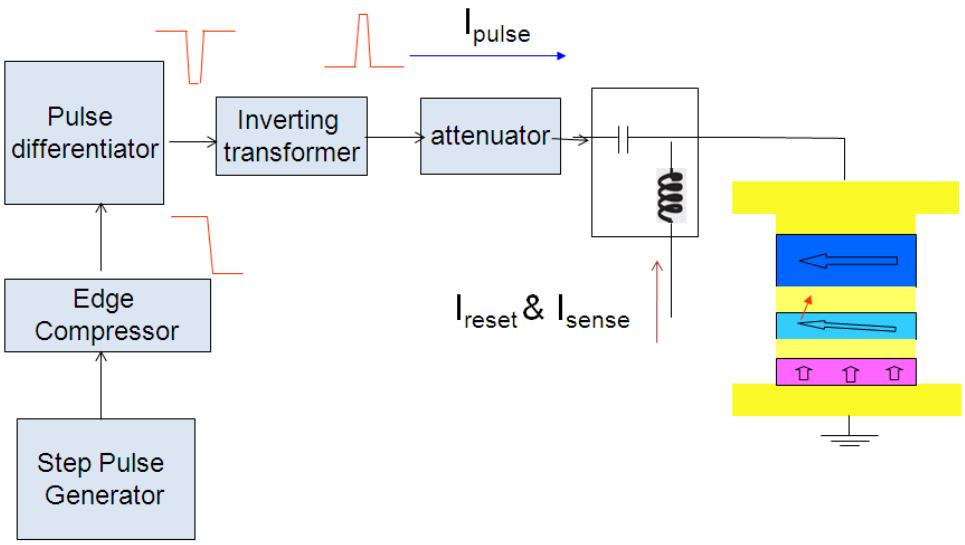

Figure 3.8: Scheme of pulsed switching measurement with 50 ps impulses generated from 4015D step pulse generator, 4015D-RPH edge compressor, 5210-IFN Impulse Forming Network, 5100 Inverter, attenuators (5510) and bias-tee (5541A). The bandwidth (< 18 GHz) of the bias-tee and the attenuators limit the pulse width of the current impulses. Measured impulse shape is provided in Fig. 3.9. Reset currents and sense currents are applied through the low frequency part of the bias tee.

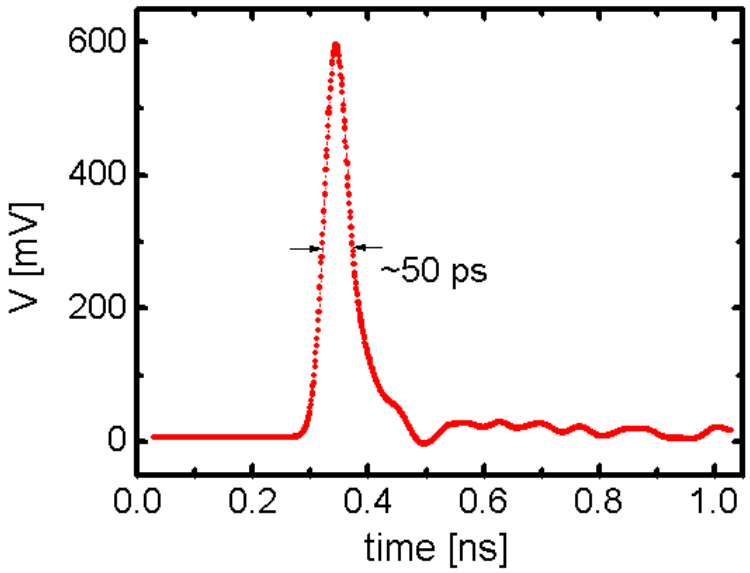

Figure 3.9: Measured waveform of the ~ 50 ps (Full width half maximum) voltage impulse injected into the device.

pulsed switching measurements: reset current and sense currents were applied through the low frequency part of the bias tee and the device resistance was measured via the Wheatstone bridge box. The current amplitudes through the device were calculated from the voltage amplitude of the impulses, measured with TDS 8000B oscilloscope, by taking into account the impedance mismatch between the device and 50 Ω transmission line.

3.4 Short-pulsed measurement

We generated 50 ps current impulses (Fig. 3.9) by differentiating a sharply falling step pulse, while pulses with 100 ps widths were generated with a commercial pulse generator. The current through the device was calculated taking into account the impedance mismatch between the load resistance and the 50 Ω transmission line [135, 151]. All measurements were performed at room temperature under an applied magnetic field canceling the average in-plane dipole field from the IPP. Ten devices were studied in detail and similar behavior was obtained in all cases. We define positive current to correspond to electron flow from the OPP to the FL (and to the IPP). Fig. 3.10a-b show switching probabilities (P_s) obtained from one device as functions of current amplitude, polarity, and switching direction (P-to-AP or AP-to-P) using both 50 ps and 100 ps current impulses. For the 50 ps case, reliable P-to-AP switching ($P_s \geq 95$ %) was achieved for current pulse amplitudes beyond $I^+_{r,P-to-AP} \sim 11$ mA but AP-to-P switching was not observed up to the highest pulse level employed, from which we conclude that the threshold current ($P_s \geq 5$ %) to initiate switching is $I^+_{th,AP-to-P} > 17$ mA. This yields a deterministic window at positive pulse amplitudes for ST switching to the AP state of $\Delta^+(50ps) \equiv I^+_{th,AP-to-P} - I^+_{r,P-to-AP} > 6$ mA (Fig.

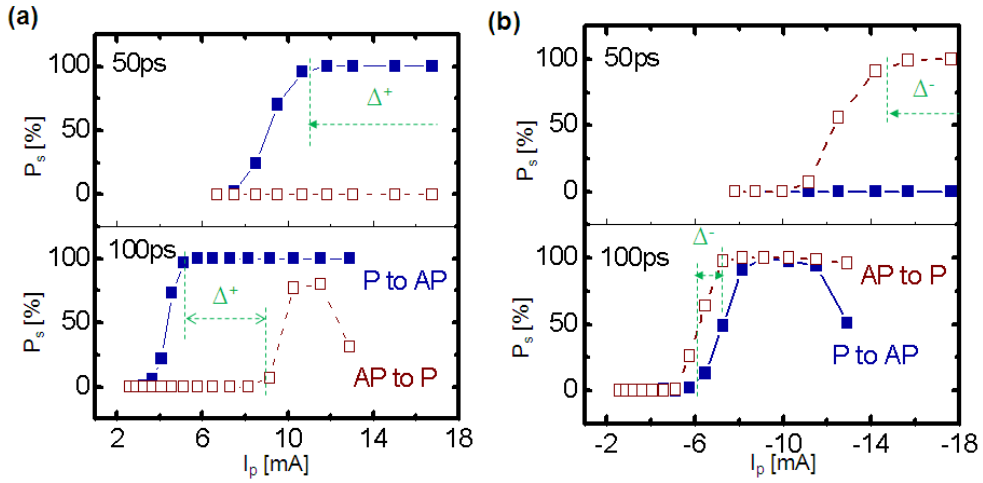

Figure 3.10: Measured switching probabilities (P_s) using (a) positive, and (b) negative 50 ps or 100 ps current impulses.

3.10a), while $\Delta^{+}(100ps) \sim 4$ mA (Fig. 3.10a). For negative 50 ps impulses the pulse amplitude required for reliable AP-to-P switching was larger in magnitude, $I^{-}_{r,AP-to-P} \sim$ -15 mA, resulting in a window $\Delta^{-}(50ps) \equiv -(I^{-}_{th,P-to-AP} - I^{-}_{r,AP-to-P})$ > 3 mA (Fig. 3.10b), while $\Delta^{-}(100ps)$ was negligible. The increase in the switching windows Δ^{+} and Δ^{-} with the reduction of pulse width to 50 ps demonstrates the possibility of implementing ultra-fast *deterministic* STBPS.

3.5 Macrospin Analysis

Certain aspects of the switching behavior, including the origin of the deterministic switching windows, can be understood with a simple zero-temperature (T = 0) macrospin model that utilizes the Landau-Lifshitz-Gilbert (LLG) equation including the effects of ST [152, 17, 153] from the two spin polarizers:

$$\frac{d\hat{m}}{dt} = -\gamma \hat{m} \times \vec{H}_{eff} + \alpha \hat{m} \times \frac{d\hat{m}}{dt} + \gamma a_{op}(\theta_{op}) \hat{m} \times \hat{p}_{op} \times \hat{m} - \gamma a_{ip}(\theta_{ip}) \hat{m} \times \hat{p}_{ip} \times \hat{m} \quad (3.1)$$

where $a_{op(ip)}(\theta) = \frac{\hbar}{2e}\frac{I_p(t)}{\mu_o M_o V}P_{op(ip)}\eta_{op(ip)}(\theta)$ and $\vec{H}_{eff} = (H_k m_x + H_{dx} + H_a)\hat{x} + (H_{dz} - 4\pi M_o m_z)\hat{z}$. Here γ is the gyromagnetic ratio, $\hat{m}$ is the unit vector of the FL, H_k is the anisotropy field of the FL, H_{dx} and H_{dz} are the IP and OP components of the effective dipole field H_d acting on the FL, H_a is the external applied field along the FL easy axis, $\hat{p}_{op}$ is the spin polarization axis of the OPP ($\hat{z}$) and $\hat{p}_{ip}$ is of the IPP ($-\hat{x}$), $\eta(\theta) = 2\Lambda^2/[(\Lambda^2+1) + (\Lambda^2-1)cos\theta]$, $\theta_{op(ip)}$ is the angle between the FL and OPP (IPP), Λ is a torque asymmetry parameter due to spin accumulation effects (we assume symmetric electrodes), M_o is the saturation magnetization of the FL, and $P_{op(ip)}$ is the spin polarization of the OPP(IPP) [1].

Details of macrospin analysis on the deterministic window

We discuss about the origin of the deterministic window with the abbreviated macrospin model. In the STBPS the reversals are mostly governed by the initial out-of-plane rotation angle generated by the OPP-ST because this angle determines the strength of the H_{demag} that induces the rotation of the magnetic free layer (FL). Let's assume that an ideal rectangular impulse is immediately applied in order to easily calculate the change of ε, where ε is the out-of-plane offset angle of the FL moment relative to the equilibrium angle ($\theta_o = H_{dz}/4\pi M_o$) due to the dipole field (H_z) from the OPP (it is equivalent to m_z if θ_o is zero in the small angle approximation). For simplicity we ignore the in-plane rotation about the out-of-plane demagnetization field. Suppose that there is a torque (a_{op}) from the OPP proportional to $a \cdot I$ and a torque (a_{ip}) from the IPP proportional to $b \cdot I$ (where the sign of b changes when the initial state of the FL is reversed). From Eq. 4.14, in the small angle approximation, we have the ini-

[1] The field-like spin torque (J. C. Slonszewski, Phys. Rev. B 71, 024411 (2005)) is not included here as it is negligible in spin valve devices.

tial equation of motion for the out-of-plane rotation (see Section 5.2.4 for more details):

$$\frac{d\varepsilon}{d\tau} = (a_{op} + a_{ip}\theta_o) + (a_{ip} - \alpha 4\pi M_s)\varepsilon \tag{3.2}$$

where α is the damping parameter, $\varepsilon(\tau = 0) = 0$, and assuming that the applied current is a rectangular pulse, i.e. $I(\tau) = I_p$ for $0 < \tau < \tau_p$ but $I(t) = 0$ for $\tau > \tau_p = \gamma t_p/(1 + \alpha^2) \approx \gamma t_p$. Let's assume $\theta_o = 0$ ($H_z = 0$), then

$$\frac{d\varepsilon}{d\tau} = a_{op} + (a_{ip} - \alpha 4\pi M_s)\varepsilon \tag{3.3}$$

In the absence of an IPP ($a_{ip} = 0$), the current required to achieve a given out-of-plane rotation angle is independent of both current polarity and switching direction. However, in the presence of an IPP, as τ_{OP} forces the FL out of plane the IPP causes an additional non-zero torque perpendicular to the sample plane, $\tau_{IP} \propto a_{ip}\varepsilon$ (see Fig. 3.1), that, assuming the $a_{op} > 0$ case, either accelerates ($a_{ip} > 0$) or retards ($a_{ip} < 0$) the out-of-plane rotation of the FL moment driven by τ_{OP}. This additional torque $a_{ip}\varepsilon$ causes a difference between the currents required for AP-to-P and P-to-AP switching for a given pulse polarity (compare Fig. 3.10).

In the absence of the damping torque (i.e. $\alpha = 0$), the final angle $\varepsilon(\tau_p) = (a/b)(e^{bI_p\tau_p} - 1)$ depends only on the $I_p \times \tau_p$. Therefore, in this case, the critical current (and also the deterministic window) should scale inversely with the pulse length. However, if the damping torque is considered, the rotation angle $\varepsilon(\tau_p)$ when the pulse is terminated is

$$\varepsilon(\tau_p) = \frac{a_{op}}{a_{ip} - \alpha 4\pi M_s}[e^{(a_{ip} - \alpha 4\pi M_s)\tau_p} - 1] \tag{3.4}$$

In this case, the result is not a simple function of $I_p \times \tau_p$. The difference of $\varepsilon(\tau_p)$ at the end of pulse between a $a_{ip} > 0$ and a $a_{ip} < 0$ is given by

$$\Delta\varepsilon = \varepsilon(\tau_p, +a_{ip}) - \varepsilon(\tau_p, -a_{ip}) = a_{op}\left[\frac{e^{(a_{ip} - \alpha 4\pi M_s)\tau_p} - 1}{a_{ip} - \alpha 4\pi M_s} + \frac{e^{-(a_{ip} + \alpha 4\pi M_s)\tau_p} - 1}{a_{ip} + \alpha 4\pi M_s}\right] \tag{3.5}$$

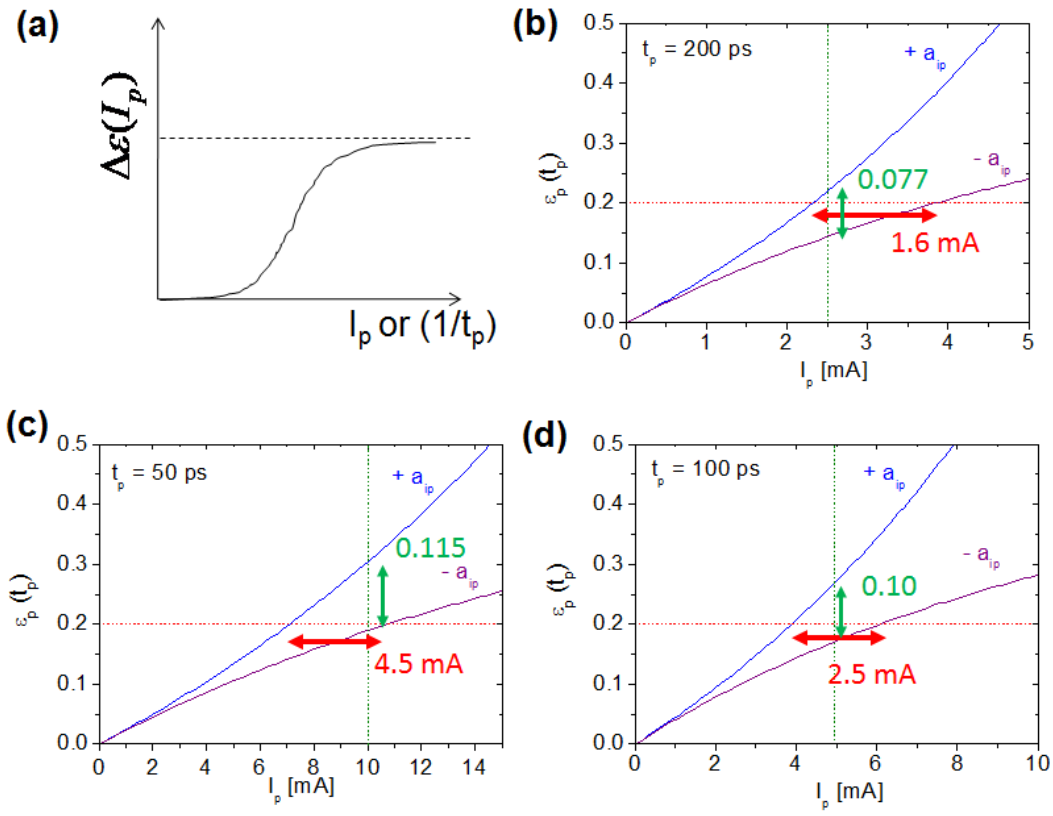

Figure 3.11: (a) Asymptotic plot of $\Delta\varepsilon(I_p)$ as a function of I_p while $I_p \times t_p \sim$ const, Calculated $\varepsilon(t_p)$ as a function of I_p for (b) t_p = 200 ps, (c) t_p = 50 ps, (d) t_p = 100 ps. To achieve a certain tilt angle, the required I_p increases but differently with the sign of a_{ip} relative to the a_{op}

For a long pulse but small amplitude (while $I_p \times \tau_p \sim$ const), i.e. $a_{ip} << \alpha 4\pi M_s$, $\Delta\varepsilon - > 0$. For a $a_{ip} \sim \alpha 4\pi M_s$, $\Delta\varepsilon - > aI_p\tau_p\left[1 + \frac{e^{-2bI_p\tau_p}-1}{2bI_p\tau_p}\right]$ that is positive, indicating that there is a small deterministic window. For a short but strong amplitude, i.e. $bI_p >> \alpha 4\pi M_s$, $\Delta\varepsilon(\tau_p) - > (\frac{2a}{b})[cosh(bI_p\tau_p) - 1]$ that becomes approximately constant, provided that $I_p \times \tau_p$ is constant.

To obtain more practical insight, we estimate the size of the deterministic window with Eq. 3.4 and 3.5. From the spin-torque term in the LLGS equation, $\frac{a_{op(ip)}}{I} = \frac{\hbar}{2e}\frac{P_{op(ip)}}{M_s V}$, we have $a_{op}/I = 30\ Oe/mA$ (if $P_{op} = 0.2$) and $a_{ip}/I = 56\ Oe/mA$

(if $P_{ip} = 0.37$) for $M_s = 650\ emu/cm^3$, $V = (\pi/4) \times 50 \times 170 \times 5\ nm^3$, and with the assumption that there is no angular dependence of ST-efficiency ($\eta(\theta)$) on the a_{op} and a_{ip}. Using Eq. 3.5 we have $\Delta\varepsilon \approx 0.077$ for $I_p = 2.5\ mA$, $t_p = 200\ ps$, $\Delta\varepsilon \approx 0.10$ for $I_p = 5\ mA$, $t_p = 100\ ps$, and $\Delta\varepsilon \approx 0.115$ for $I_p = 10\ mA$, $t_p = 50\ ps$. Lastly we plot $\varepsilon(t_p)$, using Eq. 3.4, with variable I_p and t_p in Fig. 3.11 b-d. The figures suggest the estimated deterministic window for a given pulse width (t_p). For achieving a certain tilt angle, the required amplitude of I_p increases with decreasing t_p but differently for $a_{ip} > 0$ or for $a_{ip} < 0$ for a given $a_{op} > 0$. For $\varepsilon(t_p) = 0.2$ the calculated $\Delta I_p \equiv I_p(a_{ip} > 0) - I_p(a_{ip} < 0) \approx 1.6\ mA$, $2.5\ mA$ and $4.5\ mA$ for $t_p = 200\ ps$, $100\ ps$ and $50\ ps$ respectively.

Of course for shorter impulses, the offset angle should be progressively higher to ensure that the moment completes the π rotation before the damping torque relaxes the FL back to equilibrium. That will increase the windows a bit more for the shorter impulses as well as the threshold currents. The stray fields in our STNO structure cause more complications but the measured deterministic windows are of the similar magnitude as the macrospin results.

3.6 Micromagnetic Analysis

Our devices have the interesting features that the P-to-AP switching current at positive bias is always less than the magnitude of the AP-to-P switching current at negative bias (τ_{IP} is favorable to the switching direction in both cases) and that the deterministic window for the positive current pulses is invariably larger than for the negative. To understand these features and the details of the STBPS, we performed T = 0 K micromagnetic simulations that utilized Eq. 4.14, and

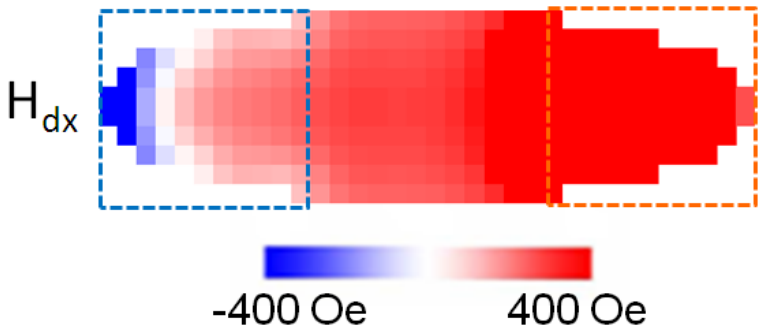

Figure 3.12: The calculated easy-axis component of the inhomogeneous dipole fields (H_{dx}) acting on the FL. The position dependent non-uniform field shifts the effective anisotropy field differently for the P or AP configuration.

employed the following magnetic parameters: M_o(IPP) = 850 emu/cm^3, M_o(FL) = 650 emu/cm^3, M_o(OPP) = 870 emu/cm^3, exchange constants A(IPP) = A(FL) = 13×10^{-6} erg, A(OPP) = 26×10^{-6} erg, OPP anisotropy $K^{\perp}$(OPP)= 8×10^6 erg/cm^3, and FL damping α = 0.03 [35]. The simulated nano-pillar had an elliptical cross-section of 50×170 nm^2 and the mesh size was $5 \times 5 \times 2.5$ nm^3. The static magnetic configurations were first calculated by the energy minimization method [154] for an external magnetic field located at the center of the minor loop for the P and AP states. Then a current impulse ($I_p(t)$) was applied at time t = 0 taking into account nonzero rise and fall times, with the calculated ST exerted on the interface cells of each magnetic layer.

The micromagnetic ST simulations reveal that STBPS in this device structure is initiated by reversal at one end of the FL ellipse, with the remainder of the FL following (See Fig. 3.14). Fig. 3.13 shows the simulated time-traces of $< m_x >$ (Fig. 3.13a and 3.13b) and $< m_z >$ (Fig. 3.13c and 3.13d) for the left 60 nm and the right 60 nm of the FL for positive (Fig. 3.13a and 3.13c) and negative (Fig. 3.13b and 3.13d) 50 ps impulses. In this simulation Λ = 1.5, P_1 = 0.20 and P_2 = 0.37. For both current polarities, and even for P_2 = 0.0, the FL reversal is an

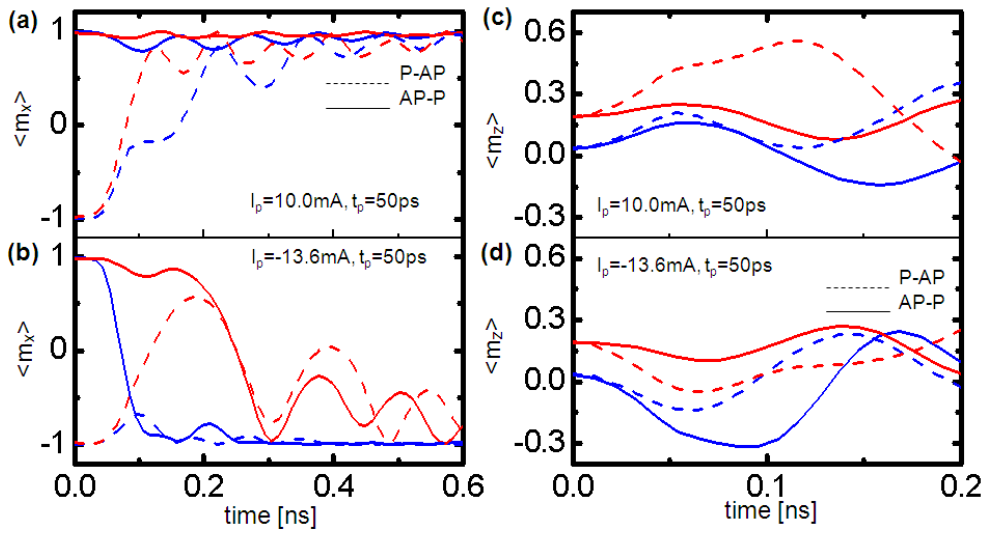

Figure 3.13: (a) Micromagnetic simulation (with the non-uniform fringe fields from the two RL's) of the time trace of $< m_x >$ at the two ends (blue, as averaged over the left 60 nm of the FL, and red, averaged over right 60 nm) of the FL for AP ($< m_x > \approx 1$) and P ($< m_x > \approx -1$) initial configurations using a positive impulse $I_p = +10\ mA$, $t_p = 50\ ps$ (FWHM). Dashed lines: initial P configuration, solid lines: initially AP. (b) Simulated time trace of $< m_x >$ for AP and P initial configurations using a negative impulse $I_p = -13.6\ mA$ and $t_p = 50\ ps$. (c, d) Simulated time trace of $< m_z >$ for the same conditions as a, b, respectively; note different time scale for (c) and (d).

inhomogeneous process in which the right (left) side rotates faster for P-to-AP (AP-to-P) reversal, rather than the uniform rotation of a macrospin [147].

This nonuniform reversal occurs because the reference layers' dipole fields are inhomogeneous at the position of the FL (H_{dx} is plotted in Fig. 3.12) and the local critical current density J_c for OP ST excited precession depends on this field, $J_c \propto H_{k,x}^{eff} = | \pm H_k/2 + H_a + H_{dx} |$ (ref. [114] ; + corresponds to AP-to-P, − to P-to-AP). For the simulated device in the AP configuration, $\overline{H_{k,L}^{eff}} \approx 230$ Oe when averaged over the leftmost 60 nm of the FL, while $\overline{H_{k,R}^{eff}} \approx 460$ Oe for the rightmost 60 nm. For the P configuration the variation in H_k^{eff} is even greater, with

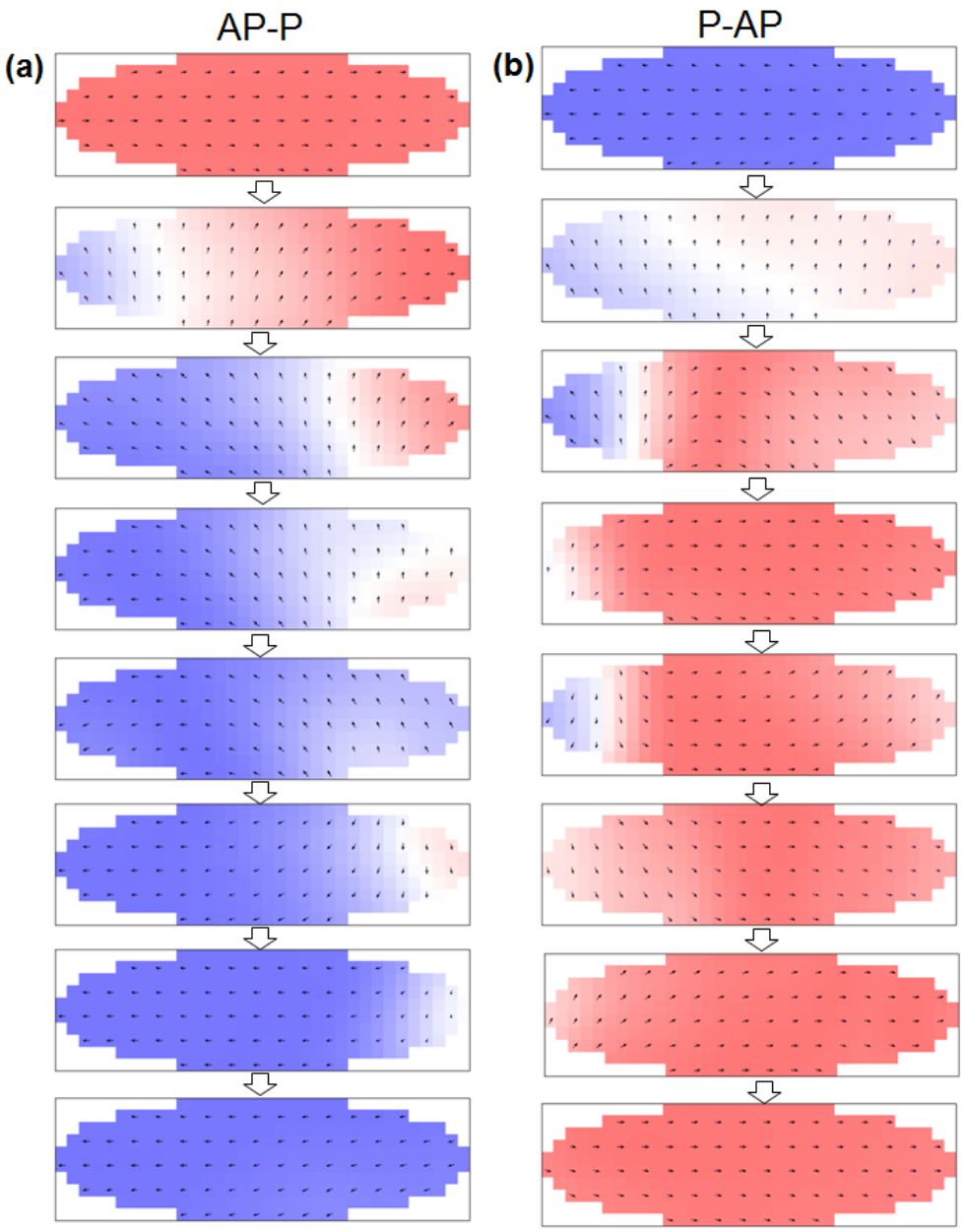

Figure 3.14: (a) Micromagnetic STBPS process of the FL for AP to P using a negative impulse $I_p = -13.6\ mA$, $t_p = 50\ ps$ (FWHM). The left ends start the reversals due to the relatively lower H_k^{eff}. Then the reversed domain is expanding to the right ends. After the impulse is done the reflected spin-wave is damped out and the FL is stabilized to the opposite (P) state. (b) Micromagnetic STBPS process of the FL for P to AP using a positive impulse $I_p = +10.0\ mA$, $t_p = 50\ ps$ (FWHM). The switching direction is opposite with the one for AP to P. These non-uniform switching directions are independent with the pulse polarity and the ST from the IPP. Initial configuration (P or AP) determines this switching directions, originated from the non-uniform dipole stray fields from the two polarizers.

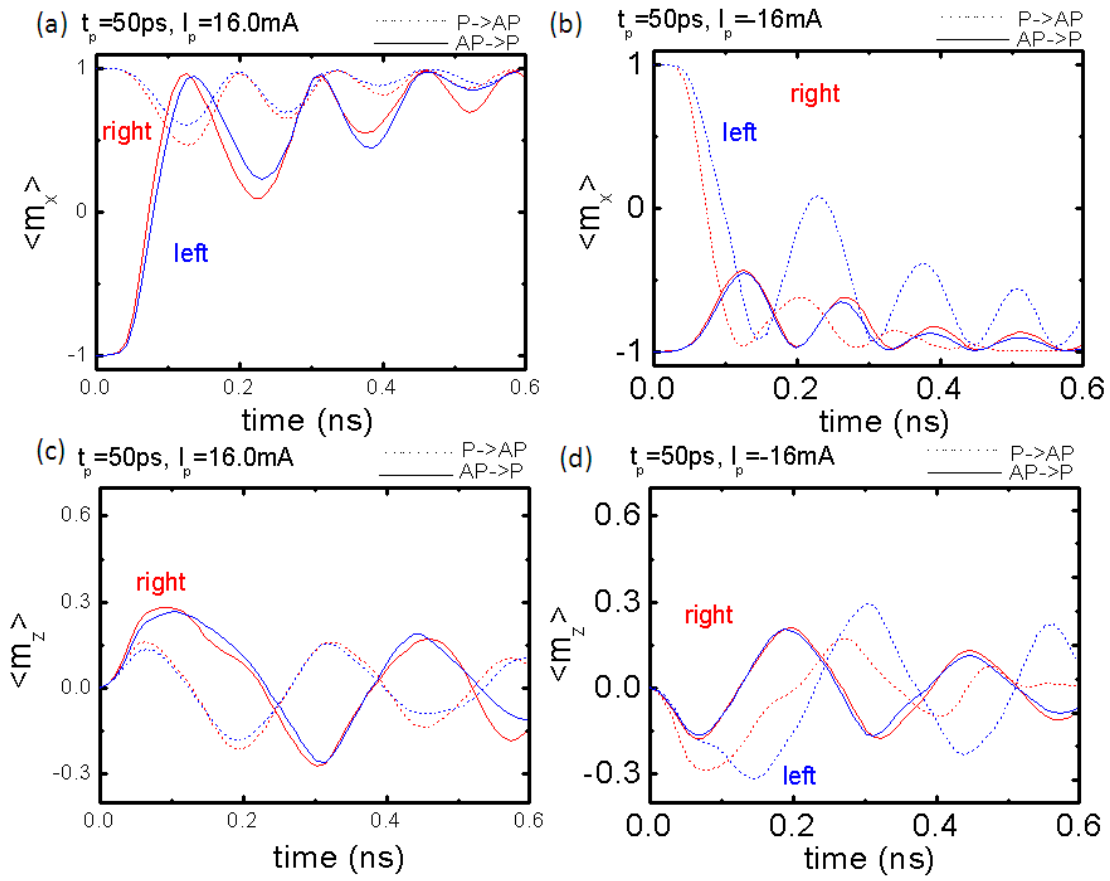

Figure 3.15: (a) Micromagnetic simulation (without the non-uniform fringe fields from the two RL's) of the time trace of $< m_x >$ at the two ends (blue, as averaged over the left 60 nm of the FL, and red, averaged over right 60 nm) of the FL for AP ($< m_x > \approx 1$) and P ($< m_x > \approx -1$) initial configurations using a positive impulse $I_p = +16\ mA, t_p = 50\ ps$ (FWHM). Dashed lines: initial P configuration, solid lines: initially AP. (b) Simulated time trace of $< m_x >$ for AP and P initial configurations using a negative impulse $I_p = -16\ mA$ and $t_p = 50\ ps$. (c, d) Simulated time trace of $< m_z >$ for the same conditions as (a), (b), respectively; note different time scale for (c) and (d). We observed more uniform and coherent switching between two ends.

$\overline{H_{k,L}^{eff}} \approx 490$ Oe and $\overline{H_{k,R}^{eff}} \approx 140$ Oe. Furthermore H_{dz} causes the magnetization of the FL to tilt out of plane, with this effect being stronger (weaker) on the right (left) end of the FL due to the additive (subtractive) combination of the IPP and

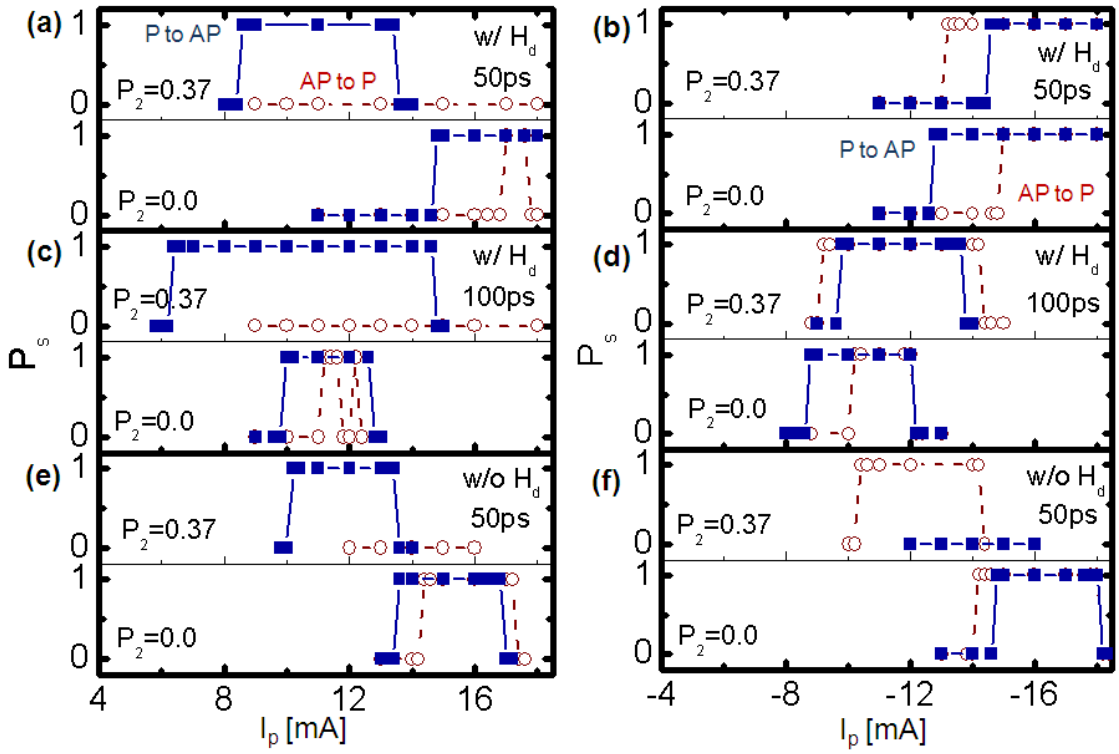

Figure 3.16: Simulated switching probabilities P_s at zero temperature. Top figures: $P_1 = 0.2$ and $P_2 = 0.37$, bottom figures: $P_1 = 0.2$ and $P_2 = 0.0$, i.e. no spin-torque from the in-plane polarizer/analyzer. Rectangles: P-to-AP switching, circles: AP-to-P. (a,b) P_s for 50 ps I_p impulses for (a) positive and (b) negative pulses. (c,d) P_s for 100 ps impulses. (e,f) P_s for 50 ps impulses without dipole field from the polarizer layers acting on the FL.

OPP fields. The effect of H_{dz} for $+I$ is to increase the influence of the τ_{IP} due to the significant equilibrium $< m_z >$ ($\varepsilon_o > 0$) on the right side of the FL (Fig. 3.13c and Eq. 3.3) for P-to-AP (τ_{IP} is favorable to this direction) but $\varepsilon_o \approx 0$ on the left side for AP-to-P. For $-I$, the effect of H_{dz} provides a ε_o that is opposite to the displacement driven by the OP-ST, resulting in a smaller maximum value of $< m_z >$ for a given pulse amplitude, and hence a reduction in the influence of τ_{IP}. The consequences of the influence of the τ_{IP} within the micromagnetic simulations can be seen in Fig. 3.16 which compares the $P_2 = 0.37$ and $P_2 = 0.0$ cases, and

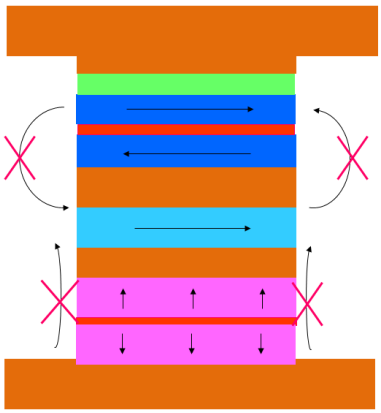

Figure 3.17: Synthetic Anti-Ferromagnetic reference layers in both spin-polarizers to minimize the stray fields onto the magnetic FL. We expect to achieve nearly symmetric deterministic windows for both impulse current polarities.

the consequences of the nonuniform dipole fields can be seen by comparing Fig. 3.16a-d (w/ H_d) to Fig. 3.16e,f (w/o H_d). Without H_d we obtain, as in the original macrospin model, more uniform FL reversals and large and symmetric values for Δ^- and Δ^+ , with only a small difference between $\mid I^+_{th,P-to-AP} \mid$ and $\mid I^-_{th,AP-to-P} \mid$ arising from our use of $\Lambda = 1.5$ (Fig. 3.16e,f). With H_d we find that for 50 ps pulses $\mid I^+_{th,P-to-AP} \mid$ is reduced while $\mid I^-_{th,AP-to-P} \mid$ is increased, and $\Delta^+ > \Delta^-$. For 100 ps pulses (Fig. 3.16c, d), the simulations show that both Δ^- and Δ^+ are reduced further relative to the 50 ps case (the reduction in Δ^+ is not visible in Fig. 3.16 because $I^+_{th,AP-to-P}(100\ ps) > 18\ mA$). This is consistent with the experiment and Eq. 3.3.

3.7 Conclusion

In summary we have demonstrated reliable and deterministic STBPS with a 50 ps spin polarized impulse current where the shorter current impulse enhances

the deterministic write operation. If the fringe fields can be reduced close to zero (see 3.17) then nearly symmetric deterministic windows should be achievable for both pulse polarities, enabling very fast, energy efficient STBPS.

3.8 Suppression of magnetic ringing after spin-torque driven ballistic precessional switching

In a collinear spin-torque (ST) device it has been demonstrated that the ST driven magnetic reversals take in general three steps [155]: (1) amplifying pre-oscillation during the incubation time (typically $>$ 1 ns), (2) sharp switching event and (3) relaxation of the FL to the reversed equilibrium state, as summarized in Fig. 3.18. Intuitionally the pre-amplifying (#1 in the figure) and post-damped oscillations (#3 in the figure) are unnecessary and should be minimized for the efficient and fast switching while the sharp transition is only essential in the whole reversal process. We have eliminated the incubation time or pre-amplifying oscillation by utilizing the nanopillar spin-valve structure that produced a ST with both strong in-plane and out-of-plane spin polarization components, as we have discussed. The result is a quick π-rotation of the FL about the out-of-plane demagnetization field during the impulse current, followed by, after the termination of the pulse, the completion of the reversal along with the relaxation of the FL moment to the equilibrium position. However we expect the relaxation time is still long (1 $\sim$ 2 ns) in the ST devices, based on our micromagnetic studies (see Fig. 3.13 and 3.15). Moreover the post-damped oscillations might generate stochastic errors in the write operation because a large oscillation could induce the relaxation of the FL back to the original equilibrium

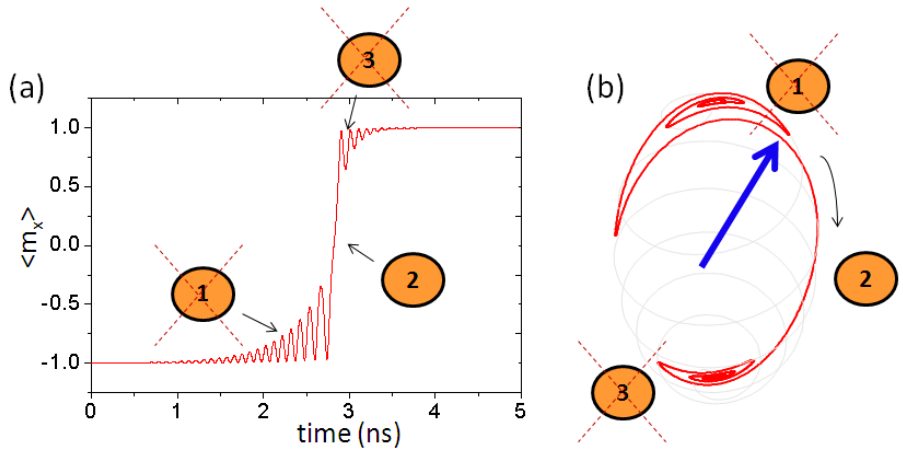

Figure 3.18: Illustration of ideal switching process without pre-amplifying oscillations (in #1) and with a quick relaxation of the reversed magnetic free layer to the equilibrium state (in #3).

state with the help of thermal fluctuations. For achieving quicker stabilization without sacrificing the rapid rotation, I propose two schemes to suppress the magnetic ringing after the STBPS: utilization of a quasi-monocycle pulse (consisting of two successive short pulses with opposite polarities and with a time-delay) or introduction of high magnetic damping (α) to the FL.

3.8.1 Two successive short pulses with opposite polarities and with a time-delay

The first proposed method is the application of a quasi-monocycle pulse to the FL instead of a single unipolar pulse (see Fig. 3.19). The subsequent pulse, that has the opposite polarity to the preceding pulse, applies the torque opposite to the motion of the FL and makes it slow down. Therefore the second pulse can suppress the magnetic ringing if the delay timing is properly set.

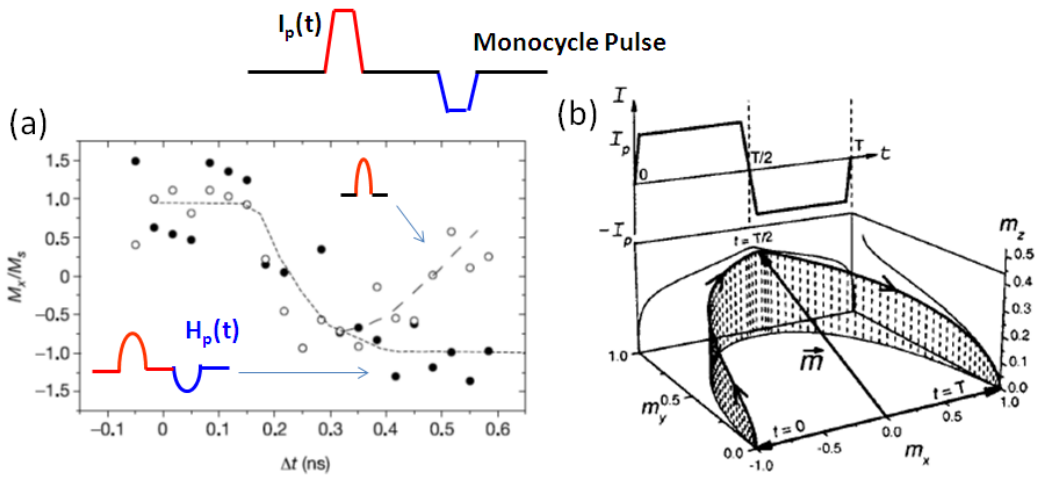

Figure 3.19: Illustration of switching scheme by two successive short pulses with opposite polarities and with a time-delay in order to suppress the magnetic ringing. (a) Gerrits et al. [156] demonstrated a rapid rotation and a quick relaxation of a FL moment to the reversed equilibrium position or no back-hopping to the original state with a quasi-monocycle ″hard axis magnetic field pulse″. (b) Kent et al. [99] suggested a monocycle pulse scheme for the ballistic switching and rapid relaxation in the proposed non-collinear device structure.

This idea is basically similar to the experimental work by Gerrits et al. [156] that demonstrated a quick relaxation to the reversed equilibrium position or no back-hopping to the original state with a quasi-monocycle hard axis magnetic field pulse. They observed optically the magnetic switching dynamics of Py-based FL and compared it to the one by a single unipolar pulse that easily induced the back-hopping of the FL (see Fig. 3.19a). Kent et al. [99] also suggested a monocycle pulse scheme for the STBPS with the proposed non-collinear device structure (see Fig. 3.19b).

I carried out proof-of-concept experiment with our ST device that did not exhibit a good switching fidelity for AP-to-P. The device had an elliptical cross-section of $\sim 55 \times 165\ nm^2$. Fig. 3.20a shows the switching probabilities (P_s) as a

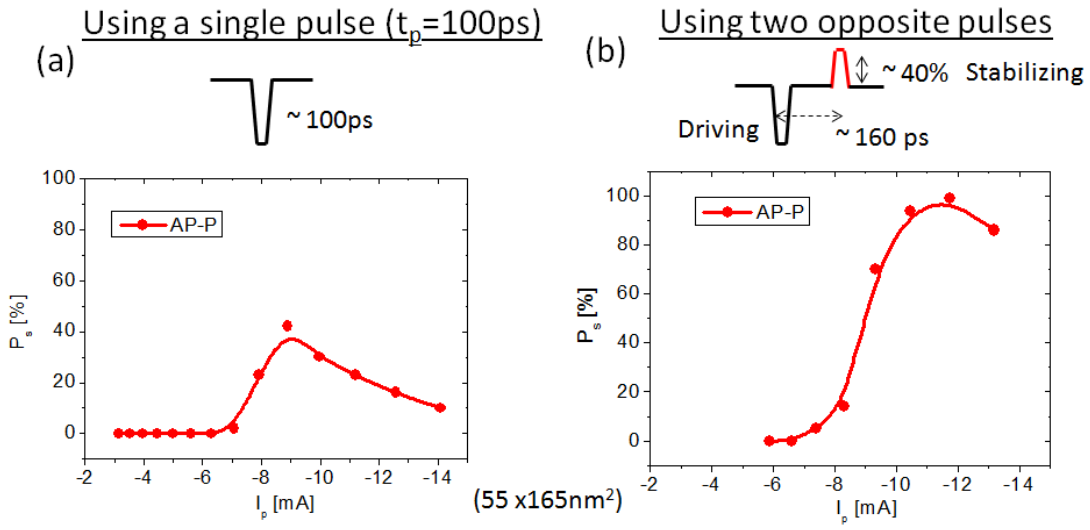

Figure 3.20: Results of switching fidelity test for AP-to-P by two successive opposite pulses (quasi-monocycle pulse). (a) Measured switching probability (P_s), applying a single unipolar pulse to the ST device, as a function of $-I_p$ with t_p = 100 ps. (b) Measured P_s as a function of $-I_p$ (the amplitude of the preceding pulse) applying a quasi-monocycle pulse that was generated by adding an Impulse Forming Network between the bias-Tee and the pulse generator. The improved P_s indicated that the subsequent pulse can significantly suppress the magnetic ringing with a proper time control.

function of $-I_p$ with t_p = 100 ps. The achieved maximum P_s was ~ 45 % with the pulse width. Of course shorter but stronger current pulses will give better switching fidelities as we have discussed in this chapter. On the other hand the device exhibited a good switching behavior for P-to-AP with a $+I_p$ as it was general in the devices.

We measured the P_s using a quasi-monocycle pulse that was generated by adding an Impulse Forming Network (5212A IFN) between the bias-Tee and the pulse generator (10,070A) in the pulsed switching measurement circuit with set of t_p = 100 – 300 ps in the pulse generator. This generates ~ 80 ps pulse width in the preceding pulse while the subsequent pulse has a longer (depending on

the set of the pulse width in the pulse generator) but ~ 40 % lower in the pulse amplitude. Fig. 3.20b shows the P_s with set of 160 ps as a function of pulse amplitude in the preceding pulse. The switching fidelity was achieved up-to $P_s \sim 95$ % that was much enhanced compared to the one by the single unipolar pulse. The write fidelity was still not ideal (100 % of P_s in broad ranges of I_p) but our results indicates that the subsequent pulse can significantly suppress the magnetic ringing with a proper time-control similar to the work by Gerrits et al [156].

3.8.2 Magnetic damping effect on the spin-torque driven ballistic precessional switching

The second method to suppress the magnetic ringing is by using a FL material with a high magnetic damping (α). In our macrospin study (in Section 3.5), the ST (a_{op}) from the OPP is much larger than the damping torque at least several times: for example, $a_{op} > H_k/2 = 100$ Oe while the damping torque ($\alpha 4\pi M_s \varepsilon$) is ~ 10 Oe if $H_k = 200$ Oe, $\alpha = 0.01$ and $\varepsilon = 0.1$, from Eq. 3.3. This simple estimation suggests that the α may have little effect on the threshold currents in our device structure, but with a higher α, after the termination of the impulse, one can expect quicker relaxation of the FL to the equilibrium.

Device Information

In order to study the damping (α) effect on the STBPS I fabricated three different types of devices varying α of the FL by doping 0 %, 2 % or 4 % of Ter-

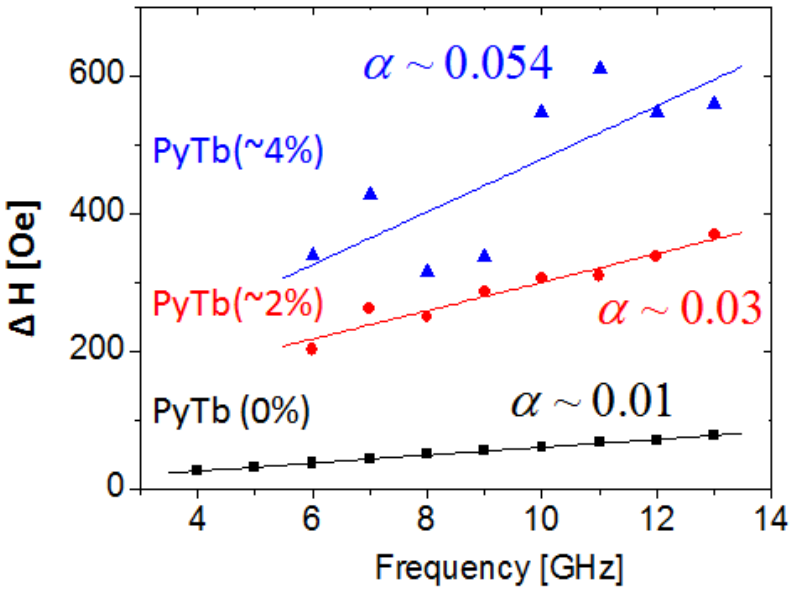

Figure 3.21: Measured linewidth (ΔH) as a function of applied microwave field frequency (f) from Py thin films with 0 %, 2 % and 4 % Tb-doping, in the conventional FMR experiment. The obtained damping (α) from the fitting directly increases with the Tb-impurity ratio. The measured α's are quite similar to the reported values from NIST [157].

bium (Tb) to the Py-based FL [157]. The devices had a multilayer structure of substrate/bottom-lead/$[Co0.44/Pt0.68]_4$/Co0.66/Cu0.3/Co0.66/Cu20/Tb-doped-Py5/Cu12/Py20/ top-lead (nm) and an elliptical cross-section of $\sim 40 \times 155\ nm^2$. The Tb-doped-Py was grown by co-sputtering in AJA with the power of Tb = 3 W (for 2 %) and 6 W (for 4 %) while the power of Py = 250 W, with the help of Praveen. This small Tb-doping to Py has been well known to increase the Gilbert damping (α) with less change of the magnetic properties such as magnetic anisotropy or saturation magnetization [157]. We checked the enhancement of α with the conventional FMR experiment, using a microwave strip setup by Taka, of the thin films. Fig. 3.21 shows the fitting of a linewidth to

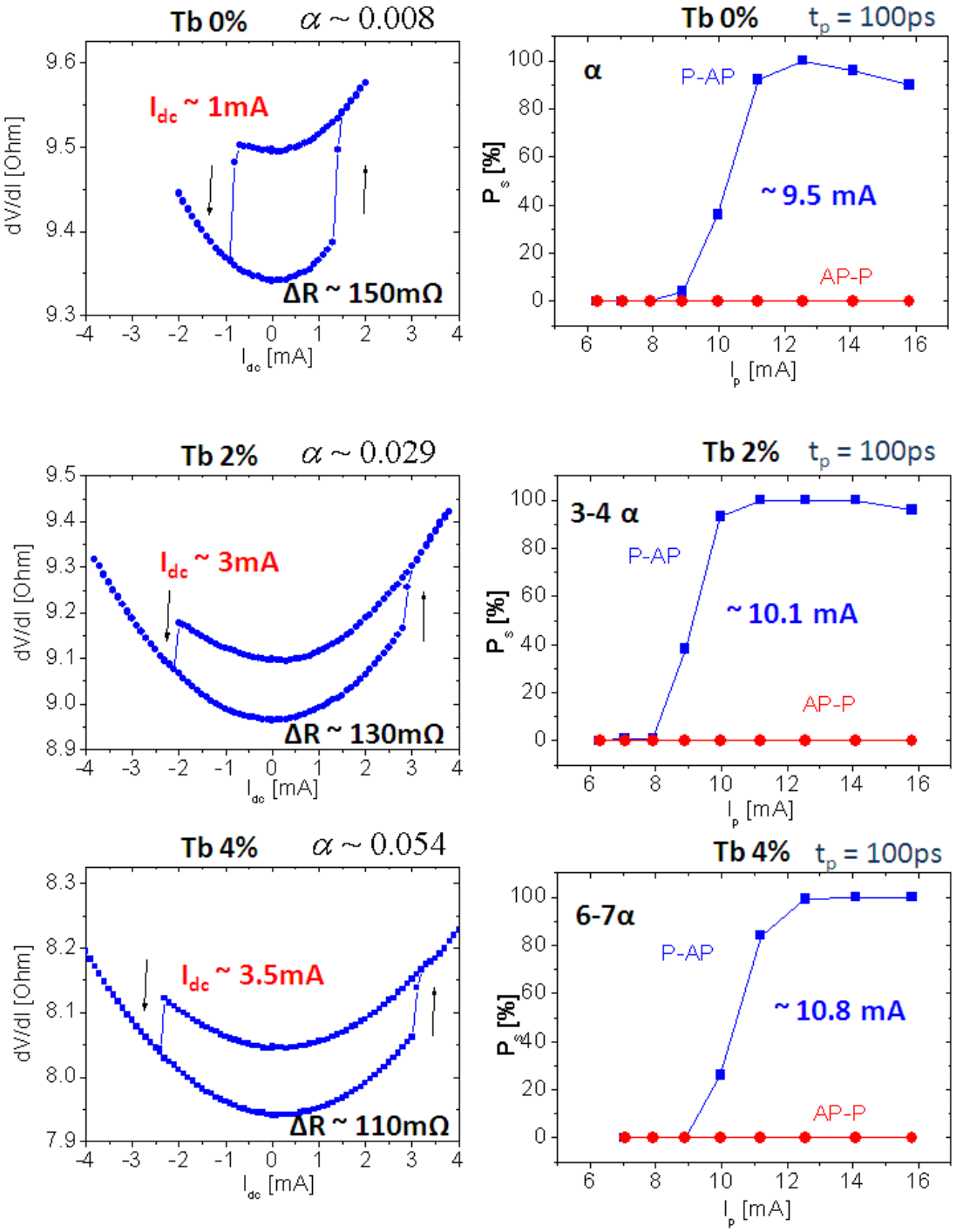

Figure 3.22: Results of dc current induced switching (left column) and pulsed current induced switching (right column) from the representative devices with 0 %, 2 % and 4 % Tb-doped FL. The switching current increased directly with α at the thermally activated switching regime, but not as much as the enhancement in the α. In the STBPS regime there was little increase (~ 10 %) in the current amplitude with a short pulse (t_p = 100 ps).

the frequency, and we found that Py thin film with 2 % Tb-doping has $\alpha \sim 0.03$ (3 times increase), 4 % doping has $\alpha \sim 0.054$ (5 – 6 times increase) while pure Py (0 %) has $\alpha \sim 0.01$. The measured α's depending on the doping ratio were quite close to the reported values by NIST [157].

Experimental results

Fig. 3.22 compares the dc current induced switching (left column) and the short pulsed current switching (right column) from the devices with 0 %, 2 % and 4 % Tb-doped FL. We selected representative samples from each type that had similar H_c (~ 200 Oe). As expected the switching current increased directly with the increased α at the thermally activated switching regime, but not as much as the enhancement of the damping. In the STBPS regime with a short pulse (t_p = 100 ps) there was little increase (~ 10 %) in the current: for P_s = 50 %, corresponding I_p ~ 9.5, 10.1 and 10.8 mA for each 0 %, 2 % and 4 % device. The result is consistent with above expectation and it characterizes the STBPS in which the magnetic damping of the FL has little influence on the threshold currents due to the strong OPP-ST. For higher pulse currents (> 14 mA) the P_s slightly decreased (stochastic back-hopping) as the α decreased. We can interpret that the higher α help suppressing the magnetic ringing or induce quicker relaxation of the FL to the equilibrium state.

Micromagnetic simulations for the damping effect

The damping effect to the STBPS was verified with the micromagnetic simulations in which α of the FL was varied from 0.01 to 0.06 under the similar con-

ditions to the experiment: t_p = 100 ps and at the center of the minor loop. Fig. 3.23a shows the time-traces of m_x for α = 0.01, 0.03, and 0.06 of the FL with the same current amplitude (I_p = 10 mA) for P-to-AP. Interestingly the initial motions of the FL are almost identical or independent with the magnitude of α. However, after the pulse is terminated, the relaxation process is quite different. As expected, higher α induces quicker relaxation of the FL to the reversed magnetic state. Fig. 3.23b is the summary of P_s as functions of I_p and α (= 0.01, 0.03 and 0.06) with t_p = 100 ps at zero temperature, obtained with the help of Junbo. The threshold currents are varied within $\sim$ 10 %, which is consistent with our experimental observation. However the I_p for the back-hopping exhibits different behavior. With low α (0.01 and 0.03), the threshold I_p's were almost same but the I_p was hugely enhanced with α = 0.06. The results suggest that the I_p for 2π rotation could be more sensitive to the α than the one for π rotation as well as to the t_p.

For the experimental demonstration of the reduced magnetic ringing with a higher α, we need to compare the time-traced magnetic signals. However, as we discuss next section, our time-domain studies couldn't resolve the oscillatory information due to the lots of average and phase difference between events although we observed the signature of the π, 2π and 3π rotations of the FL. Nevertheless we believe that a higher α may improve the fidelity of the STBPS by suppressing the magnetic ringing, based on our understanding and work in this section.

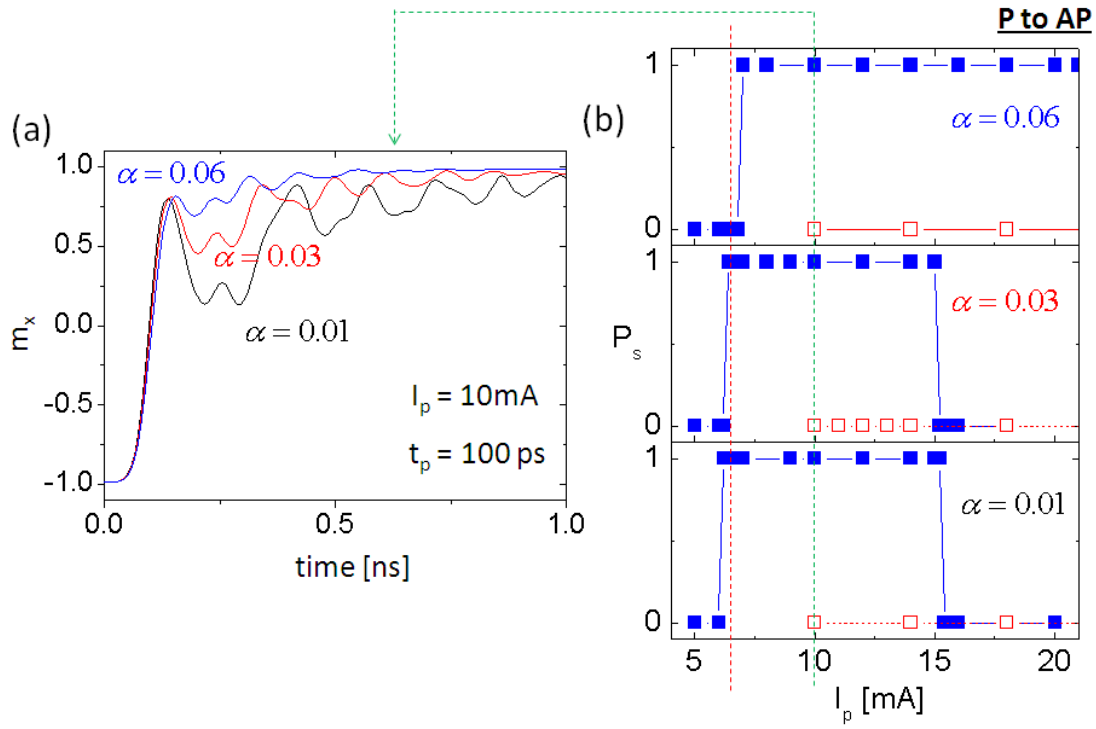

Figure 3.23: Results from the micromagnetic simulations for the magnetic damping effect on the ballistic switching in which α of the FL was varied from 0.01 to 0.06. (a) Initial motions of the FL are almost identical or independent with the magnitude of α. (b) Obtained switching probabilities (P_s) as functions of I_p and α (= 0.01, 0.03 and 0.06) for t_p = 100 ps at zero temperature. The results indicate that the I_p for 2π rotation could be more sensitive to the α than the one for π rotation as well as to the t_p.

3.9 Measurement at Low-Temperature (< 10 K)

It has been observed that α of the FL significantly increases as the background temperature (T) goes down (< 100 K) due to native anti-ferromagnetic (AF) surface oxides. Contrarily, the ST devices in this chapter are characterized by the ballistic switching in which the α has a minor influence on the threshold currents for the fast switching. Therefore it is interesting to see how our ST devices work at low temperature or how the devices behave as a function of T.

In addition ST memory devices working at low-T (~ 4 K) has been asked by our funding agent eventually for integration with superconducting logic devices. In this section we study the switching of the FL at room-T (RT ~ 300 K) and at low-T (LT ~ 10 K) with DC currents and short pulsed currents.

Antiferromagnetic surface oxide effect

Previously Nathan [158] and Ozhan [144] from our group experimentally proved the presence of a native AF oxide (NiO, FeO or Fe_2O_3) layer at the Py surface with a total thickness of ~ 2 nm in Py/Cu/Py nanopillar spin-valve devices. This sidewall oxide is created when the patterned nanopillar is exposed to air or during the nano-fabrication process mostly when insulating SiO_x is deposited with the IPE-PECVD at CNF. As a consequence of the surface AF oxide, the ST devices exhibited a huge enhancement of α at lower T (< 40 K), a reduction of thermal stability at RT, and a stochastic fluctuation in coercive fields and loop displacement. The magnetic disorder or unstable domain was caused even above the blocking temperature (~ 40 K). Moreover the magnetic dynamics can be significantly different from the case in the absence of the exchange bias effect from the surface because the additional field alters the magnetic potential for the stable states or the non-uniform dynamic modes, especially as the lateral dimension of device gets smaller (then the surface effect is bigger). The passivation treatment, in which a thin Al layer is coated on the sidewalls right after the pattern of the nanopillar without breaking the vacuum, was suggested to avoid the formation of the surface AF oxide [144].

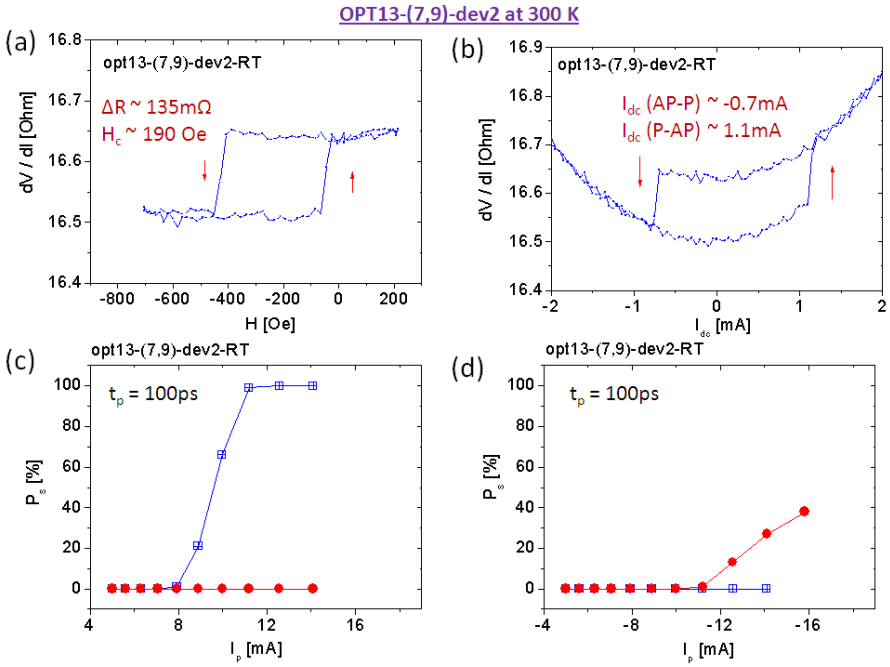

Figure 3.24: Measured data at room temperature (~ 300 K) (a) minor loop (b) dc-current induced switching (c) pulsed current induced switching with $+I_p$ and t_p = 100 ps, (d) pulsed current induced switching with $-I_p$ and t_p = 100 ps.

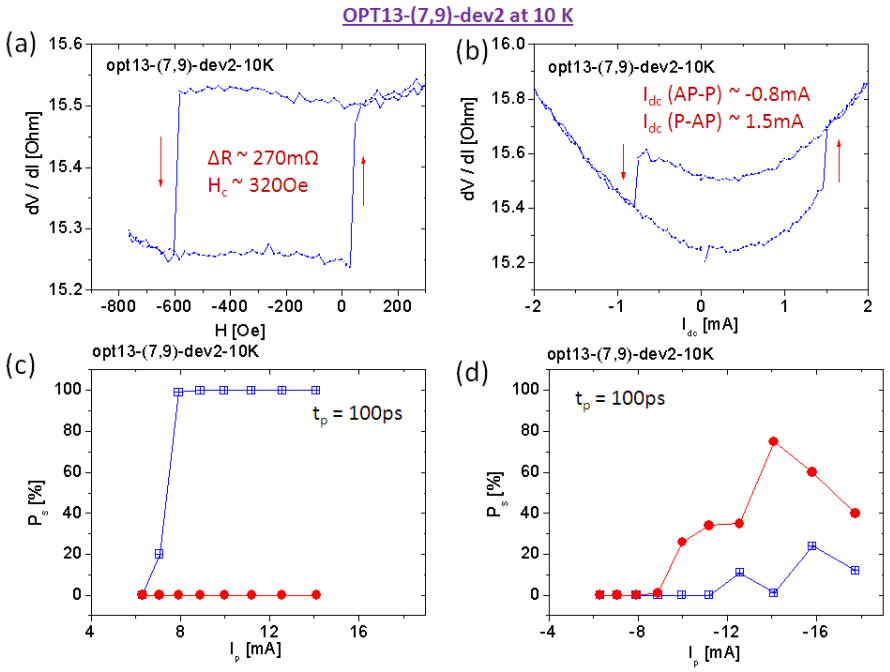

Figure 3.25: Measured data at room temperature (~ 10 K) (a) minor loop (b) dc-current induced switching (c) pulsed current induced switching with $+I_p$ and t_p = 100 ps, (d) pulsed current induced switching with $-I_p$ and t_p = 100 ps.

Device Information

The nanopillar spin-valve devices in this section have a multilayer structure of substrate/bottom-lead/$[Co0.44/Pt0.68]_4$/Co0.66/Cu0.3/Co0.66/Cu20/Py5/Cu12/Py20/top-lead (nm) and an elliptical cross-section of $\sim 40 \times 155\ nm^2$. We note that the spacer distance between the OPP and the FL was increased to 20 nm from 5 nm which was used in the previous devices in order to reduce the stray field from the OPP layer. Our measurements were performed in Table top probe station at Clark D-10. (Based on my experience this setup requires improvements in the temperature control, noise level, stability of the magnet and connection of high-frequency probe.) Three different devices were measured and similar behaviors were observed.

Experimental results

We present the field-induced minor loop, dc current induced switching, and pulsed current induced switching with t_p = 100 ps, at RT (in Fig. 3.24) and at LT (in Fig. 3.25). We obtained $\Delta R \sim 135\ m\Omega$, $H_c \sim 190$ Oe, I_c(AP to P) ~ -0.7 mA and I_c(P to AP) $\sim +1.1$ mA at RT while $\Delta R \sim 270\ m\Omega$, $H_c \sim 320$ Oe, I_c(AP to P) ~ -0.8 mA and I_c(P to AP) $\sim +1.5$ mA at LT. The increases in ΔR and H_c are expected at LT due to the enhanced spin-polarization (and MR signal) and less thermal fluctuations. However the I_c's did not increase at LT as much as the collinear spin-valve device (Py/Cu/Py) in which at least more than factor of two was enhanced in the I_c's though the enhancement of spin-polarization (see Ozhan et al. [144]). This is probably due to the different switching mechanism with/without the OPP layer even with slowly ramp-rate currents. In collinear devices the ST from the IPP changes the effective α or effective barrier height at the thermally

active switching regime ($I < I_{c0}$). Instead, in the non-collinear device with the OPP layer, the FL takes a quasi-static rotation on the in-plane by the ST from the OPP layer with slowly increasing currents, thereby with a little effect from the α, as we discuss in the previous section. However this interpretation is not compatible with our previous results from the devices with Tb-doped FL in which the I_c increased with α at the thermally activated switching.

Another possibility is from one additional treatment during my nanofabrication process. In the standard recipe for the nanopillar fabrication in our group we deposit ~ 5 nm of SiO_x (or AlO_x) with the old IBD at Clark for protecting the nanopillar, after that thicker SiO_x is deposited with IPE-PECVD. Since I noticed the existence of the surface oxide layer at the Py layer, the nanopillar was cleaned with 20 sec ion-milling before the deposition of SiO_x with the IBD, which was enough to clean the peripheral AF oxide. This possibly made little increase of the α at LT.

We obtained more un-expected results in the pulsed current switching: the current amplitude was lower at LT than at RT: $I_p \sim +8$ mA at LT (see Fig. 3.25c) while $I_p \sim +10$ mA at RT (see Fig. 3.24c) for $P_s \sim 50$ % and for P-to-AP. This might be originated from the huge enhancement of spin-polarization in the OPP layer at LT. Another possible explanation is the capacitance loss at RT as we discuss in Section 4.10. We have used Si/SiO_x substrate and there may be a leakage current through the semi-conducting Si-substrate at microwave frequencies (> a few GHz) at RT while Si-substrate acts as an insulator at LT because the carriers freeze out. This capacitance depends on the geometry of contact pads and thickness of insulating SiO_x on the substrate and it was highly possible we overestimated the amplitude of current if we had current-leakage through the

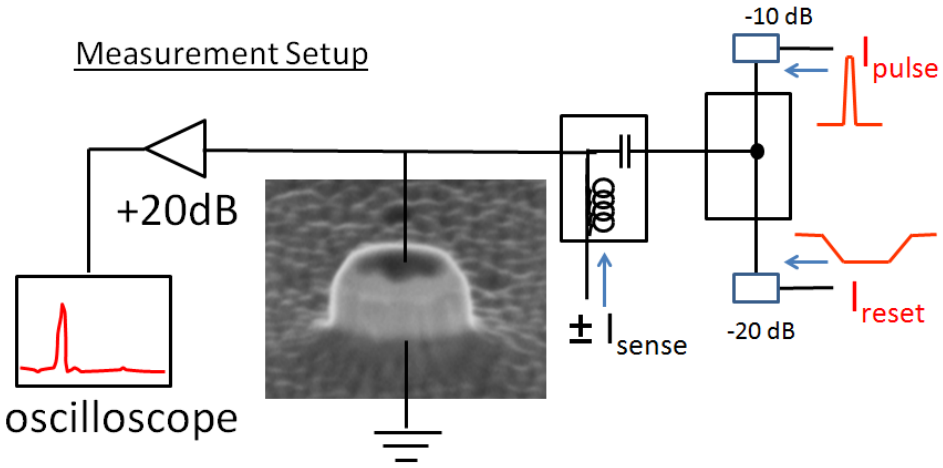

Figure 3.26: Scheme of time-resolved experiment for the spin-torque driven ballistic precessional switching.

substrate when very short pulsed currents were applied. Nevertheless our results indicate that the ST device with the OPP layer works well at LT (< 10 K) because it has a little influence from the T or α.

3.10 Time-domain observations of spin-torque driven ballistic precessional switching

In this section we present our primary results from the time-resolved experiment in the STBPS. The purpose of this experiment was related to the switching experiment with Tb-doped Py: to prove quicker stabilization to the reversed state by comparing the post-damped oscillations after the STBPS with a various α. Electric time-resolved measurements have been carried out in different types of ST devices since Ilya [35] and Nathan [158] demonstrated for the first time, recently time-resolved spin-torque ferro-magnetic resonance (ST-FMR) by

Wang [159]. Our devices have several challenges in which the most important and interesting dynamics occur within $1 \sim 2$ ns after the application of a short pulse current and small sense currents are required to observe the magnetic oscillation signal.

Discussion about the setup

Fig. 3.26 shows the scheme of the time resolved setup and we comment several important aspects of the measurement in the followings. (1) The short pulses (< 1 ns) from the pulse generator (PSPL 10,070A) and reset pulses (1 μs) from the function generator (Agilent 33250A) are applied through the power divider and high-frequency part of bias Tee (5541A). (2) The attenuators are connected in both side of power-divider for protecting the pulse generators. (3) The small sense currents ($I_s = \pm 0.3 - 0.5$ mA) are applied through the low-frequency part of the bias Tee. (4) The transmitted voltage signals are amplified with linear RF amplifiers (PPLs 5867) and recorded in the sampling oscilloscope (TDS 8000B). (5) The trigger signals generated from the internal source of 10,070A are sent to the oscilloscope and to the function generator, with 10 kHz repetition frequency (or 100 μs time interval between the triggers). (6) The trigger delay is set in the equipment to synchronize the short pulse, reset pulse and the output signal: e.g. 10 μs in the function generator and 60 ns in the oscilloscope. (7) The standard pulse switching measurement is required to find right amplitude of the reset pulse before the time-resolved measurement. (8) The number of data points is set in the sampling oscilloscope by adjusting the measurement time after the trigger pulse: e.g. 2 ns of dynamics can be recorded with 250 points with 8 ps resolution. (9) The transmitted signal is averaged over 20,000 times. We set 200

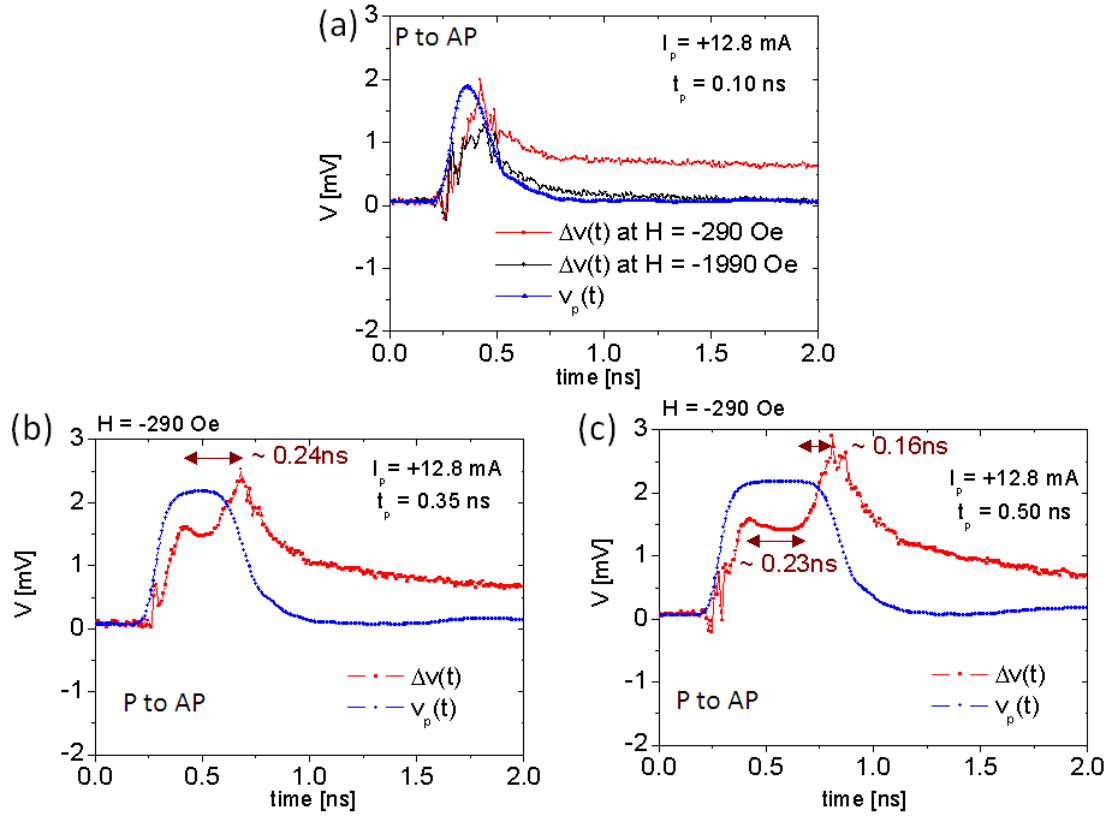

Figure 3.27: Measured time-traces ($\Delta v(t)$) and reduced pulse voltage ($v_p(t)$) with the ″P″ initial state (a) for $I_p = 12.8$ mA and $t_p = 100$ ps and under an external easy axis magnetic field $H = -290$ Oe (at the center of the minor loop) and $H = -1990$ Oe. (b) for $I_p = 12.8$ mA and $t_p = 350$ ps and under $H = -290$ Oe. (c) for $I_p = 12.8$ mA and $t_p = 500$ ps and under $H = -290$ Oe. The $\Delta v(t)$ had additional periodic peaks that were not seen in the $v_p(t)$ as t_p longer, reflecting the nature of precessional motion.

of the soft averages and 100 of the scope averages in the oscilloscope.

The basic idea for obtaining the magnetic signal ($\Delta v(t)$) is the subtraction of two transmitted voltage signals with the opposite polarities of sense currents ($+I_s$ and $-I_s$). We have $\Delta v(t) = v_+(t) - v_-(t) = 2I_s \cdot R(t)$ or $R(t) = \Delta v(t)/2I_s$ from

$$v_+(t) = (I_p(t) + I_s) \cdot (R_p + R(t)) = I_p(t) \cdot R_p + I_p(t) \cdot R(t) + I_s \cdot R(t)$$

$$v_{-}(t) = (I_p(t) - I_s) \cdot (R_p + R(t)) = I_p(t) \cdot R_p + I_p(t) \cdot R(t) - I_s \cdot R(t)$$

where R_p is the initial device resistance. Here we assume that $R(t)$ is identical in both $v_{+}(t)$ and $v_{-}(t)$ due to $2I_s << I_p(t)$ and drop the DC component of voltage ($I_s \cdot R_p$) since the RF amplifier filters the low-frequency component (lower 3 dB frequency = 10 kHz). However we cannot exclude the possibility of some other contributions in the measured $\Delta v(t)$ especially from the short pulse ($I_p(t)$). If there is a small deviation in the base resistance (R_p) due to the different sign of I_s, the measured $\Delta v(t)$ have two components consisting of the magnetic signal we want to measure and the reduced pulse voltage signal: $R(t) = \left[\frac{\Delta v(t)}{2I_s}\right] - \left[\frac{R_{p1}-R_{p2}}{2I_s} \cdot I_p(t)\right]$ from

$$v_1(t) = (I_p(t) + I_s) \cdot (R_{p1} + R(t)) = I_p(t) \cdot R_{p1} + I_p(t) \cdot R(t) + I_s \cdot R(t)$$

$$v_2(t) = (I_p(t) - I_s) \cdot (R_{p2} + R(t)) = I_p(t) \cdot R_{p2} + I_p(t) \cdot R(t) - I_s \cdot R(t)$$

and $v_p(t) = \frac{v_1(t)+v_2(t)}{2} = \left(\frac{R_{p1}+R_{p2}}{2}\right) \cdot I_p(t) + R(t) \cdot I_p(t) \approx \left(\frac{R_{p1}+R_{p2}}{2}\right) \cdot I_p(t) \approx R_p I_p(t)$ because $R_p >> R(t)$ and $I_p(t) >> 2I_s$. Then $\Delta v(t) = 2I_s \cdot R(t) + \eta \cdot v_p(t)$ where $v_p(t) \approx R_p I_p(t)$ and $\eta = (R_{p1} - R_{p2})/R_p$. The later ($\eta \cdot v_p(t)$) could be comparable to the former ($2I_s \cdot R(t)$) even though η is small. For instance, we have $\eta \cdot v_p(t) \approx 0.01$ mV if $v_p(t) = 300$ mV, $\Delta R = 0.1\ \Omega$, $R_p = 30\ \Omega$ with assuming $R_{p1} - R_{p2} \approx 0.01\Delta R$, while $2I_s \cdot R(t) \approx 0.06$ mV if $I_s = 0.3$ mA and $R(t) = \Delta R$.

Results of time-trace measurement for the P initial state

We present results from a device that had nominally same structure and dimension used in the previous section. Fig. 3.27a shows the example of measured $\Delta v(t)$ for the ″P″ initial state with $I_p = 12.8$ mA and $t_p = 100$ ps, and under $H = -290$ Oe (at the center of the minor loop) and $H = -1990$ Oe (at which the

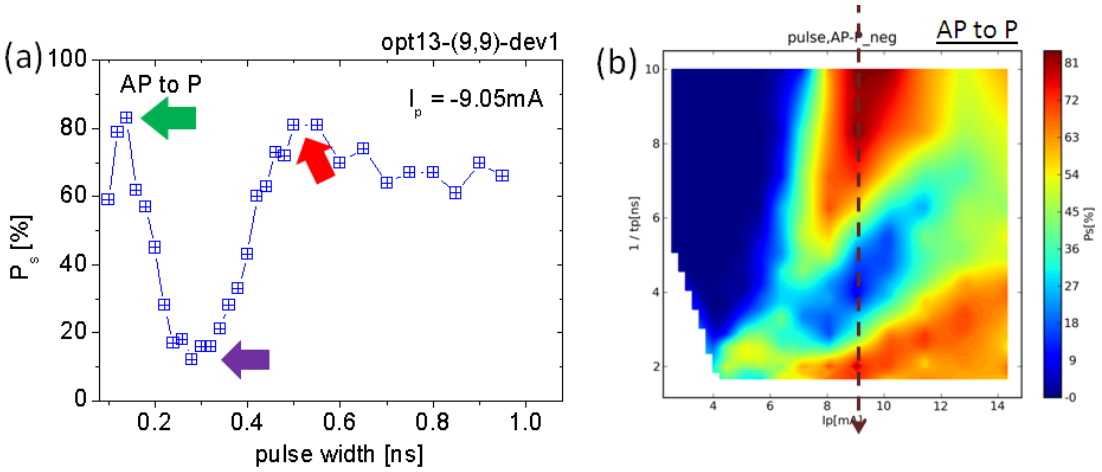

Figure 3.28: (a) Measured switching probabilities (P_s) for AP-to-P as a function of t_p for $I_p = -9.05$ mA. The oscillating feature of P_s implies that the FL takes a half of rotation (π) with $t_p \sim 140 - 160$ ps, 2π with $t_p \sim 260 - 280$ ps and 3π with $t_p \sim 500$ ps. (b) Measured contour map of P_s as functions of t_p and I_p.

FL is always stable for "P"). The reduced $v_p(t)$ is also plotted for the comparison with the $\Delta v(t)$ in which we used arbitrary $\eta \approx 0.003$ but giving similar height at the maximum. (Of course we have to find some reliable way to determine the η precisely: possibly from the dV/dI curve vs I). The final $\Delta v(t)$ at $H = -290$ Oe approached to 0.6 mV, which was consistent with the pulsed switching probability measurement ($\sim$ 100 %) , while the $\Delta v(t)$ at $H = -1990$ Oe went to 0 mV, i.e. the FL relaxed back to the original P state. For longer pulse widths, $t_p = 350$ ps or 500 ps, the $\Delta v(t)$ had additional periodic peaks that were not seen in the $v_p(t)$. This was from the magnetic signal and the time-interval between peaks was roughly $\sim$ 200 ps. Of course we have to quantify η precisely and subtract $\eta \cdot v_p(t)$ for obtaining the pure averaged magnetic signal ($2I_s \cdot R(t)$).

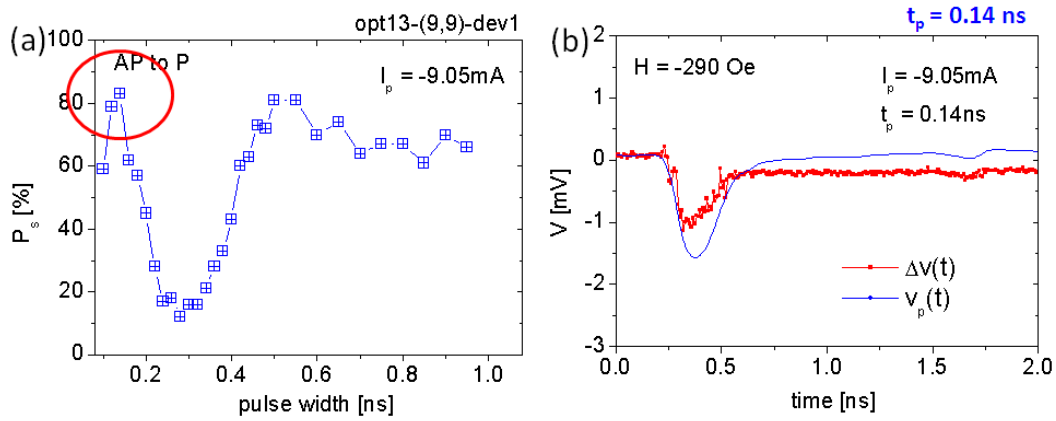

Figure 3.29: Measured time-traced signal ($\Delta v(t)$) for t_p = 140 ps and I_p = −9.05 mA. The measured P_s as a function of t_p is also shown for the comparison. The $\Delta v(t)$ approached to a different value from the baseline of $v_p(t)$ because the FL took a half of rotation (π) with $t_p \sim 140 - 160$ ps.

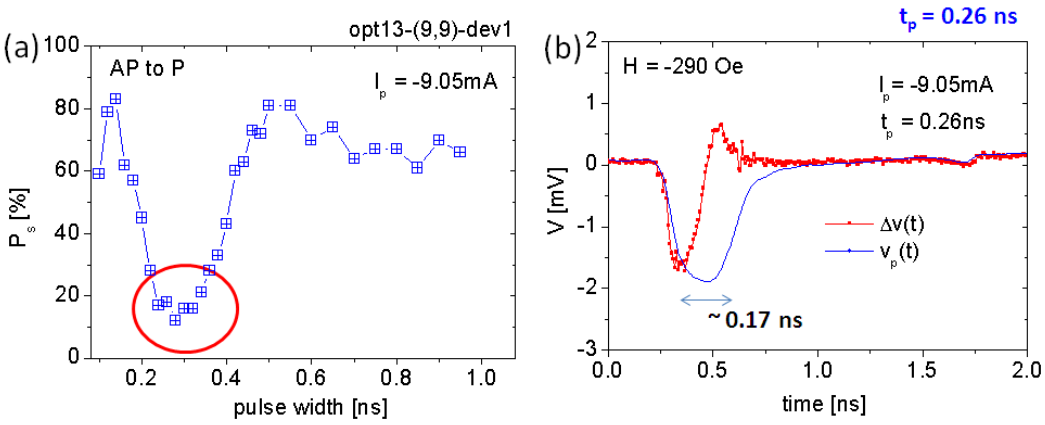

Figure 3.30: Measured time-traced signal ($\Delta v(t)$) for t_p = 260 ps and I_p = −9.05 mA. The measured P_s as a function of t_p is also shown for the comparison. The $\Delta v(t)$ approached to the baseline of $v_p(t)$ because the FL took a full rotation (2π) with $t_p \sim 260 - 280$ ps.

Results of time-trace measurement for AP-to-P

The direct signature of precessional dynamics, or π, 2π and 3π rotations, can be verified by comparing the $\Delta v(t)$ to the switching probabilities (P_s) as a function

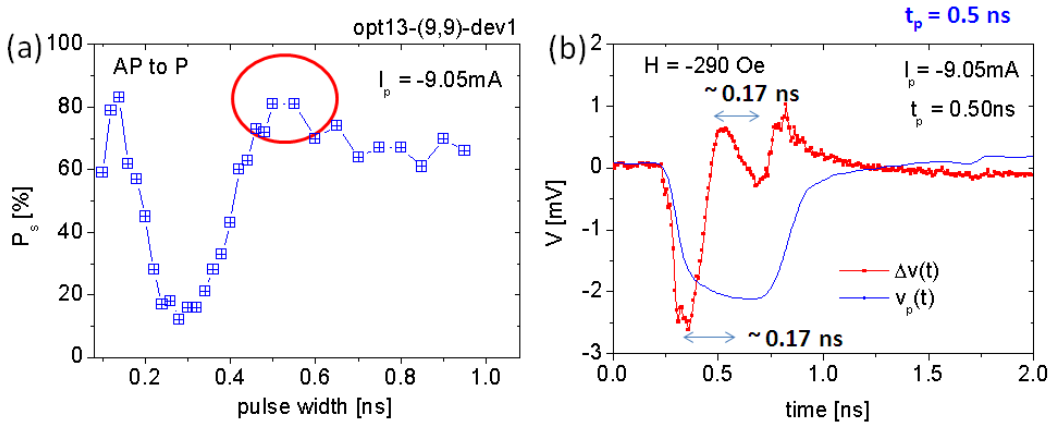

Figure 3.31: Measured time-traced signal ($\Delta v(t)$) for t_p = 500 ps and I_p = −9.05 mA. The measured P_s as a function of t_p is also shown for the comparison. The $\Delta v(t)$ approached to a different value from the baseline of $v_p(t)$ because the FL took one and half of rotation (3π) with $t_p \sim 500$ ps.

of t_p. Fig. 3.28b shows the contour map of the measured P_s for AP-to-P as functions of I_p and t_p. Fig. 3.28a shows the P_s as a function of t_p for fixed I_p = −9.05 mA, and the oscillating feature of P_s implies that the FL takes a half of rotation (π) with $t_p \sim 0.14 - 0.16$ ns, 2π with $t_p \sim 0.26 - 28$ ns and 3π with $t_p \sim 0.5$ ns. The measured $\Delta v(t)$'s are shown, with I_s = +0.4 mA and −0.2 mA, in Fig. 3.29, 3.30 and 3.31. With t_p = 0.14 ns (see Fig. 3.29) the $\Delta v(t)$ approached to −0.3 mV where the π-rotation or the magnetic switching occurred. With t_p = 0.26 ns the $\Delta v(t)$ approached to the baseline of $v_p(t)$ and exhibited two peaks, or quasi sinusoidal shape (see Fig. 3.30). With t_p = 0.5 ns the $\Delta v(t)$ deviated from the baseline of the $v_p(t)$ and had three clear peaks with ~ 0.17 ns of interval time (see Fig. 3.31). This time was a little bit longer (~ 0.03 – 0.04 ns) but approximately consistent with the pulse width for the highest P_s ($t_p \sim 0.14 - 0.15$ ns) or half of the pulse width for the lowest P_s ($t_p \sim 0.26 - 0.28$ ns). If we assume the validity of this number without further analysis, the result implies the t_p should be a little bit shorter than the half of the natural precessional time ($T_p \sim 2 \times 0.17$ ns)

for the ballistic switching or we obtain empirically $t_p \sim 0.4\ T_p$. Of course we need to consider possible side-effects on the measurement to get the conclusion.

We succeeded the observation of the signatures of π, 2π and 3π rotations and the nature of precessional dynamics, but we were not able to detect the post-damping oscillations due to the lots of signal average, different phases in each event and/or signal jittering in the pulses. In addition we cannot exclude the possibility of the other contributions in the measured voltage signal. We believe we can observe improved signals with more precise controls, careful calibration and removal of possible side-effects.

CHAPTER 4

A QUASI-LINEAR SPIN-TORQUE NANO-OSCILLATOR VIA ENHANCED NEGATIVE FEEDBACK OF POWER FLUCTUATIONS

Spin torque nano-oscillators (STNOs) utilize the spin-transfer effect to produce microwave oscillations in nanoscale ferromagnetic elements. STNOs generally are frequency agile but this agility results in a strong non-linear coupling between fluctuations in the oscillator power and phase. This limits phase stability and broadens the oscillator linewidth (Δf) by an amount determined by a nonlinear coupling factor $\nu \equiv N/\Gamma_{eff}$, where N is the change in frequency with oscillator power and Γ_{eff} is the change in effective damping rate with power. Previous research to reduce STNO linewidths has focused primarily on decreasing N. Here I show improved results from a device design that provides $power-dependent\ negative\ feedback$ that results in a significantly enhanced effective damping Γ_{eff}. This, in combination with a small value of N, allows us to achieve a $quasi-linear$ STNO, with $|\nu| \leq 1$ over a large range of current and magnetic field. I realize room temperature oscillator linewidths, $\Delta f \approx 5$ MHz, much narrower than typically obtained, yet the STNO can still be frequency tuned by current over a range $>> \Delta f$.

4.1 Introduction

In a spin-torque nano-oscillator (STNO) a spin-polarized current (I) excites persistent magnetic precession at microwave frequencies in an unpinned magnetic element when the anti-damping spin torque (τ_{st}) is sufficient to compensate for the magnetic damping torque (τ_d) [17, 46, 107, 33]. A seemingly attractive feature of STNOs is that they have high agility, *i.e.* a strong variation of oscil-

lation frequency with oscillator power, but this results in a strong non-linear coupling between amplitude and phase fluctuations that limits phase stability (broadens the oscillator linewidth Δf). Most technological applications will require considerable improvements in STNO phase stability. Here we report on an implementation of a STNO device that results in a quasi-linear oscillator with low field, room temperature linewidths much narrower than typically obtained with a conventional STNO. The device utilizes a magnetic configuration such that there is a strong spatial variation in the spin polarization direction of the excitation current that yields a high effective dynamic damping ($\Gamma_{eff}/2\pi$) of the oscillation, and also such that the frequency shifts with oscillator amplitude due to the magnetic anisotropy fields can be approximately balanced over a broad range of magnetic field bias. This combination strongly reduces the non-linear coupling between amplitude and phase fluctuations resulting in a STNO with a room temperature $\Delta f \approx 5$ MHz, very close to that predicted for a linear STNO of the same oscillator energy, yet the STNO still can be frequency tuned with current over a range $>> \Delta f$. These results demonstrate an effective pathway to substantially enhancing the phase stability of STNOs.

4.1.1 Summary of non-linear auto-oscillator theory

The basic behavior of a STNO can be described with the Landau-Lifshitz-Gilbert-Slonczewski (LLGS) equation [153]. On that basis, a recent non-linear auto-oscillator (NLAO) analysis [122, 131, 46] has described how the amplitude fluctuations of a STNO mode additionally renormalizes its thermally generated intrinsic phase noise via a dimensionless nonlinear coupling (ν), and predicts that for a single mode STNO based on an isotropic thin film nanomagnet the

spectral linewidth (Δf) of a STNO can be described by

$$\Delta f = \frac{\Gamma_o}{2\pi}\left(\frac{k_B T}{E}\right)(1+\nu^2) = \left(\frac{\gamma^3 \alpha_G M_s k_B T}{2\pi V}\right)\cdot\left(\frac{1+\nu^2}{f^2 p}\right) \tag{4.1}$$

Here $E = \beta p$ is the time averaged energy of the oscillator where $\beta = \left(\frac{2\pi V f^2}{\gamma^2}\right)$ for the in-plane magnetized precession (see Section 4.1.3 for the derivation), $\Gamma_o = \alpha_G \cdot \gamma \cdot 2\pi M_s$ and M_s is the saturation magnetization of the oscillating magnetic free layer (FL), p (≤ 1) is the normalized oscillator power ($p \equiv sin^2(\varepsilon/2)$ where ε is the in-plane maximum excursion angle from the precession axis), f is the frequency, V is the FL volume, α_G is the Gilbert damping parameter, k_B is the Boltzmann constant, T is the temperature, γ is the electron gyromagnetic ratio. In general the nonlinear coupling factor (ν) is given by

$$\nu \equiv \frac{N}{\Gamma_{eff}} \equiv \frac{2\pi\, df/dp}{\partial\Gamma(p,I)/\partial p} \tag{4.2}$$

where $N/2\pi \equiv df/dp$ is the agility of the STNO, and where the total damping $\Gamma(p,I) = \Gamma_+(p) - \Gamma_-(p,I)$, which is zero during steady state oscillation, is the difference between the natural positive (dissipative) damping $\Gamma_+(p) = \Gamma_o(1 + \eta(p)) \approx \Gamma_o$, (neglecting any power dependence of the positive damping [160], i.e. assuming $\eta(p) << 1$), and the negative damping $\Gamma_-(p,I) = \sigma I$ caused by τ_{st} . Here $\sigma = \sigma_o g(p)$ is the anti-damping effectiveness of the spin-polarized current with $g(p)$ representing its power dependence ($g(0) = 1$). In general $\sigma_o = \Gamma_o/I_c$, where I_c is the current required for oscillation onset.

The linewidth Δf, microwave power P, and agility of various types of STNOs [161, 162, 163] have been extensively studied, with many results in general accord with the NLAO analysis. In the case of a 4.2 K spin valve study [160] where the precession axis of the FL was collinear *w.r.t* the orientation of the spin polarization of I quantitative agreement with the NLAO model was obtained over a range of bias conditions and for $p \leq 0.35$, albeit with $\Delta f_{min} \geq 25$ MHz,

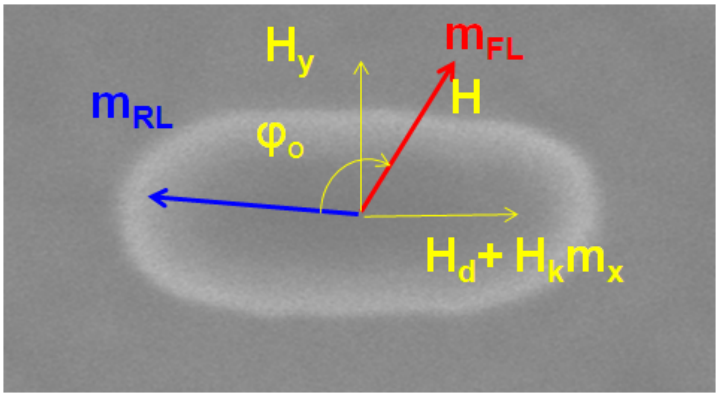

Figure 4.1: Scheme of the internal/external fields and magnetic configuration in the STNO. The externally applied hard axis magnetic field (H_y) shifts the precession axis of the magnetic free layer (FL) and the offset angle from the reference layer (RL). These two angles determine the nonlinear coupling between the amplitude noises and the phase noises in the STNO.

indicative of $|\nu| >> 1$. Strategies [131, 133, 164] to reduce $|\nu|$ in STNO's have generally focused on reducing $N/2\pi$ through the application of either in-plane hard axis magnetic field (H_y) biases [116, 165, 118, 166, 167, 168, 169], or strong out-of-plane field biases [34], to balance out opposing red and blue shifts with p due to the effect of the different anisotropy fields, and experiments have typically demonstrated that a lower Δf is obtained in bias regimes where $N/2\pi$ is low. However since even with a hard axis bias we typically have $|N/2\pi = df/dp| > 1$ GHz, except perhaps in a quite narrow bias range, and since we also usually have $\Gamma_{eff}/2\pi \left(\equiv (2\pi)^{-1}\partial\Gamma(p,I)/\partial p\right) \sim \Gamma_o/2\pi << 1$ GHz, the STNO remains nonlinear with $|\nu| >> 1$.

4.1.2 Idea for achieving a quasi-linear STNO

The most straightforward approach to achieving a quasi-linear STNO is to also increase the dynamic effective damping $\Gamma_{eff}/2\pi \geq 1$ GHz. This can be obtained by employing a magnetic structure such that the variation of STNO power with I above oscillation onset is much weaker than in a typical STNO. It is straightforward to show (see Section 4.1.4) that in general for a STNO

$$\Gamma_{eff}/2\pi = \left(\frac{\Gamma_o}{2\pi}\right)\left(I\frac{dp}{dI}\right)^{-1} \quad \text{and} \quad \nu = \frac{2\pi I}{\Gamma_o}\left(\frac{dp}{dI}\right)\left(\frac{df}{dp}\right) = \left(\frac{2\pi}{\Gamma_o}\right)\left(I\frac{df}{dI}\right) \tag{4.3}$$

In combination with a H_y in the range that provides an approximate balance between the oscillator power dependence of the red-shift due to the out-of-plane demagnetization field and that of the blue-shift due to the in-plane anisotropy field such that $|N/2\pi| < 2$ GHz, a small Idp/dI and hence large $\Gamma_{eff}/2\pi \sim 1 - 3$ GHz will result in $|\nu| \leq 1$.

4.1.3 Correction of magnetic oscillator energy for the in-plane precession

The oscillation energy is given by $E = \beta p$ where β is the power-energy proportionality. The non-linear auto-oscillator model [130, 46, 122] derived the coefficient $\beta = \frac{2\pi M_s V f}{\gamma}$ for the out-of-plane circular precession of the FL when the oscillator frequency f is proportional to the strong out-of-plane applied field. However the β should be different for the in-plane FL precession, because the f is not linear with the applied field and the orbit of the FL is elliptical due to the strong out-of-plane demagnetization field as we have discussed. The energy (E) associated with the precessing magnetic moment is

simply given by the excess energy for tilting the moment away from the effective magnetic field direction (H) or the precession axis (φ_o) of the FL. Then, using the magnetic energy in Eq. 4.10, we have $E(\varepsilon) = E(\varphi_o + \varepsilon) - E(\varphi_o) \approx [-H_d sin\varphi_o - H_y cos\varphi_o + \frac{1}{2}H_k sin2\varphi_o]M_s\varepsilon + \frac{1}{2}[-H_d cos\varphi_o + H_y sin\varphi_o + H_k cos2\varphi_o]M_s\varepsilon^2$ where $m = (-cos\varphi, sin\varphi, 0)$ for an in-plane excursion angle ε ($\varphi = \varphi_o + \varepsilon$). We have $E(\varepsilon) \approx \frac{1}{2}[H - H_k sin^2\varphi_o]M_s\varepsilon^2$, assuming that the φ_o is not shifted much with the oscillation amplitude (ε), which is approximately valid in the limit of small angle dynamics, and applying Eq. 4.11. Then we obtain $\beta = \frac{2\pi V f^2}{\gamma^2}$ for the in-plane oscillation from the FMR frequency of the FL, $\frac{(2\pi f)^2}{\gamma^2 4\pi M_s} \approx H - H_k sin^2\varphi$ (See Eq. 4.12) and the oscillator power $p = sin^2(\varepsilon/2)$ where ε is the maximum precession amplitude. This leads the predicted linewidth(Δf_{pred}) for the in-plane FL precession as

$$\Delta f_{pred} = \frac{\Gamma_o}{2\pi}\left(\frac{k_B T}{E}\right)(1+\nu^2) \approx \left(\frac{\gamma^3 \alpha_G M_s k_B T}{2\pi V}\right)\left(\frac{1+\nu^2}{f^2 p}\right).$$

Employing the appropriate parameters ($\alpha_G = 0.01$, $M_s = 560\ emu/cm^3$) for the Py FL, we have $\Delta f_{pred} \approx (6.86\ MHz)(1+\nu^2)/f^2 p$ for the in-plane FL precession at $T = 300$ K where f is the oscillator frequency in GHz.

4.1.4 Derivation of nonlinear effective damping ($\Gamma_{eff}/2\pi$) of a STNO

Starting from the Landau-Lifshitz-Gilbert Slonczewski (LLGS) equation the non-nonlinear auto-oscillation model [46, 122] derives the following governing equation for a single mode STNO:

$$\frac{\partial a}{\partial t} + i\omega(p)a + [\Gamma_+(p) - \Gamma_-(I,p)] = f_n(t) \tag{4.4}$$

Here $w(p) = w_o(1 + \xi(p))$ is the power-dependent oscillation frequency, $\Gamma_+(p) = \Gamma_o(1 + \eta(p))$ is the dissipative positive damping, and $\Gamma_-(I, p)$ is the negative damping from the spin-transfer-torque, which can be generally expressed as $\Gamma_-(I, p) = \sigma_o I g(p)$ where $g(p = 0) = 1$ at $I = I_c(= \Gamma_o/\sigma_o)$. For a *stationary* (steady-state) auto-oscillation the total, time-averaged damping is zero, or

$$\Gamma(I, p) \mid_{p=p_o} \equiv [\Gamma_+(p) - \Gamma_-(I, p)] \mid_{p=p_o} = 0 = [\Gamma_o(1 + \eta(p)) - \sigma_o I g(p)] \mid_{p=p_o} \tag{4.5}$$

Note that for the case of a *collinear* STNO oscillator $g(p) = 1 - p$, neglecting corrections due to spin accumulation effects in a spin valve device [46]. As we discuss later in this chapter, for a non-collinear device $g(p)$ can be a much weaker and slower function of p. From Eq. 4.5 we have,

$$\frac{1 + \eta(p)}{I} = \frac{g(p)}{I_c}, \quad \frac{\partial \Gamma(I, p)}{\partial I} = -\Gamma_o \frac{g(p)}{I_c} \tag{4.6}$$

Since $d\Gamma(I, p) = \frac{\partial \Gamma}{\partial I} dI + \frac{\partial \Gamma}{\partial p} dp = 0$ and using Eq. 4.6, we have

$$\Gamma_{eff}/2\pi \equiv \frac{1}{2\pi} \frac{\partial \Gamma}{\partial p} = -\frac{1}{2\pi} \frac{\partial \Gamma}{\partial I} \frac{dI}{dp} = \frac{\Gamma_o}{2\pi} \frac{g(p)}{I_c} \left(\frac{dp}{dI} \right)^{-1} = \frac{\Gamma_o}{2\pi} \frac{1 + \eta(p)}{I} \left(\frac{dp}{dI} \right)^{-1} \tag{4.7}$$

and

$$\nu \equiv \frac{N}{\Gamma_{eff}} = \frac{2\pi \frac{df}{dp}}{\Gamma_o \frac{1+\eta(p)}{I} \left(\frac{dp}{dI} \right)^{-1}} = \frac{2\pi}{\Gamma_o} \frac{I}{1 + \eta(p)} \left(\frac{df}{dI} \right) \tag{4.8}$$

Recent work [160] has found that $\eta(p)$ is negligible in a collinear spin valve STNO, and given the low normalized power levels in the single mode regime we assume that also to be the case for our STNO, resulting in:

$$\Gamma_{eff}/2\pi = \frac{\Gamma_o}{2\pi} \left(I \frac{dp}{dI} \right)^{-1} \quad \text{and} \quad \nu = \frac{2\pi}{\Gamma_o} \left(I \frac{df}{dI} \right) \tag{4.9}$$

4.2 Device structure and Details

To demonstrate and study this means of implementing a quasi-linear STNO I fabricated (see Methods) a tapered simple Py(5)-Cu(12)-Py(20) (thickness

in nm and Py = $Ni_{80}Fe_{20}$) nanopillar spin-valve STNO consisting of a thin FL located closer to the substrate than the thicker ferromagnetic reference layer (RL). The STNO was fabricated from a thin film multilayer stack of Py(5)/Cu(120)/Py(5)/Cu(12)/Py(20)/Cu(2)/Pt(30) (thickness in nm) deposited on an oxidized Si substrate, where Py = $Ni_{80}Fe_{20}$. The device had an elliptical cross-sectional area of ~ $50\times145\ nm^2$ at the bottom of the nanopillar, as measured by scanning electron microscopy (±5 nm). In this structure the thinner FL is located closer to the substrate than the thicker ferromagnetic reference layer (RL) and hence the latter has a higher aspect ratio than the former due to the sidewall tapering ($20^o - 30^o$) during the ion-mill process. Therefore the shape anisotropy field (H_k) of the RL is much higher than for the FL, which fairly strongly fixes the unpinned RL, with a measured coercivity H_c(RL) ≈ 1300 Oe, over the Hy range employed in the experiments, while H_c(FL) ≈ 170 Oe. This geometry results in a significant out of plane magnetization component in the bottom two end regions of the elliptical RL, which as discussed below modifies the effective of the spin torque across the FL. The dipolar field (H_d ≈ 250 Oe) from the RL acts to orient the FL anti-parallel (AP) to it ($\varphi_o = 180^o$), with H_y acting to reduce the offset angle φ_o towards 90^o, for $H_y \leq 1000$ Oe. Because of this alignment, coherent oscillations in the FL were generated with a current bias ($I < 0$) such that electrons flowed from the RL to the FL. In the following we will report results from one particular device although the general behavior was quite similar for all of the five devices measured, with the moderate variations in optimum bias conditions, minimum Δf and p attributed to device geometry variations in the fabrication process.

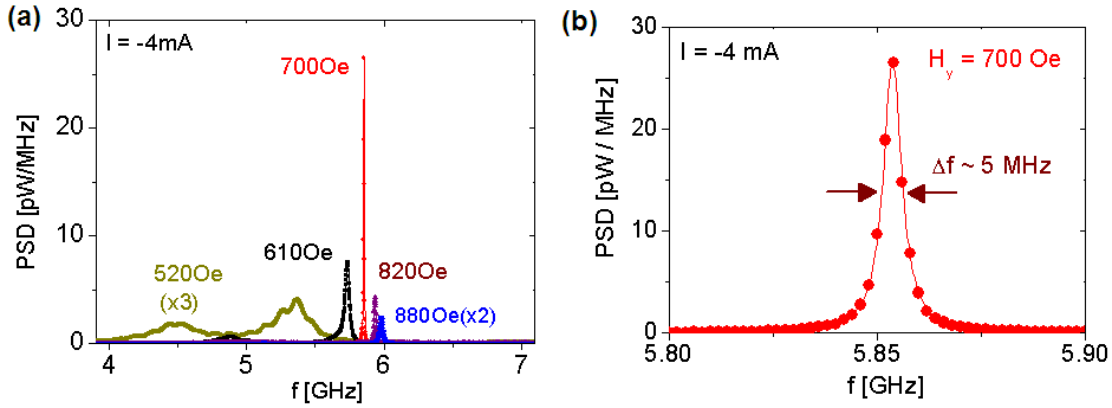

Figure 4.2: Measured power spectral densities (PSD's) for $H_y = 520, 610, 700, 790$ and 880 Oe at $I_{dc} = -4$ mA. For lower $H_y < 600$ Oe the STNO exhibited two modes which we attribute to the relatively wide spatial distribution of the natural oscillation frequency (internal field) across the FL. At and above 650 Oe this distribution is much more uniform and generally a single microwave mode is observed.

4.3 Experimental frequency, power and linewdith as functions of bias currents and hard axis fields

Fig. 4.2 shows the measured power spectral densities (PSD's) of a typical device at 520, 610, 700, 820 and 880 Oe for $I = -4$ mA. As illustrated in the inset, for lower H_y (250 Oe $< H_y <$ 650 Oe) the STNO exhibited two, or more, modes, which we attribute to the relatively wide spatial distribution of the natural oscillation frequency (internal field) across the FL (see Section 4.3.1), and which results in broad Δf's. At and above 650 Oe this distribution is much more uniform and generally a single microwave mode is observed for the current biases employed, as illustrated in Fig. 4.2, with f increasing with H_y as expected for a ST excited in-plane oscillation. In this bias regime the power in the 2nd harmonic was much weaker than the fundamental due to the offset an-

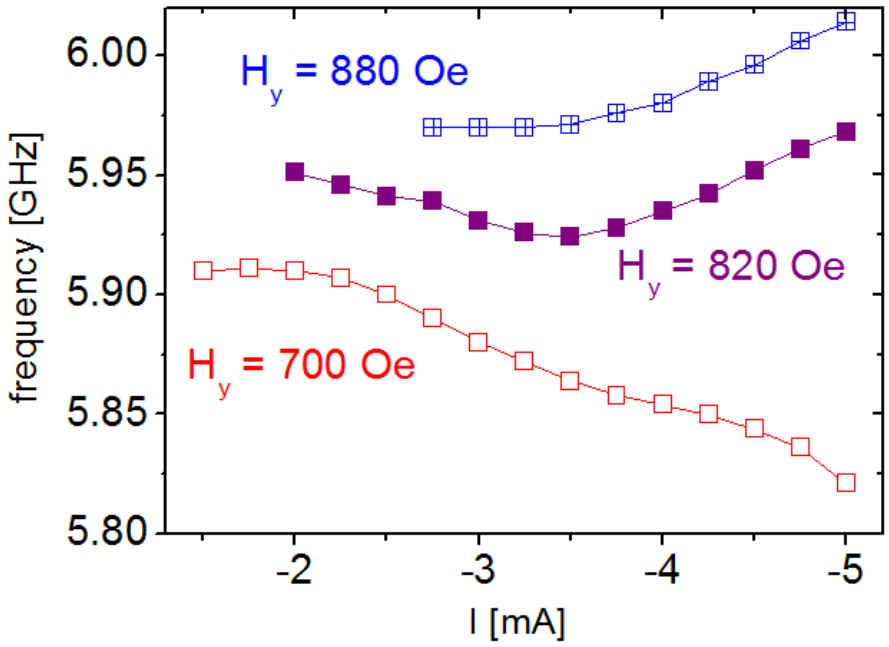

Figure 4.3: Measured oscillator frequency f as a function of I for H_y = 700 Oe, 820 Oe and 880 Oe. At 700 Oe f exhibits a weak red-shift with I. At 820 Oe there is a current dependent transition from a weak red-shift to a weak blue-shift. At 880 Oe the STNO exhibits a monotonic blue-shift.

gle ($90^o < \varphi_o < 135^o$) between the RL and the precession axis of the FL. For the remainder of this paper we will focus on the single mode STNO excitation and its coherent properties for 650 Oe $\leq H_y \leq$ 900 Oe.

In Fig. 4.3, 4.4 and 4.5 we show f, the normalized microwave power p_n ($=P/I^2$ yielding the power underlying resistance oscillations), and Δf, as obtained from Lorentzian fits to the measured PSD's of the STNO as a function of I for three different H_y's; 700, 820, and 880 Oe, in the single mode regime. At 700 Oe f exhibits a weak red-shift with I, $df/d|I| < 20$ MHz/mA, much less than that seen at lower fields, > 100 MHz/mA, while Δf goes through a broad minimum with the lowest Δf ($\approx$ 5 MHz) being reached at approximately the current where p_n begins to vary only weakly for $|I| >$ 3.5 mA. (For $|I| >$ 4.25 mA there

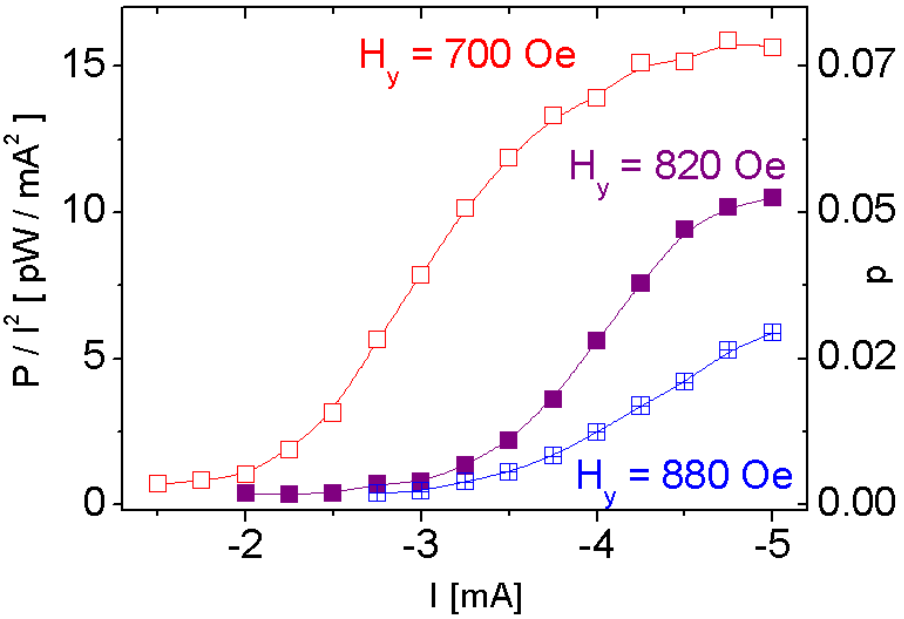

Figure 4.4: Measured oscillator power p_n (= P/I^2) and normalized power p as a function of I for H_y = 700 Oe, 820 Oe and 880 Oe. The p_n begins to vary weakly at which the measured Δf approaches a broad minimum with the lowest Δf. (see Fig. 4.5)

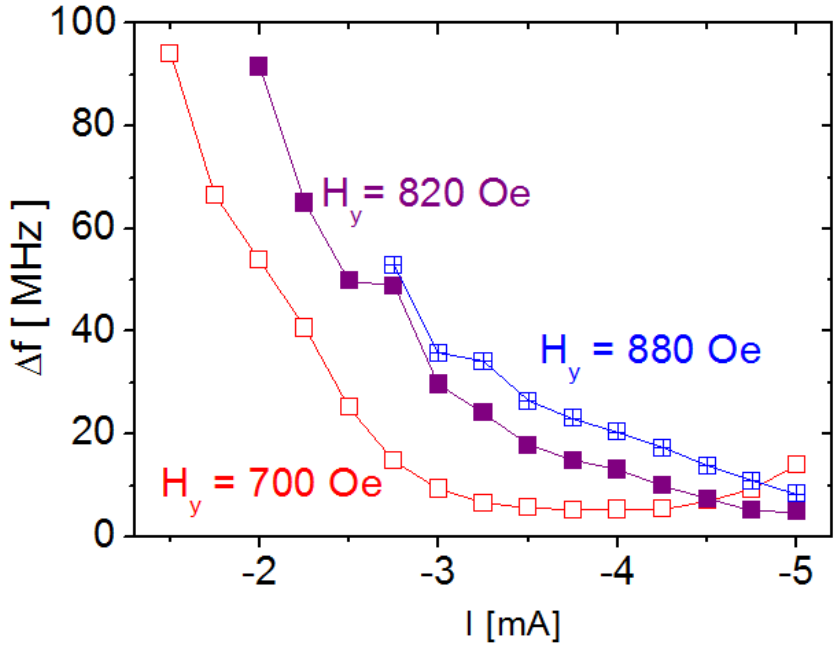

Figure 4.5: Measured linewidth (Δf_{meas}) as a function of I for H_y = 700 Oe, 820 Oe and 880 Oe. The measured Δf approaches a broad minimum with the lowest Δf (~ 5 MHz) at which the measured p_n (= P/I^2) begins to vary weakly. (see Fig. 4.4)

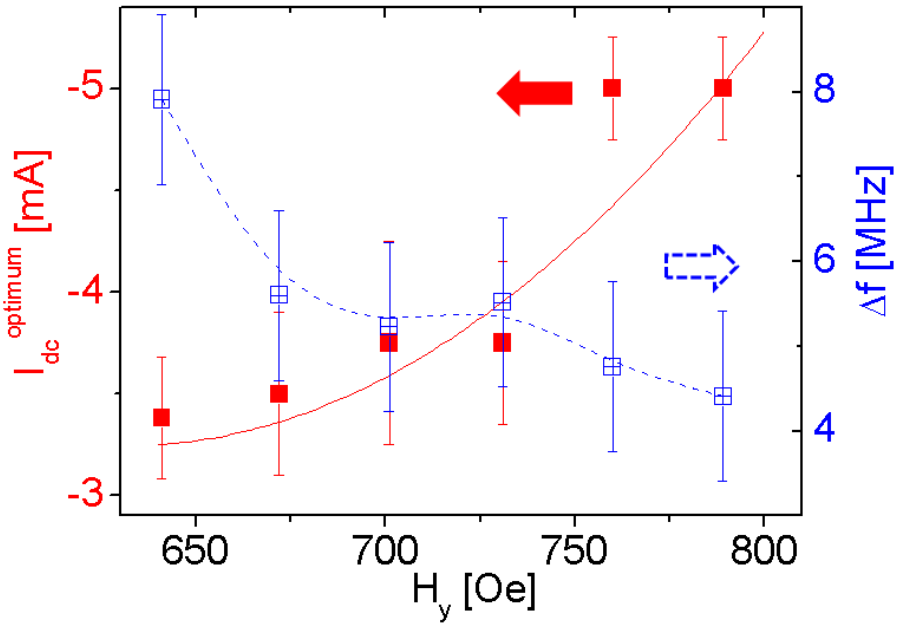

Figure 4.6: Measured minimum Δf and dc current bias (I_{dc}^{opt}) (at the minimum Δf) as a function of H_y. For H_y from 650 Oe to 800 Oe, the optimum current $|I_{dc}^{opt}|$ increased from 3.5 mA to 5 mA with the minimum Δf varying slightly from 8 MHz to 4.5 MHz. Compare with Fig. 4.5

is a slight rise in Δf which is correlated with the onset of a non-uniform mode (see Section 4.6.1) and thus the onset of weak mode jumping.) The general behavior of a saturating p_n, beginning at a steadily increasing optimum current $I^{opt} \approx 2 \sim 2.5 \times I_c$, and a minimum Δf, was obtained for H_y from 650 Oe to 800 Oe, over which I^{opt} increased from -3.5 mA to -5 mA, the highest current employed in the experiment, while Δf_{min} varied slightly from 8 MHz to 5 MHz. At 820 Oe, there was a current dependent transition from a weak red-shift to a weak blue-shift (Fig. 4.3) while p_n appeared to just begin to saturate at 5 mA with Δf approaching 5 MHz at that point. At 880 Oe (Fig. 4.3) the STNO exhibited a monotonic blue-shift ($df/d|I| > 0$) and a monotonically decreasing Δf (Fig. 4.5) while p_n was much lower overall but increased through the higher

part of the range of I (Fig. 4.4). Thus as illustrated in Fig. 4.3, 4.4 and 4.5, this STNO device has a broad range of field bias where Δf can be quite low, in comparison to most previous room temperature spin valve STNO results, and still be frequency tunable $|Idf/dI| >> \Delta f$.

4.3.1 Spatial distribution of STNO internal field at equilibrium

We employed micromagnetic calculations [154] to compute by the energy minimization method the internal field distribution ($\vec{H}_{int}(\vec{r})$) for our STNO device under an external field H_y. The modeled multilayer structure had a tapered elliptical shape with a sidewall taper of 20^o and with cross-sectional dimensions of $50 \times 150\ nm^2$ at the bottom of the nanopillar stack. The modeling digitized the volume into $2.5 \times 2.5 \times 2.5\ nm^3$ unit cells. Starting from the bottom the multilayer consisted of Py(5)/Cu(12.5)/Py(20), with the thickness in nm. An exchange parameter $A = 13 \times 10^{-12} J/m$ was assumed for Py ($Ni_{80}Fe_{20}$), and the other material parameters employed in the modeling have been provided in the main text. The contributors to $\vec{H}_{int}(\vec{r})$ were $\vec{H}_y$, the dipolar field ($\vec{H}_d(\vec{r})$) from the RL and the demagnetization field ($\vec{H}_{demag}(\vec{r})$) of the FL itself. The internal field determines the "natural" oscillation frequency of each element of the FL at the onset of oscillation, and hence, given the limited strength of the exchange coupling between the elements, the width and character of this distribution provides a measure of the tendency of the FL to have multiple, spatially distributed, modes of oscillation as opposed to exhibiting a single, more or less spatially uniform oscillation when the distribution is sufficiently narrow.

In general $\vec{H}_{int}(\vec{r})$ of the FL of a spin value nanopillar has a *spatial non-*

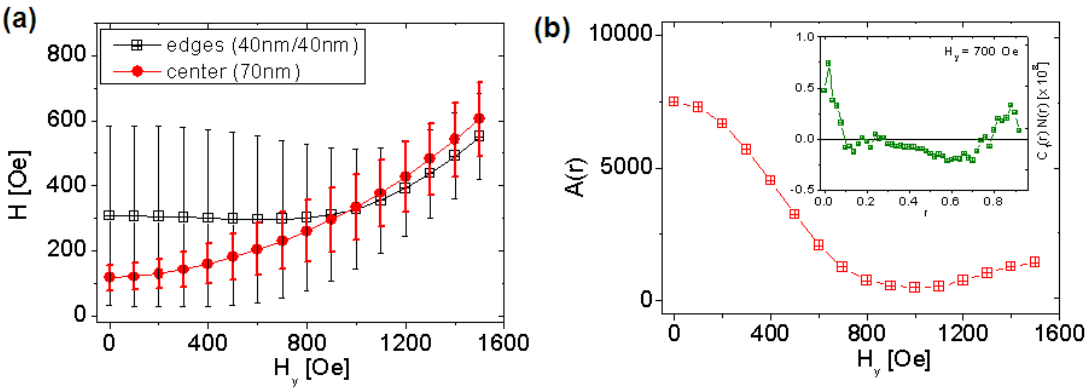

Figure 4.7: (a) Local average and dispersion of the internal fields ($|\ \vec{H}_{int}(\vec{r})\ |$), calculated by micromagnetics [154], on the edges (40nm) and the center (70nm) of the FL as a function of H_y for $I = 0$. (b) The calculated correlation function $A(H_y)$, which is a weighted measure of the spatial non-uniformity in $\vec{H}_{int}(\vec{r})$. Both analyses indicate that the internal field distribution is much more uniform when H_y approaches and exceeds 700 Oe than at lower bias fields, consistent with the view that a relatively uniform internal field distribution is required for single mode behavior.

uniformity, with both its local average and dispersion being strongly dependent on the location and H_y. To quantify the topographical inhomogeneity of $\vec{H}_{int}(\vec{r})$ in our structure we employed two different methods. The first was to compare the local average and dispersion of $|\ \vec{H}_{int}(\vec{r})\ |$ in three different regions of the FL defined as the regions encompassed by the left 40 nm of the long axis of the ellipse, the center 70 nm and the right 40 nm. As Fig. 4.7a shows, there is a significant difference in the averages of $|\ \vec{H}_{int}(\vec{r})\ |$ between the edges and the center region at low H_y, but as H_y increases to $\approx 700 - 800\ Oe$ this difference reduces substantially, indicating a convergence in the average, natural oscillation frequency in the different regions of the FL.

The second method used to characterize the internal field distribution was to calculate the correlation function $A(H_y) = \sqrt{\int dr\ |\ C(r)\ |\ /\ \int drN(r)}$ where

$C(r) = \int\int_{|\vec{r}''-\vec{r}'|=r} dr''dr'(\vec{H}(\vec{r}') - \bar{H}) \cdot (\vec{H}(\vec{r}'') - \bar{H})$ is the auto-correlation function of the internal field distribution and $N(r) = \int\int_{|\vec{r}''-\vec{r}'|=r} dr''dr'$ is the normalization function. $A(H_y)$ provides a quantitative, weighted measure of the spatial non-uniformity in $\vec{H}_{int}(\vec{r})$ as a function of the hard axis bias. As shown in Fig. 4.7b, $A(H_y)$ decreases markedly, by more than a factor of six as H_y is increased to $\sim$ 700 *Oe*, and reaches its minimum value at $\approx$ 1000 *Oe*. Thus both approaches indicate that the internal field distribution is much more uniform when H_y is in the 700 to 1000 *Oe* than at lower bias fields, consistent with view that a relatively uniform internal field distribution will result in single mode behavior in a STNO.

4.4 Comparison with the nonlinear auto-oscillator theory

Approximate values for the normalized oscillator power p can be obtained within the context of the macrospin model (see Section 4.4.1). This requires as inputs p_n (=P/I^2) and φ_o. We obtain the latter through the use of the predicted [95, 170, 131] φ dependence of the onset current, $I_c = I_{c0}/|cos\varphi_o|$ (see Section 4.6.2). In Fig. 4.8 we plot I_c vs. H_y, as determined by the point where the oscillator mode is first clearly established, along with the value of φ_o for each H_y as indicated by the fit of the predicted variation of I_c. In Fig. 4.9 we plot $\Delta f \times p$ as determined from the measured data of Fig. 4.3, 4.4 and 4.5 for the three different field values. Over a wide range of current and field, we see that while p varies by a factor of 30, $\Delta f \times p$ varies by ≤ 2 and is close to the predicted linear oscillator value $\Delta f_{pred} \times p \approx 0.19$ MHz (for $\nu = 0$ and $f = 6$ GHz) within the factor of 2, demonstrating that Eq. 5.1 provides a rather good description of Δf of this STNO, despite the approximations in estimating p, and that the non-linear

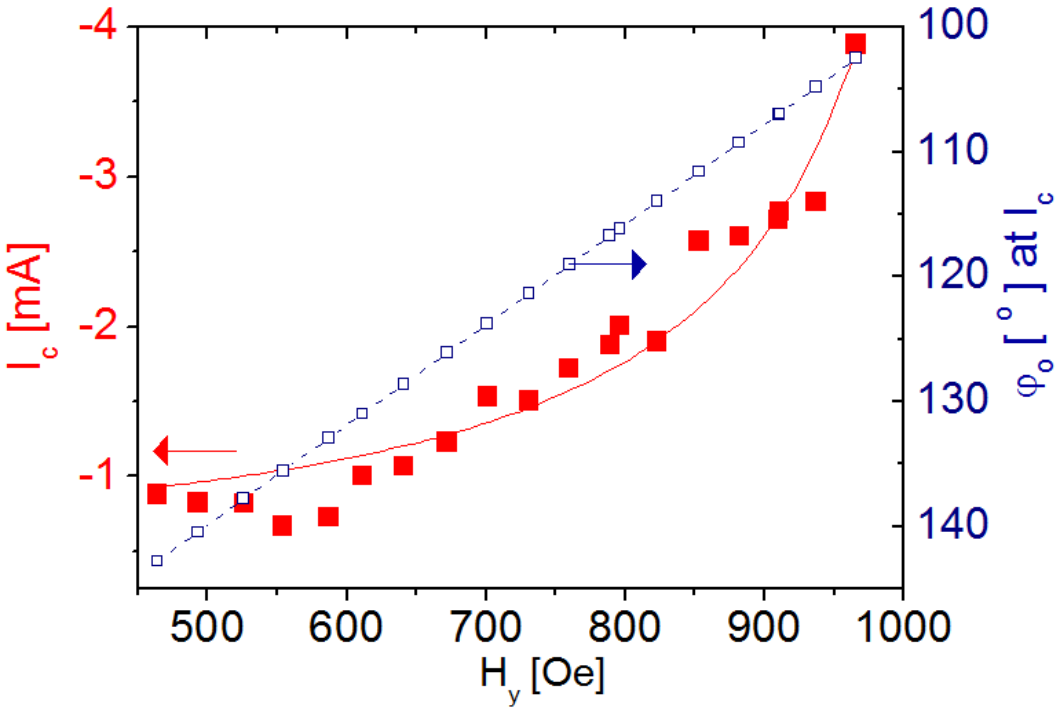

Figure 4.8: Measured threshold current (I_c) for the on-set of the auto-oscillation and fitted offset angle (φ_o) as a function of H_y. We obtain the φ_o through the use of the predicted φ dependence of the onset current, $I_c = I_{c0}/|cos\varphi_o|$ (see Section 4.6.2).

coupling constant $|\nu| \leq 1$ in this bias regime.

To further demonstrate the agreement with the NLAO analysis Fig. 4.11 shows the measured Δf and estimated normalized power p as a function of H_y for a fixed bias current $I = -4$ mA. As H_y increases from 400 Oe Δf decreases rapidly, reaching its minimum $\approx$ 5 MHz at $H_y^{opt} \approx 700$ Oe, and then increases again with higher H_y, while p decreases monotonically from 400 Oe. Also shown in Fig. 4.11 is Δf_{pred}, as determined from Eq. 5.1 and Eq. 4.3 using the estimated p and the measured Idf/dI (see Section 4.4.1). Here again there is quite good agreement between experiment and prediction from 675 Oe to 800 Oe.

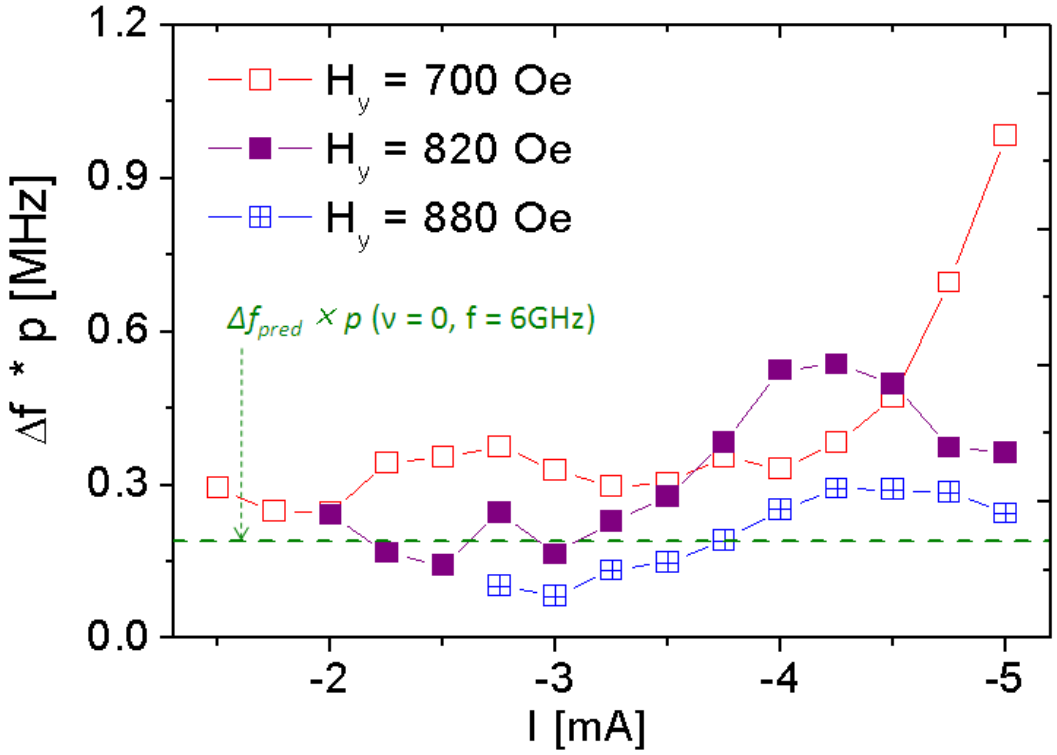

Figure 4.9: Measured $\Delta f \times p$ at H_y = 700 Oe, 820 Oe and 880 Oe. The dotted line corresponds to the predicted $\Delta f \times p$ from Eq. 5.1 for $\nu = 0$ and $f = 6$ GHz. Over a wide range of current and field, we see that while p varies by a factor of 30, $\Delta f \times p$ varies by ≤ 2 and is close to the predicted linear oscillator value $\Delta f_{pred} \times p \approx 0.19$ MHz (for $\nu = 0$ and $f = 6$ GHz).

4.4.1 Experimental estimation of the STNO's normalized oscillator power p and nonlinear coupling ν

Employing the appropriate parameters ($\alpha_G = 0.01$, $M_s = 560$ emu/cm^3) for the Py free layer we have from Eq. 5.1, $\Delta f_{pred} \approx \left[6.86\left(\frac{1+\nu^2}{f^2 p}\right)\right]$ MHz at $T = 300$ K, where f is the oscillator frequency in GHz. To compare the measured linewidth Δf_{exp} with Δf_{pred} we obtained appropriate values for p under various field and current biases from the measured power (P_L), delivered to the 50 Ω (R_L) transmission line [151], that is $P_L = \frac{1}{2} V_g^2 \frac{R_L}{(R_L+R_S)^2}$ where R_S is the device resistance ($R_S \approx 25$ Ω)

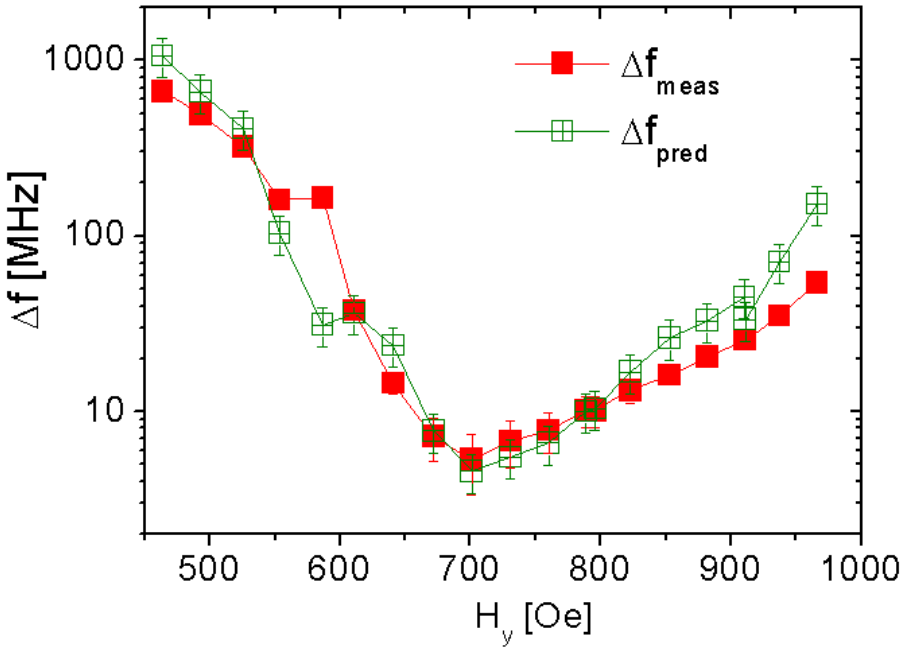

Figure 4.10: Measured oscillator linewidth (Δf_{meas}), as obtained from Lorentzian fits to the output of the spectrum analyzer, as a function of H_y at $I_{dc} = -4$ mA. The predicted linewidth Δf_{pred} from Eq. 5.1 is also compared. We see the quite consistency between Δf_{pred} and Δf_{meas} for $H_y < 800$ Oe.

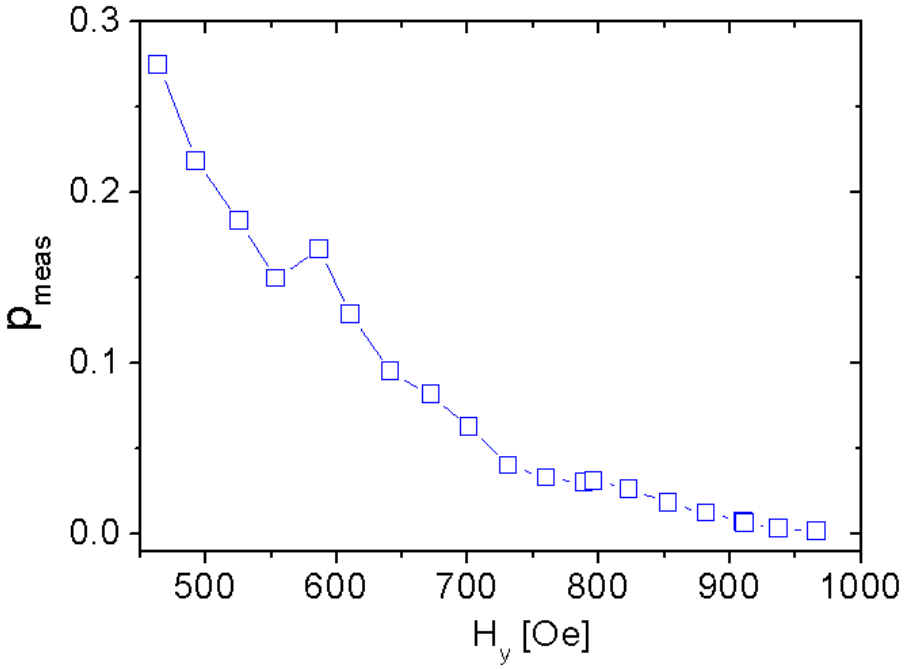

Figure 4.11: Experimental oscillator dimensionless power (p) as a function of H_y at $I_{dc} = -4$ mA. The p decreases monotonically from 400 Oe due to the reduced anti-damping ST efficiency as the offset angle (φ_o) approaches to 90^o.

and V_g is the amplitude of the generated microwave signal ($\Delta V(t) = V_g sin(\omega t)$). We assumed that the magnetoresistance voltage signal is $\Delta V(t) = I \cdot R(t) \approx I \cdot (\partial R/\partial \varphi\,|_{\varphi_o}) \cdot sin(\omega t) \cdot \varepsilon$ (as appropriate for the case $90^o \leq \varphi_o \leq 135^o$) where $R(\varphi(t)) = \Delta R_o \left(\frac{sin^2(\frac{\varphi(t)}{2})}{1+\chi cos^2(\frac{\varphi(t)}{2})} \right)$ and $\varphi(t) = \varphi_o + \varepsilon\ sin(\omega t)$. We measured $\Delta R_o = 0.2\ \Omega$ and assumed $\chi = 1$ as previously reported [160] for Py.

We converted the measured P_L to p (assuming $p = sin^2(\varepsilon/2)$) with $\varepsilon \approx \sqrt{\frac{2P_L}{R_L}} \frac{R_L+R_S}{I \cdot R'(\varphi_o)}$ and the obtained offset angle (φ_o) in Fig. 4.8 for $R'(\varphi_o) = \partial R(\varphi_o)/\partial \varphi_o$. As an example, we obtained $P \approx 225$ pW at $H_y^{opt} = 700$ Oe and $I^{opt} = -4$ mA. From the measured onset current of $I_c \sim -1.25$ mA for $H_y = 700$ Oe, we estimated $\varphi_o \approx 124^o$ (see Fig. 4.8), and thus obtained $\varepsilon \approx 28.9^o$. We note however that both macrospin and micromagnetic modeling indicate that the orientation of the precession axis φ_o shifts toward 90^o with bias current (oscillation power) in this field regime due to the non-parabolic nature of the magnetic energy potential, and thus $\varphi_{o,-4mA}$ could be as low as $\sim 116^o$ which would result a negligible difference ($\varepsilon \approx 29.1^o$). With the assumed $p = sin^2(\varepsilon/2)$, although this is also not strictly correct due to the energy potential, we have $p \approx 0.063$. At $I = -4.0$ mA we measured $f \approx 5.854$ GHz and $df/d|I| \approx -16$ MHz/mA, which yields $\nu \approx -0.65$ and thus $\Delta f_{pred} \approx 4.6 \pm 1.3$ MHz, quite close to $\Delta f_{exp} \approx 5 \pm 2$ MHz.

4.5 Quasi-linear behaviors of the STNO device

The quasi-linear ($|\nu| \leq 1$) STNO behavior that is obtained over a rather broad range of field and current in the optimum field bias regime as illustrated by Fig. 4.13, is caused by a combination of a reduced agility, $|N/2\pi \equiv df/dp| \leq 2$ GHz, with a high effective damping $\Gamma_{eff}/2\pi \sim 1 - 3$ GHz. The lower $N/2\pi$

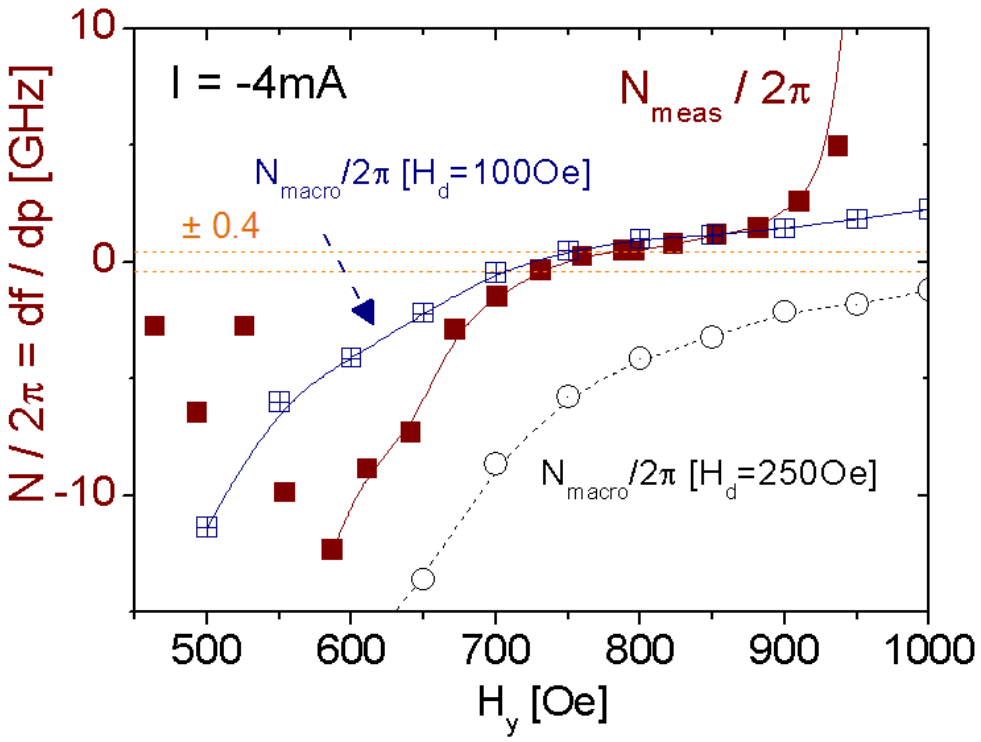

Figure 4.12: Experimental $N/2\pi = df/dp$ as a function of H_y at −4 mA. $N/2\pi$ as obtained from macrospin simulations for H_k = 450 Oe, and for H_d = 100 Oe and 250 Oe.

arises from the fact that for an in-plane magnetized FL with a significant H_k such that $145^o > \varphi_o > 90^o$ the strong red shift with oscillator power due to the out-of-plane demagnetization field can be substantially balanced by a blue shift resulting from H_k (see Section 4.5.1). In Fig. 4.12 we show $N_{meas}/2\pi$ as obtained experimentally for our device at $I = -4$ mA along with the prediction from a macrospin modeling (& simulation) of the LLGS equation for $N_{macro}/2\pi$ at the onset of oscillation for H_k = 450 Oe and two different values of H_d (100 and 250 Oe). The lower H_d provides the somewhat better match to the data despite being well below the experimentally determined H_d = 250 Oe. In general macrospin modeling does not provide a good quantitative description of $N_{meas}/2\pi$ because of the significant spatial variations in the magnetization orientation across the

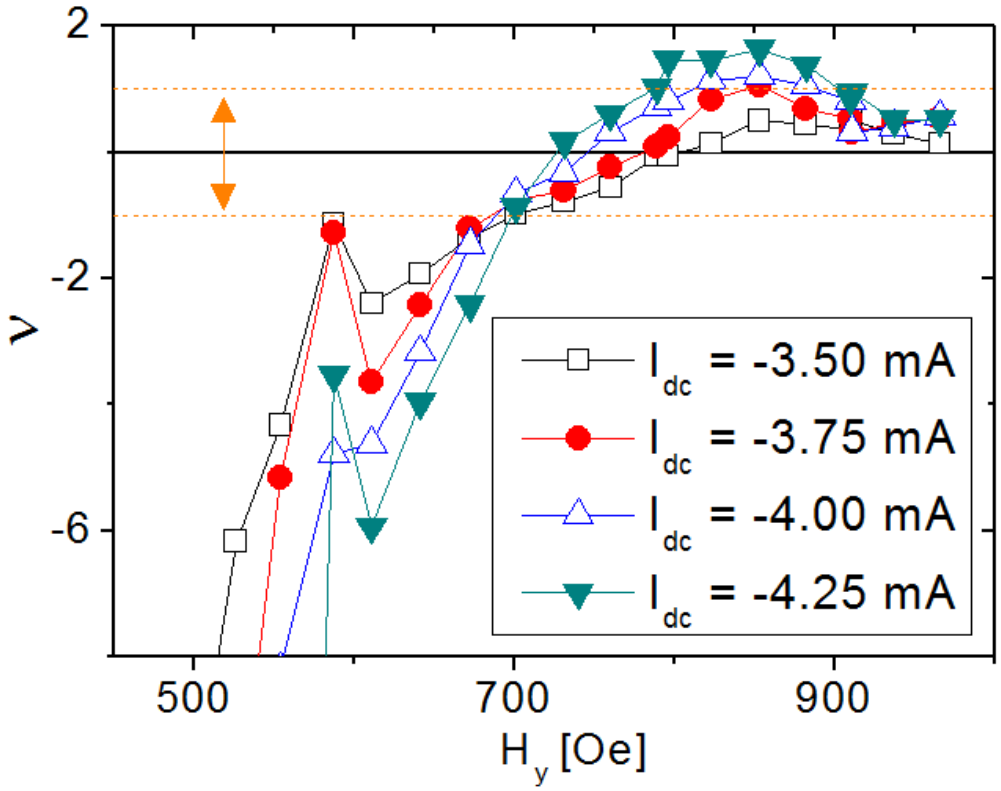

Figure 4.13: Experimental non-linearity ν as determined from measured $I, df/dI$ and Eq. 4.3 as a function of H_y at several I's. In general $|\nu| \leq 1$ for $H_y > 700$ Oe.

FL (see below). (For additional discussion of the macrospin modeling and analysis and their values and limitations in predicting $N/2\pi$, see Section 4.5.1) A key point to note is that $N_{meas}/2\pi$ ranges between ±2 GHz for 700 Oe $< H_y <$ 900 Oe, yet in general $|\nu| \leq 1$ in this field range (see Fig. 4.13). This is the result of the high effective damping $\Gamma_{eff}/2\pi \equiv (2\pi)^{-1}\partial\Gamma(p,I)/\partial p = (\Gamma_o/2\pi I)(dp/dI)^{-1}$ of our STNO device in this field range that arises from its non-uniform magnetic configuration.

4.5.1 Macrospin modeling, and analytical predictions, of STNO agility

To obtain a quasi-linear STNO it is necessary that its agility be no more than comparable to the effective damping of the oscillator $\Gamma_{eff}/2\pi$; in our case $| N/2\pi = df/dp | \leq 2$ GHz. This is achieved by magnetic biasing the oscillator, by some combination of external and internal effective fields, such that the red and blue frequency shifts as a function of oscillator amplitude that arise from anisotropy field effects are approximately balanced. For an in-plane magnetized spin valve or magnetic tunnel junction STNO the suggested approach [133, 165], is to apply an external field with a substantial hard axis component so that the red shift due to the power dependence of the oscillation frequency from the out-of-plane demagnetization field is balanced by the blue shift arising from the in-plane anisotropy field. Analysis treating the FL as a rigid domain, or alternatively macrospin modeling, can provide understanding of the origin of the reduced agility, and some general guidance as to what field configuration to employ to achieve it.

Within the macrospin approximation the magnetic energy of the FL under the assumption that the RL does not rotate at all with H_y, is given by

$$E(\varphi,\theta) = -H_d M_s cos\theta cos\varphi - H_y M_s cos\theta sin\varphi - (H_k M_s/2) cos^2\theta cos^2\varphi + 2\pi M_s^2 sin^2\theta \quad (4.10)$$

where θ is the out-of-plane tilt angle of the FL moment. At equilibrium ($\vec{m} \parallel \vec{H}$) the FL lies in-plane and we have

$$(H_k - H) cos\varphi_o = H_d \text{ and } H sin\varphi_o = H_y \quad (4.11)$$

where H is the effective in-plane internal field. The ferromagnetic resonance

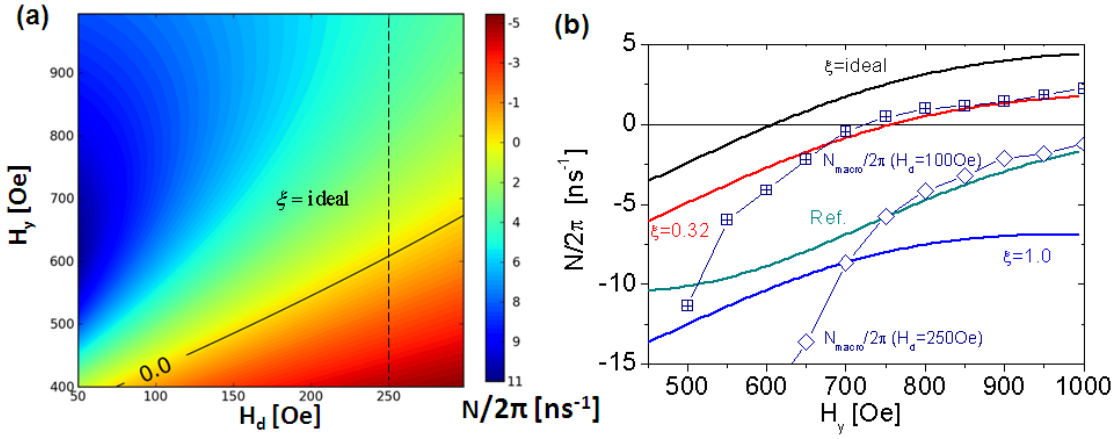

Figure 4.14: (a) Calculated contour map of $N/2\pi(H_d, H_y)$ using Eq. 4.13, for $H_k = 450\ Oe$ and for the case where the precessing moment maps out an ideal elliptical orbit. $N/2\pi = 0$ occurs at $H_y \sim 600\ Oe$ for $H_d = 250\ Oe$ while our experimental STNO exhibits $N/2\pi \approx 0$ at $H_y \sim 750 - 800\ Oe$. (b) Calculated $N/2\pi(H_y)$ for the ideal elliptical precessional orbit, for a circular precessional orbit ($\xi = 1$), for an arbitrary $\xi = 0.32$, from the analysis of Ref. [133]. (all for $H_k = 450\ Oe$ and $H_d = 250\ Oe$), and $N/2\pi(H_y)$ obtained from the macrospin simulation (Section 4.6.2) (for $H_k = 450 Oe$ and $H_d = 100$ or $250\ Oe$).

frequency of the FL, $\omega_o^2 = \left(\frac{\gamma}{M_s cos\theta}\right)^2 \left[\frac{\partial^2 E}{\partial \varphi^2}\frac{\partial^2 E}{\partial \theta^2} - \left(\frac{\partial^2 E}{\partial \varphi \partial \theta}\right)^2\right]$, is then

$$\omega_o^2 \approx \gamma^2[H - H_k sin^2\varphi_o][H + 4\pi M_s cos^2\theta]_{\theta=0^o} \tag{4.12}$$

and thus ω_o is determined by the effective in-plane anisotropy field ($H_{k,eff} = -H_k sin^2\varphi$) and the out-of-plane demagnetization field ($4\pi M_{eff} = 4\pi M_s cos^2\theta$). When the FL is ST excited, the mean oscillation frequency varies with amplitude. To examine this we assume a (small angle) in-plane precession of the FL about H ($\varphi = \varphi_o + \varepsilon\ sin(\omega t)$), although we note that the τ_{st} also shifts the oscillation's in-plane (φ_o). We then have $< H_k sin^2\varphi > \approx H_k(sin^2\varphi_o + cos2\varphi_o \cdot 4p)$ and $4\pi M_{eff} =< 4\pi M_s \cdot \xi \cdot cos^2(\varepsilon) > \approx 4\pi M_s(1 - \xi \cdot 4p)$ where $p \equiv < sin^2(\varepsilon/2) > \approx < \varepsilon^2 > /4$ and ξ is the ellipticity factor due to $4\pi M_{eff} >> H$. The *time-averaged* ω^2 is

$\omega^2 \approx \gamma^2[H - H_k(sin^2\varphi_o + cos2\varphi_o \cdot 4p)][H + 4\pi M_s(1 - \xi \cdot 4p)]$ and we have

$$N/2\pi \equiv \frac{\partial f}{\partial p} \approx -\frac{\gamma^2}{\pi\omega}[(H_k cos2\varphi_o)(H+4\pi M_s(1-4\xi p))+4\pi M_s\xi(H-H_k(sin^2\varphi_o+cos2\varphi_o\cdot 4p))] \tag{4.13}$$

In Fig. 4.14a we show a contour map of $N/2\pi$ calculated via Eq. 4.13 as functions of H_d and H_y for $H_k = 450\ Oe$, $p = 0.03$, and for an idealized simple elliptical orbit where $\xi \approx (H - H_k sin^2\varphi_o)/4\pi M_s$ due to the energy balance between the maximum out-of-plane and in-plane excursions. For the case of $H_d = 250\ Oe$ this result predicts a transition from a red shift, $N/2\pi < 0$, to a blue shift, $N/2\pi > 0$, at $H_y \approx 600\ Oe$ (Fig. 4.14b), which is somewhat below the experimentally observed transition point, $H_y \approx 750\ Oe$, that depends weakly on I_{dc} (Fig. 4.12). Fig. 4.14b also shows the result for the elliptical case, and also, for comparisons, the $\xi = 1$ case (circular precession), the $\xi = 0.32$ case (arbitrary but close to the experimental observation), and the result of a previous somewhat different analysis [133], all for the case of $H_k = 450\ Oe, H_d = 250\ Oe$.

We also employed macrospin simulations to estimate $N/2\pi$, utilizing Eq. 4.14. The result for the case of $H_k = 450\ Oe, H_d = 100\ Oe$ and $250\ Oe$ is also shown in Fig. 4.14b. That result lies between the prediction of the analytical approximation that assumes a pure elliptical orbit and those that assume a circular orbit. This is due to the fact that the non-conservative, φ-dependent ST affects the time-averaged dynamic energy balance of the precessional orbit and somewhat reduces its ellipticity, but does not result in circular precession. This point in illustrated by the inset in Fig. 4.14b that compares the small amplitude precession orbit as determined by full macrospin modeling with the elliptical orbit expected from a simple in-plane and out-of-plane energy balance.

Fig. 4.12 and Fig. 4.14 show that while the macrospin approximation pro-

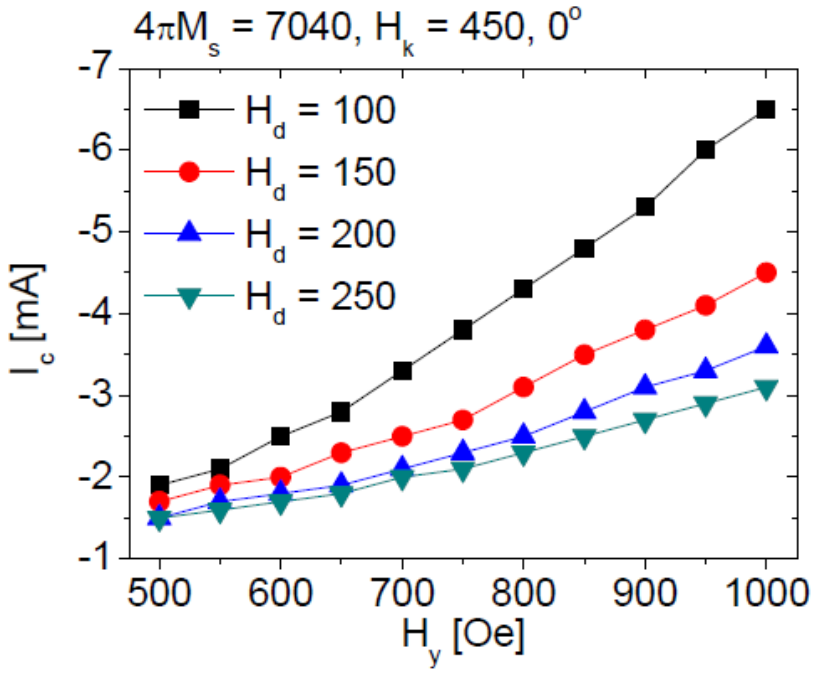

Figure 4.15: Threshold currents (I_c) as determined from the macrospin simulation as a function of H_y for H_d = 100, 150, 200 and 250 Oe and for H_k = 450 Oe. The out-of-plane tilt angle of the RL is zero.

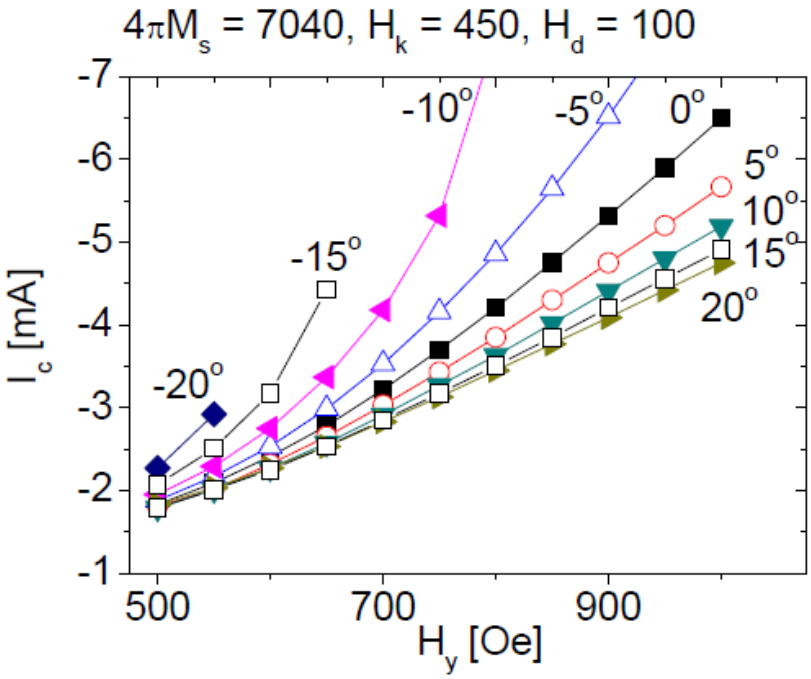

Figure 4.16: Threshold currents (I_c) for the tilted RL as determined from the macrospin simulation as functions of H_y for its tilted angle (θ_{RL}) from -20^o to 20^o and for H_k = 450 Oe, H_d = 100 Oe.

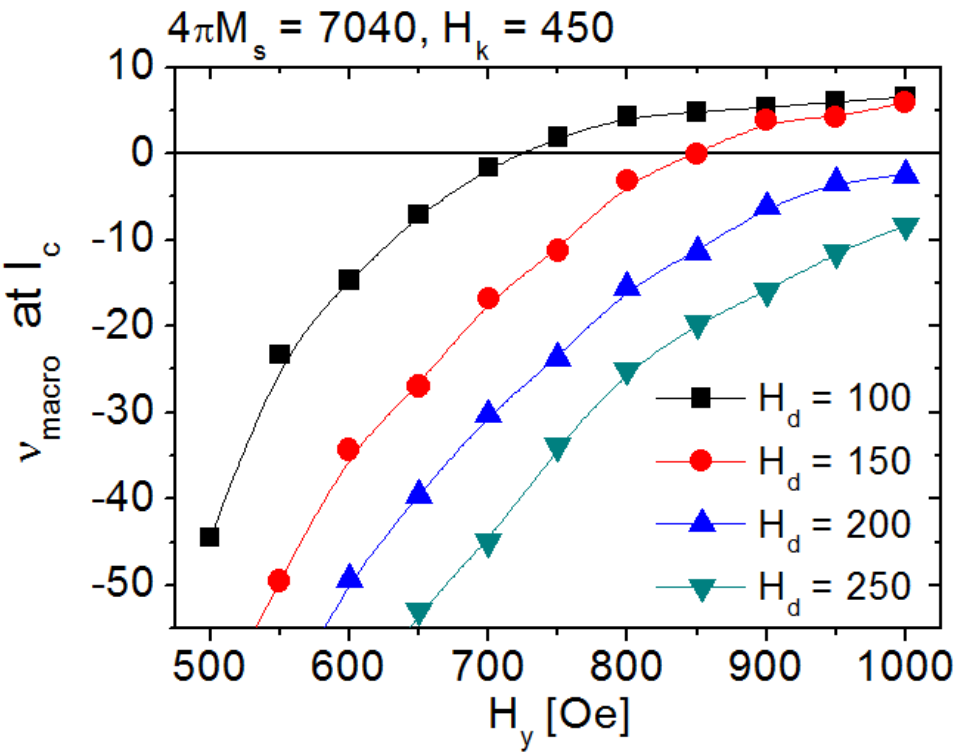

Figure 4.17: Non-linearity (ν) as determined from the macrospin simulation as a function of H_y at I_c for $H_d = 100, 150, 200$ and 250 Oe and for $H_k = 450$ Oe. In general ν decreases with increasing H_y.

vides a general understanding of the cross-over between red shift and blue shift behavior as H_y is increased, even full macrospin modeling gives only an approximate indication of the variation of the agility as a function of the applied field in the non-collinear case. This is attributable to the non-uniform nature of the magnetization of the FL in this field regime that requires micromagnetics to fully model and, if desired, to provide more precise guidance as the field bias that will minimize $N/2\pi$.

4.6 Origin of the largely enhanced $\Gamma_{eff}/2\pi$

In the bottom of Fig. 4.22 we show the result of $T = 0$ micromagnetic modeling of the (idealized) device structure for the case of $H_y = 800$ Oe, for $I = 0$. There is significant variation $\delta\varphi_o \approx 10^o$ in the in-plane orientation of the magnetization across the FL relative to that of the RL (see Fig. 4.21a), which results in approximately a factor of two variation in the spin torque efficiency and hence the critical current density J_c for the onset of ST oscillation between the FL ends and center for $H_y > 700$ Oe (see Fig. 4.21). Because of this spatial variation, as H_y is increased it requires lower values of oscillation amplitude to rotate the magnetization of the end regions to an orientation $\varphi_o \leq 90^o$ relative to that of the RL, at which point the ST at the ends begins to act to *damp* the oscillation while it continues to provide anti-damping excitation to the middle region. The result, as indicated by snap-shots of the FL at various points during one period of oscillation (Fig. 4.18), is that at sufficiently high I, the end regions rotate to or slightly past $\varphi_o \sim 90^o$ and then stop while the middle regions continue to rotate towards the same orientation. For the opposite part of the oscillation cycle the center is first to begin to back move towards the easy axis orientation while the ends lag (see Section 4.6.1 for more details). This "pinning" and "lagging" of the end regions, which becomes stronger for increasing H_y, provides the greatly enhanced dynamic damping ($Idp/dI \rightarrow 0$) that, together with the reduced agility ($\sim$ low $N/2\pi$), lowers or eliminates the non-linearity of the system.

4.6.1 Micromagnetic Simulations

The micromagnetic simulations incorporate the LLGS equation appropriate for a spin valve structure at $T = 0$ with the exchange constant $A = 13 \times 10^{-12}$ J/m, saturation magnetization $M_s = 560\ emu/cm^3$, Gilbert damping parameter $\alpha = 0.01$, spin polarization $P = 0.37$ and the volume discretized into 2.5 nm cubes for computational purposes. Static ($I = 0$) simulations of a spin valve structure are used to determine the initial micromagnetic state of the free and reference layers at the desired hard axis magnetic field. Dynamic ($I \neq 0$) simulations include effects from magnetic interactions between the two layers and the Oersted field due to I. Spin torque is exerted upon both layers, with the local spin polarization of the current incident upon a layer being dependent on the local magnetization vector of the second ferromagnet, *i.e.* the current flow was assumed to be one-dimensional. We treat spins classically and use the simplifying assumption that spins transmit the parallel component and reflect the antiparallel component of the local magnetization perfectly, depending on the direction the electrons traverse.

To gain further understanding of the origins of the enhanced dynamic effective damping and the coherent oscillations in this STNO design, we performed zero T micromagnetic simulations of the idealized elliptical STNO utilizing Eq. 4.14. The simulations include the non-uniform circumferential Oersted field (H_{oe}) generated by the bias current. In general for hard axis biases $H_y = 700 - 1000$ Oe, and for current biases from -3 mA to -5 mA, we consistently obtained quite coherent oscillations of the FL as illustrated for example by Fig. 4.18 for $H_y = 800\ Oe$, $I = -4$ mA. The precession amplitude $\varepsilon \sim 30^o$ is rather close to the estimate obtained from the experimental results (see Section

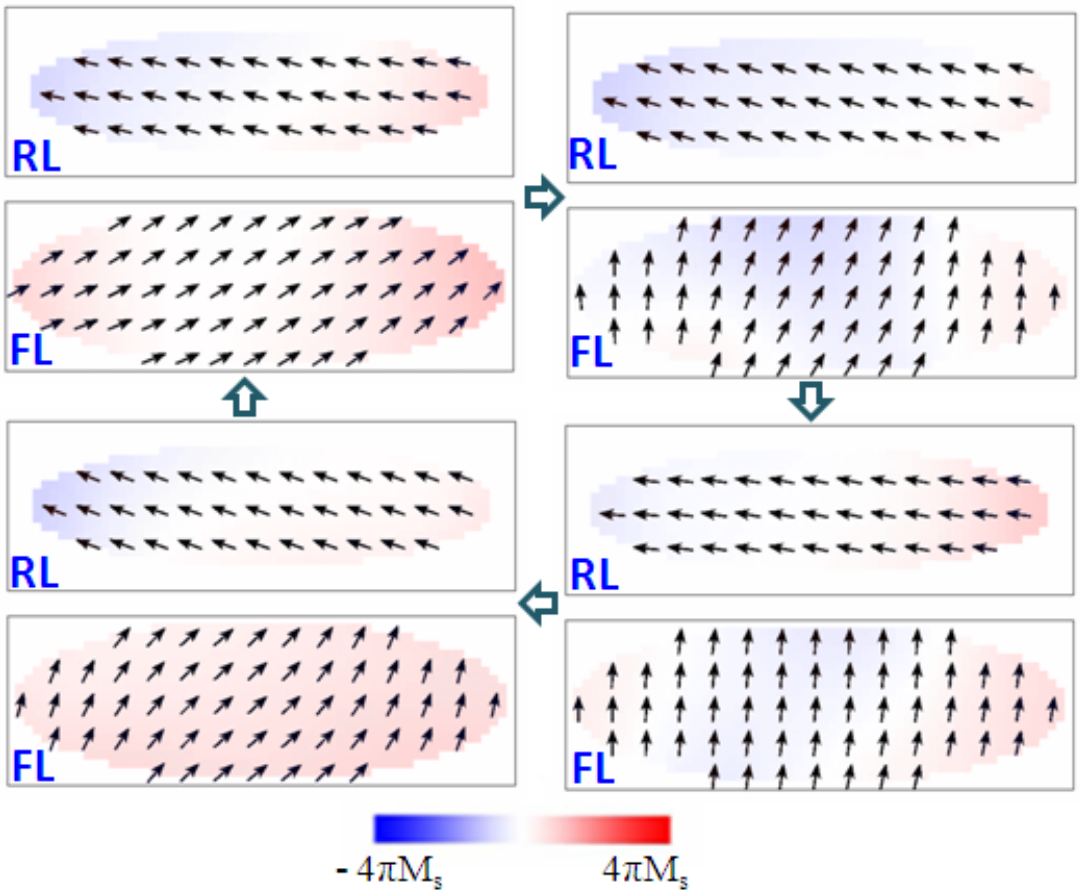

Figure 4.18: Time varying snapshots of the free layer (FL) and reference layer (RL) magnetization during one cycle of the micromagnetic simulated oscillation for $H_y = 800\ Oe, I = -4\ mA$. The ST applied to the center area drives the oscillations while the ST at the edges provides dynamic damping (or lagging) when the local orientation between the FL and RL magnetization is $\leq 90^o$.

4.4.1). While coherent the oscillations are not uniform. This is seen by looking at snap-shots of the FL and RL magnetization during one oscillation cycle, Fig. 4.18, for the case of $H_y = 800$ Oe and $I = -4$ mA. There we see clear differences between the behavior of the FL center area and its end regions. As discussed in the main text this is due first to the variation across the FL of the offset angle φ of the FL magnetization relative to that of the RL above it. In the absence of a ST bias the two FL regions are rotated closer to the hard axis than the center

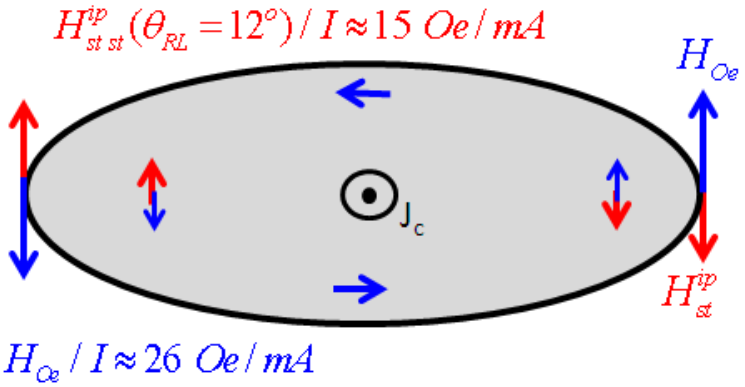

Figure 4.19: Schematic illustration of H_{oe} and H^{ip}_{st} as seen by ends of the FL for the same bias conditions. The estimated $H_{oe}/I \approx 26\ Oe/mA$ is partially cancelled by $H^{ip}_{st}/I \approx 15\ Oe/mA$ in the end regions of the FL. The modeled value of $\theta_{RL} \approx 12^{o}$ as determined by averaging the result of the static micromagnetic simulation over several unit cells of the end of the RL.

region, which increases the critical current density for ST oscillation onset in the end regions. When the ST is applied the end regions remain more rotated towards the hard axis than the center at the ”easy axis” extrema of the oscillation (first panel). As the oscillation proceeds towards the hard axis direction (second panel) the magnetization of the end regions reaches the hard axis direction before the center region. At that point $\varphi \leq 90^{o}$ and the spin torque retards further rotation of the FL magnetization in the end regions while the center region continues to rotate toward the hard axis (panel 2). At this bias level the hard axis extrema of the oscillation occurs when the FL is more or less uniform in the hard axis direction (panel 3). The FL magnetization then moves away from this point in a non-uniform manner with the center region leading and the end regions lagging (panel 4). The simulations also indicate that there is a smaller ST oscillation in the magnetization of the bottom of the RL which is largely concentrated in the end regions and which acts to enhance the ST damping of the FL end regions.

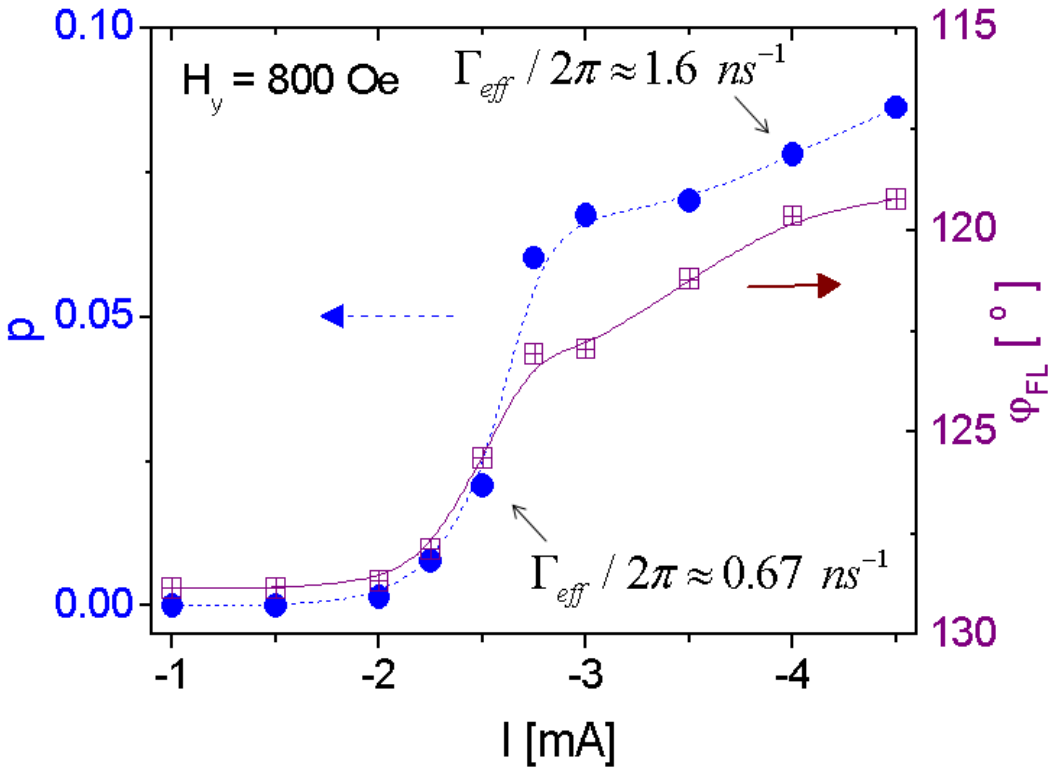

Figure 4.20: (a) Oscillator dimensionless power ($p = sin^2(\varepsilon/2)$), obtained from the micromagnetic simulation (see Fig. 4.18), as a function of I for $H_y = 800Oe$. (b) The precession axis ($< \phi_{FL} >$) from the negative direction of the easy axis ($-\hat{x}$). The ε and $< \phi_{FL} >$ were calculated from the trajectory of $\vec{m}$ on the in-plane as an example is shown in inset of Fig. 4.23a. The p begins to vary weakly after −3 mA, indicating the enhancement of the dynamic damping (Γ_{eff}). The calculated $\Gamma_{eff}/2\pi$, using Eq. 4.9, is 0.67 ns^{-1} at -2.5 mA while 1.6 ns^{-1} at -4.0 mA. This is consistent with the measured p_n in Fig. 4.4 due to the negative feedback from the spin-torque especially on the edge parts. After the onset of the precession, the ϕ_{FL} shifts toward 90^o at which the anti-damping spin-torque efficiencies are cancelled.

The micromagnetic simulations also serve to demonstrate the beneficial effect of the out-of-plane magnetization in the end regions the RL in promoting a more coherent mode of FL oscillation particularly at the higher bias currents. As discussed the in-plane effective ST field $\vec{H}_{st}^{ip}$ that arises from the perpendicular spin current component acts to counter-balance the circumferential Oersted field generated by the bias current in the end regions as illustrated in Fig. 4.19. On the FL along the easy axis, H_{st}^{ip} is clockwise, opposite to H_{oe} and the estimated $H_{oe} \approx 26\ Oe/mA$ for $I = -4$ mA is partially cancelled by $H_{st}^{ip} \approx\ 15 Oe/mA$ assuming $\theta_{RL} \approx 12^o$ as determined by averaging the modeled RL magnetization over several end region cells. We established the importance of this counterbalancing by carrying out simulations where the Oersted field was not included. This resulted in the oscillation becoming much less coherent at high current biases due to the substantially different effective fields at the two ends of the FL. Since H_{st}^{ip} depends on the local out-of-plane orientation of the RL magnetization θ_{RL} , the current polarization P, and the angular dependence of the spin torque function $g(\varphi)$ an even closer balance of the Oersted and ST fields might be achievable with careful tuning of the device geometry (taper) and choice of material.

There is an additional feature of this particular STNO structure that further aids in the achievement of highly coherent quasi-uniform oscillations. This is the significant out-of-plane magnetization component at the bottom of the RL which results in the spin current incident on the FL having an orthogonal, out-of-plane component that exerts an effective magnetic field, $\vec{H}_{st}^{ip} \sim \vec{m} \times \vec{p} sin(\theta_{RL})$ in the end regions (see Section 4.6.2 for details), where $\vec{p}$ is the spin-polarization of the RL and θ_{RL} is the out-of-plane angle of that polarization (see Fig. 4.22). This $\vec{H}_{st}^{ip}$ acts to rotate the in-plane FL magnetization in a clock-wise manner, opposite to the counter-clock rotation that the Oersted field (H_{Oe}) from the bias

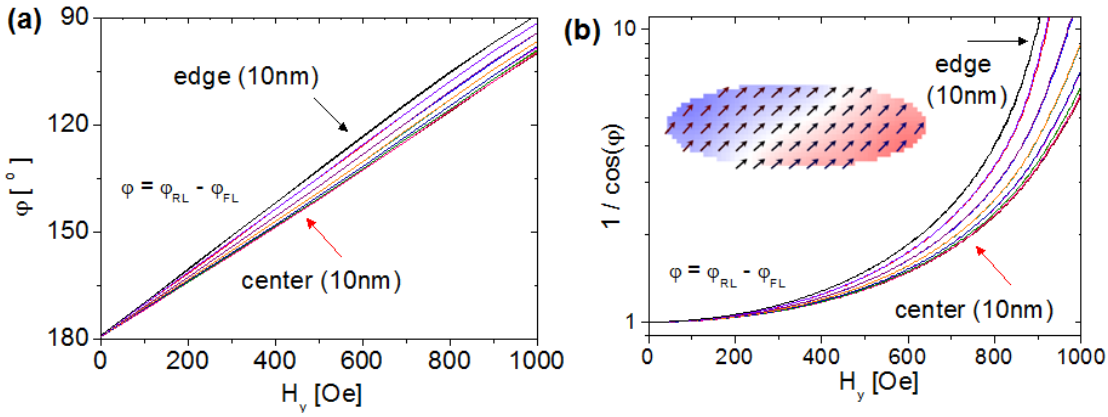

Figure 4.21: Variation of φ and $1/cos(\varphi)$ ($\sim J_c$) along the easy axis of the FL where φ is the in-plane offset angle between the FL and RL magnetization as determined by micromagnetics calculations.

current promotes (see Fig. 4.19). The substantial balancing of the non-uniform H_{Oe} by H_{st}^{ip} results in more symmetric behavior at the two ends of the FL and in quasi-uniform oscillations despite the spatially varying ST and non-uniform fields (see Section 4.6.1 for details).

4.6.2 Effect of spin-polarization direction on the critical current (I_c) and p in the macrospin approximation

Our STNO has a low non-linearity ν ($= N/\Gamma_{eff}$) in large part due to a strong enhancement of $\Gamma_{eff}/2\pi$, or equivalently a substantial reduction of ST efficiency ($\propto Idp/dI$). This is the result of a significant spatial variation in the orientations of the magnetization of both the FL and the RL in the field bias regime where a coherent single mode oscillation is obtained (see Section 4.6.1). To gain insight into how different orientations of the FL magnetization and of the incident spin

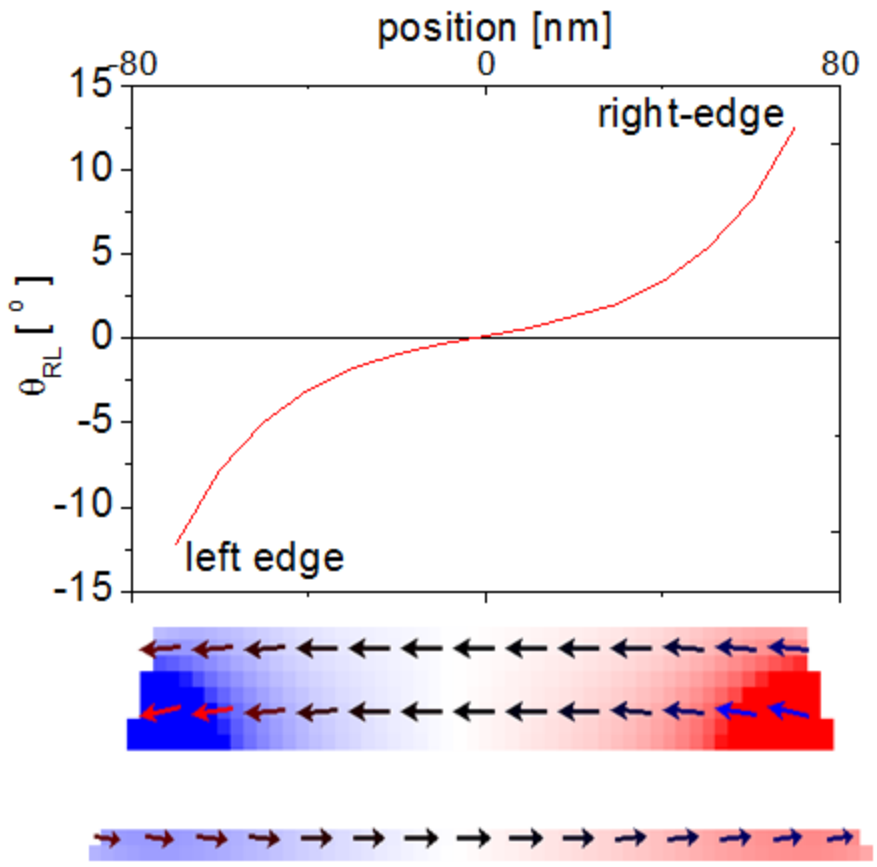

Figure 4.22: Top: Out-of-plane orientation angle (θ_{RL}) of the RL magnetization as a function of the position along its elongated (easy) axis, as determined by micromagnetic calculations for H_y = 800 Oe. Bottom: the micromagnetic configuration of the STNO (top view of the FL and side view), for H_y = 800 Oe.

polarization, which is determined by the local RL magnetization, affect the local spin torque efficiency we have performed zero temperature ($T = 0$) macrospin modeling for different rigid domain orientations, in addition to the micromagnetic simulations discussed below in Section 4.6.1. The macrospin modeling utilized the LLGS equation [17, 14, 15, 153]:

$$\frac{d\hat{m}}{dt} = -\gamma \hat{m} \times \vec{H}_{eff} + \alpha_G \hat{m} \times \frac{d\hat{m}}{dt} + \gamma a_J(\theta) \hat{m} \times \hat{p} \times \hat{m} \tag{4.14}$$

where $a_J(\theta) = \frac{\hbar}{2e}\frac{I}{M_s V}Pg(\theta)$ and $\vec{H}_{eff} = (H_k m_x + H_d)\vec{x} + H_y\vec{y} - 4\pi M_s m_z\vec{z}$. Here γ is the gyromagnetic ratio, $\vec{m} = (m_x, m_y, m_z)$ is the unit vector of the FL, H_k is the anisotropy field of the FL along the easy axis, H_d is the dipole field from the RL, H_y is the externally applied hard axis magnetic field, $g(\theta) = 1/2$, and the spin-polarization $P = 0.37$. With Eq. 4.14 we obtained $\hat{m}(t)$ and from this time dependence of the rigid FL moment we determined its precessional axis (φ_{FL} and θ_{FL}) and $p = sin^2(\varepsilon/2)$ as functions of I, H_y and H_d for $H_k = 450\ Oe$, where φ_{FL} is the in-plane orientation of the FL as measured from $-\hat{x}$, θ_{FL} is its out-of-plane tilt angle and ε is the maximum in-plane precessional excursion angle (see Fig. 4.23a). The simulations were run for different out-of-plane orientations of the incident spin polarized current $\hat{p}$. The current for the onset of oscillation (I_c) was extracted from $p(I)$ for each set of field values (H_d and H_y) (e.g. see Fig. 4.23b for the case H_d = 100 Oe, and $\hat{p} = (-1, 0, 0)$).

In a strongly non-collinear configuration such as our STNO, τ_{st} has two significant components; the anti-damping effect from $\vec{p}_\parallel$ and a magnetic field effect from $\vec{p}_\perp$, where $\vec{p}_\perp$ ($\vec{p}_\parallel$) is the orthogonal (parallel) component of $\hat{p}$ to $\hat{m}$ (i.e. $\hat{p} = \vec{p}_\parallel + \vec{p}_\perp$). The anti-damping spin torque $\tau_{st}(\vec{p}_\parallel) \propto \hat{m} \times \vec{p}_\parallel \times \hat{m}$ counters the damping torque τ_d to excite the FL oscillations once the onset current I_c is reached. Since $\tau_{st} \propto cos\varphi_{FL}$ this results in $I_c = I_{c0}/\ |\ cos\varphi_{FL}\ |$ as employed in Fig. 4.8 and as illustrated in Fig. 4.23b an increasing I_c with increasing H_y .

The spin torque effective field $\vec{H}_{st} \propto \hat{m} \times \hat{p}_\perp$ becomes an important factor when the incident spin current has a substantial out-of-plane polarization component, $\hat{p} = (-cos\theta_{RL}, 0, sin\theta_{RL})$. In that case there can be a significant in-plane $\vec{H}_{st}^{ip}$ that alters φ_{FL}, in a manner dependent on the sign of θ_{RL}. For $\theta_{RL} < 0^o$ $\vec{H}_{st}^{ip}$ acts to decrease φ_{FL} (rotate the FL moment towards the hard axis). Thus a $-\hat{z}$

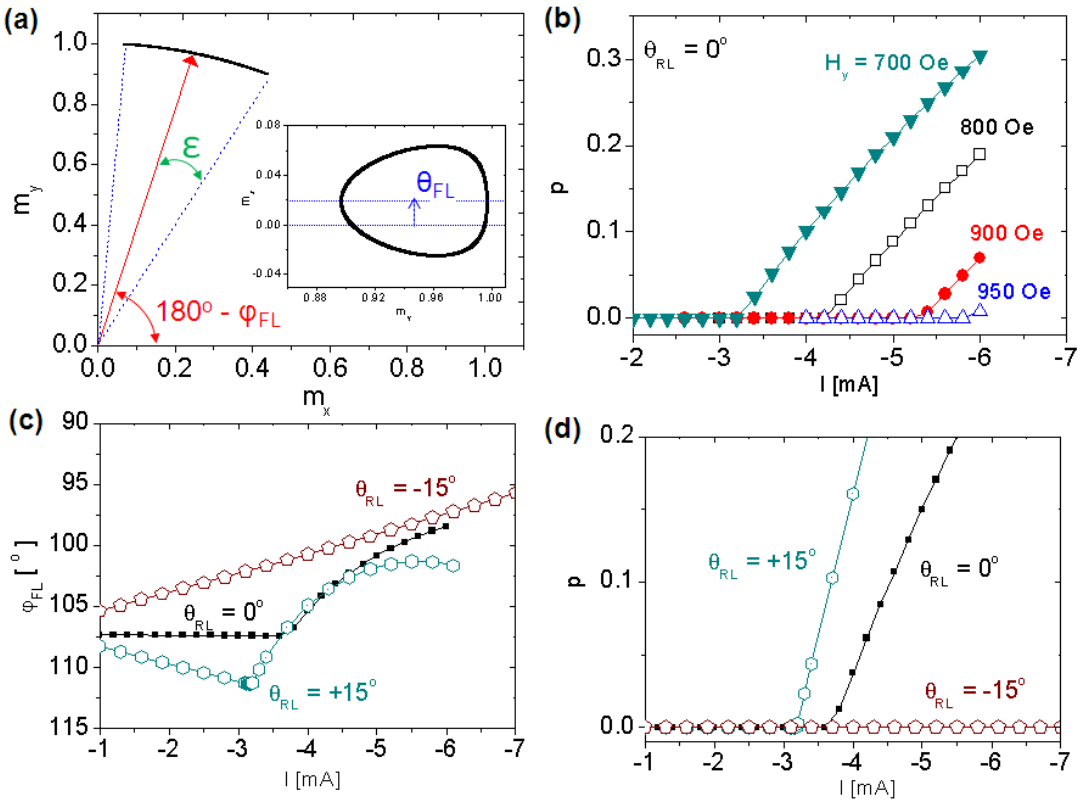

Figure 4.23: Results of macrospin-simulation for the cases where, (a) and (b), the incident spin polarization direction $\hat{p}$ is along the easy-axis (i.e. $\hat{p} = (-1, 0, 0)$) and (c) and (d) $\hat{p}$ is tilted somewhat out-of-plane (i.e.$\hat{p} = (-cos\theta_{RL}, 0, sin\theta_{RL})$): (a) The in-plane (m_x, m_y) trajectory and the out-of-plane (m_y, m_z) trajectory (inset) of the magnetic moment, the precessional axis $(\varphi_{FL}, \theta_{FL})$ and precession amplitude (ε) for $H_y = 800$ Oe, $H_d = 100$ Oe, $I = -4.25$ mA. (b) The normalized power $(p = sin^2(\varepsilon/2))$ as a function of I for $H_y = 800\ Oe, H_d = 100\ Oe, H_k = 450\ Oe$. (c) Free layer moment orientation angle φ_{FL} and (d) normalized oscillation power p as functions of I and θ_{RL} for $H_k = 450\ Oe, H_d = 100\ Oe$ and $H_y = 750\ Oe$. For $\theta_{RL} = -15^o$ the ST cannot induce dynamics at any bias current due to the effect of the current dependent in-plane spin torque field H_{st}^{ip} in shifting φ_{FL} towards 90^o.

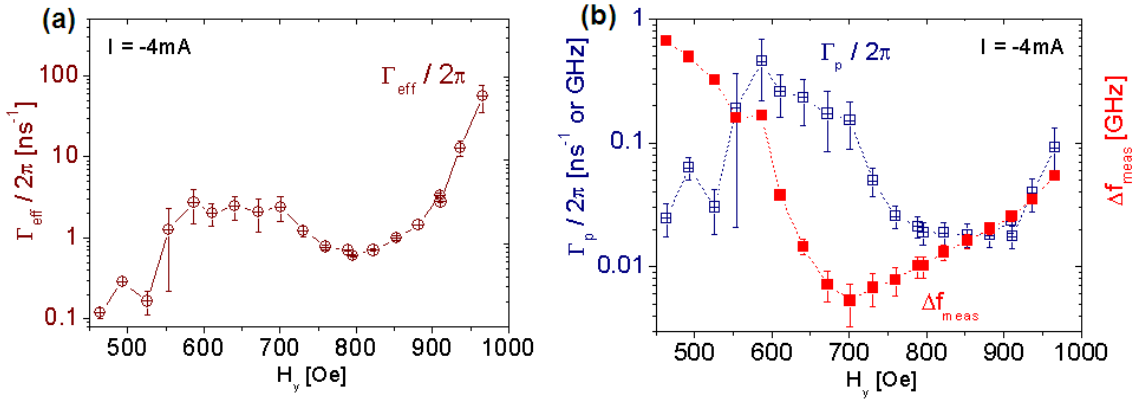

Figure 4.24: (a) Effective damping parameter $\Gamma_{eff}/2\pi$ of the STNO as determined from the experimental data using Eq. 4.3 as a function of H_y, for $I = -4$ mA. (b) Dynamic damping or power restoration rate $\Gamma_p/2\pi = p\ \Gamma_{eff}/2\pi$ is plotted and compared to Δf_{meas}.

out-of-plane spin polarization acts to increase the onset current I_c and, if sufficiently strong can completely suppress the onset of ST oscillation as in the -15^o case illustrated in Fig. 4.23c and d. For a $+\hat{z}$ out-of-plane spin current polarization component the resultant $\vec{H}_{st}^{ip}$ acts to rotate the FL towards its easy axis, decreasing I_c ($+\theta_{RL}$) below the I_c ($\theta_{RL} = 0^o$) case, as also illustrated in Fig. 4.23. Note that in this non-collinear configuration above the onset of oscillation φ_{FL} in general increases as the precession axis changes due to the non-parabolic nature of the energy potential in this non-collinear configuration, but with that change modified by the effect of $\vec{H}_{st}^{ip}$.

4.7 Experimental nonlinear effective damping ($\Gamma_{eff}/2\pi$)

In Fig. 4.24a we plot experimental $\Gamma_{eff}/2\pi(H_y)$ for $I_{dc} = -4$ mA, using Eq. 4.3. For 600 Oe $\leq H_y \leq$ 750 Oe, $I_{dc} = -4$ mA places the STNO in the quasi-saturated power regime and we have $\Gamma_{eff}/2\pi \approx 1 - 3\ ns^{-1}$, much higher than $\Gamma_o/2\pi \approx$

0.1 ns^{-1}. For 750 Oe $\leq H_y \leq$ 850 Oe p_n is in the regime where for $I_{dc} = -4$ mA it varies quasi-linearly with I and dp/dI is approximately constant yielding $\Gamma_{eff}/2\pi \approx 0.8-1.5\ ns^{-1}$, but now the small agility $N/2\pi$ due to the close balance of the red and blue shift effects ($|N/2\pi| < 0.5$ GHz) (Fig. 4.12) again result in a small non-linearity (ν). For $H_y > 850$ Oe, $\Gamma_{eff}/2\pi$ grows even larger as dp/dI decreases rapidly due to the rapidly diminishing ST efficiency and enhanced damping of the left end region of the FL, as discussed above.

4.8 Experimental power restoration rate ($\Gamma_p/2\pi$)

Fig. 4.24b also shows the power restoration rate $\Gamma_p \equiv p\ \Gamma_{eff}$ that characterizes the dynamic damping of a STNO [122]. For 600 Oe $< H_y <$ 850 Oe, $\Gamma_p/2\pi$ ranges from 0.3 ns^{-1} to 0.02 ns^{-1}. This rapid relaxation of power fluctuations is the result of the very strong $\Gamma_{eff}/2\pi$ in our device configuration despite its relatively low power p. Above 900 Oe, $\Gamma_p/2\pi$ increases still further despite the rapid decrease in p due to the very strong enhancement in $\Gamma_{eff}/2\pi$ ($dp/dI \rightarrow 0$) as φ_o approaches 90^o, indicating that here deviations in oscillator amplitude very quickly stabilize to the mean precession orbit, as previously implied with micromagnetic simulations [170]. We also plot the oscillator linewidth Δf_{meas} in Fig. 4.24b for comparison to $\Gamma_p/2\pi$. Note that above 850 Oe the two are comparable which explains why in this field regime Δf_{meas}, while increasing rapidly due to the decreasing p, becomes progressively less than predicted by the nonlinear theory [122] (see Fig. 4.10) since the derivation of the renormalization factor $(1 + \nu^2)$ requires $\Delta f << \Gamma_p/2\pi$.

4.9 Conclusion

These results demonstrate that spin currents if applied in an effective non-uniform manner can be utilized not only to excite magnetic oscillations by an anti-damping effect, but also to provide a non-linear effective damping that restricts power excursions and thus reduce if not fully eliminate the non-linear coupling between amplitude and phase fluctuations that limit the phase stability of conventional STNOs with uniform excitation currents. The STNO is still frequency agile to a useful degree since the ST results in a moderate Idf/dI ($\gg \Delta f$) even where $|\nu| \leq 1$. In the implementation of this basic approach discussed here the maximum normalized power is relatively low, $p \leq 0.08$, in the quasi-linear regime. This helps ensure that the oscillating FL does not have sufficient energy to break up into multiple modes in the presence of the spatially non-uniform anti-damping and damping spin torques, but it also limits the minimum attainable linewidth, $\Delta f \propto 1/p$. If refinements to the design can be made that will result in a quasi-linear STNO that can reach higher normalized power levels, $p > 0.1$, before being saturated by the non-linear damping, room temperature nanoscale oscillators with linewidths < 1 MHz should be possible. This would be a considerable advance in the development of STNO's, particularly if this can be achieved in a higher impedance device that operates successfully without the requirement of an externally applied magnetic field.

4.10 Appendix: Discussion about current shunting to Si-substrate

The capacitance shunting in nanoscale devices has been a problem at high operation frequency due to the leakage current through the surrounding insulator. Without considering this we may underestimate the generated power from the spin-torque oscillator, overestimate the pulsed current amplitude for the ultrafast switching, or miss the phase-shift in the time-domain or ferromangetic resonance measurement. In this section we discuss about the shunting effect in our device geometry and will estimate how much the power was lost for our spin-torque oscillator case. We can think that there are three possible effective capacitance in our device side as shown in Fig. 4.25a.

The first capacitance (C_1) results from the overlapping area ($< (20\mu m)^2$) between the top-lead and the bottom-lead. We estimate $C_1 < \varepsilon_r \varepsilon_o \frac{A}{d} = 4 \times (8.9 \times 10^{-12} F/m) \times \frac{20\mu m \times 20\mu m}{100\ nm} = 1.4 \times 10^{-13} F$ with a typical height of our nanopillar > 100 nm and $\varepsilon_r \approx 4$ for SiO_x that has been used for insulating between them. This C_1 can be ignored for a spin-valve device because we simply expect the cut-off frequency (f_c) $\sim \frac{1}{2\pi RC} = \frac{1}{2\pi \times 25\Omega \times 1.4 \times 10^{-4}} GHz > 45\ GHz$ is much higher than an usual device characterisitic frequency (< 10 GHz) where we assume $R \sim 25\ \Omega$. We also expect that leakage current through this channel should be small because the effective impedance from the C_1, $X(C_1) > \frac{1}{2\pi \times 6GHz \times 1.4 \times 10^{-4} F} = 190\ \Omega$, is much larger than the device resistance (25 Ω) for example at 6 GHz. However it cannot be neglectable for a magnetic tunnel junction because the f_c could be lower than 1 GHz or the high-device resistance ($R > 1\ k\Omega$) is bigger than the estimated $X(C_1)$.

The second capacitance (C_2) is from the device itself when the STNO has an

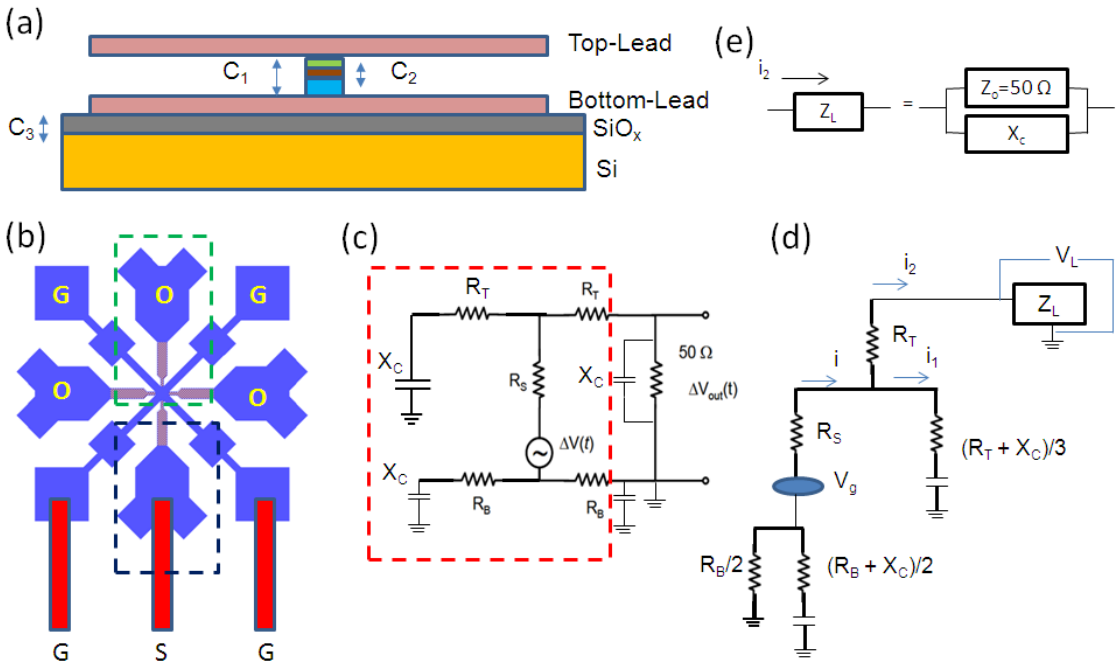

Figure 4.25: Power-loss due to the current-leakage to Si-substrate. (a) Possible effective capacitances in our STNO devices. (b) Device geometry including contact pads and leads. The STNO is located and embedded at the center. (c) and (d) Equivalent circuit of the STNO side with the resistances and capacitances from the leads and contact pads. (e) Equivalent circuit of the load resistance side.

insulating layer between the electrodes. For a typical MgO-MTJ ($\varepsilon_r = 10$ for MgO) we expect $C_2 \approx 10 \times (8.9 \times 10^{-12} F/m) \times \frac{100\ nm \times 100\ nm}{1\ nm} = 9 \times 10^{-16}\ F$ if we have 1 nm thickness of MgO layer, $(100\ nm)^2$ of junction area and $\varepsilon_r = 10$ for MgO. This is much lower than C_1 so we can ignore it.

The last capacitance (C_3) is from the area between the bottom&top pads and the semi-conducting Si-substrate. We have used thermally oxidized Si substrate because it is relatively cheap and the nanofabrication process has been quite reliable in our group. However it turned out that there is a considerable leakage current (or signal loss) to this capacitance channel even at sub 10 GHz since the

Si-substrate is metallic ($\rho = 1 - 10\ \Omega cm$) at room tempearture, our contact pads are relatively large (Area $\sim$ 9200 μm^2 per each contact pad) and the thickness of oxidized-Si is relatively thin ($\sim$ 500 nm). Simply we estimate the effective capacitance (C) of each pad is $C = 4\times(8.9\times10^{-12}F/m)\times\frac{9200\ \mu m^2}{500\ nm} = 6.6\times10^{-13}F$, or the effective impedance (X_c) at $f = 6$ GHz is $X_c = \frac{1}{2\pi\times6\ GHz\times6.6\times10^{-4}F} = 40\ \Omega$, which is comparable to the spin-valve device resistance (25 Ω). Hence we cannot ignore the signal loss or current leakage to the substrate through the contact pads at room temperature.

Fig. 4.25c-d shows the equivalent circuit with the resistances and capacicances from the leads and contact pads, taking into account for the multiple paths of the top-lead and the bottom-lead and for the short of the bottom pads to the ground. In the circuit the capacitances are located outside from the center (nanopillar device) because the resistances of the top-lead and bottom lead are mostly contributed from the narrow channel while the capactiances are from the contact pads that have larger area. From the circuit theory we have

$$(1)\ V_L = i_2 Z_L \quad (2)\ i = i_1 + i_2 \quad (3)\ i_2(R_T + Z_L) = i_1(R_T + X_C)/3$$

$$(4)\ V_g = i_2(R_T + Z_L) + i\left(R_S + \frac{1}{\frac{2}{R_B} + \frac{2}{R_B + X_C}}\right)$$

where V_g is the voltage generated from the spin-torque oscillator, R_s is the spin-valve device resistance, $R_B(R_T)$ is the resistance of each bottom(top) lead, X_c is the effective capacitance of each lead, Z_L is the load resistance, $\frac{1}{Z_L} = \frac{1}{Z_o} + \frac{1}{X_c}$, V_L is the voltage across the load-resistance and Z_o is the resistance of spectrum analyzer (50 Ω). Solving these equations, we obtain the voltage across the load resistance, $\frac{V_L}{Z_L} = \frac{V_g}{\beta}$ where $\beta = \left[(R_T + Z_L) + \left[1 + \frac{3(R_T+Z_L)}{R_T+X_C}\right](R_S + \frac{1}{\frac{2}{R_B}+\frac{2}{R_B+X_C}})\right]$, and the delivered power to the spectrum analyzer (P_{SA}) is $P_{SA} = \frac{1}{2}Re\{V_o i_o^*\} = \frac{1}{2}\frac{|V_L|^2}{Z_o} = \frac{1}{2}\frac{|V_L|^2}{|Z_L|^2}\frac{|Z_L|^2}{Z_o} = \frac{1}{2}V_g^2\frac{1}{|\beta|^2}\frac{|Z_L|^2}{Z_o}$. We check the validity of the solution: (1) for X_c− > infinity, Z_L− > Z_o,

$\beta -> [R_S + \frac{R_B}{2} + R_T + Z_o]$ and $P_o -> \frac{V_g^2}{2}\frac{Z_o}{[R_s+R_B/2+R_T+Z_o]^2}$ which is the expression we already used it, (2) for $X_c -> 0$, $Z_L -> X_c$, $\beta -> finite$, then $P_o -> X_c^2/Z_o -> 0$ (no delivery to the spectrum analyzer). When applying for our spin-valve device where $Z_o = 50\ \Omega, R_S = 10.5\ \Omega, R_T = 11.5\ \Omega, 2R_B = 10\ \Omega, X_C = -i40\ \Omega$ (at 6 GHz), we have $\frac{P_{SA}(X_c=-i40\Omega)}{P_{SA}(X_c->\infty)} \approx 0.4$. The result indicates that we underestimated ~ 60 % of the generated power from our STNO device at $f = 6$ GHz, and should consider the factor (~ 2.5 times) in the measured power.

The current shuntting through the Si-substrate should be much weaker at Liquid He temperature ($<$ 10 K) because the carriers in the substrate will be freezed out. This has been implied in our ultrafast switching data. In Section 3.9, we observed that the switching current amplitudes with 100 ps pulse width were lower at $\sim$ 10 K than the ones at $\sim$ 300 K, possibly due to the less current leakage at lower temperature. At the beginning we guessed that the spin-polarization of the out-of-plane polarizer could be enhanced at lower tempearture, but it could be balanced out with the increase of anisotropy field (H_k). Similar above analysis, we surmised that a facor of 2 or 3 times was over-estimated in the current amplitude in the 50 ps pulsed switching data, and this could explain why Junbo Park observed much lower switching current amplitudes at low temperature ($<$ 10 K). We should re-design the device geometry for miniming the capacitance coupling at the high-frequency regime at room tempearture by (1) using an highly insulating substrate, (2) minimizing overlapping area between the top-lead and the bottom-lead, and (3) minimizing un-necessary contact-pads and leads.

CHAPTER 5

A SPIN-TORQUE NANO-OSCILLATOR EXCITED BY A COMBINED OUT-OF-PLANE AND IN-PLANE SPIN POLARIZED CURRENT

5.1 A spin-torque nano-oscillator excited by a combined out-of-plane and in-plane spin polarized current

In this section I present a relatively coherent spin-torque nano-oscillator (STNO) with spectral linewidths ≤ 10 MHz, based on a nanopillar spin-valve device in which an in-plane magnetic free layer (FL) is excited by a combined out-of-plane and in-plane spin polarized current under external magnetic field biases approximately cancelling the average in-plane dipolar field. The STNO exhibits an enhancement of nonlinear effective damping (Γ_{eff}) in the coherent regime, resulted from the torque competition from the two spin polarizers and the spatial variation of the anti-damping effectiveness. This efficiently reduces the nonlinear coupling (ν) between the amplitude and phase fluctuations.

5.1.1 Introduction

Spin transfer torque (τ_{st}) [14, 15, 17] exerted by a spin-polarized dc current (I) can excite steady-state magnetic precessions [107, 33] in magnetic nanostructures around the effective magnetic field when the τ_{st} is strong enough to compensate for dissipative damping torque (τ_d), thereby generating electrical microwave signals via magnetoresistance (MR) effect. This auto-oscillation phenomenon is a promising approach for on-chip, current-tunable microwave os-

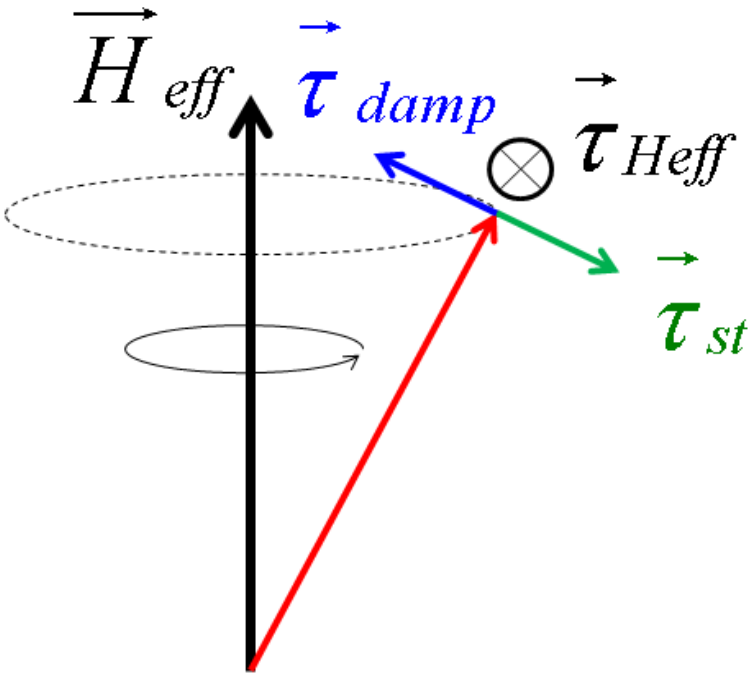

Figure 5.1: Concept of Spin-Torque Nano-Oscillator (STNO). In a STNO a spin-polarized current (I) excites persistent magnetic precession around the effective magnetic field (H_{eff}) at microwave frequencies when the anti-damping spin torque (τ_{st}) is sufficient to compensate for the magnetic damping torque (τ_{damp}).

cillators in a nano-scale device structure. For practical applications, of course, a STNO must exhibit a considerable microwave output power (P), and a narrow spectral linewidth (Δf), preferably at room temperature, and preferably without requiring an external magnetic field bias.

The spectral linewidth (Δf) of such auto-oscillations is the reciprocal measure of their precession phase stability. Several intrinsic sources of Δf-broadening have been extensively investigated in order to identify, eventually for more coherent oscillation in STNOs, such as Langevin fields, mode-mode interactions or inherent chaotic motions. In the meanwhile the nonlinear auto-oscillator (NLAO) model [46, 122] suggested that the Δf of a single mode STNO

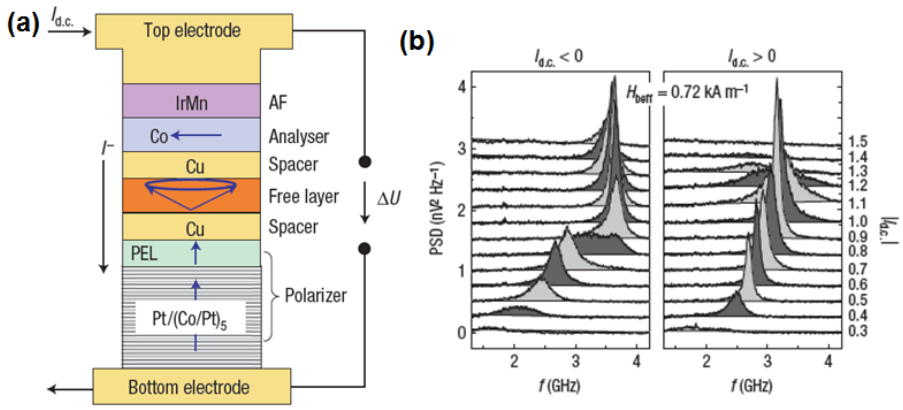

Figure 5.2: (a) Illustration of STNO excited only by an out-of-plane spin-torque. (b) The out-of-plane precession is characterized by the increase of oscillation frequency with the dc current amplitude. From Ref. [114].

can be enhanced due to the intrinsic nonlinearity (ν), and described with

$$\Delta f = \frac{\Gamma_o}{2\pi}\left(\frac{k_B T}{E}\right)(1+\nu^2) = \left(\frac{\gamma^3 \alpha_G M_s k_B T}{2\pi V}\right)\cdot\left(\frac{1+\nu^2}{f^2 p}\right) \tag{5.1}$$

Here $E \approx \frac{2\pi V f^2}{\gamma^2} p$ is the time averaged energy of the oscillator for an in-plane magnetic precession (see Section 4.1.3 for the derivation), $\Gamma_o = \alpha_G \cdot \gamma \cdot 2\pi M_s$, M_s is the saturation magnetization of the FL, α_G is the Gilbert damping parameter, γ is the electron gyromagnetic ratio, k_B is the Boltzmann constant, T is the temperature, V is the FL volume, f is the oscillation frequency and p is the dimensionless power that represents the precession amplitude of the FL. The Δf decreases as the magnetic energy (E or p) increases, as expected from the general oscillator theory, until it breaks a single mode excitation. The parameter ν of a STNO indicates how the amplitude fluctuations additionally renormalize the thermally-driven phase noise, and is generally given by $\nu \equiv N/\Gamma_{eff}$ where

$$\frac{\Gamma_{eff}}{2\pi} = \left(\frac{\Gamma_o}{2\pi}\right)\left(I\frac{dp}{dI}\right)^{-1} \quad \text{and} \quad \frac{N}{2\pi} = \left(\frac{df}{dp}\right), \quad \text{then} \quad \nu = \left(\frac{2\pi}{\Gamma_o}\right)\left(I\frac{df}{dI}\right) \tag{5.2}$$

In the previous chapter we reported a *quasi-linear* STNO [171] exhibiting single mode excitations and low agilities of f and p w.r.t. I. The STNO was based

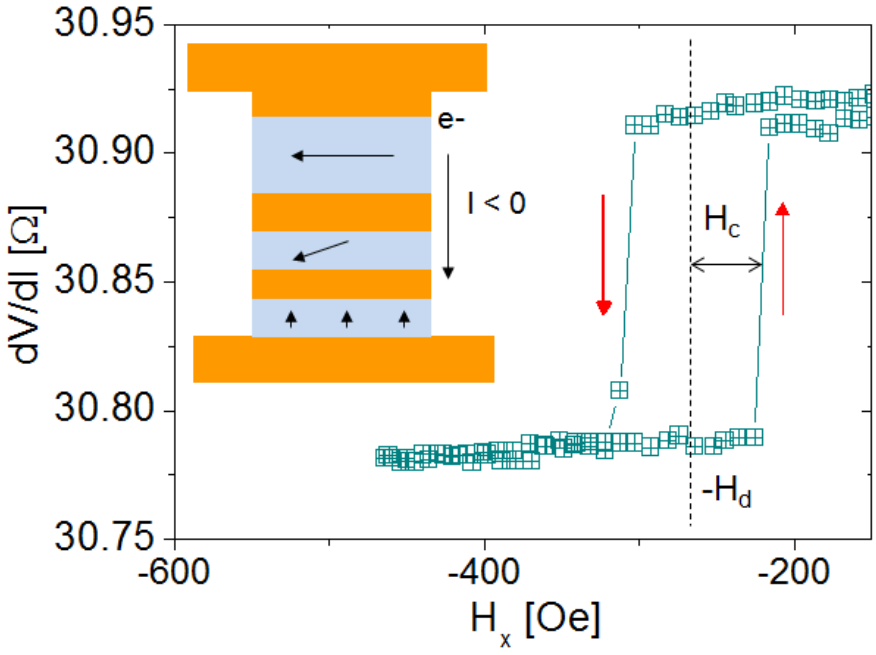

Figure 5.3: Minor-loop of the representative device (Device #1). Inset: Device structure of the STNO. The spin-torque onto the FL has two components from the two polarizers: the out-of-plane spin polarizer (OPP) located at the bottom of the FL and the in-plane spin-polarizer (IPP) located above the FL.

on a highly shape anisotropic Py/Cu/Py nanopillar spin-valve under external hard axis magnetic fields (H_y's) that changed the precessional axis (φ_a) of the FL and its offset angle (φ_o) from the reference layer (RL). The STNO achieved a $N/2\pi \sim 0$ with certain H_y's that shifted the φ_a of FL close to a position where the p-dependent red-shift due to the demagnetization effect is balanced out with the p-dependent blue-shift from the anisotropy effect. Moreover the nonlinear effective damping ($\Gamma_{eff}/2\pi$) was hugely enhanced at the H_y's due to the spatial variation of ST efficiencies together with the utilization of the fact that the anti-damping effectiveness of the τ_{st} becomes less efficient as the φ_o approaches orthogonal to the RL. The combination of those effects, low $N/2\pi$ and high $\Gamma_{eff}/2\pi$,

resulted in effectively reducing $|\nu|$ (< 1) in broad ranges of biases, and making the measured Δf very close to the predicted Δf by Eq. 5.1 at the optimum biases.

In this chapter we report a STNO driven by two spin polarizers: an out-of-plane polarizer (OPP) and an in-plane polarizer (IPP), as the device scheme is shown in the inset of Fig. 5.3. In this configuration the τ_{st} from the IPP (τ_{ip}) accelerates or retards the excitation of the FL by the τ_{st} from the OPP (τ_{op}) depending on the initial FL state and current polarity while this device structure was demonstrated to have advantages in the switching speeds [99, 149, 100, 101, 102, 172]. The STNO device exhibits coherent oscillations ($\Delta f \leq 10$ MHz) at around field biases that effectively cancel the average in-plane component of the dipolar field (see Fig.5.3). The device also has a very low p variation ($dp/dI \approx 0$) in the coherent regime while f is still tunable ($df/dI \sim 20\ MHz/mA$): i.e. a large Γ_{eff} (and Γ_p) and a finite ν in the frame of NLAO. The greatly enhanced $\Gamma_{eff}/2\pi$ results from the spatial dependent interaction between the two spin torques in which the τ_{ip} accelerates or retards the excitation of the FL while the τ_{op} rotates the FL.

5.1.2 Device Information

The all-metallic nanopillar device structure we employed in this chapter has been described elsewhere [149]. The device has an elliptical cross-section area of $\sim 60 \times 140\ nm^2$ at the bottom of nanopillar. The OPP (based on Co/Pt multilayers) lies beneath the FL (5 nm of Py) and a simple, single-layer IPP (20 nm of Py) lies above, with the latter designed to exert a strong τ_{st} on the FL, not just to monitor its dynamics via MR. The negative current bias ($I < 0$) is defined when

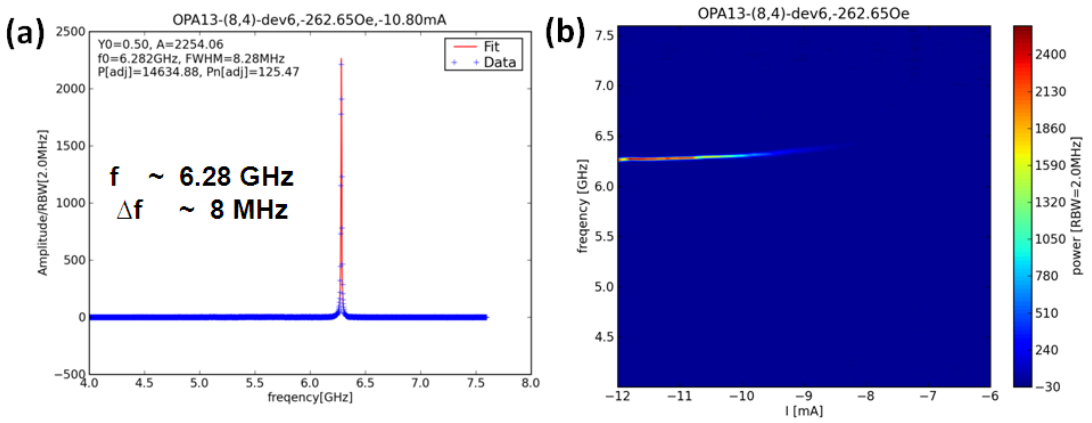

Figure 5.4: (a) Measured power spectral densities (PSD's) from the device #1 for $I = -10.8$ mA and $H_x = -262$ Oe (at the center of the minor loop, see Fig. 5.3a). (b) Contour plot of the measured PSD from the device as a function of I for $H = -262$ Oe. The device exhibited very coherent oscillations with $\Delta f \sim 8$ MHz at around the current and field biases.

electrons flow from the IPP to the FL (and to the OPP) in that the parallel (P) between the FL and the IPP is preferable with the current polarity while the τ_{op} rotates the FL counterclockwise. In this chapter we will report results from two particular devices while general behaviors were quite similar in six devices with some variations in the f and Δf, due to the variations in the shape anisotropy (± 5 *nm*) which is crucial for the dynamics generated by τ_{op}.

5.1.3 Measured Data

We determined f and Δf from Lorentzian fits to the measured power spectral densities (PSD's) of the STNO device under applied in-plane fields (H_x's) around the bias that cancels the average in-plane component of dipolar fields (~ 265 Oe) from the two polarizers, or at around the center of the minor loop (see Fig.5.3). We observed that, when a strong negative I (~ -11 mA) was ap-

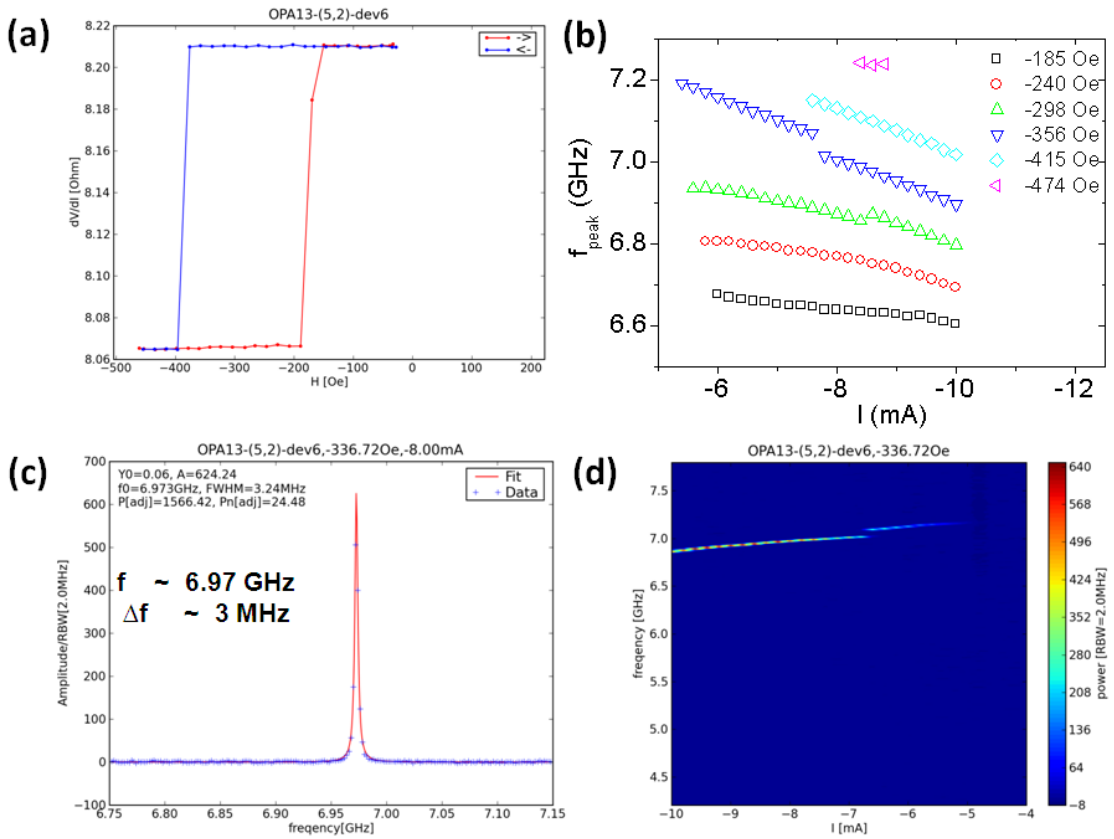

Figure 5.5: (a) Minor-loop of the second representative device (device#2) (b) Measured peak frequency (f) as functions of I and H_x (c) Measured power spectral densities (PSD's) from the device for $I = -8.0$ mA and $H_x = -337$ Oe (at the center of the minor loop, see Fig. 5.3a). We observed relatively very coherent oscillations with $\Delta f \sim 3$ MHz at around the current and field biases. (d) Contour plot of the measured PSD from the device as a function of I for $H_x = -337$ Oe.

plied, relatively coherent oscillations, at bias dependent f's in the 6 to 7 GHz range, with Δf's ≤ 10 MHz. Fig. 5.6 shows the measured peak-f as functions of H_x and I, in that the f exhibits a weak red-shift with $|I|$, $df/d|I| \sim 20-60\ MHz/mA$, but a blue shift with $|H_x|$, $df/d|H_x| \sim 1-4$ MHz/Oe. Such f-dependence on the $|H_x|$ and $|I|$ indicated that the oscillations had the characteristics of the in-plane precession, different to the previous experiment (see Fig. 5.2) and simulations

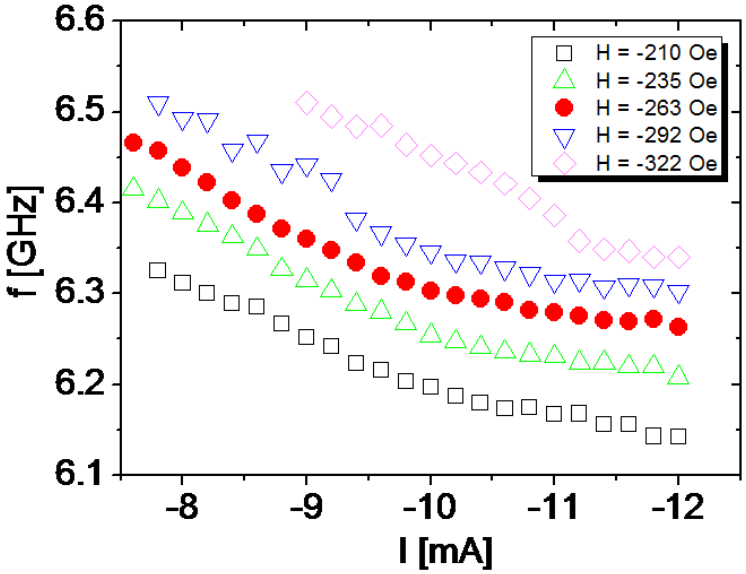

Figure 5.6: Oscillation peak frequency of the device #1 as functions of I and H_x. The f-dependence on the $|H_x|$ and $|I|$ indicates that the oscillation has the characteristics of the in-plane precession: red-shift with $|I|$ and blue-shift with $|H_x|$. This is different to the out-of-plane precession (blue-shift with $|I|$) excited by only τ_{op} (without τ_{ip}).

[147, 114, 173] reported that by only τ_{op} (without τ_{ip}) the precession was characterized by the out-of-plane precession in which the f increases with $|I|$.

Fig. 5.7 shows Δf and the normalized microwave power p_n ($= P/I^2$) as a function of I at the center of minor loop (or $H_x = -265$ Oe). The Δf decreases with $|I|$ but approaches to a broad minimum Δf (≈ 8 MHz) approximately at the current where p_n starts to saturate for $|I| > 11$ mA. In general, with the external H_x at around the minor loop, p_n begins to saturate with Δf approaching the minimum at the high currents as df/dI becomes smaller as shown in the figure. We checked the nonlinear behaviors in the STNO, by plotting $\Delta f \times p_n$ in Fig. 5.8 as a function of I from the measured data of Fig. 5.7 for the field bias. At low current biases $\Delta f \times p_n$ increased by ≤ 4 while p_n decreased by a factor of 14,

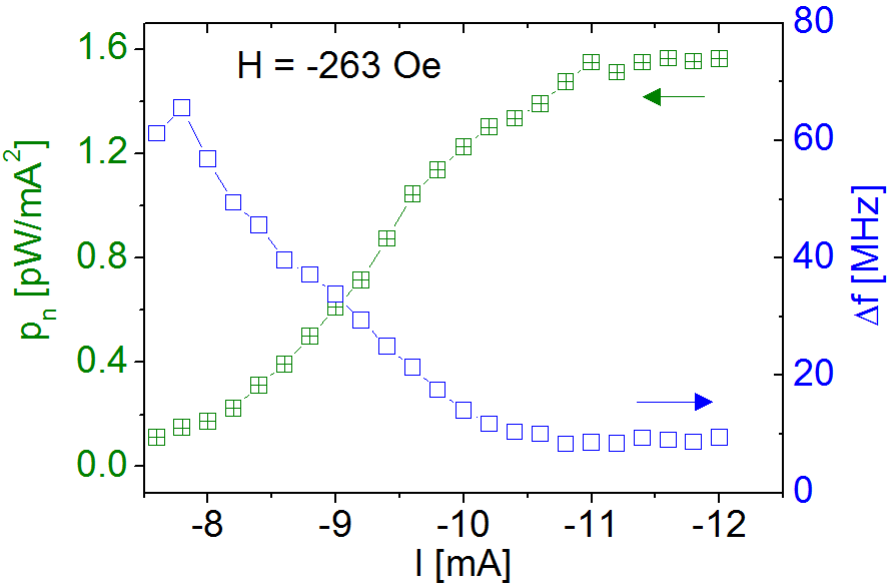

Figure 5.7: Measured normalized power p_n (= P/I^2) and spectral linewidth Δf of the device #1 as a function of I for H_x = −263 Oe (at the center of the minor loop). The Δf approaches to a broad minimum (~ 8 MHz) when the p_n starts to saturate, indicating the effective nonlinear damping (Γ_{eff}) is possibly enhanced hugely at these biases.

meaning that the $|\nu|$ was varied by ≤ 2, while $\Delta f \times p_n$ approaches to a constant at high current biases, suggesting that there is a source for reducing $N/2\pi$ or enhancing $\Gamma_{eff}/2\pi$ at the coherent regime in the device.

The observed behaviors of f and p_n strongly indicated that the STNO had a large $N/2\pi$ (= df/dp) at the coherent bias regime as f was tunable while p_n ($\propto p$) was varied very weakly w.r.t. I. However the STNO could attain a reasonably small ν and low Δf from the circumstance that the large $N/2\pi$ was compensated by a hugely enhanced Γ_{eff} ($\propto (Idp/dI)^{-1}$), similar observation to our previous quasi-linear STNO. Fig. 5.9a-b plots the estimated ν and Γ_p (= $p\Gamma_{eff}$), using Eq. 5.2 with the experimental $I(df/dI)$ and $(p_n/I)(dp_n/dI)^{-1}$, as a function of H_x for I = −11 mA. The average ν in the STNO was ~ −2.2 ± 0.5 and $\Gamma_p/2\pi$ was

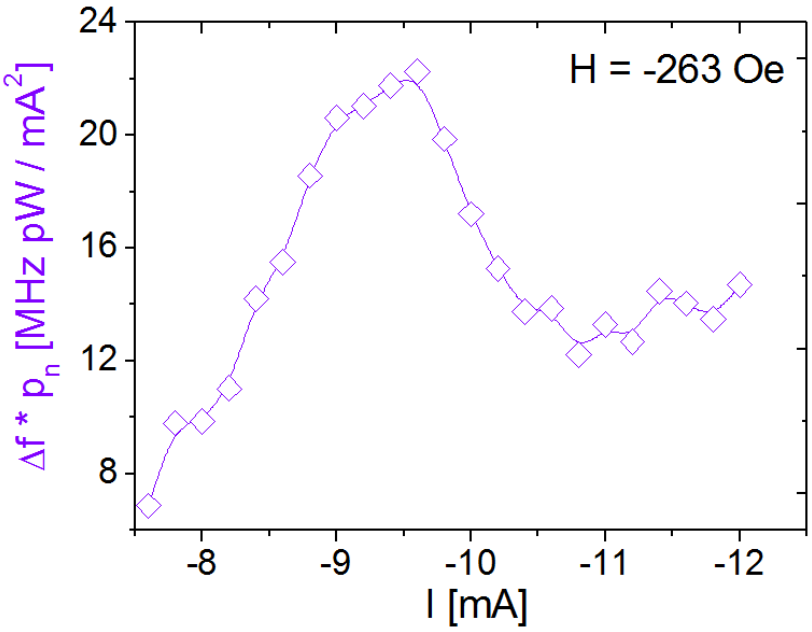

Figure 5.8: Measured $\Delta f \times p_n$ of the device #1 as a function I for $H_x = -263$ Oe (at the center of the minor loop). The $\Delta f \times p_n$ is quasi-constant at the coherent regime ($|I| > 11$ mA), indicating the nonlinear (ν) could be independent with the current-bias. On the other hand the ν might be the strong function of the current at low current biases.

$0.1 - 0.2\ ns^{-1}$. (Note that we estimated Γ_p first of all instead of Γ_{eff} since p was undecided as we discuss below.) The STNO could not accomplish to the thermal limits in the Δf since $|\nu| > 1$, but still achieved very low Δf (< 10 MHz).

5.1.4 Estimation of p, ν and $\Gamma_p/2\pi$

As important parameter we need to estimate p, but its direct approximation of p is very tricky in this STNO from the measured parameters (p_n, $R_s = 30.85\ \Omega$ and $\Delta R = 0.13\ \Omega$) due to the possibility of the signal mixing from the additional MR with the OPP and to the uncertainty in the φ_o. In case of ignoring the MR from

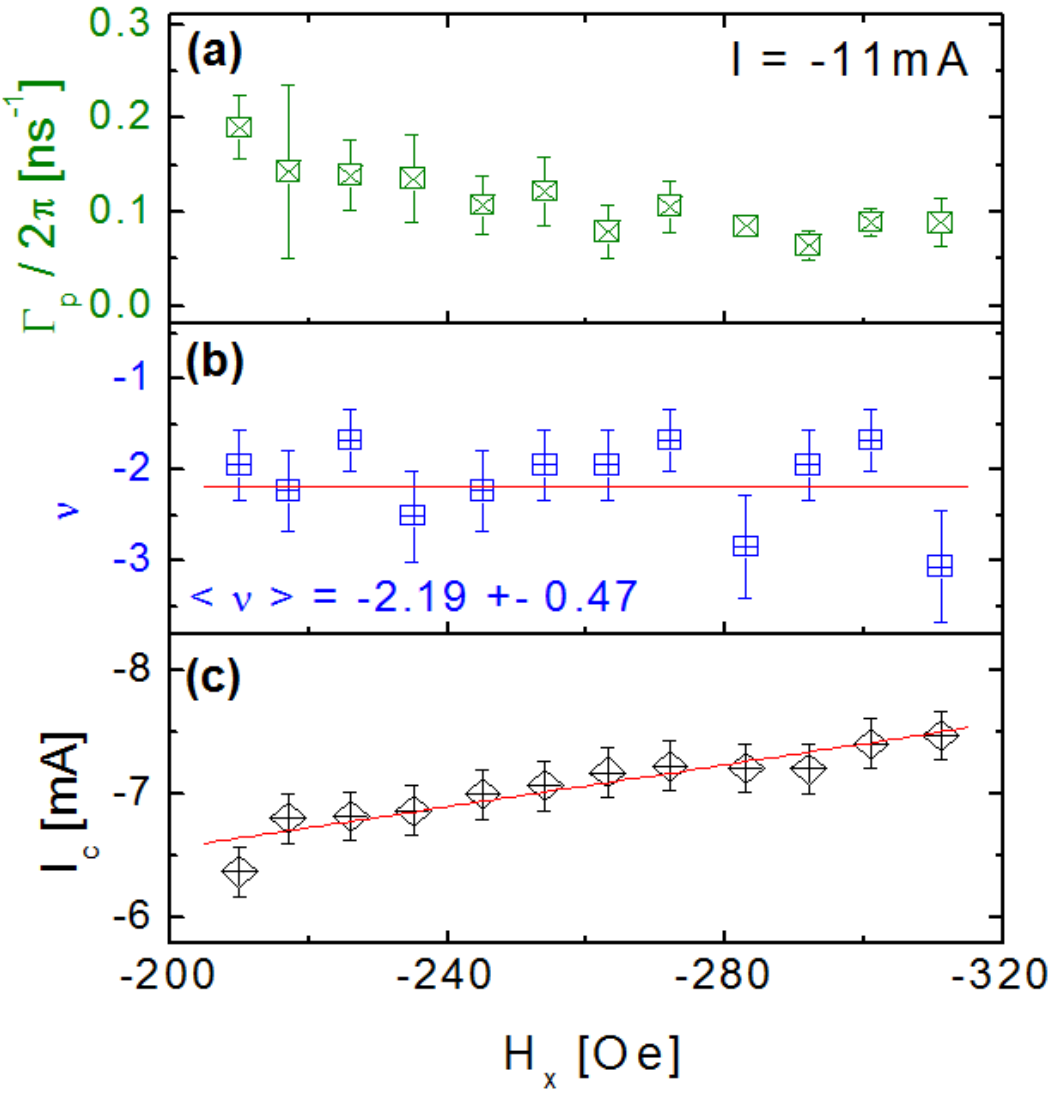

Figure 5.9: Experimentally estimated (a) dynamic damping ($\Gamma_p/2\pi = p\Gamma_{eff}/2\pi$), (b) nonlinear coupling (ν) of the device #1, using Eq. 5.2 with the measured df/dI, $(I/p_n)\ dp_n/dI$ as a function of H_x for $I = -11$ mA. (c) Measured threshold current (I_c) for the on-set of the auto-oscillation as a function of H_x. The $|I_c|$ linearly increases with $|H_x|$, which is roughly consistent with the analytical results in Fig. 5.12, because the τ_{ip} with a negative current bias favors the parallel (relative to the IPP) of the FL while τ_{op} generates the instability of the FL.

the OPP, however, we can estimate p from $\varepsilon = (R_L + R_S)\sqrt{2p_n/R_L}/R'(\varphi_o)$ where $R(\varphi(t))$ is the angle dependent MR and $R_L = 50\ \Omega$ and $R'(\varphi_o) = \partial R(\varphi_o)/\partial\varphi_o$. For example, we have $\varepsilon \approx 17.7^o/|sin(\varphi_o)|$ with the measured $p_n = 1.55\ pW/mA^2$ for $I = -11$ mA and $H_x = -265$ Oe, if assuming the symmetric $R(\varphi) = \Delta R_o sin^2(\varphi/2)$, $p = sin^2(\varphi/2)$ and $\varphi(t) = \varphi_o + \varepsilon sin(\omega t)$, although this is not exactly correct due to the non-parabolic energy potential (especially when the precession axis is titled to the out-of-plane). Then $\varepsilon \approx 18^o - 25^o$ is expected with the most probable range in $\varphi_o(45^o < \varphi_o < 135^o)$, yielding $0.024 < p < 0.047$. However, this range of p might be under-estimated since the measured $\Delta f(= 8 \pm 2$ MHz) is much smaller than the predicted $\Delta f \approx 16 - 31$ MHz, with $\Delta f \approx [6.1(1 + \nu^2)/f^2 p]$ MHz at $T = 300$ K, where f is the oscillation frequency in GHz, obtained from Eq. 5.1 with the appropriate parameters ($\alpha_G = 0.01$, $M_s = 560\ emu/cm^3$) for the Py FL, with the estimated p, and with the measured $f = 6.28$ GHz and $\nu = -1.95$ for $I = -11$ mA and $H_x = -265$ Oe.

We can estimate p, from Eq. 5.1 and with the measured f , Δf and ν for the same I and H_x, then we have $p \approx 0.071 \pm 0.018$ and $\varphi \approx 31 \pm 7^o$, where the p is $1.2 - 3.7$ times larger than the estimated p above. The reduction in the microwave output power was very probable from the phase difference in the two MR signals: one from FL and IPP (R_{ip}) while the other from FL and OPP (R_{op}). The phase difference between $R_{ip}(t)$ and $R_{op}(t)$ should be $\pi/2$ or $3\pi/2$ for ideally symmetric cases, or is expected between them for non-ideal trajectories, for a small angle precession of the FL around its precession axis laying somewhere between the principal axes. Adopting the estimated p we obtain the nonlinear effective damping $\Gamma_{eff}/2\pi\ (= \Gamma_p/(2\pi)p) \approx 1.13 \pm 0.28\ ns^{-1}$, much higher than $\Gamma_o/2\pi$ ($\approx 0.1\ ns^{-1}$), and the agility $N/2\pi\ (= \nu\Gamma_{eff}/2\pi) \approx -2.20 \pm 0.55$ GHz, quite comparable to previously estimated values in several STNOs [171, 160]. In any cases the

huge enhancement of $\Gamma_{eff}/2\pi$ was unambiguous in the STNO, implying that the anti-damping efficiency of the ST was greatly reduced at the coherent oscillation regime.

5.1.5 Understanding of spin-torque competition

To understand the origin in the enhancement of $\Gamma_{eff}/2\pi$, we qualitatively examine the motion of the FL in the single domain under the two spin torques. For $I < 0$ the equivalent τ_{op} field ($H_{op} \propto -\gamma\hat{m} \times \hat{z}$) is toward counterclockwise of the FL moment, inducing the rotation of the FL to this direction, while the in-plane H_k to the one of the easy axis, the effective τ_{ip} field ($H_{ip} \propto -\gamma\hat{m} \times \hat{x}$) to z competing to H_{demag} ($+z$), as shown in Fig. 5.10. For the τ_{st}-driven auto-oscillations, there should be anti-damping components in τ_{op} and τ_{ip} onto the FL. Before the onset of persistent oscillations, the τ_{ip} adds to the positive damping as long as $m_x < 0$, in which the initial P-state is already set with a small $I < 0$, that makes the threshold currents (I_c) for the dynamics higher than the STNO only by the τ_{op}. However the τ_{ip} will give an anti-damping torque as the FL passes the hard axis ($-y$) and $m_x > 0$. On the other hand, the H_{ip} is applied to $-z$, the FL toward AP with the OPP, thus the τ_{op} is also added to the damping torque when $m_z < 0$. Fig. 5.9c plots I_c vs H_x, as determined by the point where the oscillator mode is first clearly established. The I_c increases with $|H_x|$ because the direction of the field bias is preferable for the P configuration.

As indicated by our previous micromagnetic analysis [150], the inhomogeneous stray fields from the two polarizers shift the effective anisotropy field (H_k^{eff}) as a function of position along the easy axis on the FL, and we have

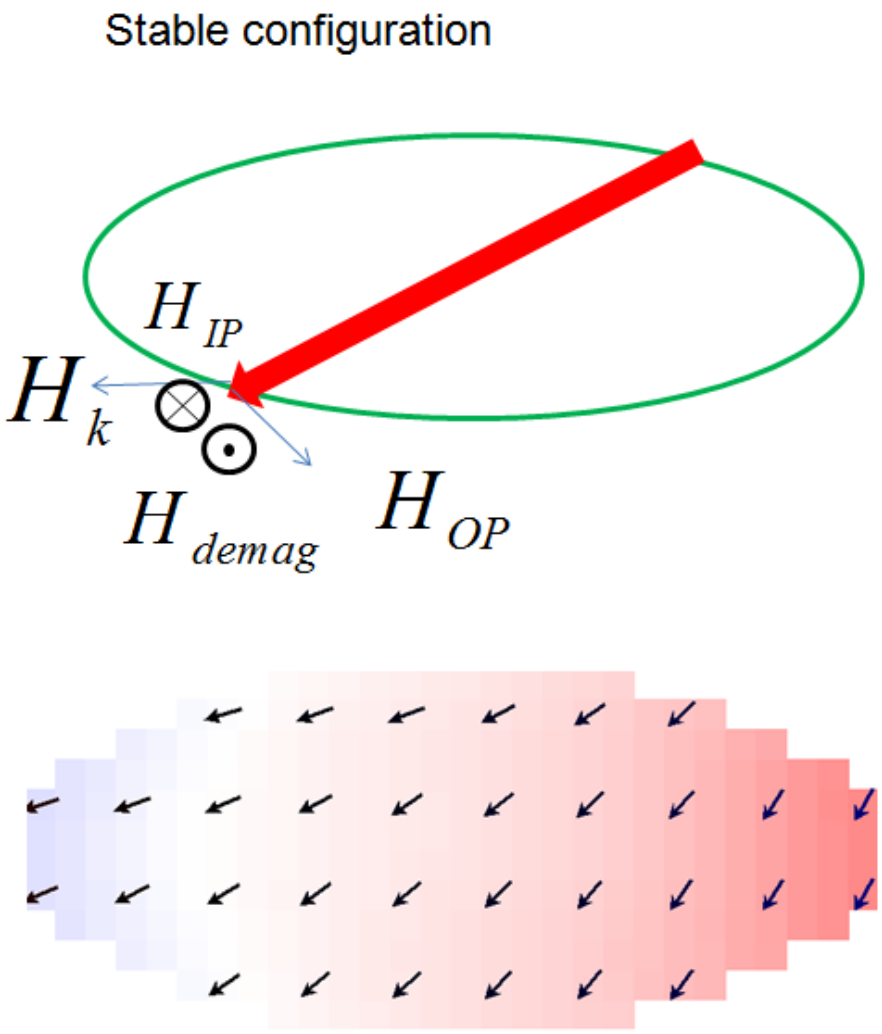

Figure 5.10: (*top*) Scheme of the field competition in the STNO device with a negative current bias. Here H_k is the in-plane anisotropy ($\sim -\hat{x}$), H_{demag} is the out-of-plane demagnetization field ($\sim \hat{z}$) induced by the τ_{op}, H_{op} is the effective spin-torque field from the τ_{op} that rotates the FL counterclockwise, and H_{ip} ($\sim -\hat{z}$) is the effective spin-torque field from the τ_{ip} and opposite to the H_{demag}. The H_{ip} (and τ_{ip}) is against to the τ_{op}, retarding the oscillation or acting as the source of enhanced nonlinear effective damping ($\Gamma_{eff}/2\pi$) or dynamic damping ($\Gamma_p/2\pi$). (The effective field in the Slonczewski spin-torque term is discussed in Section 4.6.2 when the spin-polarization is strongly non-collinear to the FL.) (*bottom*) Stable magnetization configuration before the onset of auto-oscillation, obtained by micromagnetics (see Fig. 5.11). The inhomogeneous stray fields from the two polarizers change the local effective anisotropy field and generate different rotation angles along the elongated (easy) axis as the position on the FL.

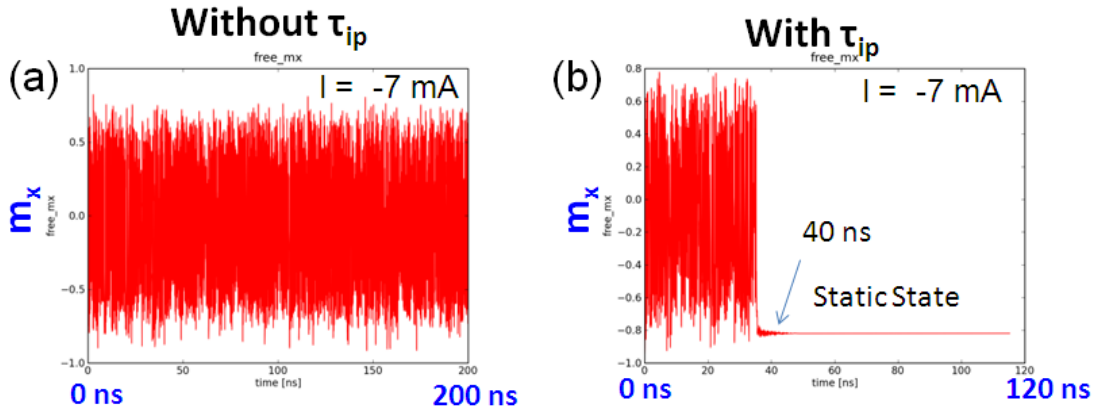

Figure 5.11: Micromagnetic simulation of the time trace of $< m_x >$ with the application of dc current (I = -7 mA) (a) without τ_{ip} (i.e. $P_{ip} = 0$) (b) with strong τ_{ip} (i.e. $P_{ip} = 0.37$ and $P_{op} = 0.20$). With the strong τ_{ip}, the FL is stabilized to a new equilibrium after 40 ns at which all of the torques are balanced out, implying the τ_{ip} acts as a dynamic damping or against to the τ_{op}.

$H^{eff}_{k,right} < H^{eff}_{k,left}$ for the P configuration. Therefore, during the static rotation with slowly ramped up currents ($I < 0$), the FL rotates differently due to this inhomogeneity in the H^{eff}_{k} as shown in Fig. 5.10, in which the right edge part rotates further than the left part. As the right side passes the orthogonal position, the τ_{ip} acts as an anti-damping torque that can generate the auto-oscillation in this area while in the other side the τ_{ip} is still added to the damping for the oscillation. Thus, the $\Gamma_{eff}/2\pi$ can be hugely enhanced due to the spatial variation of the anti-damping effectiveness of the τ_{st}, which is very similar observation to our previous quasi-linear oscillator [171].

5.1.6 Conclusion

In summary we demonstrated a relatively coherent STNO with $\Delta f \leq 10$ MHz, based on a nanopillar spin-valve device in which the FL was excited by a com-

bined τ_{op} and τ_{ip}, at around the minor loop, possibly having the advantage in the operation without an external field bias. The STNO exhibited the enhancement of $\Gamma_{eff}/2\pi$ ($> 1\ ns^{-1}$) at the coherent regime as consequences of the spin-torque competition between the two spin-polarizers and the spatial variation of the anti-damping efficiencies in the τ_{st}'s, effectively reducing the $|\nu|$ (~ 2) while the agility $N/2\pi$ was finite (> 1 GHz). Significant progress in this effort would substantially enhance both the coherence ($\Delta f < 1$ MHz) and the output power ($p > 0.1$) of STNOs as well as advance our understanding of and ability to control nanomagnetic dynamics.

5.2 Instability analysis of a magnetic free layer excited by a combined out-of-plane and in-plane spin torques

In this section, in order to obtain insight into the underlying physics and the instability condition, I develop the *analytical model* in the device structure where an in-plane magnetic free layer (FL) is excited by the spin torque from combined out-of-plane (OPP) and in-plane (IPP) spin-polarizers [99, 140, 174, 172, 175, 147]. Within a zero-temperature single domain approximation, the magnetic dynamics of the FL can be described by the Landau-Lifshitz-Gilbert-Slonczewski (LLGS) equation [14, 15, 17] including two spin-torque terms:

$$\frac{d\hat{m}}{dt} = -\gamma \hat{m} \times \vec{H}_{eff} + \alpha \hat{m} \times \frac{d\hat{m}}{dt} - \gamma a_{op} \hat{m} \times \hat{p}_{op} \times \hat{m} + \gamma a_{ip} \hat{m} \times \hat{p}_{ip} \times \hat{m} \qquad (5.3)$$

where $\vec{H}_{eff} = (H_k m_x + H_e)\hat{x} + (H_z - 4\pi M_o m_z)\hat{z}$, $\hat{p}_{op} = \hat{z}$ and $\hat{p}_{ip} = -\hat{x}$. Here $H_e (= H_a + H_d)$ is the in-plane easy-axis component of the external magnetic field, H_a is the applied field and H_d (H_z) is the stray field from the IPP (OPP). The field-like spin-torque ($\sim \hat{m} \times \hat{p}$) is not included as it is very small in metallic spin-valve

devices [51, 52, 55, 56]. The LLGS equation (Eq. 5.3) can be rewritten into the following two equations in a spherical coordinate system:

$$\frac{1+\alpha^2}{\gamma}\frac{d\theta}{dt} = f_1(\theta,\phi) + \alpha f_2(\theta,\phi)$$

$$\frac{1+\alpha^2}{\gamma}cos\theta\frac{d\phi}{dt} = -\alpha f_1(\theta,\phi) + f_2(\theta,\phi) \tag{5.4}$$

with

$$f_1(\theta,\phi) = -a_{op}cos\theta + a_{ip}cos\phi sin\theta + H_e sin\phi + \frac{H_k}{2}cos\theta sin2\phi$$

$$f_2(\theta,\phi) = a_{ip}sin\phi - H_e cos\phi sin\theta + H_z cos\theta - (4\pi M_o + H_k cos^2\phi)sin\theta cos\theta \tag{5.5}$$

Here $\hat{m} = (cos\theta cos\phi, cos\theta sin\phi, sin\theta)$ is the normalized magnetization vector of the FL where θ is the out-of-plane tilt angle and ϕ is the in-plane rotation angle from the x-axis. The equilibrium or the dynamic states of the FL are determined by four major parameters that we can control by engineering materials or structures: a_{op} (ST from OPP), a_{ip} (ST from IPP), H_e (external field along the easy axis), H_z (external field along the out-of-plane). For a quasi-static state (i.e. $\dot{\theta} = \dot{\phi} = 0$), it should be $f_1(\theta,\phi) = f_2(\theta,\phi) = 0$ because of $1 + \alpha^2 > 0$ in Eq. 5.4. Significant amount of mathematical tasks are rquired for obtaining the complete solution with all of these parameters, so we will determine the analytical solutions for several simplified cases that can be experimentally implementable.

5.2.1 $I = 0$ and $H_e = 0$

The simplest static case is for $I = 0$ ($a_{op} = a_{ip} = 0$) and $H_e = 0$ since the magnetic state of the FL is usually measured with a very small sense current at this field bias (i.e. at the center of the minor loop). The trivial solution is $\phi = 0$ or π and $sin\theta = \frac{H_z}{4\pi M_o + H_k} \approx \frac{H_z}{4\pi M_o}$ since $4\pi M_o >> H_k$ in general.

5.2.2 $H_e = 0$, $a_{ip} = 0$ but $a_{op} \neq 0, H_z \neq 0$

This corresponds to the case that the device has only an OPP layer. Eq. 5.5 becomes

$$f_1(\theta, \phi) = \left[-a_{op} + \frac{H_k}{2} sin2\phi\right] cos\theta$$

$$f_2(\theta, \phi) = [H_z - (4\pi M_o + H_k cos^2\phi) sin\theta] cos\theta$$

The solution of $f_1(\theta, \phi) = f_2(\theta, \phi) = 0$ is $sin2\phi = \frac{a_{op}}{H_k/2}$ and $sin\theta \approx \frac{H_z}{4\pi M_o}$ if $4\pi M_o >> H_k$, and the instability condition is $a_{op} > \frac{H_k}{2}$ from the former.

5.2.3 $H_z = 0$, $a_{ip} = 0$ but $a_{op} \neq 0$, $H_e \neq 0$

This case has been studied experimentally [114] and analytically [140, 175] in which the spin torque only from an OPP excites the FL but no dipole field is experienced on the FL from the OPP. For the former condition ($a_{ip} \rightarrow 0$) the straightforward method is the utilization of the device without the IPP. However this has a problem because we need a detector for measuring the magnetoresistance (MR) voltage signal. Instead it has been proposed that an IPP layer can serve only as an analyzer [114] if the thickness of the IPP is much smaller than its spin diffusion length, causing the reduction of its spin-polarization. Eq. 5.5 are simplified to

$$f_1(\theta, \phi) = -a_{op} cos\theta + H_e sin\phi + \frac{H_k}{2} cos\theta sin2\phi$$

$$f_2(\theta, \phi) = [-H_e cos\phi - (4\pi M_o + H_k cos^2\phi) cos\theta] sin\theta \tag{5.6}$$

The solution of $f_2(\theta, \phi) = 0$ is $\theta = 0$, then $f_1(0, \phi) = -a_{op} + H_e sin\phi + (\frac{H_k}{2}) sin2\phi = 0$ at the static state. From Eq. 5.4, $\left(\frac{1+\alpha^2}{\gamma}\right)\dot{\phi} = -\alpha f_1(0, \phi) = -\frac{\partial E_{eff}}{\partial \phi}$, and by integrating

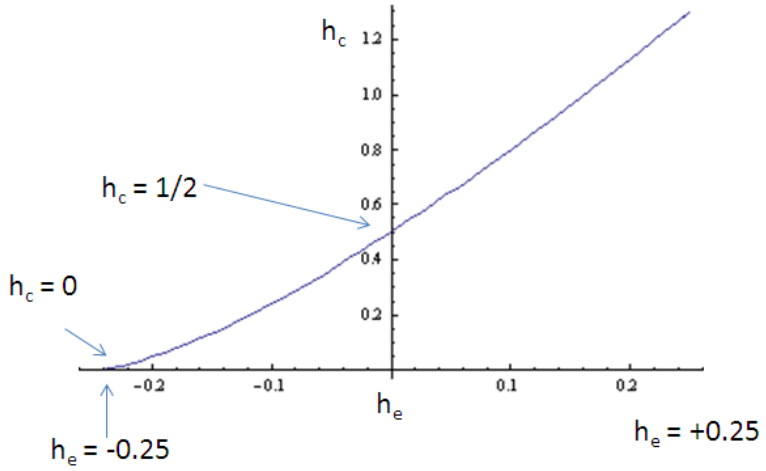

Figure 5.12: Calculated h_c $\left(= \frac{a_{op,c}}{H_k}\right)$ as a function of h_e $\left(= \frac{H_e}{4H_k}\right)$, using Eq. 5.8, for $H_z = 0$ and $a_{ip} = 0$. The critical current (I_c) shifts almost linearly with a small in-plane field (H_e).

this, we have one dimensional effective energy function ($E_{eff}(\phi)$) on the in-plane ($\theta = 0$):

$$E_{eff}(\phi) = -\alpha\left[a_{op}\phi + H_e cos\phi + \frac{H_k}{4}cos2\phi\right] \tag{5.7}$$

The conditions for the critical equilibrium points, at which the FL begins unstable, are $\frac{\partial E_{eff}}{\partial \phi} = \frac{\partial^2 E_{eff}}{\partial \phi^2} = 0$ where $\frac{\partial^2 E_{eff}}{\partial \phi^2} = \alpha[H_e cos\phi + H_k cos2\phi]$. A critical point ($\phi_c$) should exist for $0 < \phi < \frac{\pi}{2}$ because $\frac{\partial^2 E_{eff}}{\partial \phi^2}\,|_{\phi=0} = \alpha[H_e + H_k] > 0$ but $\frac{\partial^2 E_{eff}}{\partial \phi^2}\,|_{\phi=\frac{\pi}{2}} = \alpha[-H_k] < 0$. The equations for the critical angle (ϕ_c) are then given by

$$a_{op,c} = H_e sin\phi_c + \frac{H_k}{2}sin2\phi_c$$

$$H_e cos\phi_c + H_k cos2\phi_c = 0$$

and we obtain the solution for the ϕ_c:

$$cos\phi_c = -\frac{H_e}{4H_k} \pm \sqrt{\frac{1}{2} + \left(\frac{H_e}{4H_k}\right)^2}$$

For the most symmetric case ($H_e = 0$), we have $\phi_c = \frac{\pi}{4}, \frac{3\pi}{4}$ and $a_{op,c} = \frac{H_k}{2}, -\frac{H_k}{2}$ which is same to the results from the previous studies [147, 140, 175]. Let's

define $h_e = \frac{H_e}{4H_k}$ and $h_c = \frac{a_{op,c}}{H_k}$. For $0 < \phi < \frac{\pi}{2}$ we have the solution:

$$\phi_c = arccos\left[-h_e + \sqrt{\frac{1}{2} + h_e^2}\right]$$

$$h_c = \left(\sqrt{\frac{1}{2} + h_e^2} + 3h_e\right)\sqrt{\left(\sqrt{\frac{1}{2} + h_e^2} + 3h_e\right)\left(\sqrt{\frac{1}{2} + h_e^2} - h_e\right)} \tag{5.8}$$

Fig. 5.12 plots the h_c as a function of h_e, using Eq. 5.8, where the h_c decreases for $h_e < 0$ because the in-plane field (H_e) makes the FL energetically favorable to the equilibrium position at $\phi = \pi$ while the h_c increases for the other case.

5.2.4 $H_z \neq 0, a_{ip} \neq 0, a_{op} \neq 0$ and $H_e \neq 0$

This case includes most external parameters, and obtaining the complete analytical solution is desirable but requires huge mathematical works. However Eq. 5.5 can be solved for some specific cases, or we can have further simplified equations of motion at the extremely initial state when a very short but strong impulse current is applied.

Let's define $\theta_o \approx \frac{H_z}{4\pi M_o + H_k}$ and $\theta = \theta_o + \varepsilon$. Assume that $4\pi M_o >> H_k, H_z$ and that the out-of-plane tilt angles are very small and i.e. $\theta, \theta_o, \varepsilon << 1$. Then within the 1st order approximation in the θ, θ_o and ε, Eq. 5.5 becomes

$$f_1(\varepsilon, \phi) \approx -a_{op} + a_{ip}(\theta_o + \varepsilon)cos\phi + H_e sin\phi + \frac{H_k}{2} sin2\phi$$

$$f_2(\varepsilon, \phi) \approx [a_{ip} sin\phi - H_e \theta_o cos\phi] - \varepsilon[4\pi M_o] \tag{5.9}$$

The solution for $f_2(\varepsilon, \phi) = 0$ is $\varepsilon \approx \frac{a_{ip} sin\phi - H_e \theta_o cos\phi}{4\pi M_o}$, and subsequently we have

$$f_1(\phi) = \left(-a_{op} - \frac{a_{ip} H_e \theta_o}{8\pi M_o}\right) + \left(a_{ip}\theta_o cos\phi + H_e sin\phi\right) + \left(\frac{H_k}{2} + \frac{(a_{ip})^2}{8\pi M_o}\right) sin2\phi - \left(\frac{a_{ip} H_e \theta_o}{8\pi M_o}\right) cos2\phi \tag{5.10}$$

In principle one can obtain the critical equilibrium angle (ϕ_c) from the conditions, $f_1(\phi)\mid_{\phi=\phi_c}= 0$ and $\frac{\partial f_1(\phi)}{\partial \phi}\mid_{\phi=\phi_c}= 0$. We will determine the analytical solutions in further simple cases later at which we perform the experiment most of time.

Let's simplify the equations of motion at the extremely beginning when the motion to the out-of-plane determines the ballistic switching with a short but strong current impulse. Assuming that the angle ϕ is small ($cos\phi \approx 1$), Eq. 5.9 becomes

$$f_1(\varepsilon, \phi) \approx -a_{op} + a_{ip}(\theta_o + \varepsilon) + (H_e + H_k)sin\phi$$

$$f_2(\varepsilon, \phi) \approx a_{ip}sin\phi - H_e\theta_o - 4\pi M_o\varepsilon$$

and Eq. 5.4 are transformed to

$$\frac{1+\alpha^2}{\gamma}\frac{d\varepsilon}{dt} \approx (-a_{op} + a_{ip}\theta_o) + \varepsilon(a_{ip} - \alpha 4\pi M_o) + (H_k + H_e)sin\phi$$

$$\frac{1+\alpha^2}{\gamma}\frac{d\phi}{dt} \approx -4\pi M_o\varepsilon + a_{ip}sin\phi + \alpha a_{op} - H_e(\theta_o + \varepsilon) \tag{5.11}$$

These equations are only applicable for the initial motion of the FL after the current impulse turned on, but can explain the mechanism of the ultrafast switching [150, 149, 100, 101, 102] in the device structure. The strong out-of-plane torque ($-a_{op}$) induces the FL tilted to the out-of-plane, but competes with the torque from the IPP ($a_{ip}(\theta_o + \varepsilon)$) and the damping-torque ($-\alpha 4\pi M_o\varepsilon$) during the process. More importantly the strongly induced out-of-plane demagnetization field ($-4\pi M_o\varepsilon$) is the main force (largest term) in the second equation that drives the rotation of ϕ.

5.2.5 $H_e = 0$ but $H_z \neq 0, a_{ip} \neq 0, a_{op} \neq 0$

This is the special case of Section 5.2.4, i.e. the spin torque is exerted to the FL at the center of the minor loop. From the solution in Section 5.2.4, Eq. 5.9 can be simplified to

$$f_1(\varepsilon, \phi) \approx -a_{op} + a_{ip}(\theta_o + \varepsilon)cos\phi + \frac{H_k}{2}sin2\phi$$

$$f_2(\varepsilon, \phi) \approx a_{ip}sin\phi - \varepsilon 4\pi M_o$$

The quasi-static solution for $f_2(\varepsilon, \phi) = 0$ is $\varepsilon \approx \frac{a_{ip}sin\phi}{4\pi M_o}$, then we have $f_1(\phi) = -a_{op} + a_{ip}\theta_o cos\phi + \left(\frac{H_k}{2} + \frac{(a_{ip})^2}{8\pi M_o}\right) sin2\phi$. By integrating this $f_1(\phi)$ over ϕ, we have $E_{eff}(\phi)$:

$$E_{eff}(\phi) = \alpha\left[-a_{op}\phi + a_{ip}\theta_o sin\phi - \frac{1}{2}\left(\frac{H_k}{2} + \frac{(a_{ip})^2}{8\pi M_o}\right)cos2\phi\right]$$

The critical equilibrium condition at $\phi = \phi_c$, satisfying $\frac{\partial E_{eff}}{\partial \phi} = \frac{\partial^2 E_{eff}}{\partial \phi^2} = 0$, gives the following equations:

$$-a_{ip,c}sin\phi_c + \left(H_k + \frac{(a_{ip,c})^2}{4\pi M_o}\right)cos2\phi_c = 0$$

$$-a_{op,c} + a_{ip,c}\theta_o cos\phi_c + \left(\frac{H_k}{2} + \frac{(a_{ip,c})^2}{8\pi M_o}\right)sin2\phi_c = 0 \tag{5.12}$$

We can obtain the exact solution of Eq. 5.12 for the special case, $\theta_o = 0$ (or $H_z = 0$), that is the situation in the absence of external fields on the FL. Then we have $\phi_c = \frac{\pi}{4}$ and

$$a_{op,c} = \frac{H_k}{2} + \frac{(a_{ip,c})^2}{8\pi M_o}$$

Interestingly the $a_{op,c} > \frac{H_k}{2}$, implying that the spin-torque from the IPP retards the instability, and the sign of $a_{ip,c}$ does not matter for the onset of the instability. Since the spin polarizations of two polarizers are in general dissimilar, the strengths of a_{op} and a_{ip} are different. Let's define $a_{op,c} = r\ a_{ip,c}$, then $x^2 - srx + s = 0$ where $x = \frac{a_{ip,c}}{H_k/2}$ and $s = \frac{16\pi M_o}{H_k}$. For having the instability solutions,

it should $(sr)^2 - 4s > 0$ or $r > r_c \equiv \sqrt{\frac{H_k}{4\pi M_o}}$. On the other case ($r < r_c$) we expect no instability solution.

For a non-zero but small H_z ($<< 4\pi M_o$), i.e. $0 < \theta_o << 1$, the solution of Eq. 5.12 can be obtained using the perturbation technique .With a trial solution $\phi_c = \frac{\pi}{4} + \delta$ ($\delta << 1$), Eq. 5.12 is changed to

$$-a_{ip,c}\theta_o \frac{1}{\sqrt{2}}(1+\delta) - 2\delta\left(H_k + \frac{(a_{ip,c})^2}{4\pi M_o}\right) \approx 0$$

$$-a_{op,c} + a_{ip,c}\theta_o \frac{1}{2} + \left(\frac{H_k}{2} + \frac{(a_{ip,c})^2}{8\pi M_o}\right) \approx 0$$

Then we have

$$\delta \approx \frac{a_{ip,c}\theta_o/\sqrt{2}}{a_{ip,c}\theta_o/\sqrt{2} + 2\left(H_k + \frac{(a_{ip,c})^2}{4\pi M_o}\right)}$$

$$a_{op,c} \approx a_{ip,c}\theta_o \frac{1}{\sqrt{2}} + \frac{1}{2}\left(H_k + \frac{(a_{ip,c})^2}{4\pi M_o}\right)$$

Similarly we obtain $x^2 \mp (r \mp \frac{\theta_o}{\sqrt{2}})sx + s \approx 0$ by defining $a_{op,c} = \pm r a_{ip,c}$. For existing the instability solutions, $(r \mp \frac{\theta_o}{\sqrt{2}})^2 s^2 - 4s > 0$ or $r > r_c \pm \frac{\theta_o}{\sqrt{2}}$. The equation can have instability solutions when the OPP-ST becomes stronger. For $r < r_c \pm \frac{\theta_o}{\sqrt{2}}$ the equation has no instability solution, implying that the FL always rotates quasi-statically (no dynamics), because the stabilizing IPP-ST is much stronger than the destabilizing OPP-ST.

5.2.6 Conclusion

In summary we obtain the analytical solutions, for several specific cases that can be realizable in the device and/or in the lab, in the device structure where an in-plane magnetic free layer (FL) is excited by spin torque from combined out-of-plane (OPP) and in-plane (IPP) spin-polarizers. The tuning of 4 parameters, a_{op},

a_{ip}, H_e, and H_z, are essential to determine the magnetic dynamics of the FL for different purposes. The ideal and symmetric case is that no external fields are exerted on the FL. Minimized stray field ($H_x = H_z = 0$) from the OPP (IPP) layer can be realized by using a synthetic antiferromagnetic OPP(IPP) polarizer [176]. Based on our analytical analysis, the ST ratio ($r_c = \frac{a_{op,c}}{a_{ip,c}} = \frac{P_{op}}{P_{ip}}$) from the two spin-polarizers is especially critical for determining the existence of the instability points. For example, $r_c = 0.17$ if $H_k = 200\ Oe$ and $r_c = 0.24$ if $H_k = 400\ Oe$ for a given $4\pi M_o = 7040\ Oe$. Given material parameters ($4\pi M_o, P_{op}, P_{ip}$), the r_c can be adjusted by the shape anisotropic ratio (H_k). For a perfect deterministic (non-toggling) mode switching, it should be $r < r_c$, but for a spin-torque oscillator, $r > r_c$. The P_{ip} (or r) can be controlled geometrically by adjusting the thickness of the IPP layer relative to its spin-diffusion length [114].

CHAPTER 6

PERPENDICULAR MAGNETIZATION SWITCHING VIA SPIN-HALL INDUCED SPIN-CURRENTS IN THERMALLY ACTIVATED SWITCHING REGIME

I study the switching of a perpendicularly magnetized Co nano-dot in Pt/Co/MgO/Ta via the spin-Hall induced spin currents. In the thermally activated reversals we estimate the current induced equivalent field (H_s) that has a strength consistent with the predicted magnitude from the spin Hall effect in Pt when taking into account the Joule heating effect on the ultrathin magnetic system. In the reversal process an excitation/activation of a subvolume drives the entire magnetization switching, thus even a small but heat-assisted H_s can reverse such a Co dot with a strong perpendicular magnetic anisotropy. We investigate the switching currents and the activation energy barriers as functions of the Co-thickness (from 0.8 to 1.0 nm) and the current-channel width (200 nm to 1000 nm), and find consistency with the sub-volume excitation model.

6.1 Introduction

The electrical manipulations of thin nanomagnets have attracted considerable interest for potential technological applications such as magnetic memory and logic, possibly having advantages in low power and in high speed operation. Over the last decade the direct injection of spin-polarized currents has been utilized to induce nanomagnet switching, persistent magnetic oscillation or magnetic domain wall motion via spin-transfer-torque (ST) effect [17] in various device structures including nanopillar spin-valves, magnetic tunnel junctions, nano-constrictions, non-local lateral spin-valves and ferromagnetic nanowires.

Recently alternative electrical methods [74, 72, 73] have demonstrated the manipulation of ultra-thin (~ a few atomic layers) ferromagnetic dot or layer in the configuration of current-in-plane (CIP). The multilayers in the structures generally consist of NM/FM/MO_x where NM is a non-magnetic heavy-metal, FM is an ultra-thin transition ferromagnet and MO_x is a metal-oxide: e.g. Pt/Co/AlO_x or Ta/CoFeB/MgO. This new geometric configuration utilizes materials with a large spin-orbit coupling to generate torques on the FM moment and suggests a new pathway for nanomagnet controls without a magnetic spin polarizer and/or with the separation of write and read channels. The observations of current-driven magnetization control in NM/FM/MO_x structures have been interpreted with two different mechanisms; *Rashba effect* [177, 178, 179] or *spin-Hall effect* (SHE) [82, 180, 181]. In general recent theories have suggested that the current induced torque has a form of $\vec{\tau} = -\gamma H_R \hat{m} \times \hat{y} + \gamma H_S \hat{m} \times (\hat{y} \times \hat{m})$ in both cases, but each magnitude or relative strengths might be strongly dependent on the underlying physics, structures and materials.

6.2 Rashba effect vs Spin hall effect

In the frame of Rashba effect, the effective Rashba field ($H_R \approx \hat{j} \times \nabla E = \alpha_R \hat{y}$) or the torque ($\vec{\tau_R} = -\gamma H_R \hat{m} \times \hat{y}$) is exerted on moving electrons by spin-orbit coupling if an intrinsic electrical potential ($\nabla E = E\hat{z}$) is built up at the dissimilar interfaces and the electrical current density is $\hat{j} = j\hat{x}$, while recent theoretical studies [75, 81, 80] have suggested that the current-induced torque has an additional (secondary) Slonczewksi-like (SL) ST, $\vec{\tau_S} = \gamma H_S \hat{m} \times (\hat{y} \times \hat{m})$, from the spin-precession due to the exchange coupling with the FM magnetization.

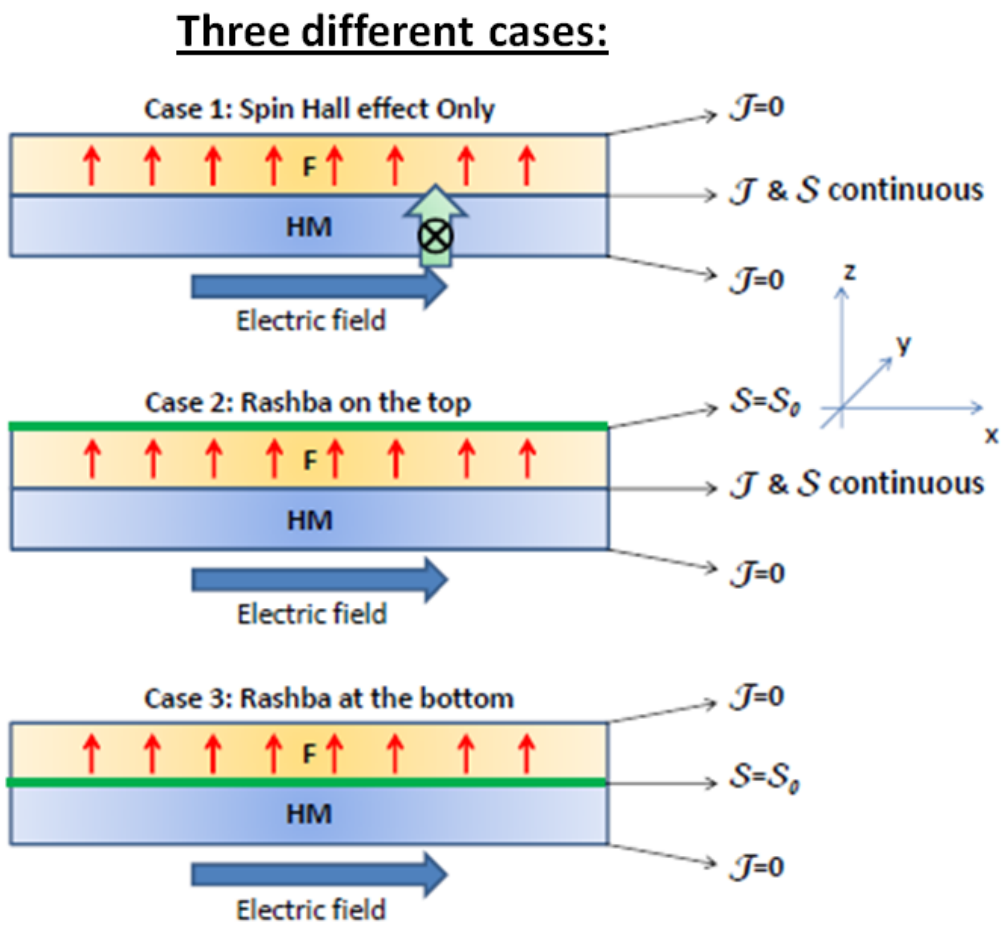

Figure 6.1: Illustration of HM/FM/MO_x and three possible origins of spin-torques on the FM layer, where HM is a heavy normal metal, FM is a ferromagnet and MOx is a metal-oxide. (top) spin-Hall-effect (SHE) only. (middle) Rashba effect at the FM/MO_x interface. (bottom) Rashba effect at the HM/FM interface. The SHE torque is proportional to the current density in the HM while the Rashba torque is proportional to the interfacial current. Manchon suggested that the current induced torques in the bilayer structure might be on the form $\vec{\tau} = -\gamma H_R \hat{m} \times \hat{y} + \gamma H_S \hat{m} \times (\hat{y} \times \hat{m})$ in both Rashba and SHE cases. But the relative strength could strongly depend on the thickness, structures, materials and underlying physics. From [75].

Contrarily the SHE generates opposite spin accumulation on the opposing lateral surface of current-carrying NM wire via a relativistic spin-orbit interaction between a charge current ($\hat{j} = j\hat{x}$) and a transverse spin current ($\hat{\sigma}//\hat{y}$). Then SHE-ST ($\hat{\tau_S} = \gamma H_S \hat{m} \times (\hat{y} \times \hat{m})$) acts on the magnetic moment on the neighboring FM by absorbing the spin currents at the interface. In the mean time, a recent theory [75] has suggested the possibility of the existence of an additional torque ($\vec{\tau_R} = -\gamma H_R \hat{m} \times \hat{y}$), if the thickness of the FM is not longer than its spin-dephasing length and a diffusive spin-current is not perfectly absorbed at the interface of the FM layer, which is similar to the field-like ST in MgO-MTJs or the non-adiabatic ST in FM-nanowires.

Although the SL-ST ($\vec{\tau}_S$) has a form of the anti-damping, that acts to the free layer magnetization when the spin-polarization ($\hat{\sigma}$) has a collinear component to the moment ($\hat{m}$), the ST is equivalent to having a longitudinal field ($H_S \hat{m} \times \hat{y}$) added to the total effective fields when $\hat{\sigma}$ ($//\hat{y}$) is perpendicular to the $\hat{m}$, that qualitatively explains the observed abnormal switching where the switching direction of a perpendicular magnetic moment is determined by the sign of $J_c \cdot H_x$ where H_x is the external in-plane field to $\pm\hat{x}$ and J_c is the applied current density. In the case of an in-plane magnetization ($\hat{m}// \pm \hat{y}$), $\vec{\tau}_S$ acts as an anti-damping torque to change the effective magnetic damping, inducing the magnetization switching. From these observations [74, 72, 73] the SL-ST are more significant than the field-like-ST in the NM/FM/MO_x structures, strongly suggesting the behind physics for the magnetic excitation is due to the SHE rather than from the Rashba effect. If there exists a field-like ST or corresponding transverse field it does not contribute to the case for a perpendicular magnetization switching as we discuss below.

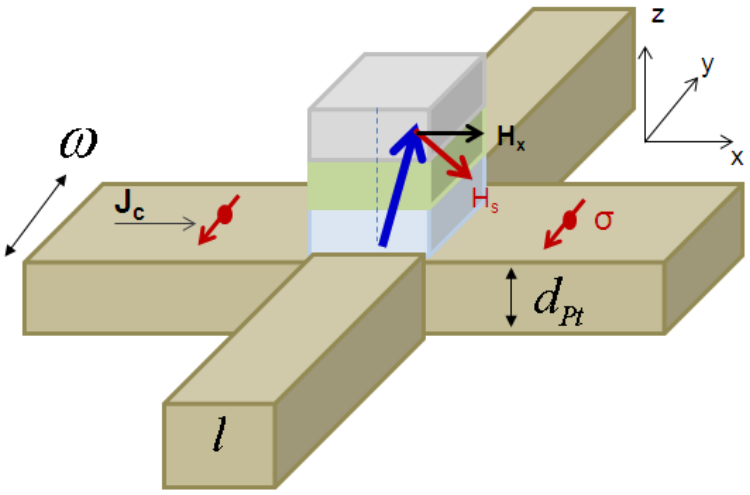

Figure 6.2: Schematic of Hall-cross bar device structure. A square shape of FM/MO_x/Cap multilayer dot is patterned at the center of a NM cross-bar, where FM/MO_x/Cap = Co/MgO/Ta and NM = Pt in this chapter. Spin-Hall effect generates opposite spin accumulation on the opposite lateral surface of current-carrying Pt nanowire. This spin current exerts a torque on the perpendicularly magnetized Co-dot at the interface. The magnetic state can be monitored by measuring the extraordinary Hall voltage across the other channel.

Another unsolved issue is that the magnitude of SHE-induced equivalent field (H_{SH}) seems to be small to drive a magnetization switching of a ferromagnetic dot (or layer) with a large perpendicular magnetic anisotropy (PMA): for instance, in Pt/Co, the estimated $H_S/J_c = (\hbar/2e)\theta_{SH}/M_S t_{Co} \approx 2.3\ Oe \cdot cm^2/MA$ when $M_s = 10^6\ A/m$, $t_{Co} = 0.9\ nm$ and θ_{SH}(Pt) $\sim$ 0.06 for $d_{Pt} = 4\ nm$ while the effective field (H_k^{eff}) of a PMA layer is typically very large, usually $H_k^{eff} > 1$ kOe. For a coherent rotation magnetic switching, the hard axis switching field should be at least more than $\sim H_k^{eff}/2$ (which would require $J_c > 210\ MA/cm^2$) in the absence of thermal agitation. (Note that the Oersted field $H_{oe}/J_c = d_{Pt}/2 \approx 0.25\ Oe \cdot cm^2/MA$ is one order of magnitude smaller).

In this paper we study a perpendicular magnetization switching in the

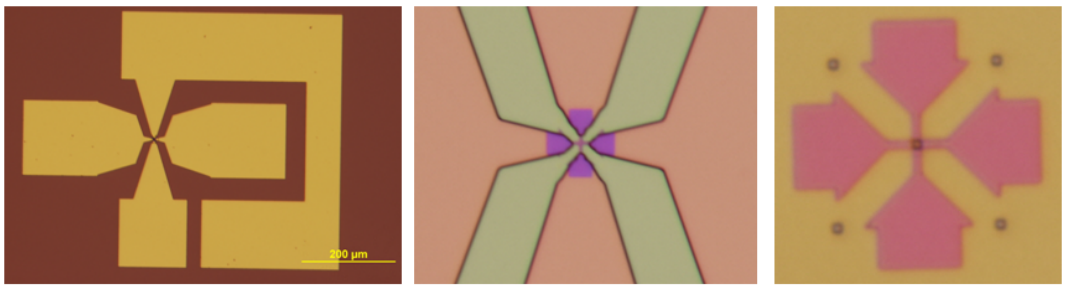

Figure 6.3: Optical images of the fabricated Hall-cross bar devices. (left) whole device including contact pads and Hall-cross bar. (center) zoomed image center area before depositing the electrical contact. (c) zoomed image with e-beam resists before patterning the square dot at the center. Additional four dots were defined in order to check the e-beam alignment and exposure.

multi-layer structure of Pt/Co/MgO/Ta via SHE-induced spin currents, and estimate the current-induced equivalent field or switching field (H_s) in the thermally activated switching regime, which is consistent with the predicted magnitude from the SHE. In fact we show that with the assist of Joule heating H_s can readily excite the reversal of a subvolume that drives the whole magnetization switching. We also investigate the switching currents and activation energy barriers as functions of Co-thickness (from 0.8 to 1.0 nm) and the current-channel widths (200 nm to 1000 nm), and obtain results that are fully consistent with thermally assisted H_s switching of subvolume domains that then drive the reversal of the entire nanodot.

6.3 Device Fabrication

We fabricated Hall-cross bar devices (see Fig. 6.2 and 6.3) from the thin film multilayer of, from bottom to top, Pt(4)/Co(0.8-1.0)/MgO(2)/Ta(2) (thickness in nm), deposited on thermally oxidized Si substrate by DC/RF magnetron sput-

tering at room temperature. The base pressure was $< 2 \times 10^{-8}$ Torr and the growth rates were kept low (< 0.3 Å$/s$). We deposited MgO instead AlOx on top of Pt/Co to test the diverse interface effect between the top oxide and the FM layer and to check the generality of the structure (NM/FM/MO_x) although the oxide-layer on top of the Co-layer affects the magnetic anisotropy. The Ta capping layer, a good oxygen absorber and compatible with MgO, protects the under-layers well during the fabrication and annealing, and the air-exposed oxidized Ta (or even pure Ta) is expected to have very high resistance so we can neglect the current-shunting effect through the Ta layer. We used e-beam lithography and ion-milling to define the current channel and the detection channel, with variations of the widths from 200 nm to 1000 nm. The square shape of Co-ferromagnetic dots was patterned at the center of the cross bars by subsequent aligned e-beam lithography and ion-milling, where the etching was stopped as close as possible at the Pt/Co interface by the use of mass-spectroscopy monitoring of the sputtering process. We evaporated Ti(5nm)/Au(100nm) for electrical contacts defined by photo-lithograph. After the fabrication the devices were annealed under high vacuum ($< 5 \times 10^{-7}$ Torr) at 320 ^oC for 1 hour to enhance the out-of-plane anisotropy of the Co and probably to improve the interface at Co/MgO by changing oxygen stoichiometry. (But this requires further analysis and work with different conditions and tools.) For monitoring the p(erpendicular)-Co magnetic state DC current (I) and AC current ($\sim 20\,\mu A$) were applied through the current-channel and DC (V_h) & AC (dV_h/dI) extraordinary (or referred to as anomalous) Hall voltages were measured through the detection channel (See Fig. 6.4). We also estimated the Joule heated temperature with the current-channel resistance (R_c).

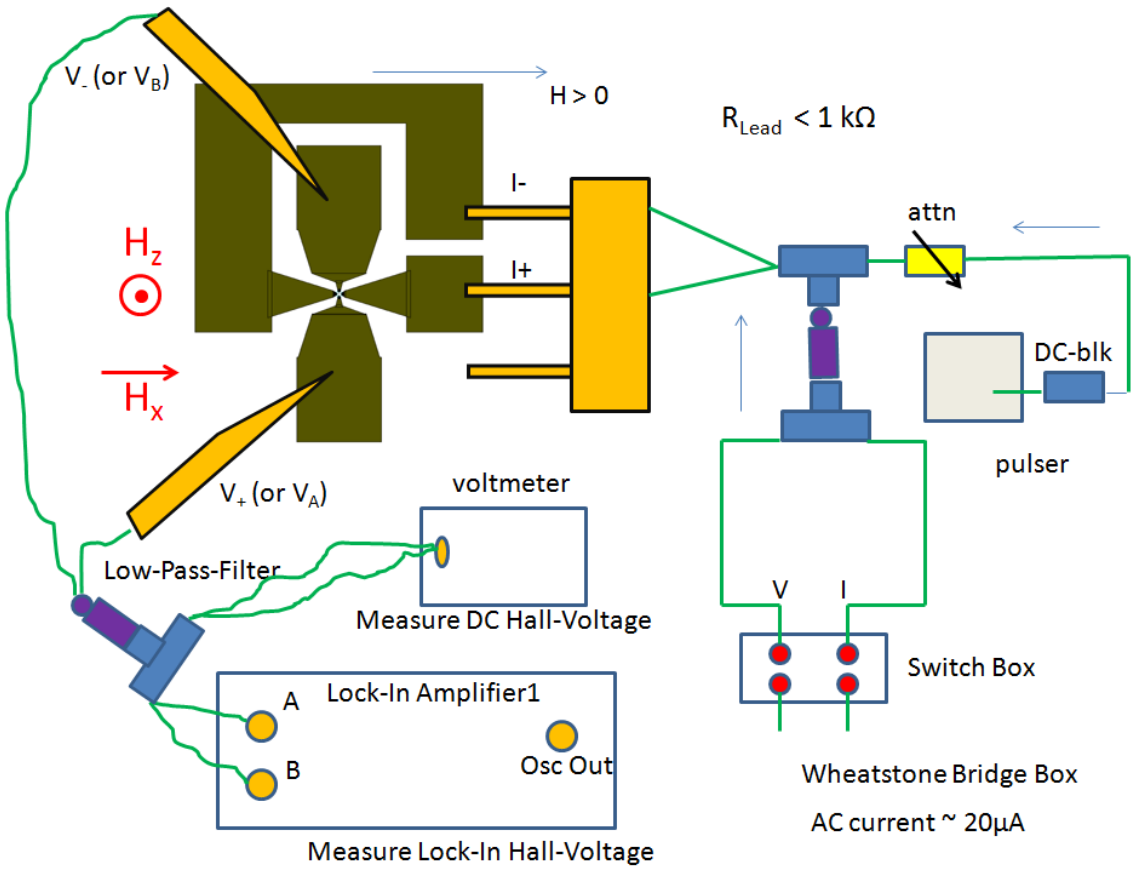

Figure 6.4: Scheme of measurement-setup (in the cage room of F20 at Clark). A DC current (I) is applied through the current channel to excite the perpendicular-Co dot while an external magnetic field is applied through the underneath GMW magnet. And a sensing AC current ($\sim 20\ \mu A$) is applied together through the Wheatstone bridge box for monitoring the magnetic state. DC (V_h) & AC (dV_h/dI) components extraordinary-Hall voltages are measured through the detection channel with a voltmeter and a lock-in-amplifier. The current-channel resistance (dV_c/dI) is also measured to estimate Joule heated temperature.

6.4 Sub-volume Excitation

First of all we characterize one particular device with l (detection channel length) = w (current channel width) ≈ 300 nm and $t_{Co} \approx 0.9$ nm while the general behavior was quite similar for all of the devices we measured. The inset of Fig. 6.5 shows the hysteresis loop measuring the dV_h/dI w.r.t. the out-of-plane field (H_z) at $I = 0$: the device exhibited a good PMA with the out-of-plane switching field (H_c) ∼ 360 Oe while the estimated $H_k \sim 4$ kOe by applying the in-plane field. To quantify the effective activation energy barrier (E_a) and the effective coercive field (H_{c0}) in the absence of thermal fluctuations of the device, we performed a typical ramp-rate measurement, measuring the average coercive field ($< H_c >$) as a function of the measured time (t_m) at room temperature (T_o = 295 K) (see Fig. 6.5). We obtained the thermal stability factor $\Delta = E_a/k_BT_o = 40.6 \pm 8$ ($E_a = 1.02 \pm 0.2$ eV) and $H_{c0} = 1440 \pm 190$ Oe from fitting the data to the Sharrock model:

$$< H_c >= H_{c0}\left[1 - \left[\frac{k_BT}{E_a} ln\left(\frac{f_o t_m}{ln2}\right)\right]^{1/2}\right] \tag{6.1}$$

where f_o is the characteristic fluctuation frequency (assuming f_o =1 GHz).

Within the single domain (or whole-volume excitation) model, the calculated $E_a(= \mu_o M_s H_{c0} V/2) \sim 37$ eV, with $H_{c0} = 1440$ Oe and $V = l\ w\ t_{Co}$, is much higher than the measured E_a, as well as $H_{c0} << H_k \sim 4$ kOe. This large discrepancy in the E_a and H_{c0} of the p-Co-dot can be understood with the presence of subvolume thermal activation and reversal [182, 183]. The sub-volume excitation has been suggested in p-MTJs based on Ta/CoFeB/MgO to explain that the intrinsic critical current (I_{c0}) increases with junction area ($A = l\ w$), whereas the Δ is almost constant if the junction size > 50 nm. This predicted $E_a \approx (\pi^3/4)A_{ex}t_{Co}$, when the lateral dimension of the p-Co dot is larger than

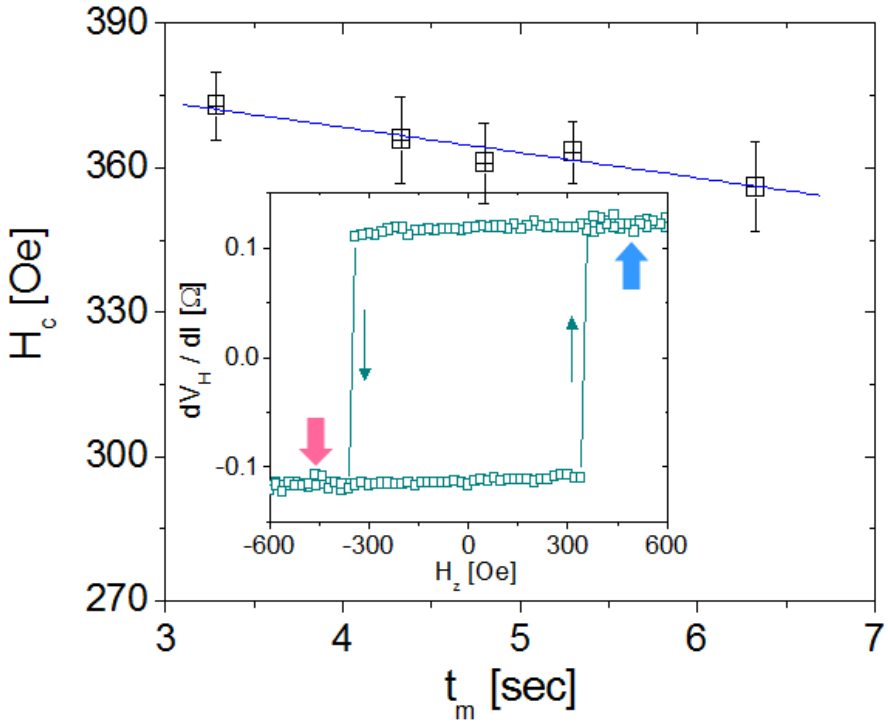

Figure 6.5: Measured average switching field or coercive field ($< |H_c| >$) of the device as a function of the measured time (t_m) at room temperature. This is a typical ramp-rate measurement for estimating the effective activation energy barrier (E_a) and the effective coercive field (H_{c0}) for a magnetic device in the absence of thermal fluctuations, by fitting the data to the Sharrock model. The estimated $E_a/k_BT_o = 40.6 \pm 8$ and $H_{c0} = 1440 \pm 190$ Oe. Inset: An example of hysteresis loop measuring dV_h/dI as a function of out-of-plane magnetic field (H_z) at $I = 0$.

the domain-wall with (δ_{dw}), where A_{ex} is the exchange-stiffness, $E_a = K_{eff}V_S$, $K_{eff} = \mu_o H_{c0} M_s/2$, $V_s = \pi(\delta_{dw}/2)^2 t_{Co}$ and $\delta_{dw} = \pi(A_{ex}/K_{eff})^{1/2}$. With the measured E_a and H_{c0}, the diameter of the sub-volume (V_s) is estimated $\approx$ 55 nm (if it is circular), which is comparable to the experimentally obtained sizes (40 – 50 nm) in the Ta/CoFeB/MgO p-MTJs. From our activation energy measurement we suppose that for a patterned p-Co dot that is greater than 50 nm the moment is reversed at the switching field (H_c) by a thermally activated sub-volume whose

anisotropy is lower than other that is immediately propagated to the rest of the p-Co dot.

6.5 Current-induced deterministic switching

Fig. 6.6 shows the examples of the current-induced switching under an external H_z = ±200 Oe. In the measurements the p-Co dot was initially set to m_z = +1 (-1) and the opposite direction of field H_z = -200 (+200) Oe was applied, then the I was swept back-and-forth with positive or negative initial direction. In the current sweepings, we observed that the p-Co-dot did not swing back to the original magnetic state after it became parallel to the H_z (from 20 Oe to 400 Oe) and that there was no dependence of the $|I_s|$'s on the initial current direction or the initial magnetic states, indicating the reversals were mostly thermally-driven reversals due to the enhanced background T from the Joule heating.

Fig. 6.7 shows the examples of the current-induced deterministic switching of the p-Co dot under an external H_x = ±300 Oe. The sudden reversals in dV_H/dI, at $|I_s| \sim 0.65 \pm 0.02$ mA ($J_c \sim 44\ MA/cm^2$), correspond to the perpendicular switching of the Co dot, at which V_H exhibits the sharp jumps. (Note that in both dV_H/dI & V_H curves there was a background signal, which was linear with current, probably due to the small deviation of the p-Co dot from the center (the accuracy of the e-beam alignment was ~ ±20 nm), which has been often observed in Hall effect measurements. The p-Co was switched from $m_z \approx +1 > -1$ when $I_s \cdot H_x > 0$ while $-1 > +1$ when $I_s \cdot H_x < 0$, which is consistent with previous observations [74, 72] in Pt/Co/AlOx structures. At higher currents, $|I_p| \sim 0.94 \pm 0.02$ mA ($J_c \sim 64\ MA/cm^2$), we observed peaks & dips in dV_H/dI above which

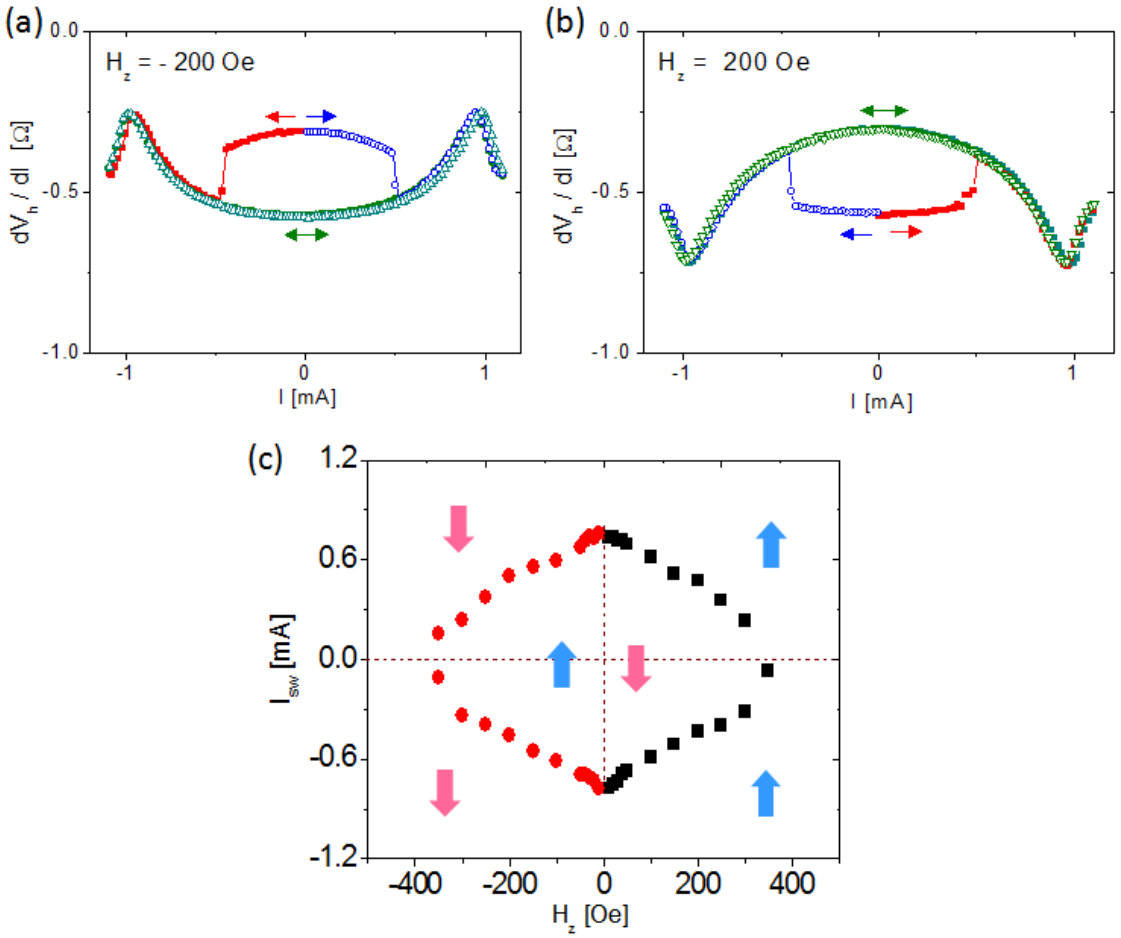

Figure 6.6: Examples of the current-induced switching under an out-of-plane external field (H_z). (a) The p-Co dot was initially set to "up" (m_z = +1), then opposite direction of field H_z = -200 Oe was applied. The current (I) was swept back-and-forth with two different initial directions: the first direction of current was positive (blue) or negative (red). (b) the other case of (a). In both cases, the p-Co-dot did not swing back to the original magnetic state after it is parallel to the H_z. (c) Measured switching current (I_{SW}) as functions of H_z and I. H_z was varied from 20 Oe to 400 Oe ($\sim H_c$). We observed no dependence of the magnitude of switching currents on the current directions or on the initial magnetic state, indicating the switching was purely (or almost) thermally-driven reversals. Fig. 6.10 plots the average of $|I_{SW}|$ as the function of H_z.

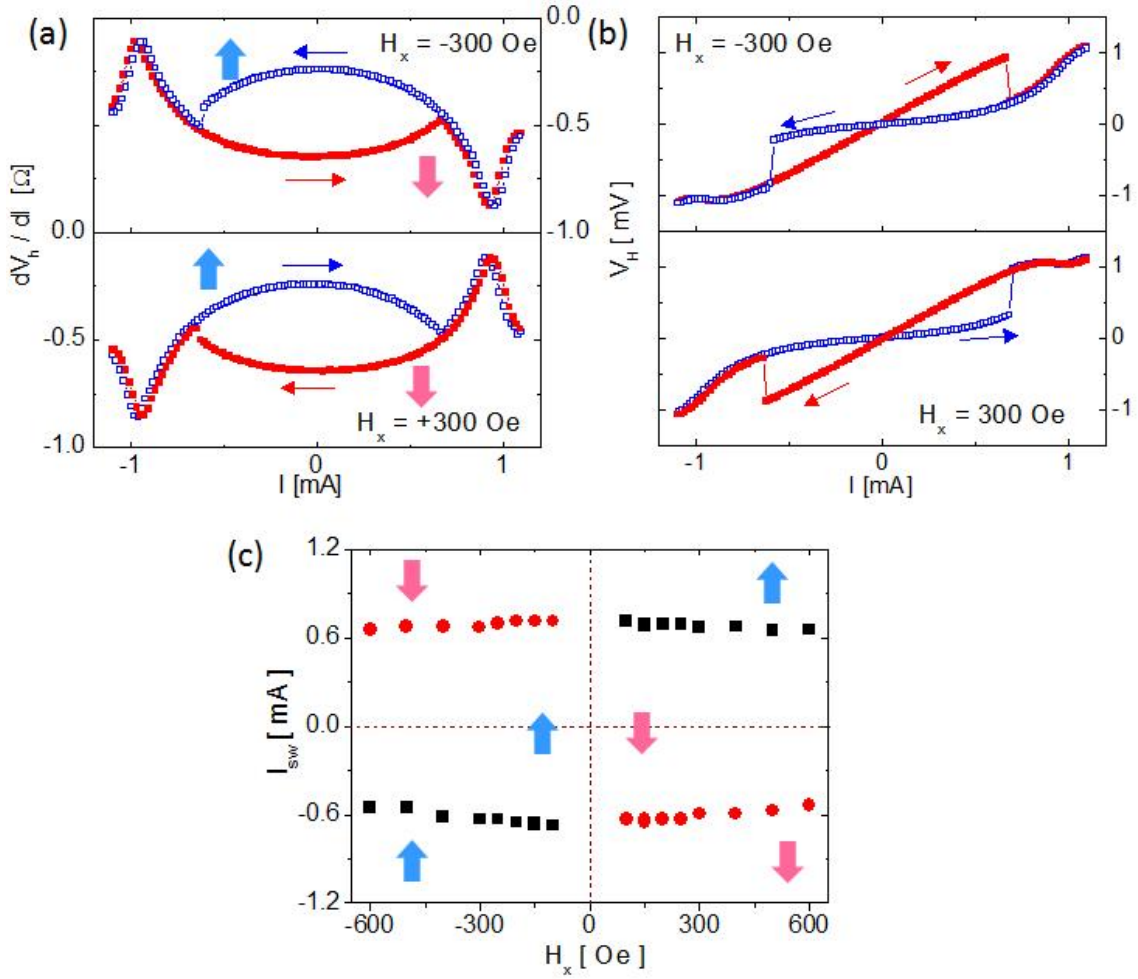

Figure 6.7: Examples of current-induced deterministic switching of p-Co dot under an external $H_x = \pm 300$ Oe where H_x is the in-plane field along the current channel. (a) Measured dV_H/dI (b) Measured V_H as a function of I. (c) Measured switching current (I_{SW}) as a function of H_x. The p-Co dot was switched from $m_z \approx +1 > -1$ when $I \cdot H_x > 0$ while $-1 > +1$ when $I \cdot H_x < 0$, which is consistent with previous observations in $Pt/Co/AlO_x$ multilayer structures [74, 72]. Fig. 6.10 plots the average of $|I_{SW}|$ as the function of H_x.

the Hall resistance sharply decreases towards the background signal. From the observations that the currents for the peaks & dips were independent of the external field orientation (see Fig. 6.6 and 6.7), we concluded that these resulted from the strong loss of PMA in the p-Co dot due to the Joule heating. Note the $|I_p|$ for the peaks & dips slightly increased with a large $|H_z|$.

6.6 Estimation of device temperature from the Joule heating

To quantify the Joule heating, which is important in understanding, we compared the measured R_c when the substrate was heated to T and the measured R_c when $|I|$ was applied. We empirically obtained the joule heated device temperature (T), $T \approx T_o + 227(K/mA^2) \times I^2$. From this the T was estimated $\sim$ 391 K at $|I_s| \sim 0.65 \pm 0.02$ mA ($J_c \sim 44\ MA/cm^2$), and $T \sim 496$ K at $|I_p| \sim 0.94 \pm 0.02$ mA ($J_c \sim 64\ MA/cm^2$). Furthermore we expected its Curie temperature, $T_c \sim (583 \pm 23)$ K, from the fitting to $R_h^*(T(I)) = R_{h0}^*(1 - (T(I)/T_c)^\alpha)^\beta$, as shown in Fig. 6.8, where $R_h^*(I) = \Delta V_h(I)/2I$ is the maximum hall-resistance (or $|m_z| \approx 1$) at I by measuring the difference of V_h at large $H_z = \pm 1.5$ kOe, with the assumption of $R_h^*(T(I)) \propto M_s(T)$ [186]. The estimated T_c was very close to the annealing temperature and the reported T_c ($\sim$ 600 K) of a few atomic layers of Co thin-film on a NM [184, 185]. At the maximum applied current, $|I_m| \sim 1.1$ mA ($J_c \sim 75\ MA/cm^2$), the $T \sim 570$ K and both Hall signals were almost similar to the background signal, at which the ferromagnetic Co layer is expected to start a re-orientation of the easy-axis. We observed $\sim$ 10 % of reduction in $dV_H/dI(m_z \approx +1) - dV_H/dI(m_z \approx -1)$ at $I = 0$ after the 1^{st} scan with I, possibly due to the diffusion or inter-mixing of atoms at the interfaces. The magnetic signal permanently disappeared after a very high current $|I| > 1.5$ mA ($J_c > 100$

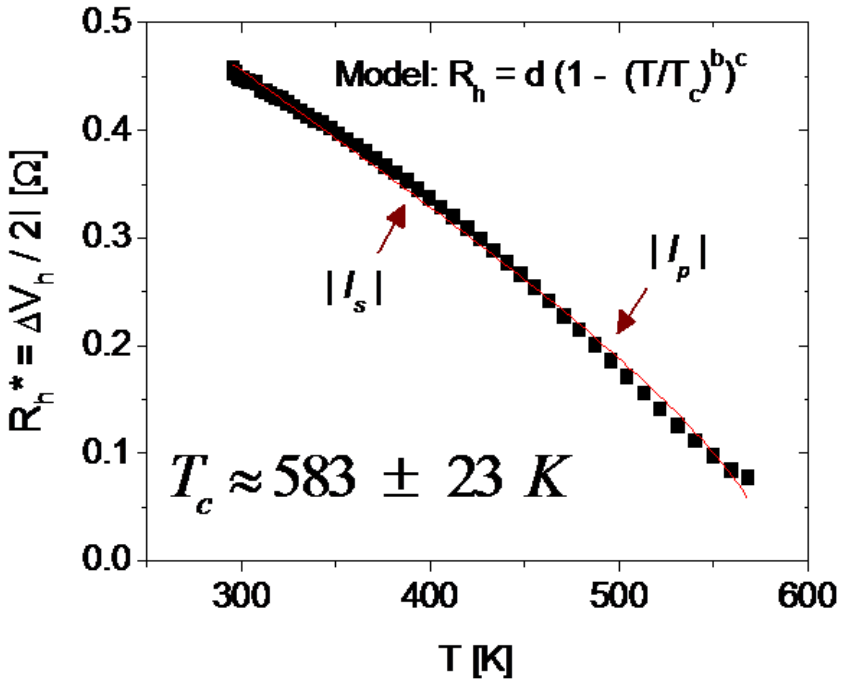

Figure 6.8: Estimated Curie temperature (T_c) of the device is $\approx$ 583 $\pm$ 23 K, which is obtained from the fitting to $R_h^*(T(I)) = R_{h0}^*(1 - (T(I)/T_c)^\alpha)^\beta$ where $R_h^*(I) = \Delta V_h(I)/2I$ is the maximum Hall-resistance (or $|m_z| \approx 1$) at I by measuring the difference of V_h at large $H_z = \pm 1.5$ kOe. We assume that $R_h^*(T(I))$ is linearly proportional to $M_s(T)$. The estimated T_c of a few atomic layers of Co thin-film on the NM is very close to the reported values [184, 185] and much lower than the T_c of bulk Co (~ 1400 K).

MA/cm^2) was applied in other devices.

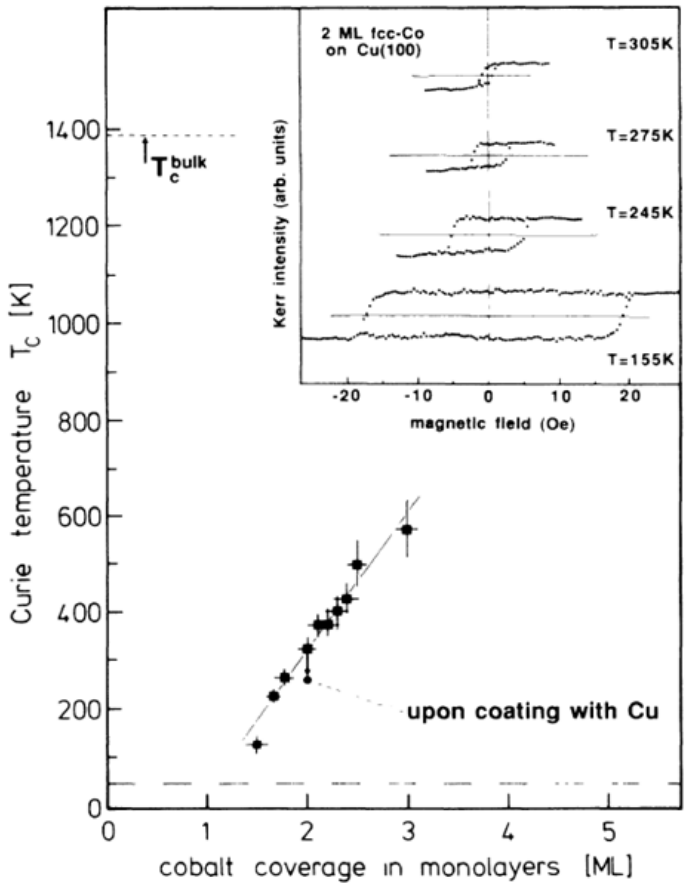

Figure 6.9: Illustration of Curie temperature (T_c) of ultrathin films of Co grown on Cu surfaces as a function of Co-thickness. The T_c increases with its thickness. The T_c of 3 monolayers (~ 1 nm) is ~ 600 K, which is much lower than T_c of the bulk Co ~ 1400 K. Inset: Variation of hysteresis loop of a 2-mononlayer (ML) film with temperature. From [184].

6.7 Estimation of current-induced field for the thermally actived switching

If the p-Co dot follows the Stoner-Wohlfarth switching behavior [187], the switching field (H_c) should decrease with a tilt angle (θ) of an applied field from the easy axis until $\theta = 45^o$ and increase with the θ for $45^o < \theta < 90^o$, i.e.

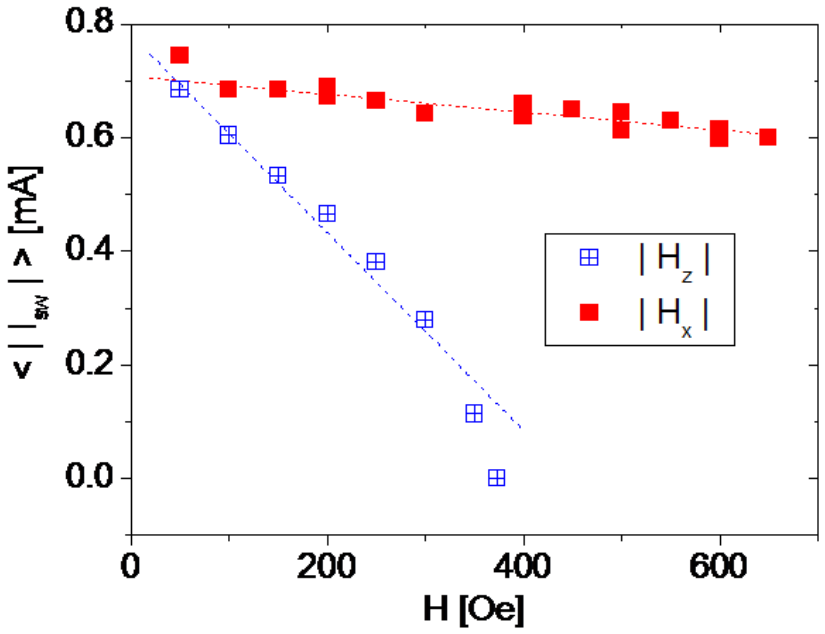

Figure 6.10: Measured average switching currents ($< |I_{sw}| >$) as functions of the $|H_z|$, directed to normal-to-plane (easy-axis of the Co-dot), and the $|H_x|$, parallel to the current-direction in the Pt nanowire. The latter direction is one of the hard-axis but parallel (or anti-parallel) to the spin-hall-induced equivalent field.

$H_c(\theta)/H_c(\theta = 0^o) = 1/\left(cos^{2/3}\theta + sin^{2/3}\theta\right)^{3/2}$. However the observed H_c in our devices increased with θ, roughly (but not exactly) following $\sim 1/cos\theta$ as shown in Fig. 6.11, which was already implied in previous experiments [74, 72]. In a magnetization reversal involving a domain nucleation (or sub-volume excitation) and propagation [188, 189], if multiple-domain state is stable and the domain walls are weakly pinned by a pinning potential, the angular dependence of H_c should follow Kondorsky function ($1/cos\theta$) [190, 191] because the pressure on the domain walls is a function of $1/cos\theta$. In the figure, however, the measured angular dependence of H_c slightly deviates from the Kondorsky function as the θ approaches to 90^o. This is due to the coherent rotation of the magnetization vectors in the pinned domains with a strong in-plane hard-axis field, leading to

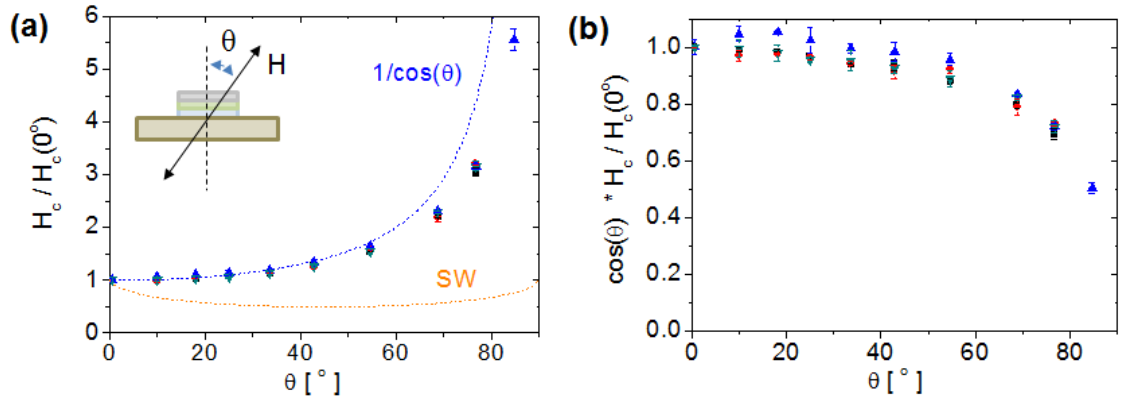

Figure 6.11: (a) Measured switching field (H_c), normalized by $H_c(\theta = 0^o)$, as a function of a tilt angle (θ) from the easy axis ($\theta = 0^o$). (b) Replot of (a) with $cos(\theta) \times H_c(\theta)/H_c(0^o)$. If the p-Co dot follows the Stoner-Wohlfarth (SW) switching behavior [187], the angular dependence of the H_c should be the yellow-dot curve, i.e. $H_c(\theta)/H_c(\theta = 0^o) = 1/\left(cos^{2/3}\theta + sin^{2/3}\theta\right)^{3/2}$. For a magnetization reversal involving a domain nucleation and propagation, and multiple-domain state is stable and the domain walls are weakly pinned by a pinning potential, the angular dependence of H_c should follow the blue dot or Kondorsky function $(1/cos\theta)$.

the modification of Kondorsky function [191].

Based on our observations, the magnetic reversal is dominated by the effective torque (or field) acting on the pinned DW (probably located at the boundaries of the p-Co dot). Moreover the out-of-plane component of the total external field is the principal factor for the thermally activated reversals by shifting the thermal stability factor (Δ) if the p-Co dot system perfectly follows the Kondorsky reversal behavior. For a Bloch DW one of the configurations in Fig. 6.12 is energetically favorable under $H_x > 0$ or $H_x < 0$, and the average of the out-of-plane field from the spin-Hall field (H_{SH}) is simply $(1/\pi)\int_0^{\pi} d\varphi\, H_{SH} sin\varphi = (2/\pi)H_{SH}$ on the pinned DW. Thus, as subsequent to Eq.

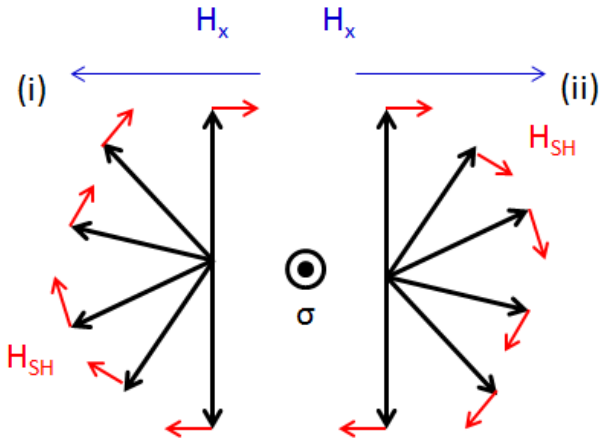

Figure 6.12: Schematic of spin-Hall field (H_s) acting on the Bloch wall and two possible orientations of the Bloch wall along the current direction ($//\hat{x}$). For $H_x < 0$ the orientation in (i) is more energetically favorable than the other in (ii). For $H_x > 0$, the direction in (ii) is preferable.

6.2 within the context of Arrhenius law, the Δ has a form of

$$\Delta = \left(\frac{E_a(I)}{k_B T_o(1+\kappa I^2)}\right)\left(1 - \frac{H_z + H_s(I)}{H_{c0}(I)}\right)^2 \tag{6.2}$$

where H_z is the out-of-plane applied field, $H_s(I)$ is the current-induced equivalent field for the switching, $T_o = 295$ K, $\kappa = 227\ K/mA^2$ (as we mentioned above), $E_a(I)$ is the energy barrier as a function of I (or enhanced T) and $H_{c0}(I)$ is the effective coercive field in the absence of thermal fluctuations as a function of I (or enhanced T).

Fig. 6.10 shows the averaged $|I_s|$ of the p-Co dot under an external H_x or H_z at which the Δ was equal as long as the t_m was similar. (Note that t_m was $\sim 3.47s$ in the current-induced switching, giving < 1 % error in Eq. 6.1 so we can neglect the small difference.) The simplest case we can assume is that the magnetic properties are invariant with the environment T: i.e. $E_a(I) = E_a(0)$ and $H_{c0}(I) = H_{c0}(0)$. With the measured parameters ($E_a(0)$, T_o, κ, I, $h_z \equiv H_z/H_{c0}(0)$),

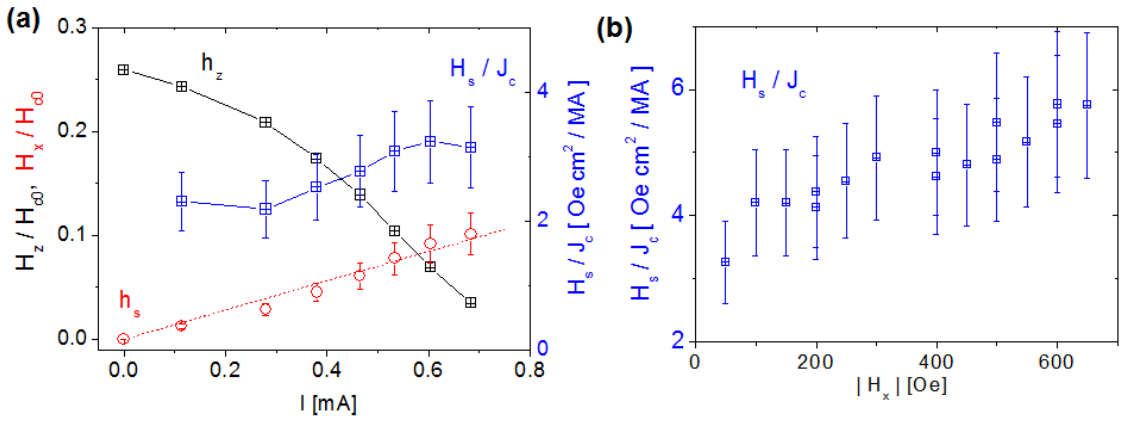

Figure 6.13: Estimation of the current induced effective or switching field (H_s/J_c) with the assumption of no joule-heating effect on the magnetic system except the increase of the background temperature: i.e. $E_a(I) = E_a(0)$ and $H_{c0}(I) = H_{c0}(0)$. (a) Plot of measured $h_z = H_z/H_{c0}$ (black) from Fig. 6.10. Calculated $h_s = H_s/H_{c0}$ (red) using Eq. 6.2 and converted H_S/J_c (blue) under H_z. (b) Estimated H_S/J_c under H_x.

the h_s ($H_s(I)/H_{c0}(0)$) and H_s/J_c (= $h_s H_{c0}(0)$ $(t_{Co} + d_{Pt})$ w/I) were calculated using Eq. 6.2 (and assuming $\sigma_{Pt} = \sigma_{Co}$) and plotted in Fig. 6.13 under H_z (Fig. 6.13a) and H_x (Fig. 6.13b). The estimated H_s/J_c was $\sim 2-3$ Oe cm^2/MA under H_z, while the H_s/J_c varied from ~ 3 to ~ 6 Oe cm^2/MA under H_x, which are quite comparable to previous experiments [74, 72, 192]. The increase of H_s/J_c with H_x is due to the deviation from the Kondorsky function with H_x, because the coherent rotation of the magnetization at the pinned domain gives more the average out-of-plane field from the spin-Hall field (H_{SH}) or lowers the effective energy barrier, where the latter is consistent with the modified Kondorsky and with measured $(H_c(\theta)/H_c(\theta = 0^o))\, cos\theta$ as shown in Fig. 6.11. The esimated magnitudes are at least $1.5-4$ times larger than the expected one from the SHE ($(2/\pi)H_{SH}/J_c \approx 1.5\ Oe \cdot cm^2/MA$). These results were from the assumption that the magnetic device does not have any heating effect on the magnetic system except the elevations of the background temperature (T) and of the strength of

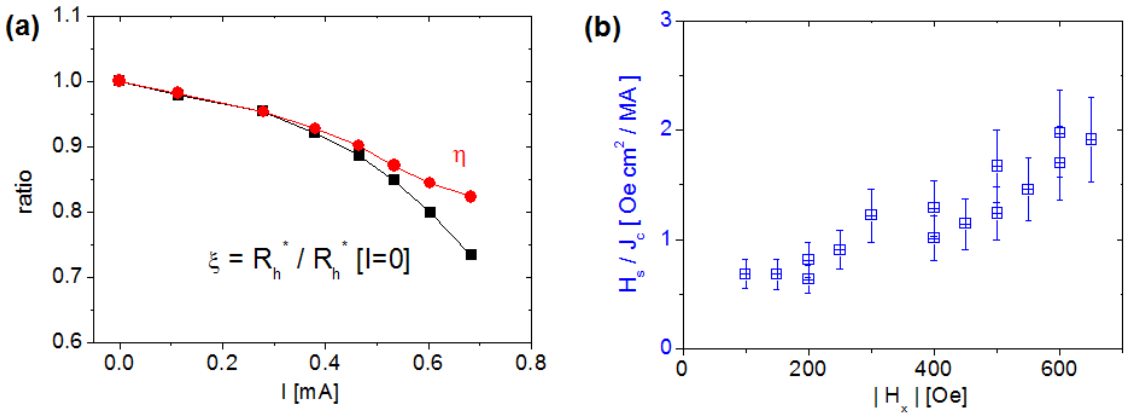

Figure 6.14: Estimation of the current induced effective or switching field (H_s/J_c) considering heating effect on the magnetic system. (a) Estimated heating effect on the magnetic system. The $\eta(I)$ is the reduction factor in the E_a and the $\xi(I)$ is the reduction factor in the H_{c0} due to the enhanced temperature from Joule heating. (b) Estimated current induced field (H_S) for a given current density (J_c) that was obtained from Fig. 6.10 under the in-plane field (H_x) and using Eq. 6.2.

the thermal fluctuations, or at least provide the upper bound in the estimation of H_s/J_c for the device.

Now we consider the case for the maximized heating effect on the magnetic system. The SHE induced fields are expected to exert symmetrically on the pinned DWs under H_z (i.e. net H_{SH} is zero) because there is no energetically preference between two Bloch DW configurations in Fig. 6.12. Hence the switching under H_z was mostly from the reduction of E_a ($\sim A_{ex}$) and H_{c0} ($\sim M_s$) because the variation of T/T_c was very significant in the device as discussed above. Assuming that $E_a(I) = \eta(I)E_a(0)$ and $H_{c0}(I) = \xi(I)H_{c0}(0)$ where $\eta(I)$ is the reduction factor in E_a and $\xi(I) = R_h^*(I)/R_h^*(0)$ because $H_{c0} \propto M_s \propto R_h^*(I)$, and that $H_s(I) = 0$ under H_z, we calculated $\eta(I)$ using Eq. 6.2 and compared it to the calculated $\xi(I)$ in Fig. 6.14a. Both values similarly decrease with I (or T) although they

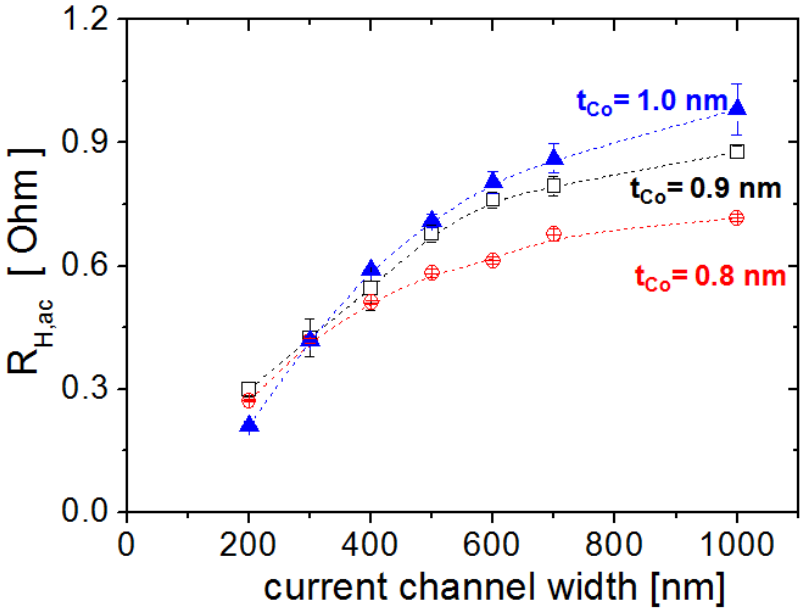

Figure 6.15: Measured AC extra-ordinary Hall resistances as a function of the current channel width (= detection channel width) for t_{Co} (thickness of Co) = 0.8, 0.9 and 1.0 nm.

are deviated at higher I, implying that the E_a and H_{c0} might be a little different functions with T. With the estimated $\eta(I)$ we calculated H_s/J_c under H_x , using Eq. 6.2, as shown in Fig. 6.14b. The estimated H_s/J_c increases from $\sim$ 1 to $\sim$ 2 $Oe \cdot cm^2/MA$ as H_x ranges, that varies within the predicted magnitude from the SHE ($(2/\pi)H_{SH}/J_c \approx 1.5\ Oe \cdot cm^2/MA$).

6.8 Dependence on the thickness of Co and current channel width

Lastly we investigated $R_{H,ac}$, E_a and I_s as functions of t_{Co} (from 0.8 to 1.0 nm) and w (200 nm to 1000 nm), and the results are shown in Fig. 6.15, 6.16 and

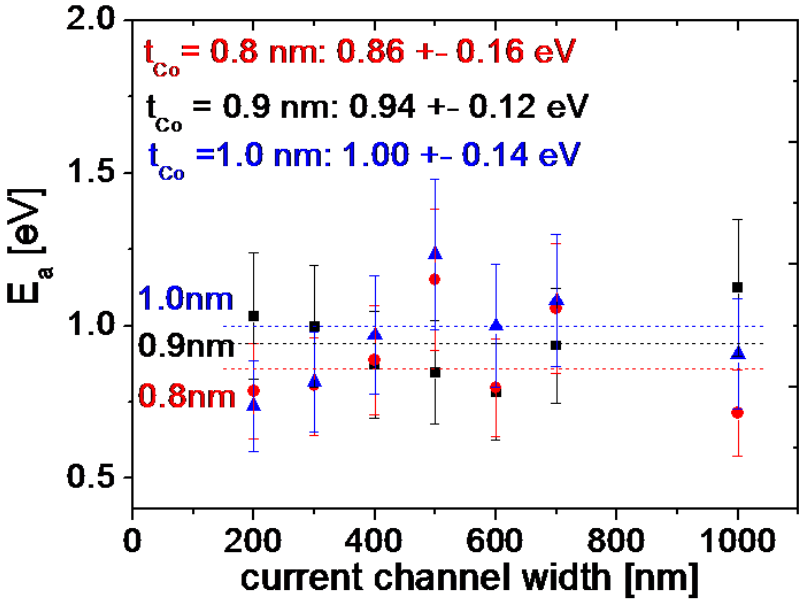

Figure 6.16: Estimated Energy barrier (E_a) as a function of the current channel width (w) for t_{Co} (thickness of Co) = 0.8, 0.9 and 1.0 nm. The E_a and H_{c0} are estimated for each device by the ramp-rate measurement method presented in Fig. 6.5. There is no apparent trend in the E_a w.r.t the w, but the average of E_a increases with increasing t_{Co}, which is consistent with the subvolume excitation model. A subvolume with a lower anisotropy than other determines the energy barrier of the whole confined Co moment. The dimension of the subvolume was estimated ~ 40-50 nm.

6.17. The measured ac EHE resistance, $R_{H,ac} = V_{H,ac}/I_{ac}$ increased with the w, where $I_{ac} = 20\ \mu A$, while it seemed to saturate at a large w (> 1000 nm) (see Fig. 6.15). The w-dependence of $R_{H,ac}$ was unexpected because the predicted $R_{H,ac} = A\rho + B\rho^2$ where A & B are constant values but depending on the underlying mechanism [193] and ρ is the resistivity of the p-Co, and the ρ is expected to be same for a given thickness. We surmised that this might be from the geometry-dependent current distribution in Pt and Co: as the w decreased a smaller $V_{H,ac}$ was measured because the $V_{H,ac}$ is proportional to the current amount through the ferromagnet, but probably less amount in the applied cur-

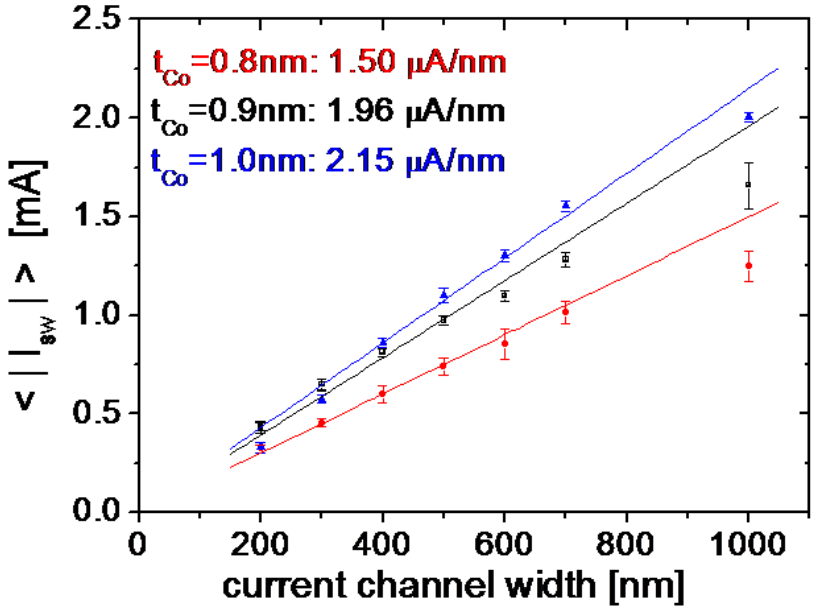

Figure 6.17: Measured switching currents ($< |I_{SW}| >$) as a function of the current channel width (= detection channel width) for t_{Co} (thickness of Co) = 0.8, 0.9 and 1.0 nm, averaged under H_x from 100 Oe to 600 Oe.

rent flowed through the p-Co dot with the decreased dimension [194]. Fig. 6.16 shows the measured E_a, obtained from the ramp-rate measurement and fit to the Sharrock model for each device. The average of E_a was proportional to the t_{Co} but did not exhibit any trend with the w, which is consistent with expectation from the sub-volume excitation model. On the other hand the $< |I_{sw}| >$, the average of $|I_{sw}|$ for H_x = 150 - 600 Oe, was directly proportional to the w (see Fig. 6.17) because the current-density (J_c) determines the increase of the background temperature (from the Joule heating) and the magnitude of the spin-Hall field (H_s). And the $< |I_{sw}| >$ was approximately increased with the t_{Co} (or E_a) and overall we obtained $I_{sw} \propto w \cdot E_a$, which is dissimilar to our previous prediction [74] of $I_{sw} \propto E_a/w$ (if $l = w$) for a coherent rotation magnetic switching. The latter should be applicable when the device's lateral dimensions are below ~ 50 nm at which point the perpendicular magnetic system would behave as a

single-domain and $E_a \propto l\, w\, t_{Co}$.

6.9 Conclusion

In summary, we have studied the thermally assisted reversal via spin-Hall induced spin currents of the perpendicular magnetization in Co/MgO/Ta multilayer nanodots patterned onto a Pt nanostrip. We found that the switching mechanism was consistent with the sub-volume excitation model in that the E_a is independent with the lateral dimensions (when > 200 nm and we expect this until the dimension $\sim$ 50 nm) but proportional to the Co thickness (t_{Co}). We estimated the current-induced equivalent field ($H_s/J_c \approx 1 - 2\ Oe \cdot cm^2/MA$) on the thermally activated switching regime that was quite consistent with the predicted value ($(2/\pi)H_{SH}/J_c \approx 1.5\ Oe \cdot cm^2/MA$) from the previous determination of the spin Hall angle (6%) [181] in sputtered Pt films. We conclude that even small field magnitude can drive the deterministic switching with the help of heating effect on the ultrathin perpendicular magnetic system. Understanding the reality in an ultrathin perpendicular magnetic system would help design a spintronic device and suggest a new pathway for a better performance.

CHAPTER 7

SUMMARY AND CONCLUSION

This dissertation summarized my experimental works on the non-collinear spin-transfer-torque effects in orthogonal magnetic nanostructures. I have studied (1) the ultrafast nanomagnet switching, (2) the quasi-linear spin-torque nano-oscillator (STNO), and (3) the spin-Hall induced perpendicular nanomagnet switching. The most important and common feature in the device structures I studied is that the spin-polarization is non-collinear to the orientation of the magnetic free layer (FL) at equilibrium in that the Slonczewksi spin-torque has both (anti-)damping and an equivalent field torque effects.

In my first study [Chapter 2 and 3], I have demonstrated experimentally the spin-torque (τ_{st}) driven ultrafast nanomagnet switching. In a conventional spin-torque device structure, where the spin polarizer (SP) is collinear with the FL, there is an incubation time (> 1ns) that is inevitable to make the FL excited enough to switch. The ballistic switching is defined as a quick half of rotation of the FL from one stable state to the other without any pre-oscillations so it provides a very fast and energy-efficient way of magnetization reversal. To achieve faster switching by τ_{st} with pulse widths < 200 ps, I fabricated nanopillar spin-valve devices incorporating both an out-of-plane spin-polarizer (OPP) and an in-plane polarizer/analyzer (IPP), and showed much improvements in the switching speed (~10 times) comparing to the spin-valve device without the OPP. I also demonstrated a reliable spin-torque driven ballistic precessional switching, with pulse widths down to 50 ps. During the investigation I explained the physical origin of the observed asymmetric threshold currents as functions of the switching direction and the pulse polarity, which is beneficial

for a non-toggle write operation. Based on my macrospin and micromagnetic studies, these strong asymmetric responses are originated from the strong τ_{st} from the IPP and the inhomogeneous stray fields from the two polarizers. Additionally, by controlling the magnetic damping, I was able to suppress the magnetic ringing that occurs after the fast switching. This made the switching more reliable without sacrificing the switching currents at the ballistic precessional switching time scale.

In my second study [Chapter 4 and 5], I have discovered the quasi-linear behavior of a spin-torque nano-oscillator (STNO). The τ_{st} can excite the persistent magnetic precession in magnetic nanostructures at microwave frequencies when the τ_{st} is sufficient to compensate the magnetic damping torque. This opens a technological possibility of the nanoscale microwave generator that can be frequency-tunable by an applied dc current (I). For a practical STNO the generated microwave power (p) and the spectral linewidth (Δf) should be improved significantly. I studied p, Δf, dp/dI, df/dI and their relations of a STNO in which the precessional axis (φ_o) of the FL was controlled by an external in-plane hard axis magnetic field (H_y). In the course of this investigation I discovered the quasi-linear regime with a small non-linearity over a broad range of field and current bias where the STNO exhibits low dp/dI, df/dI and relatively strong coherence ($\Delta f \sim 5$ MHz). I found that the unusual quasi-linear behavior of the STNO, though its small oscillation power, is related with several interesting observations: the transition from multiple (two) modes to a single mode excitation, the change of the red-to-blue shift and the power saturation at high I and the power reduction as H_y increases. From macrospin analysis, the change of the red shift to the blue shift is from the amplitude-dependent red shift effect due to the demagnetization field is closely balanced by the blue shift effect due

to the in-plane anisotropy field. The power decreases (or the threshold current increases) as the φ_o approaches to perpendicular to the RL due to the reduced τ_{st} efficiency for the auto-oscillation. However, the macrospin model does not fully explain our observations. Our micromagnetic studies reveal that the transition from multiple modes to a single mode excitation is from more homogeneous distribution of the internal fields as H_y increases and that the power saturation at high I_{dc}, or the strong enhancement of the dynamic damping, results from the increased local region that cannot be excited by the τ_{st}. The combined effects make it possible the STNO behave quasi-linearly with the help of strong enhancement of the effective nonlinear damping (and dynamic damping) at the optimum bias fields. I also studied another type of coherent STNO driven by an OPP and an IPP where the oscillator showed low Δf (< 8 MHz) and the power saturation at high I when the external field is applied along the easy axis to cancel the dipole field from the IPP. The reduction of the τ_{st} efficiency at the coherent regime, or the enhancement of the dynamic damping, is originated from the ST competition in which the strong τ_{st} from the IPP forces the FL to the easy axis while the one from the OPP rotates the FL.

In my third study [Chapter 6], I have investigated the perpendicular magnetization switching via spin Hall induced spin currents. Spin Hall effect (SHE) is the electrical transport phenomena originated from a relativistic spin-orbit interaction that leads to the coupling of a charge current and a transverse spin current. This generates opposite spin accumulation on the opposing lateral surface of a current-carrying wire. Recent experiments have demonstrated the manipulation of a magnetic moment by τ_{st} from pure spin currents when a ferromagnetic layer is adjacent to a normal metal with a large spin-Hall angle. This suggests a new way of nanomagnet control without a RL and with the sep-

aration of write and read channels. I studied a perpendicularly magnetized Co nanodot switching by the SHE-induced τ_{st} on the multilayer structure of Pt/Co/MgO/Ta. In the thermally activated reversal regime I estimated the current induced effective field (H_s) that has a strength consistent with the predicted magnitude from the spin Hall effect in Pt when taking into account the Joule heating effect on the ultrathin magnetic system. In the reversal process an excitation/activation of a subvolume drives the entire magnetization switching, thus even a small but heat-assisted H_s can reverse such a Co dot with a strong perpendicular magnetic anisotropy. I also investigated the switching currents and the activation energy barriers as function of Co-thickness (from 0.8 to 1.0 nm) and the current-channel width (200 nm to 1000 nm), and found the consistency with the sub-volume excitation model and with the spin-Hall effect.

The investigation of spin-transfer-torque driven magnetic excitations is still full of importance and challenge. I believe the research on the manipulation of nanomagnets via current-induced torques will continue as one of the main topics on the condensed matter physics and spintronics, especially in a system with a strong spin-orbit coupling. In addition, an electric field effect on the ultrathin magnetic layer would provide new functional and energy-efficient magnetic devices.

BIBLIOGRAPHY

[1] S. D. Bader and S.S.P. Parkin. "Spintronics". *Annu. Rev. Condens. Matter Phys.* **1**, 71-88, (2010).

[2] Gary A. Prinz. "Magnetoelectronics". *Science* **282**, 1660, (1998).

[3] S. A. Wolf, D. D. Awschalom, R. A. Buhrman, J. M. Daughton, S. von Molnar,M. L. Roukes, A. Y. Chtchelkanova, and D.M. Treger. "Spintronics: A spin-based electronics vision for the future". *Science* **294**, 1488, (2001).

[4] Claude Chappert, Albert Fert and Frederic Nguyen Van Dau. "The emergence of spin electronics in data storage". *Nat. Mat.* **6**, 813-823, (2007).

[5] Igor Zutic, Jaroslav Fabian and S. Das Sarma. "Spintronics: Fundamentals and applications". *Rev. Mod. Phys.* **76**, 323, (2004).

[6] S. A. Wolf, A. Y. Chtchelkanova and D. M. Treger. "Spintronics-A retrospective and perspective". *IBM J. RES. & DEV. VOL.* **50**, 101-110, (2006).

[7] M. N. Baibich, J. M. Broto, A. Fert, F. N. Van Dau, F. Petroff, P. Etienne, G. Creuzet, A. Friederich, and J. Chazelas. "Giant magnetoresistance of (001)Fe/(001)Cr magnetic superlattices". *Phys. Rev. Lett.* **61**, 2472, (1988).

[8] G. Binasch, P. Grunberg, F. Saurenbach, and W. Zinn. "Enhanced magnetoresistance in layered magnetic structures with antiferromagnetic interlayer exchange". *Phys. Rev. B* **39**, 4828, (1989).

[9] Albert Fert. "Nobel Lecture: Origin, development, and future of spintronics". *Rev. Mod. Phys.* **80**, 1517, (2008).

[10] Sarah M Thompson. "The discovery, development and future of GMR: The Nobel Prize 2007". *J. Phys. D: Appl. Phys.* **41**, 093001, (2008).

[11] S.S.P. Parkin, M. Hayashi, and L. Thomas. "Magnetic domain-wall racetrack memory". *Science* **320**, 190-194, (2008).

[12] M. Hayashi, L. Thomas, R. Moriya, C. Rettner, and S.S.P. Parkin. "Current-controlled magnetic domain-wall nanowire shift register". *Science* **320**, 209-211, (2008).

[13] J. A. Katine and E. E. Fullerton. "Device implications of spin-transfer torques". *J. Magn. Magn. Mater.* **320**, 1217, (2008).

[14] J. C. Slonczewski. "Current-driven excitation of magnetic multilayers". *J. Magn. Magn. Mater.* **159**, L1, (1996).

[15] L. Berger. "Emission of spin waves by a magnetic multilayer traversed by a current". *Phys. Rev. B* **54**, 9353, (1996).

[16] J. A. Katine, F. J. Albert, R. A. Buhrman, E. B. Myers, and D. C. Ralph. "Current-Driven Magnetization Reversal and Spin-Wave Excitations in Co/Cu/Co Pillars". *Phys. Rev. Lett.* **84**, 3149, (2000).

[17] D.C. Ralph and M.D. Stiles. "Spin transfer torques". *J. Magn. Magn. Mater.* **320**, 1190, (2008).

[18] J. Z. Sun. "Spin angular momentum transfer in currentperpendicular nanomagnetic junctions". *IBM J. RES. & DEV. VOL.* **50**, 81-100, (2006).

[19] P. M. Haney, R. A. Duine, A. S. Nunez, and A. H. MacDonald. "Current-induced torques in magnetic metals: Beyond spin-transfer". *J. Magn. Magn. Mater.* **320**, 1300-1311, (2008).

[20] A. Brataas, A. D. Kent and H. Ohno. "Current-induced torques in magnetic materials". *Nat. Mat.* **11**, 372, (2012).

[21] Y. Tserkovnyak, A. and G. E. W. Bauer. "Theory of current-driven magnetization dynamics in inhomogeneous ferromagnets". *J. Magn. Magn. Mater.* **320**, 1282-1292, (2008).

[22] J.Z. Sun and D.C. Ralph. "Magnetoresistance and spin-transfer torque in magnetic tunnel junctions". *J. Magn. Magn. Mater.* **320**, 1227-1237, (2008).

[23] J.C. Slonczewski and J.Z. Sun. "Theory of voltage-driven current and torque in magnetic tunnel junctions". *J. Magn. Magn. Mater.* **310**, 169-175, (2007).

[24] J. Grollier, V. Cros, A. Hamzic, J. M. George, H. Jaffres, A. Fert, G. Faini, J. Ben Youssef, and H. Legall. "Spin-polarized current induced switching in Co/Cu/Co pillars". *Appl. Phys. Lett.* **78**, 3663, (2001).

[25] D. Chiba, Y. Sato, T. Kita, F. Matsukura, and H. Ohno. "Current-Driven Magnetization Reversal in a Ferromagnetic Semiconductor (Ga,Mn)As/GaAs/(Ga,Mn)As Tunnel Junction". *Phys. Rev. Lett.* **93**, 216602, (2004).

[26] H. Ohno and T. Dietl. "Spin-transfer physics and the model of ferromagnetism in (Ga,Mn)As". *J. Magn. Magn. Mater.* **320**, 12931299, (2008).

[27] X. Jiang, L. Gao, J. Z. Sun, and S. S. P. Parkin. "Temperature Dependence of Current-Induced Magnetization Switching in Spin Valves with a Ferrimagnetic CoGd Free Layer". *Phys. Rev. Lett.* **97**, 217202, (2006).

[28] Z. Wei, A. Sharma, A. S. Nunez, P. M. Haney, R. A. Duine1, J. Bass, A. H. MacDonald, and M. Tsoi. "Changing Exchange Bias in Spin Valves with an Electric Current". *Phys. Rev. Lett.* **98**, 116603, (2007).

[29] Y. Kajiwara, K. Harii, S. Takahashi, J. Ohe, K. Uchida, M. Mizuguchi, H. Umezawa, H. Kawai, K. Ando, K. Takanashi, S. Maekawa and E. Saitoh. "Transmission of electrical signals by spin-wave interconversion in a magnetic insulator". *Nature* **464**, 262-266, (2010).

[30] Lei Lu, Yiyan Sun, Michael Jantz, and Mingzhong Wu. "Control of Ferromagnetic Relaxation in Magnetic Thin Films through Thermally Induced Interfacial Spin Transfer". *Phys. Rev. Lett.* **108**, 257202, (2012).

[31] M. Tsoi, A. G. M. Jansen, J. Bass, W.-C. Chiang, M. Seck, V. Tsoi, and P. Wyder. "Excitation of a Magnetic Multilayer by an Electric Current". *Phys. Rev. Lett.* **80**, 42814284, (1998).

[32] E. B. Myers, D. C. Ralph, J. A. Katine, R. N. Louie, and R. A. Buhrman. "Current-Induced switching of domains in magnetic multilayer devices". *Science* **285**, 867, (1999).

[33] W. H. Rippard, M. R. Pufall, S. Kaka, S. E. Russek, and T. J. Silva. "Directcurrent induced dynamics in Co90Fe10/Ni80Fe20 point contacts". *Phys. Rev. Lett.* **92**, 027201, (2004).

[34] W. H. Rippard,M. R. Pufall, S. Kaka, T. J. Silva, and S. E. Russek. "Currentdriven microwave dynamics in magnetic point contacts as a function of applied field angle". *Phys. Rev. B* **70**, 100406(R), (2004).

[35] I. N. Krivorotov, N. C. Emley, J. C. Sankey, S. I. Kiselev, D. C. Ralph, and R. A. Buhrman. "Time-domain measurements of nanomagnet dynamics driven by spin-transfer torques". *Science* **307**, 228, (2005).

[36] G. D. Fuchs, N. C. Emley, I. N. Krivorotov, P. M. Braganca, E. M. Ryan, S. I. Kiselev, J. C. Sankey, D. C. Ralph, R. A. Buhrman, and J. A. Katine. "Spin-transfer effects in nanoscale magnetic tunnel junctions". *Appl. Phys. Lett.* **85**, 1205, (2005).

[37] Y. Huai, F. Albert, P. Nguyen, M. Pakala, and T. Valet. "Observation of spin-transfer switching in deep submicron-sized and low-resistance magnetic tunnel junctions". *Appl. Phys. Lett.* **84**, 3118, (2004).

[38] A. M. Deac, A. Fukushima, H. Kubota, H. Maehara, Y. Suzuki, S. Yuasa, Y. Nagamine, K. Tsunekawa, D. D. Djayaprawira, and N. Watanabe. "Bias-driven high-power microwave emission from MgO-based tunnel magnetoresistance devices". *Nat. Phys.* **4**, 803, (2008).

[39] Tao Yang, T. Kimura and Y. Otani. "Giant spin-accumulation signal and pure spin-current-induced reversible magnetization switching". *Nature Phys.* **4**, 851, (2008).

[40] Y. Otani and T. Kimura. "Manipulation of spin currents in metallic systems". *Phil. Trans. R. Soc. A* **369**, 31363149, (2011).

[41] J. M. Slaughter. "Materials for Magnetoresistive Random Access Memory". *Annu. Rev. Mater. Res.* **39**, 277-296, (2009).

[42] T. M. Maffitt, J. K. DeBrosse, J. A. Gabric, E. T. Gow, M. C. Lamorey, J. S. Parenteau, D. R. Willmott, M. A. Wood and W. J. Gallagher. "Design considerations for MRAM". *IBM J. RES. & DEV. VOL.* **50**, 25-39, (2006).

[43] W. J. Gallagher and S. S. P. Parkin. "Development of the magnetic tunnel junction MRAM at IBM: From first junctions to a 16-Mb MRAM demonstrator chip". *IBM J. RES. & DEV. VOL.* **50**, 5-23, (2006).

[44] T.J. Silva and W.H. Rippard. "Developments in nano-oscillators based upon spin-transfer point-contact devices". *J. Magn. Magn. Mater.* **320**, 1260-1271, (2008).

[45] D. Berkov and J. Miltat. "Spin-torque driven magnetization dynamics: Micromagnetic modeling". *J. Magn. Magn. Mater.* **320**, 1238, (2008).

[46] A. Slavin and V. Tiberkevich. "Nonlinear auto-oscillator theory of microwave generation by spin-polarized current". *IEEE Trans. Magn.* **45**, 1875, (2009).

[47] B. Behin-Aein, D. Datta, S. Salahuddin and S. Datta. "Proposal for an all-spin logic device with built-in memory". *Nature Nanotechnology* **5**, 266-270, (2010).

[48] Igor Zutic and Michael Fuhrer. "Spintronics: A path to spin logic". *Nature Phys.* **1**, 85 - 86, (2005).

[49] G. S. D. Beach, M. Tsoi and J. L. Erskine. "Current-induced domain wall motion". *J. Magn. Magn. Mater.* **320**, 1272-1281, (2008).

[50] G. Hrkac, J. Dean and D. A. Allwood. "Nanowire spintronics for storage class memories and logic". *Phil. Trans. R. Soc. A* **369**, 3214-3228, (2011).

[51] M. D. Stiles and A. Zangwill. "Anatomy of spin-transfer torque". *Phys. Rev. B* **66**, 014407, (2002).

[52] K. Xia, P. J. Kelly, G. E. W. Bauer, A. Brataas, and I. Turek. "Spin torques in ferromagnetic/normal-metal structures". *Phys. Rev. B* **65**, 220401(R), (2002).

[53] Jiang Xiao, A. Zangwill,and M. D. Stiles. "Boltzmann test of Slonczewski's theory of spin-transfer torque". *Phys. Rev. B* **70**, 172405, (2004).

[54] F. J. Albert, J. A. Katine, R. A. Buhrman, and D. C. Ralph. "Spin-polarized current switching of a Co thin film nanomagnet". *Appl. Phys. Lett.* **77**, 3809, (2000).

[55] Keith Gilmore, Ion Garate, Allan H. MacDonald, and M. D. Stiles. "First-principles calculation of the nonadiabatic spin transfer torque in Ni and Fe". *Phys. Rev. B* **84**, 224412, (2011).

[56] G. D. Fuchs, J. C. Sankey, V. S. Pribiag, L. Qian, P. M. Braganca, A. G. F. Garcia, E. M. Ryan, Z. Li, O. Ozatay, D. C. Ralph, and R. A. Buhrman. "Spin-torque ferromagnetic resonance measurements of damping in nanomagnets". *Appl. Phys. Lett.* **91**, 062507, (2007).

[57] J. C. Sankey, Y. Cui, J. Z. Sun, J. C. Slonczewski, R. A. Buhrman, and D. C. Ralph. "Measurement of the spin-transfer-torque vector inmagnetic tunnel junctions". *Nat. Phys.* **4**, 67, (2008).

[58] H. Kubota, A. Fukushima, K. Yakushiji, T. Nagahama, S. Yuasa, K. Ando, H. Maehara, Y. Nagamine, K. Tsunekawa, D. D. Djayaprawira, N. Watanabe, and Y. Suzuki. "Quantitative measurement of voltage dependence of spin-transfer torque in MgO-based magnetic tunnel junctions". *Nat. Phys.* **4**, 37, (2008).

[59] S.-C. Oh, S.-Y. Park, A. Manchon, M. Chshiev, J.-H. Han, H.-W. Lee, J.-E. Lee, K.-T. Nam, Y. Jo, Y.-C. Kong, B. Dieny and K.-J. Lee. "Bias-voltage dependence of perpendicular spin-transfer torque in asymmetric MgO-based magnetic tunnel junctions". *Nature Physics* **5**, 898, (2009).

[60] S. Petit, C. Baraduc, C. Thirion, U. Ebels, Y. Liu, M. Li, P. Wang, and B. Dieny. "Spin-Torque Influence on the High-Frequency Magnetization Fluctuations in Magnetic Tunnel Junctions". *Phys. Rev. Lett.* **98**, 077203, (2007).

[61] F. J. Albert, N. C. Emley, E. B. Myers, D. C. Ralph, and R. A. Buhrman. "Quantitative Study of Magnetization Reversal by Spin-Polarized Current in Magnetic Multilayer Nanopillars". *Phys. Rev. Lett.* **89**, 226802, (2002).

[62] W. H. Butler, X. Zhang, T. C. Schulthess, and J. M. MacLaren. "Spindependent tunneling conductance of Fe—MgO—Fe sandwiches". *Phys. Rev. B* **63**, 054416, (2001).

[63] J. Mathon and A. Umerski. "Theory of tunneling magnetoresistance of an epitaxial Fe/MgO/Fe(001) junction". *Phys. Rev. B* **63**, 220403, (2001).

[64] S. Ikeda, J. Hayakawa, Y. Ashizawa, Y. M. Lee, K. Miura, H. Hasegawa, M. Tsunoda, F. Matsukura, and H. Ohno. "Tunnel magnetoresistance of 604% at 300K by suppression of Ta diffusion in CoFeB/MgO/CoFeB pseudo-spin-valves annealed at high temperature". *Appl. Phys. Lett.* **93**, 082508, (2008).

[65] Yaroslav Tserkovnyak, Arne Brataas and Gerrit E. W. Bauer. "Enhanced Gilbert Damping in Thin Ferromagnetic Films". *Phys. Rev. Lett.* **88**, 117601, (2002).

[66] Yaroslav Tserkovnyak, Arne Brataas, and Gerrit E. W. Bauer. "Dynamic exchange coupling and Gilbert damping in magnetic multilayers (invited)". *J. Appl. Phys.* **93**, 7534, (2003).

[67] A. Einstein and W. J. de Haas. "Experimental proof of the existence of Ampere's molecular currents". *Verh. Dtsch. Phys. Ges.* **17**, 152, (1915).

[68] P. Mohanty, G. Zolfagharkhani, S. Kettemann, and P. Fulde. "Spin-mechanical device for detection and control of spin current by nanomechanical torque". *Phys. Rev. B* **70**, 195301, (2004).

[69] A. A. Kovalev, G. E.W. Bauer, and A. Brataas. "Current-driven ferromagnetic resonance, mechanical torques, and rotary motion in magnetic nanostructures". *Phys. Rev. B* **75**, 014430, (2007).

[70] Guiti Zolfagharkhani, Alexei Gaidarzhy, Pascal Degiovanni, Stefan Kettemann, Peter Fulde and Pritiraj Mohanty. "Nanomechanical detection of itinerant electron spin flip". *Nature Nanotech.* **3**, 720, (2008).

[71] Paul M. Haney and M. D. Stiles. "Current-Induced Torques in the Presence of Spin-Orbit Coupling". *Phys. Rev. Lett.* **105**, 126602, (2010).

[72] Ioan M. Miron, Kevin Garello, Gilles Gaudin, Pierre-Jean Zermatten, Marius V. Costache, Stephane Auffret, Sebastien Bandiera, Bernard Rodmacq, Alain Schuhl,and Pietro Gambardella. "Perpendicular switching of a single ferromagnetic layer induced by in-plane current injection". *Nature* **476**, 189-193, (2011).

[73] L. Q. Liu, C.-F. Pai, Y. Li, H. W. Tseng, D. C. Ralph, and R. A. Buhrman. "Spin-Torque Switching with the Giant Spin Hall Effect of Tantalum". *Science* **336**, 555, (2012).

[74] Luqiao Liu, O. J. Lee, T. J. Gudmundsen, D. C. Ralph and R. A. Buhrman. "Magnetic switching by spin torque from the spin Hall effect". *Phys. Rev. Lett.* **109**, 096602, (2012).

[75] A. Manchon. "Spin Hall effect versus Rashba torque: a Diffusive Approach". *arXiv:1204.4869*.

[76] Petersena, P. Hedegardb. "A simple tight-binding model of spinorbit splitting of sp-derived surface statesL". *Surface Science* **459**, 49-56, (2000).

[77] A. Manchon and S. Zhang. "Theory of nonequilibrium intrinsic spin torque in a single nanomagnet". *Phys. Rev. B* **78**, 212405, (2008).

[78] A. Manchon and S. Zhang. "Theory of spin torque due to spin-orbit coupling". *Phys. Rev. B* **79**, 094422, (2009).

[79] A. Matos-Abiague and R. L. Rodriguez-Suarez . "Spin-orbit coupling mediated spin torque in a single ferromagnetic layer". *Phys. Rev. B* **80**, 094424, (2009).

[80] Xuhui Wang and Aurelien Manchon. "Diffusive Spin Dynamics in Ferromagnetic Thin Films with a Rashba Interaction". *Phys. Rev. Lett.* **108**, 117201, (2012).

[81] K.-W. Kim, S.-M. Sea, J. Ryu, K.-J. Lee, and H.-W. Lee. "Magnetization dynamics induced by in-plane currents in ultrathin magnetic nanostructures with Rashba spin-orbit coupling". *Phys. Rev. B* **85**, 180404(R, (2012).

[82] J. E. Hirsch. "Spin Hall Effect". *Phys. Rev. Lett.* **83**, 1834, (1999).

[83] Y. K. Kato, R. C. Myers, A. C. Gossard and D. D. Awschalom. "Observation of the Spin Hall Effect in Semiconductors". *Science* **306**, 1910-1913, (2004).

[84] S. O. Valenzuela and M. Tinkham. "Electrical detection of spin currents: The spin-current induced Hall effect(invited)". *J. Appl. Phys.* **101**, 09B103, (2007).

[85] Tomas Jungwirth, Jorg Wunderlich and Kamil Olejnik. "Spin Hall effect devices". *Nat. Mat.* **11**, 382, (2012).

[86] S. Ikeda, J. Hayakawa, Y. M. Lee, F. Matsukura, Y. Ohno, T. Hanyu, and H. Ohno. "Magnetic Tunnel Junctions for Spintronic Memories and Beyond". *IEEE Trans. Electron Devices* **54**, 9911002, (2007).

[87] L. Berger. "Multilayer configuration for experiments of spin precession induced by a dc current". *J. Appl. Phys.* **93**, 7693, (2003).

[88] G. D. Fuchs, I. N. Krivorotov, P. M. Braganca, N. C. Emley, A. G. F. Garcia, D. C. Ralph, and R. A. Buhrman. "Adjustable spin torque in magnetic tunnel junctions with two fixed layers". *Appl. Phys. Lett.* **86**, 152509, (2005).

[89] P. M. Braganca, I. N. Krivorotov, O. Ozatay, A. G. F. Garcia, N. C. Emley, J. C. Sankey, D. C. Ralph, and R. A. Buhrman. "Reducing the critical current

for short-pulse spin-transfer switching of nanomagnets". *Appl. Phys. Lett.* **87**, 112507, (2005).

[90] L. Liu, T. Moriyama, D. C. Ralph, and R. A. Buhrman. "Reduction of the spin-torque critical current by partially canceling the free layer demagnetization field". *Appl. Phys. Lett.* **94**, 122508, (2009).

[91] S. Mangin, D. Ravelosona, J. A. Katine, M. J. Carey, B. D. Terris, and E. E. Fullerton. "Current-induced magnetization reversal in nanopillars with perpendicular anisotropy". *Nat. Mater.* **5**, 210, (2006).

[92] S. Mangin, Y. Henry, D. Ravelosona, J. A. Katine, and Eric E. Fullerton. "Reducing the critical current for spin-transfer switching of perpendicularly magnetized nanomagnets". *Appl. Phys. Lett.* **94**, 012502, (2009).

[93] S. Ikeda, K. Miura, H. Yamamoto, K. Mizunuma, H. D. Gan, M. Endo, S. Kanai, J. Hayakawa, F. Matsukura and H. Ohno. "A perpendicular-anisotropy CoFeBMgO magnetic tunnel junction". *Nature Mat.* **9**, 721724, (2010).

[94] D. C. Worledge, G. Hu, David W. Abraham, J. Z. Sun, P. L. Trouilloud, J. Nowak, S. Brown, M. C. Gaidis, E. J. O'Sullivan, and R. P. Robertazzi. "Spin torque switching of perpendicular Ta—CoFeB—MgO-based magnetic tunnel junctions". *Appl. Phys. Lett.* **98**, 022501, (2011).

[95] J. Z. Sun. "Spin-current interaction with a monodomain magnetic body: A model study". *Phys. Rev. B* **62**, 570, (2000).

[96] R. H. Koch, J. A. Katine, and J. Z. Sun. "Time-resolved reversal of spin-transfer switching in a nanomagnet". *Phys. Rev. Lett.* **92**, 088302, (2004).

[97] S. Garzon, L. Ye, R. A. Webb, T. M. Crawford, M. Covington, and S. Kaka. "Coherent control of nanomagnet dynamics via ultrafast spin torque pulses". *Phys. Rev. B* **78**, 180401(R), (2008).

[98] Y.-T. Cui, J. C. Sankey, C. Wang, K. V. Thadani, Z.-P. Li, R. A. Buhrman, and D. C. Ralph. "Resonant spin-transfer-driven switching of magnetic devices assisted by microwave current pulses". *Phys. Rev. B* **77**, 214440, (2008).

[99] A. D. Kent, B. Özyilmaz, and E. del Barco. "Spin-transfer-induced precessional magnetization reversal". *Appl. Phys. Lett.* **84**, 3897, (2004).

[100] C. Papusoi, B. Delat, B. Rodmacq, D. Houssameddine, J.-P. Michel, U. Ebels, R. C. Sousa, L. Buda-Prejbeanu, and B. Dieny. "100 ps precessional spin-transfer switching of a planar magnetic random access memory cell with perpendicular spin polarizer". *Appl. Phys. Lett.* **95**, 072506, (2009).

[101] H. Liu, D. Bedau, D. Backes, J. A. Katine, J. Langer and A. D. Kent. "Ultrafast switching in magnetic tunnel junction based orthogonal spin transfer devices". *Appl. Phys. Lett.* **97**, 242510, (2010).

[102] G. E. Rowlands, T. Rahman, J. A. Katine, J. Langer, A. Lyle, H. Zhao, J. G. Alzate, A. A. Kovalev, Y. Tserkovnyak, Z. M. Zeng, H. W. Jiang, K. Galatsis, Y. M. Huai, P. Khalili Amiri, K. L. Wang, I. N. Krivorotov, and J.-P. Wang. "Deep subnanosecond spin torque switching in magnetic tunnel junctions with combined in-plane and perpendicular polarizers". *Appl. Phys. Lett.* **98**, 102509, (2011).

[103] Y. Suzuki, H. Kubota, A. Tulapurkar, and T. Nozaki. "Spin control by application of electric current and voltage in FeCo-MgO junctions". *Phil. Trans. R. Soc. A* **369**, 3658-3678, (2011).

[104] X.-G. Zhang and W. H. Butler. "Large magnetoresistance in bcc Co/MgO/Co and FeCo/MgO/FeCo tunnel junctions". *Phys. Rev. B* **70**, 172407, (2004).

[105] S. S. P. Parkin, C. Kaiser, A. Panchula, P. M. Rice, B. Hughes, M. Samant, and S. Yang. "Giant tunnelling magnetoresistance at room temperature with MgO (100) tunnel barriers". *Nat. Mater.* **3**, 862, (2004).

[106] S. Yuasa, T. Nagahama, A. Fukushima, Y. Suzuki, and K. Ando. "Giant room-temperature magnetoresistance in single-crystal Fe/MgO/Fe magnetic tunnel junctions". *Nat. Mater.* **3**, 868, (2004).

[107] S. I. Kiselev, J. C. Sankey, I. N. Krivorotov, N. C. Emley, R. J. Schoelkopf, R. A. Buhrman, and D. C. Ralph. "Microwave oscillations of a nanomagnet driven by a spin-polarized current". *Nature* **425**, 380, (2003).

[108] Jiang Xiao, A. Zangwill, and M. D. Stiles. "Macrospin models of spin transfer dynamics". *Phys. Rev. B* **72**, 014446, (2005).

[109] A. A. Tulapurkar, Y. Suzuki, A. Fukushima, H. Kubota, H. Maehara, K. Tsunekawa, D. D. Djayaprawira, N. Watanabe, and S. Yuasa. "Spin torque diode effect in magnetic tunnel junctions". *Nature* **438**, 339, (2005).

[110] V. S. Pribiag, I. N. Krivorotov, G. D. Fuchs, P. M. Braganca, O. Ozatay, J. C. Sankey, D. C. Ralph, and R. A. Buhrman. "Magnetic vortex oscillator driven by d.c. spin-polarized current". *Nat. Phys.* **3**, 498, (2007).

[111] A. Dussaux, B. Georges, J. Grollier, V. Cros, A. V. Khvalkovskiy, A. Fukushima, M. Konoto, H. Kubota, K. Yakushiji, S. Yuasa, K.A. Zvezdin, K. Ando and A. Fert. "Large microwave generation from current-driven magnetic vortex oscillators in magnetic tunnel junctions". *Nat. Comms.* **1**, 8, (2010).

[112] X. W. Yu, V. S. Pribiag, Y. Acremann, A. A. Tulapurkar, T. Tyliszczak, K.W. Chou, B. Brauer, Z.-P. Li, O. J. Lee, P. G. Gowtham, D. C. Ralph, R. A. Buhrman, and J. Stohr. "Images of a Spin-Torque-Driven Magnetic Nano-Oscillator". *Phys. Rev. Lett.* **106**, 167202, (2011).

[113] D. Houssameddine, S. H. Florez, J. A. Katine, J. Michel, U. Ebels, D. Mauri, O. Ozatay, B. Delaet, B. Viala, L. Folks, B. D. Terris, and M. Cyrille. "Spin transfer induced coherent microwave emission with large power from nanoscale MgO tunnel junctions". *Appl. Phys. Lett.* **93**, 022505, (2008).

[114] D. Houssameddine, U. Ebels, B. Delat, B. Rodmacq, I. Firastrau, F. Ponthenier, M. Brunet, C. Thirion, J.-P. Michel, L. Prejbeanu-Buda, M.-C. Cyrille, O. Redon, and B. Dieny. "Spin-torque oscillator using a perpendicular polarizer and a planar free layer". *Nature Mater.* **6**, 447, (2007).

[115] J. C. Sankey, I.N. Krivorotov, S. I. Kiselev, P.M. Braganca, N. C. Emley, R. A. Buhrman, and D. C. Ralph. "Mechanisms limiting the coherence time of spontaneous magnetic oscillations driven by dc spin-polarized currents". *Phys. Rev. B* **72**, 224427, (2005).

[116] K. V. Thadani, G. Finocchio, Z. Li, O. Ozatay, J. C. Sankey, I. N. Krivorotov, Y. Cui, R. A. Buhrman, and D. C. Ralph. "Strong linewidth variation for spin-torque nano-oscillators as a function of in-planemagnetic field angle". *Phys. Rev. B* **78**, 024409, (2008).

[117] I. N. Krivorotov, D. V. Berkov, N. L. Gorn, N. C. Emley, J. C. Sankey, D. C. Ralph, and R. A. Buhrman. "Large-amplitude coherent spin waves excited by spin-polarized current in nanoscale spin valves". *Phys. Rev. B* **76**, 024418, (2007).

[118] Z. M. Zeng, P. Upadhyaya, P. Khalili Amiri, K. H. Cheung, J. A. Katine, J. Langer, K. L. Wang, and H. W. Jiang. "Enhancement of microwave emis-

sion in magnetic tunnel junction oscillators through in-plane field orientation". *Appl. Phys. Lett.* **99**, 032503, (2011).

[119] Z. M. Zeng, P. Khalili Amiri, I. Krivorotov, H. Zhao, J.-P. Wang, J. A. Katine, Y. Huai, J. Langer, K. Galatsis, K. L. Wang, and H. W. Jiang. "High-power spin-transfer oscillators based on perpendicular anisotropy in the free layer". *ACS Nano* **6 (7)**, 61156121, (2012).

[120] I. N. Krivorotov, N. C. Emley, R. A. Buhrman, and D. C. Ralph. "Time domain studies of very-large-angle magnetization dynamics excited by spin transfer torques". *Phys. Rev. B* **77**, 054440, (2008).

[121] Kyung-Jin Lee, Alina Deac, Olivier Redon, Jean-Pierre Nozieres and Bernard Dieny. "Excitations of incoherent spin-waves due to spin-transfer torque". *Nature Mat.* **3**, 877-881, (2004).

[122] J.-V. Kim, V. Tiberkevich, and A. Slavin. "Generation Linewidth of an Auto-Oscillator with a Nonlinear Frequency Shift: Spin-Torque Nano-Oscillator". *Phys. Rev. Lett.* **100**, 017207, (2008).

[123] S. Kaka, M. R. Pufall, W. H. Rippard, T. J. Silva, S. E. Russek, and J. A. Katine. "Mutual phase-locking of microwave spin torque nanooscillators". *Nature* **437**, 389, (2005).

[124] F. B. Mancoff, N. D. Rizzo, B. N. Engel, and S. Tehrani. "Phase-locking in double-point-contact spin-transfer devices". *Nature* **437**, 393, (2005).

[125] A. Ruotolo, V. Cros, B. Georges, A. Dussaux, J. Grollier, C. Deranlot, R. Guillemet, K. Bouzehouane, S. Fusil and A. Fert. "Phase-locking of magnetic vortices mediated by antivortices". *Nat. Nano.* **4**, 528, (2009).

[126] B. Georges, J. Grollier, M. Darques, V. Cros, C. Deranlot, B. Marcilhac, G. Faini, and A. Fert. "Coupling Efficiency for Phase Locking of a Spin Transfer Nano-Oscillator to a Microwave Current". *Phys. Rev. Lett.* **101**, 017201, (2008).

[127] M. Quinsat, J. F. Sierra, I. Firastrau, V. Tiberkevich, A. Slavin, D.Gusakova, L. D. Buda-Prejbeanu, M. Zarudniev, J.-P. Michel, U. Ebels, B. Dieny, M.-C. Cyrille, J. A. Katine, D. Mauri, and A. Zeltser. "Injection locking of tunnel junction oscillators to a microwave current". *Appl. Phys. Lett.* **98**, 182503, (2011).

[128] Sergei Urazhdin, Phillip Tabor, Vasil Tiberkevich and Andrei Slavin. "Fractional Synchronization of Spin-Torque Nano-Oscillators". *Phys. Rev. Lett.* **105**, 104101, (2010).

[129] Sergei Urazhdin, Vasil Tiberkevich and Andrei Slavin. "Parametric Excitation of a Magnetic Nanocontact by a Microwave Field". *Phys. Rev. Lett.* **105**, 237204, (2010).

[130] A. Slavin and Pavel Kabos. "Approximate Theory of Microwave Generation in a Current-Driven Magnetic Nanocontact Magnetized in an Arbitrary Direction". *IEEE Trans. Magn.* **41**, 1264, (2005).

[131] A. Slavin and V. Tiberkevich. "Excitation of spin waves by spin-polarized current in magnetic nano-structures". *IEEE Trans. Magn.* **44**, 1916, (2008).

[132] Joo-Von Kim, Q. Mistral, C. Chappert, V. S. Tiberkevich and A. Slavin. "Line Shape Distortion in a Nonlinear Auto-Oscillator Near Generation Threshold: Application to Spin-Torque Nano-Oscillators". *Phys. Rev. Lett.* **100**, 167201, (2008).

[133] V. Tiberkevich, I. N. Krivorotov, G. Gerhart, and A. Slavin. "Compensation of nonlinear phase noise in an in-plane-magnetized anisotropic spin-torque oscillator". *J. Magn. Magn. Mater.* **321**, L53, (2009).

[134] A. A. Tulapurkar, T. Devolder, K. Yagami, P. Crozat, C. Chappert, A. Fukushima, and Y. Suzuki. "Subnanosecond magnetization reversal in magnetic nanopillars by spin angular momentum transfer". *Appl. Phys. Lett.* **85**, 5358, (2004).

[135] S. Kaka, M. R. Pufall, W. H. Rippard, T. J. Silva, S. E. Russek, J. A. Katine, and M. Carey. "Spin transfer switching of spin valve nanopillars using nanosecond pulsed currents". *J. Magn. Magn. Mater.* **286**, 375, (2005).

[136] P. M. Braganca, O. Ozatay, A. G. F. Garcia, O. J. Lee, D. C. Ralph, and R. A. Buhrman. "Enhancement in spin-torque efficiency by nonuniform spin current generated within a tapered nanopillar spin valve". *Phys. Rev. B* **77**, 144423, (2008).

[137] T. Devolder, P. Crozat, J.-V. Kim, C. Chappert, K. Ito, J. A. Katine and M. J. Carey. "Magnetization switching by spin torque using subnanosecond current pulses assisted by hard axis magnetic field". *Appl. Phys. Lett.* **88**,152502, (2006).

[138] H. W. Schumacher, C. Chappert, P. Crozat, R. C. Sousa, P. P. Freitas, J. Miltat, J. Fassbender, and B. Hillebrands. "Phase Coherent Precessional Magnetization Reversal in Microscopic Spin Valve Elements". *Phys. Rev. Lett.* **90**, 017201, (2003).

[139] T. Seki, S. Mitani, K. Yakushiji, and K. Takanashi. "Magnetization reversal by spin-transfer torque in 90^o configuration with a perpendicular spin polarizer". *Appl. Phys. Lett.* **89**, 172504 , (2006).

[140] U. Ebels, D. Houssameddine, I. Firastrau, D. Gusakova, C. Thirion, B. Dieny, and L. D. Buda-Prejbeanu. "Macrospin description of the perpendicular polarizer-planar free-layer spin-torque oscillator". *Phys. Rev. B* **78**, 024436, (2008).

[141] I. Firastrau, D. Gusakova, D. Houssameddine, U. Ebels, M.-C. Cyrille, B. Delaet, B. Dieny, O. Redon, J.-Ch. Toussaint, and L. D. Buda-Prejbeanu. "Modeling of the perpendicular polarizer-planar free layer spin torque oscillator: Micromagnetic simulations". *Phys. Rev. B* **78**, 024437, (2008).

[142] F. Delille, A. Manchon, N. Strelkov, B. Dieny, M. Li, Y. Liu, and P. Wang and E. Favre-Nicolin. "Thermal variation of current perpendicular-to-plane giant magnetoresistance in laminated and nonlaminated spin valves". *J. Appl. Phys.* **100**,013912, (2006).

[143] J. Kurkijarvi. "Intrinsic Fluctuations in a Superconducting Ring Closed with a Josephson Junction". *Phys. Rev. B* **6**, 832, (1972).

[144] O. Ozatay, P. G. Gowtham, K. W. Tan, J. C. Read, K. A. Mkhoyan, M. G. Thomas, G. D. Fuchs, P. M. Braganca, E. M. Ryan, K. V. Thadani, J. Silcox, D. C. Ralph and R. A. Buhrman. "Sidewall oxide effects on spin-torque- and magnetic-field-induced reversal characteristics of thin-film nanomagnets". *Nat. Mater.* **7**, 567, (2008).

[145] Patrick. M. Braganca. "Material and structural enhancements to spin transfer phenomena in nanopillar spin-valve devices". *Ph.D. Dissertation, Cornell University*, (2008).

[146] Yongtao Cui. "Characterization of magnetic dynamics excited by spin transfer torque in a nanomagnet". *Ph.D. Dissertation, Cornell University*, (2012).

[147] K. J. Lee, O. Redon, and B. Dieny. "Analytical investigation of spin-transfer dynamics using a perpendicular-to-plane polarizer". *Appl. Phys. Lett.* **86**, 022505, (2005).

[148] K. Vahaplar, A. M. Kalashnikova, A. V. Kimel, D. Hinzke, U. Nowak, R. Chantrell, A. Tsukamoto, A. Itoh, A. Kirilyuk, and Th. Rasing. "Ultrafast Path for Optical Magnetization Reversal via a Strongly Nonequilibrium State". *Phys. Rev. Lett.* **103**, 117201, (2009).

[149] O. J. Lee, V. S. Pribiag, P. M. Braganca, P. G. Gowtham, D. C. Ralph, and R. A. Buhrman. "Ultrafast switching of a nanomagnet by a combined out-of-plane and in-plane polarized spin current pulse". *Appl. Phys. Lett.* **95**, 012506, (2009).

[150] O. J. Lee, D. C. Ralph, and R. A. Buhrman. "Spin-torque-driven ballistic precessional switching with 50 ps impulses". *Appl. Phys. Lett.* **99**, 102507, (2011).

[151] D. M. Pozar. "Microwave Engineering". *Wiley, New York*, (1998).

[152] J. C. Slonczewski. "Currents and torques in metallic magnetic multilayers". *J. Magn. Magn. Mater.* **247**, 324, (2002).

[153] J. Xiao, A. Zangwill, and M. D. Stiles. "Macrospin models of spin transfer dynamics". *Phys. Rev. B* **72**, 014446, (2005).

[154] M. J. Donahue and D. G. Porter. "OOMMF User's Guide, Version 1.0 (http://math.nist.gov/oommf/)". *National Institute of Standards and Technology Technical Report No. NISTIR 6376*, (1999).

[155] Y. Cui, G. Finocchio, C. Wang, J. A. Katine, R. A. Buhrman, and D. C. Ralph. "Single-shot time-domain studies of spin-torque-driven switching in magnetic tunnel junctions". *Phys. Rev. Lett.* **104**, 097201, (2010).

[156] Th. Gerrits , H. A. M. van den Berg , J. Hohlfeld , L. Bar L and Th. Rasing. "Ultrafast precessional magnetization reversal by picosecond magnetic field pulse shaping". *Nature* **418**, 509512, (2002).

[157] W. Bailey, P. Kabos, F. Mancoff, and S. Russek. "Control of magnetization dynamics in $Ni_{81}Fe_{19}$ thin films through the use of rare-earth dopants". *IEEE Trans. Magn.* **37**, 1749, (2001).

[158] N. C. Emley, I. N. Krivorotov, O. Ozatay, A. G. F. Garcia, J. C. Sankey, D. C. Ralph, and R. A. Buhrman. "Time-resolved spin-torque switching and enhanced damping in Permalloy/Cu/Permalloy spin-valve nanopillars". *Phys. Rev. Lett.* **96**, 247204, (2006).

[159] C. Wang, Y. Cui, J. A. Katine, R. A. Buhrman, and D. C. Ralph. "Time-resolved measurement of spin-transfer-driven ferromagnetic resonance and spin torque in magnetic tunnel junctions". *Nat. Phys.* **7**, 496, (2011).

[160] C. Boone, J. A. Katine, J. R. Childress, J. Zhu, X. Cheng, I. N. Krivorotov. "Experimental test of an analytical theory of spin-torque-oscillator dynamics". *Phys. Rev. B* **79**, 140404(R), (2009).

[161] B. Georges, J. Grollier, V. Cros, A. Fert, A. Fukushima, H. Kubota, K. Yakushijin, S. Yuasa, and K. Ando. "Origin of the spectral linewidth in nonlinear spin-transfer oscillators based on MgO tunnel junctions". *Phys. Rev. B* **80**, 060404(R), (2009).

[162] Ye. Pogoryelov,P. K. Muduli, S. Bonetti, Fred Mancoff, and Johan Akerman. "Spin-torque oscillator linewidth narrowing under current modulation". *Appl. Phys. Lett.* **98**, 192506, (2011).

[163] M. Quinsat, D. Gusakova, J. F. Sierra, J. P. Michel, D. Houssameddine, B. Delaet, M.-C. Cyrille, U. Ebels, B. Dieny, L. D. Buda-Prejbeanu, J. A. Katine, D. Mauri, A. Zeltser, M. Prigent, J.-C. Nallatamby, and R. Sommet. "Amplitude and phase noise of magnetic tunnel junction oscillators". *Appl. Phys. Lett.* **97**, 18207, (2010).

[164] Kiwamu Kudo, Tazumi Nagasawa, Rie Sato, and Koichi Mizushima. "Amplitude-phase coupling in a spin-torque nano-oscillator". *J. Appl. Phys.* **105**, 07D105, (2009).

[165] K. Mizushima, T. Nagasawa, K. Kudo, Y. Saito, and R. Sato. "Decrease of nonlinearity and linewidth narrowing in spin-transfer oscillators under the external field applied near the hard axis". *Appl. Phys. Lett.* **94**, 152501, (2009).

[166] Yisong Zhang, Hui Zhao, Andrew Lyle, and Jian-Ping Wang. "Power enhancement of angular polarizer spin torque oscillator in magnetic tunnel junction". *J. Appl. Phys.* **109**, 07C714, (2011).

[167] Jaivardhan Sinha, Masamitsu Hayashi, Yukiko K. Takahashi, Tomohiro Taniguchi, Maksim Drapeko, Seiji Mitani, and Kazuhiro Hono. "Large

amplitude microwave emission and reduced nonlinear phase noise in Co2Fe(Ge0.5Ga0.5) Heusler alloy based pseudo spin valve nanopillars". *Appl. Phys. Lett.* **99**, 162508, (2011).

[168] Kiwamu Kudo, Tazumi Nagasawa, Rie Sato, and Koichi Mizushima. "Measurement of nonlinear frequency shift coefficient in spin-torque oscillators based on MgO tunnel junctions". *Appl. Phys. Lett.* **95**, 022507, (2009).

[169] Giovanni Finocchio, Alessandro Prattella, Giancarlo Consolo, Luis Torres, Antonio Faba, Ermanno Cardelli and Bruno Azzerboni. "Reducing the Non-Linearities of a Spin-Torque Oscillator by Varying the Amplitude of the External Field Applied Along the In-Plane Hard-Axis". *IEEE Trans. Magn.* **46**, 1519, (2010).

[170] X. Zhu and J.G Zhu. "Angular dependence of the microwave excitation by direct current". *J. Appl. Phys.* **95**, 7318, (2004).

[171] O. J. Lee, P. M. Braganca, V. S. Pribiag, D. C. Ralph, and R. A. Buhrman. "A quasi-linear spin-torque nano-oscillator". *In Progress*, (2012).

[172] Zhiwei Hou, Zongzhi Zhang, Jianwei Zhang, and Yaowen Liu. "Modeling of spin-torque driven magnetization dynamics in a spin-valve with combined in-plane and out-of-plane polarizers". *Appl. Phys. Lett.* **99**, 222509, (2011).

[173] Yan Zhou, C. L. Zha, S. Bonetti, J. Persson, and Johan Akerman. "Spin-torque oscillator with tilted fixed layer magnetization". *Appl. Phys. Lett.* **96**, 262508, (2008).

[174] Hong Zhang, Zhiwei Hou, Jianwei Zhang, Zongzhi Zhang, and Yaowen Liu. "Precession frequency and fast switching dependence on the in-plane and out-of-plane dual spin-torque polarizers". *Appl. Phys. Lett.* **100**, 142409, (2012).

[175] J. H. Chang, H. H. Chen, and C. R. Chang. "Instabilities of a spin-valve system with perpendicular polarizer and in-plane bias field". *Phys. Rev. B* **83**,054425, (2011).

[176] A. Vaysset, C. Papusoi, L. D. Buda-Prejbeanu, S. Bandiera, M. Marins de Castro, Y. Dahmane, J.-C. Toussaint, U. Ebels, S. Auffret, R. Sousa, L. Vila,

and B. Dieny. "Improved coherence of ultrafast spin-transfer-driven precessional switching with synthetic antiferromagnet perpendicular polarizer". *Appl. Phys. Lett.* **98**,242511, (2011).

[177] I. M. Miron, Gilles Gaudin, S. Auffret, B. Rodmacq, A. Schuhl, S. Pizzini, J. Vogel, and P. Gambardella. "Current-driven spin torque induced by the Rashba effect in a ferromagnetic metal layer". *Nature Mater.* **9**, 230, (2010).

[178] U. H. Pi, K. W. Kim, J. Y. Bae, S. C. Lee, Y. J. Cho, K. S. Kim, and S. Seo. "Tilting of the spin orientation induced by Rashba effect in ferromagnetic metal layer". *Appl. Phys. Lett.* **97**, 162507, (2010).

[179] T. Suzuki, S. Fukami, N. Ishiwata, M. Yamanouchi, S. Ikeda, N. Kasai, and H. Ohno. "Current-induced effective field in perpendicularly magnetized Ta/CoFeB/MgO wire". *Appl. Phys. Lett.* **98**, 142505, (2011).

[180] K. Ando, S. Takahashi, K. Harii, K. Sasage, J. Ieda, S. Maekawa, and E. Saitoh. "Electric Manipulation of Spin Relaxation Using the Spin Hall Effect". *Phys. Rev. Lett.* **101**, 036601, (2008).

[181] L. Q. Liu, T. Moriyama, D. C. Ralph, and R. A. Buhrman. "Spin-Torque Ferromagnetic Resonance Induced by the Spin Hall Effect". *Phys. Rev. Lett.* **106**, 036601, (2011).

[182] J. Z. Sun, R. P. Robertazzi, J. Nowak, P. L. Trouilloud, G. Hu, D. W. Abraham, M. C. Gaidis, S. L. Brown, E. J. O' Sullivan, W. J. Gallagher, and D. C. Worledge. "Effect of subvolume excitation and spin-torque efficiency on magnetic switching". *Phys. Rev. B.* **84**, 064413, (2011).

[183] H. Sato, M. Yamanouchi, K. Miura, S. Ikeda, R. Koizumi, F. Matsukura, H. Ohno. "CoFeB Thickness Dependence of Thermal Stability Factor in CoFeB/MgO Perpendicular Magnetic Tunnel Junctions". *IEEE Magn. Lett.* **3**, 3000204, (2012).

[184] C. M. Schneider, P. Bressler, P. Schuster, J. Kirschner, J. J. de Miguel and R. Miranda. "Curie Temperature of Ultrathin Films of fcc Cobalt Epitaxially Grown on Atomically Flat Cu(100) Surfaces". *Phys. Rev. Lett.* **64**, 1059, (1990).

[185] P. J. Metaxas, J. P. Jamet, A. Mougin, M. Cormier, J. Ferre, V. Baltz, B. Rodmacq, B. Dieny, and R. L. Stamps. "Creep and Flow Regimes of Magnetic Domain-Wall Motion in Ultrathin Pt/Co/Pt Films with Perpendicular Anisotropy". *Phys. Rev. Lett.* **99**, 217208, (2007).

[186] D. Chiba, S. Fukami, K. Shimamura, N. Ishiwata, K. Kobayashi and T. Ono. "Electrical control of the ferromagnetic phase transition in cobalt at room temperature". *Nature Mat.* **10**, 853, (2011).

[187] Stoner E. C. and Wohlfarth E. P. "A Mechanism of Magnetic Hysteresis in Heterogeneous Alloys". *Phil. Trans. R. Soc.* **240**, 599, (1948).

[188] D. Ravelosona, S. Mangin, Y. Lemaho, J. A. Katine, B. D. Terris, and Eric E. Fullerton. "Domain Wall Creation in Nanostructures Driven by a Spin-Polarized Current". *Phys. Rev. Lett.* **96**, 186604, (2006).

[189] T. Seki, S. Mitani, and K. Takanashi. "Nucleation-type magnetization reversal by spin-polarized current in perpendicularly magnetized FePt layers". *Phys. Rev. B.* **77**, 214414, (2008).

[190] E.J. Kondorsky. *J. Exp. Theor. Fiz.* **10**, 420, (1940).

[191] F. Schumacher. "On the modification of the Kondorsky function". *J. Appl. Phys.* **70**, 3184, (1991).

[192] Satoru Emori, David C. Bono, and Geoffrey S. D. Beach. "Interfacial current-induced torques in Pt/Co/GdOx". *Appl. Phys. Lett.* **101**, 042405, (2012).

[193] Naoto Nagaosa, Jairo Sinova, Shigeki Onoda, A. H. MacDonald, and N. P. Ong. "Anomalous Hall effect". *Rev. Mod. Phys.* **82**, 1539, (2010).

[194] Luqiao Liu, R. A. Buhrman, D. C. Ralph. "Review and Analysis of Measurements of the Spin Hall Effect in Platinum". *arXiv:1111.3702*.